TOPOLOGY OPTIMIZATION OF MULTISCALE STRUCTURES COUPLING FLUID, THERMAL AND MECHANICAL ANALYSIS

A Dissertation

Submitted to the Faculty

of

Purdue University

by

Tong Wu

In Partial Fulfillment of the

Requirements for the Degree

of

Doctor of Philosophy

May 2019

Purdue University

West Lafayette, Indiana

THE PURDUE UNIVERSITY GRADUATE SCHOOL
STATEMENT OF COMMITTEE APPROVAL

Dr. Andres Tovar, co-hair

Department of Mechanical and Energy Engineering

Dr. Jitesh Panchal, co-hair

School of Mechanical Engineering

Dr. Hazim El-Mounayri

Department of Mechanical and Energy Engineering

Dr. Carlos Larriba-Andaluz

Department of Mechanical and Energy Engineering

Dr. James K Guest

Department of Civil Engineering

Johns Hopkins University

Approved by:

Dr. Jie Chen

Head of the Graduate Program

TO MY FAMILY.

ACKNOWLEDGMENTS

Firstly, I would like to express my deepest appreciation to my advisor Prof. Andres Tovar for the constantly and convincingly conveyed a spirit of adventure in regard to research, and an enjoyment in regard to teaching. Without his guidance and persistent help this dissertation would not have been possible.

I would like to thank my co-advisor Prof. Jitesh Panchal for his support and guidance. I also would like to thank the members of the committee, Prof. Hazim El-Mounayri, Prof. Carlos Larriba-Andaluz and Prof. James K Guest, for their insightful comments and encouragement. My interaction with them has greatly enriched my graduate school experience.

I thank my fellow members of the Engineering Design Research Laboratory, Kai Liu, Sajjad Raeissi, T.J. Sego, Homero Valladares-Guerra, Joel Najmon, Prasad Tapkir, Prathamesh Chaudhari, Jennifer Solis Ocampo, Jaime Arcos, and Namrata Upadhyaya. They have been indispensable in providing a stimulating and nurturing environment for my work.

Finally, I would like to thank my mother Li Gao and my father Yafei Wu for supporting me spiritually throughout writing this thesis and my my life in general.

TABLE OF CONTENTS

Page

Page

LIST OF TABLES

LIST OF FIGURES

Figure Page

Figure Page

Figure Page

ABSTRACT

Tong, Wu Ph.D., Purdue University, May 2019. Topology Optimization of Multiscale Structures Coupling Fluid, Thermal and Mechanical Analysis. Major Professors: Andres Tovar and Jitesh H. Panchal.

The objective of this dissertation is to develop new methods in the areas of multiscale topology optimization, thermomechanical topology optimization including heat convection, and thermal-fluid topology optimization. The dissertation mainly focuses on developing five innovative topology optimization algorithms with respect to structure and multistructure coupling fluid, thermal and mechanical analysis, in order to solve customary design requirements. Most of algorithms are coded as in-house code in MATLAB.

In Chapter One, a brief introduction of topology optimization, a brief literature review and the objective is presented. Five innovative algorithms are illustrated in Chapter Two to Six. From Chapter Two to Four, the methods with respect to multiscale approach are presneted. and Chapter Five and Six aims to contribute further research associated with topology optimization considering heat convection. In Chapter Two, a multiphse topology optimization of thermomechanical structures is presented, in which the optimized structure is composed of several phases of prescribed lattice unit cells. Chapter Three presents a Multiscale, thermomechanical topology optimization of self-supporting cellular structures. Each lattice unit cell have a optimised porousity and diamond shape that benefit additive manufacturing. In Chapter Four, the multiscale approach is extended to topology optimization involved with fluid mechanics problem to design optimized micropillar arrays in microfludics devices. The optimised micropillars minimize the energy loss caused by local fluid drag force. In Chapter Five, a novel thermomechanical topology optimization is developed, in order to generate optimized multifunctional lattice heat transfer structure. The algorithm approximate convective heat transfer by design-dependent heat source and natural convection. In Chapter Six, an improved thermal-fluid topology optimization method

is created to flexibly handle the changing of thermal-fluid parameters such as external heat source, Reynolds number, Prandtl number and thermal diffusivity. The results show the changing of these parameters lead versatile optimized topologies. Finally, the summary and recommendations are presented in Chapter Seven.

1. INTRODUCTION

In this Chapter, an introduction and motivation relevent to this dissertation. First, a summary of topology optimization is presented, where several key concepts with respect to the dissertation contexts are introudced. Next, a literature review of four key concepts is provided, including topology optimization considering meta-material scale and multi-scale modeling, as well as topology optimization coupling thermo-mechanical analysis and topology optimization coupling thermal-fluid analysis. Finally, the motivation, the objective and outline of this dissertation are described.

1.1 Topology optimization: the most flexible form of structural optimization

Structural optimization is the classical engineering subject of making an assemblage of materials sustain loads in the best way with respect to some anticipated performance, e.g. stiffness, temperature, or pressure drop. Methods for structural optimization can be divided into three groups depending on the geometric feature: size optimization; shape optimization; and topology optimization (Fig. 1.1) [1]. For size optimization, the design variables are the dimensions of a predefined design, i.e., the cross-sectional areas, thickness, or length of structural members. For shape optimization, the design variables control the form or contour of some part of the boundary of the structural domain. Imaging the state of a solid body is described by a set of partial differential equations, the optimization consists in choosing the integration domain for the differential equations in an optimal way without changing the connectivity [1]. Topology optimization is the most flexible form of structural optimization, which allows for the simultaneous control size, shape and topology. More specifically, Topology optimization of a solid structure involves the determination of features such as the number and location and shape of holes and the connectivity of the domain [2].

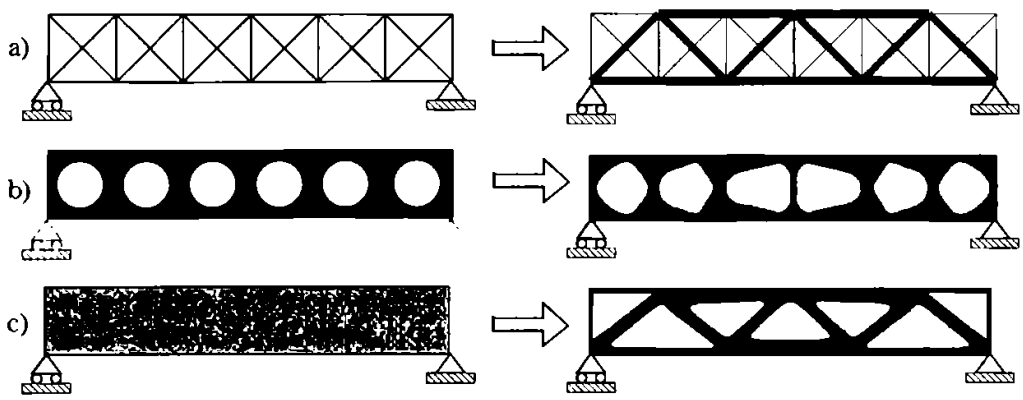

Figure 1.1.. Illustrations of (a) Size optimization (b) Shape optimization and (c) Topology optimization [2].

1.1.1 Material interpolation scheme

Topology optimization as it is recognized nowadays was established by Bendsøe and Kikuchi. Inspired by finite element analysis, topology optimization attributes a design variable associated with the material properties e.g., thickness, density, Young's modulus, heat transfer coefficient, to each of finite element. Then, the objective of optimization problem turns to find the values of these material property-related design variables that establishing a structure with best structural performance. Each design variable represented in the design domain takes the value one if the element is filled with material and zero otherwise. The most famous numerical methods for finding optimal distribution in space are known as density or SIMP (Solid Isotropic Microstructure with Penalization) approach, as well as homogenization approach [3, 4]. They are proposed by Bendsøe in early 1990s and extensively applied by Guedes, KiKuchi, Zhou, Rozvany and other scientists [5, 6]. These methods replace the 0-1 interger variables distribution with continuous variables, and then incorporate material interpolation functions containing penalty numbers or polynomial functions, to steers the solution to 0-1 values. An alternative material interpolation scheme is Rational approximation of material properties (RAMP) [7], which using a rather relaxed

penalization (Fig. 1.2).A solid-void material interpolation scheme can be extended to a numerical method enable to distribute two-materials in the design domain [8,9].

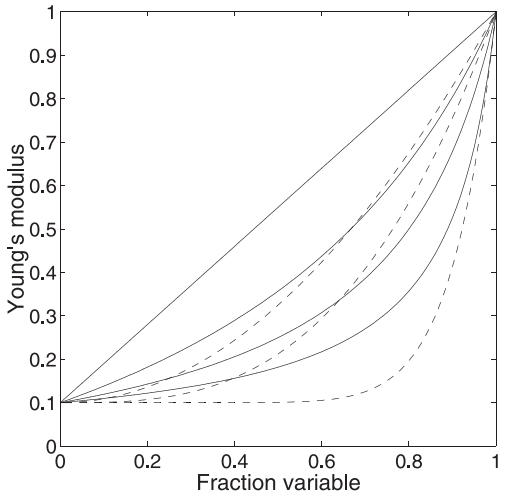

Figure 1.2.. A comparison of the SIMP model and the RAMP model when Young's modulus of a solid structure $E(\theta_0) = 1$ and minimum Young's modulus $E_{\min} = 0.1$. For SIMP, using penalty numbers $p = 2$, 3, 10, presented as dash lines; For RAMP, using penalty numbers $p = 0$, 1.5,4,9, presented as solid lines [7].

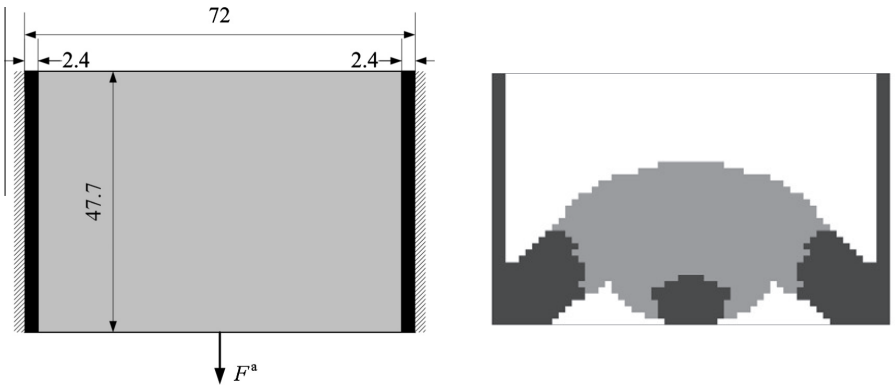

Figure 1.3.. A topology optimization result using two material interpolation scheme of a bi-clamped plane structure. Black and gray color indicates two different materials [10].

Numerical methods to distribute more than two materials have also been developed. These methods contain e.g. recursive multiphase material interpolation [10], uniform multiphase materials interpolation [11], active-phase algorithm [12] and cluster-based topology optimization [13].

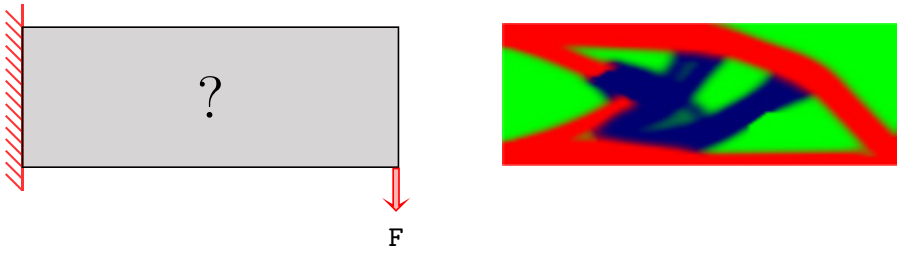

Figure 1.4.. A cantilever beam problem using three materials [12]. (For green color material: Young's modulus $E(\boldsymbol{\theta}_0)$=10^{-9}, Poisson ratio $\nu(\boldsymbol{\theta}_0)$=0.4; For blue color material: $E(\boldsymbol{\theta}_0)$=1, $\nu(\boldsymbol{\theta}_0)$= 0.2; For red color material: $E(\boldsymbol{\theta}_0)$=2, $\nu(\boldsymbol{\theta}_0)$=0.4.

1.1.2 Physics model and multiphysics model

Topology optimization is an iterative design process, where at each iteration step, the design variables are updated stem from physics models, which often discretized within finite element analysis. While finite element analysis is the most popular discretzation model, other discretization methods such as finite volume [14] and Lattice-Boltzmann method have also been successfully incorporated into topology optimization.

Topology optimization was devised within solving linear elastic model in solid mechanics, the method has since then been extended to advanced applications with wide ranges of physical phenomena. In solid mechanics, these applications include e.g., maximize and minimize dynamical response, maximize buckling load, minimize compliance with consideration of stress constraints and pressure load. Further, topology optimization with respect to non-linear finite element analysis models such as hyper-elastic [15–17], plastic [18–20]

and crashworthiness [21–23] have also been extensively studied. Beyond solid mechanics, topology optimization has been extended to heat transfer, fluidics, acoustics problems.

Especially, in recent year, topology optimization involves in multiphysics problems has attracted progressively interests from researchers. Multiphysics problems require modelling in several areas of physics, and the coupling of different physics fields [24–26]. A problem coupled two physics fields indicates that the solution from primary physics model affects the secondary physics model. Therefore, to solve a coupling multiphysics model, different physics models are required to be dependently solved in two types: they are solved either directly in a system assembled all the physics, or sequentially solved by passing first set of solution to a second set of field equations, which is solved then passed to a third set of equations, etc. Compared to a single physics model, a multiphysics model can accurately reflect the functionalities of numerous products in the many industries, such as civil and mechanical, aerospace, electrical and biomedical engineering. The coupling of physics fields generally include thermo-mechanical, thermal-fluid, fluid-structure interaction, electro-mechanical, electro-termal, electro-magneto-thermal etc. The products are varied from large scale aerospace, ground and naval vehicle systems, to smaller scale electronics, magnetic components, heat exchanger and motors, to microscale Microelectromechanical system (MEMS) and microfluidic devices. While it is appealing to exploit the strength of multiphysics models and incorporate them into topology optimization, it is also a challenging task, since it not only requires understanding all of the relevant physics in a particular problem, but also an appropriate programmed optimization module customizing the tackled multiphysics model. Nowadays, topology optimization involved multiphysics phenomena is a subject undergoing intense study and desiring further investigation, especially for thermo-mechanical, thermal-fluid, and other electromechanical systems [24].

1.1.3 Optimizer and sensitivity analysis

A topology optimization problem consists of from thousands to millions of design variables, which excludes many computational expensive optimization methods. In terms of

the low computational cost, first order optimization methods are often prefered to be utilized in the optimizer. In a first order method, analytical gradient of each design variables with respect to the objective function is required. In the objective function, the variables are often depended on each other in terms of finite element analysis models, makes the analytical gradient implicit and could not be easily derived. The procedures of deriving the analytical gradient is called sensitivity analysis. It is often a challenging yet critical task during the development a new topology optimization algorithm stem from non-linear physics or multiphysics model, which requires a comprehensive understanding of physics model and strong mathmatical background. A common used method in the sensitivity analysis called adjoint method. In this method, implicits gradients are eliminated by solving adjoint vectors in a Lagrangian function.

An alternative sensitivity analysis strategy is called level-set method [27]. This method is commonly used in image processing, moving boundary problems, fluid mechanics, etc. In topology optimization, level-set method aims to numerically tracking fronts and free boundaries of a structure by topological sensitivities and evolutional level-set functions, to obtain the optimal topology [28, 29]. It has been applied to topology optimization with respect to linear elasticity, heat conduction [30] and thermal-fluid problems [31, 32].

When the analytical gradient information is derived, it can be incorporated to commonly used first order optimizers e.g. such as Sequential Linear Programming (SLP) [33], or optimizers specifically created for structural mechanical problem e.g., CONLIN [34], Optimal Criteria (OC) [35], and Method of Moving Asymptotes (MMA) [36, 37]. However, for some reasons the analytical gradients are not always available. These reasons mainly include that the physics model is too complicated, developer has a knowlege gap, or numerical issues for solving adjoint vectors. To overcome the difficulties, considering of non-gradient based optimizers could be a substitution. These optimizers are mainly based on heuristics approach such as Hybrid Cellular Automata (HCA) [38], and evolutionary technique such as Bi-directional Evolutionary Structural Optimization (BESO) [39, 40].

1.1.4 Topology optimization considering additive manufacturing

Although remarkable design improvement could be made for the designs after topology optimization, the resulting topologies maybe so complex and irregular that impractical from conventional manufacturing point of view. Fortunately, the gradually enriched Additive Manufacturing (AM) technologies opens the possibility to overcome limitations of conventional manufacturing techniques. However, current AM still has requirements to the design's geomtries to ensure manufacturability. These requirements contain minimum feature size, manufacturable inclination angle, allowable bridging distance, and the robust accommodation of heat transfer during manufacturing process [41]. On the other hand, undesired geometries such as small inclination, long overhangs, and thin bars may appear in the optimized design. These structures are unstable during the AM process, additional material would be necessary to support them. As a result, the actual material usage is significantly increased. In addition, unwanted structures such as disconnected members may occur due to some inherent issues of the optimization and post-processing technique, and these flaws may be magnified resulting in an unfeasible product [42]. Therefore, topology optimization deserves further explorations taken in account of contemporary AM limitations.

Recently, some amendments of the density-based topology optimization can fill the gaps between topology optimization and additive manufacturing [42–44]. Zegard and Paulino alleviate the thin-bar and disconnected structure problem using specific filters [42]. Leary et al proposed a method that iteratively identify the regions infeasible to manufacture, and further optimize these regions to accommodate AM process [43]. Li et al combined additional constraints to improve structure connectivity [44]. An alternative strategy is the development of explicit topology optimization, from which optimal structural topology can be found by optimizing a set of explicit geometry parameters [45–47]. In addition, the AM constraints can be satisfied by representing the whole structure with properly designed lattice unit cells suitable for AM. These unit cells are created by inverse homogenization,

implicit surface modeling, image-based design etc [48, 49]. A Lattice structure can be also achieved by defining local volume constraint in the design domain [50].

1.2 Literature review

This dissertation aims to contribute to the exploration the area of multiscale, multiphysics topology optimizaiton associated with mechanical, thermal and fluid analysis. This area in general contains many research topic, some of them are still unexploited. To clarify the state of art of the research in this area, the following table is summarized. The first column identifies the specific single physics and multiphysics, and the second to the fourth row summarize the intensity of the resaech for each physics and representative articles, to best of author's knowledge. The non-quantative description of the research and development intensity, though inaccurate, provides an insight of the state of art of the dissertation theme.

It is well known that many research articles, open source code and commercial software are related to topology optimzation of elastic solid mechanics in a structural scale (macroscale). Also, in macroscale, numerous studies can be found related to topology optimization of non-linear solic mechanics and heat conduction. In comparision with these topics, less studies can be found with respect to heat transfer including convection and fluid mechanics. Similarly, only several studies can be found for topology optimization for a coupling field, such as thermo-mechanical, thermal-fluid and fluid-structure interaction[1]. Currently, no literature with respect to topology optimization of a thermal-fluid-structure problem has been found. In meta-material scale, as mentioned in Section 1.2.1, a majority of studies are related to elastic solid mechanics. Only a few of studies are related to non-linear solid mechanics, heat conduction, permeability, thermo-elastic, and multifunctional material that having maximized stiffness and permeability. Finally, most of multiscale approaches are related to elastic solid mechanics.

[1] A *Thermal-fluid* model aims to modeling convective heat transfer dependent on fluid field, while a *heat transfer including convection* model indicates the convection is independent of the fluid field.

Table 1.1.. State of art: multiscale, multiphysics topology optimizaiton associated with mechanical, thermal and fluid analysis. The contribution of this dissertation is marked in $\star$.

Physics	Structural scale (Macroscale)	Meta-material scale (Micro or mesoscale)	Multiscale (Multiscale)
Solid mechanics (Elastic)	Many	Some [51–56] $\star$	Several [57–68]
Solid mechanics (Non-linear)	Some [15–23]	Rare [69, 70]	No
Heat transfer (Conduction)	Some [30, 71–74]	Rare [75] $\star$	Rare
Heat transfer (Convection)	Several $\star$ [76–79]	No No	No No
Fluid mechanics (Laminar)	Several [14, 80–87]	Rare $\star$ [88]	No $\star$
Fluid mechanics (Turbulent) (Turbulent)	Rare [89, 90]	No	No
Thermo-mechanical	Several $\star$ [25, 26, 91–93]	Rare [8, 54]	No $\star$
Thermal-fluid	Several $\star$ [94–96] [24, 31, 32, 97–99]	No	No
Fluid-structure	Rare [100–102]	Rare [103, 104]	No
Thermal-fluid-structure	No	No	No

The contribution of this dissertation are related to five topics marked with stars in Table 1.1. The contribution includes new concepts, methods and improvement of existing model (Table 1.2). The details are described in Section 1.3. Before that, the following sec-

tions present a brief interview of four key concepts involved in this dissertation: Topology optimization considering meta-material scale and multiscale modeling, as well as topology optimization coupling thermo-mechanical analysis and topology optimization coupling thermal-fluid analysis.

Table 1.2.. Contribution of this dissertation: multiscale, multiphysics topology optimizaiton associated with mechanical, thermal and fluid analysis.

Physics	Structural scale (Macroscale)	Meta-material scale (Micro or mesoscale)	Multiscale (Multiscale)
Solid mechanics (Elastic)		New method	New concept
Heat transfer (Conduction)		New method	New concept
Heat transfer (Convection)	New physics		
Fluid mechanics (Laminar)		New method	New concept
Thermo-mechanical	New physics		New concept
Thermal-fluid	Model improvement		

1.2.1 Topology optimization in meta-material scale

The ideas of topology optimization in a structural scale can be applied to design the meta-material with tailored or extreme properties in a material scale. Optimal meta-materials indicate the material unit cell has a lattice or porous structure that benefit to a specific loading condition [51]. In general, these meta-materials are periodic, and their effective properties can be represented by an analysis of the smallest repetitive unit cell. Extensive experiments have demonstrate many lattice and porous meta-materials can have high multifunctional properties such as mechanical strength, stiffness, energy absoprtion, heat transfer and permeability simultaneously [105]. Numerically, the effective properties of these metamaterial can be found using homogenization method, however, the optimal properties and the related topologies of the meta-material are unknown at beginning, and should be

Table 1.3.. Design of meta-materials using inverse homogenization or similar topology optimization approaches.The description of Fig 1.5.

Physics	ID in Figure 1.5	Description
Solid mechanics	(A)-(a) & (A)-(b)	Max bulk modulus in 2D with two different initial designs [54]
(Elastic)	(A)-(c) & (A)-(d)	Max shear modulus in 2D with two different initial designs [107, 108]
	(A)-(e) & (A)-(f)	Min Poisson ratio in 2D with two different initial designs [108]
	(B)-(a)	Max bulk modulus in 3D [55]
	(B)-(b)	Max shear modulus in 3D [55]
	(B)-(b)	Min Poisson ratio in 3D [109]
Heat transfer	(C)-(a) & (C)-(b)	Max conductivity in 2D with two different initial designs [75]
(Conduction)	(C)-(c) & (C)-(d)	Max conductivity in 3D with two different initial designs [75]
Fluid mechanics	(D)-(a) to (D)-(c)	Max permeability in 2D with three different initial designs [88]
(Permeability)	(D)-(d) & (D)-(e)	Max permeability in 3D with two different initial designs [88]
Thermal expansion	(E)-(a)	Min thermal strain coefficient [8]
	(E)-(b)	Max bulk modulus for zero thermal expansion [8]
	(E)-(c)	Max isotropic thermal stress coefficient [8]
Structural damping	(F)-(a) & (F)-(b)	Max damping in 2D with two different initial designs [59]
Poroelasticity	(G)-(a) & (G)-(b)	Min average deflection with two different load cases [110]

sought to target with prescribed or extreme homogenized properties. The procedure to find the target properties and the related topologies is a special form of topology optimization, also called inverse homogenization [106]. In a discretized form, inverse homogenization or similar approaches can be formulated as a topology optimization for multiple load cases, with these homogenized properties served as objective functions. The target optimised properties for material design include e.g. extremal elastic properties [51–56, 107–109], thermal conductivity [75], thermal expansion properties [8, 9], permeability [88] as well as poroelasticity [110] and structural damping [59] properties (Fig 1.5 and Table 1.3).

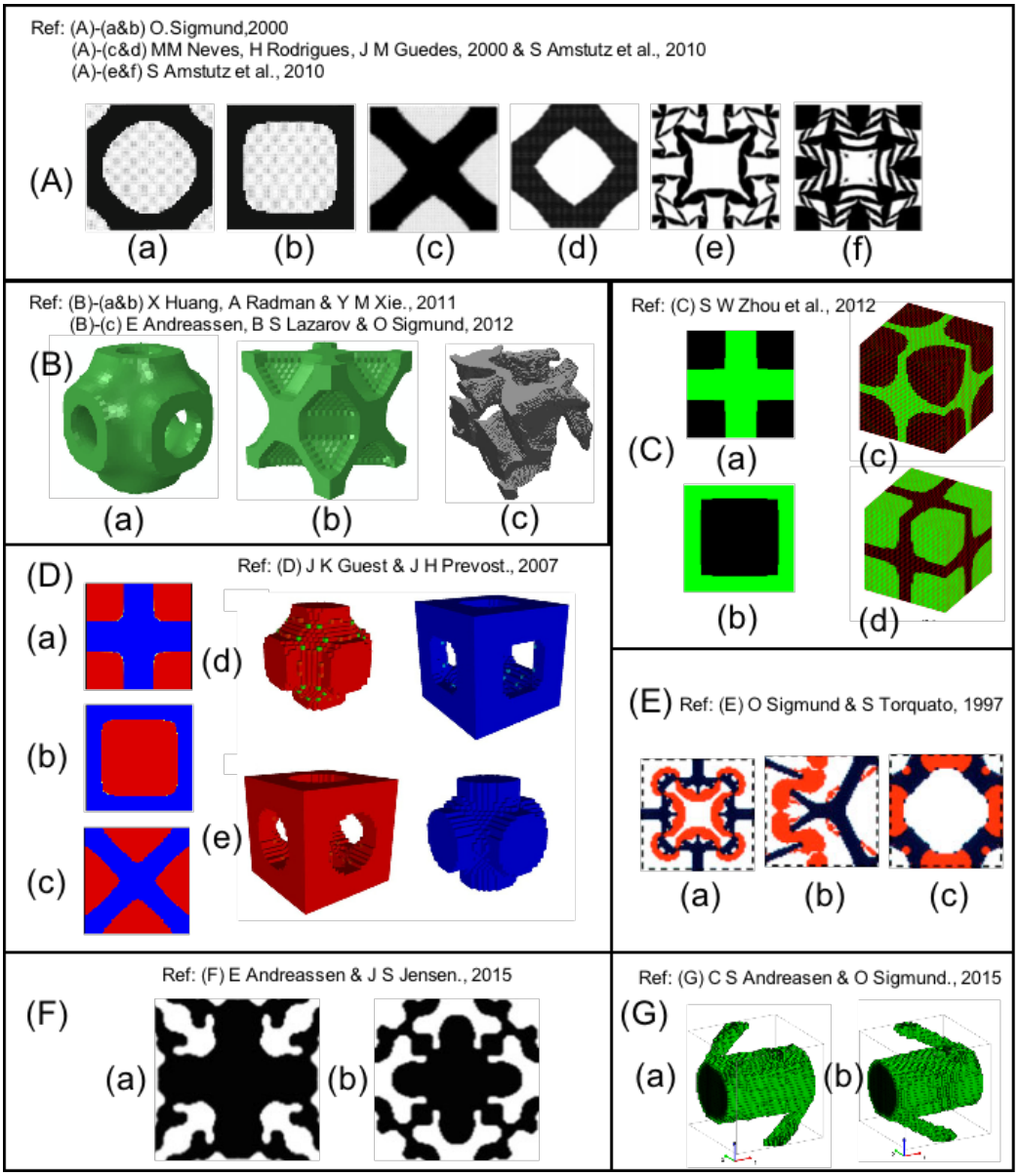

Figure 1.5.. Design of meta-materials using inverse homogenization or similar topology optimization approaches.The details description is shown in Table 1.3.

1.2.2 Topology optimization considering multiscale frameworks

Inspired by optimization of both structure (macroscale) and meta-material (mesoscale or microscale), some researchers proposed to use a multiscale frameworks to achieve an

optimal design in both scales [57–68]. A multiscale framework establishes a connection of information between the structural scale (macroscale) and meta-material scale (mesoscale or microscale), aims to find the appropriate topology of both the structure and the meta-materials. The method can also be utilized to determine the topology of the porous structure, when only the information of porosity is known in macroscale.

The existing multiscale frameworks include optimizing a macroscale structure with functionally graded materials [57–61]; concurrently obtaining a optimal macroscale structure composed of uniformly distributed cellular material [62–64]; and hierarchically optimizing structure and materials scales [65–68] (Fig 1.6 A-C). The results from first and second approaches are less optimized compared to the third option, but they can be easier manufactured using prevalent AM technologies [57, 58, 60]. Hierarchical optimization has been applied to reconstruction bone structure and the results have some similarities to organic bone structures [66–68]. This method has also be improved to solve non-linear elastic problem [111]. But this method is computational-expensive since every unit cell should be optimized. Besides, the structures generated by this approach is lack of connectivity and control of the minimum feature size, hence still can not be efficiently manufactured through current AM technologies. To overcome these difficulties, a specific multiscale finite element method has been utilized to allow the problem solved for detailed meta-materials configurations in macroscale model. This method enables to handle very large problems, but the macroscale model only contains limited meta-material phases [112] (Fig 1.6 D).

Some latest studies have been investigated to implement faster iterative linear solvers and multiscale finite element method to alleviate the computational load. Most of existing multiscale approaches are focus on pure mechanical boundary condition. Deng has included thermo-elastic load in a concurrent topology optimization [63]. Andreassen and Jensen established a multiphase topology optimization of structural damping (Fig. 1.7) [59]. But to the best of author's knowledge, few literature has investigated a multiscale topology approach involving heat transfer performance. In author's previous work, a multiscale topology optimization approach was applied to a heat sink with uniformly distributed heat source (Fig. 1.8), but further studies are still required to balance the thermal perfor-

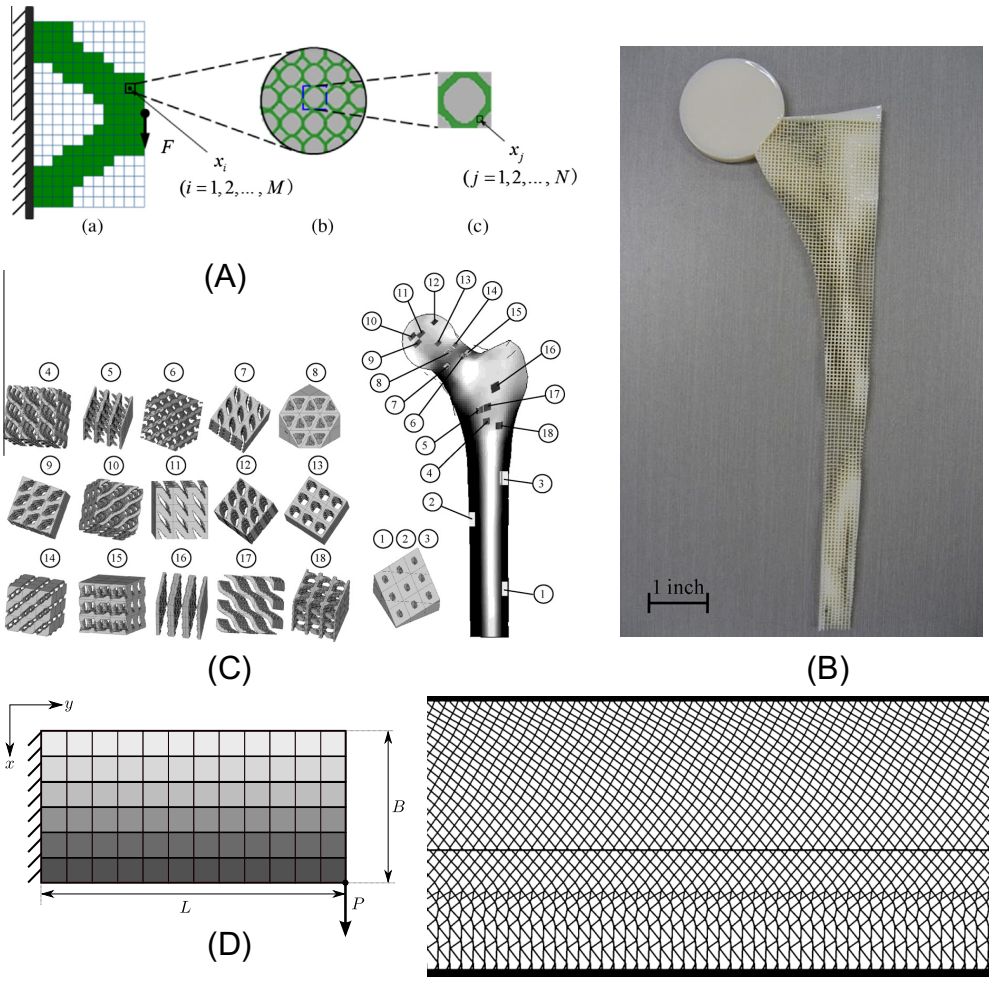

Figure 1.6.. Several multiscale topology optimization approaches: (A) concurrent topology optimization [64] (B) optimizing a structure using functionally graded material [57], (C) hierarchical approach [67] and (D) multiscale finite element method based topology optimization [112].

mance and manufacturability for the final design. Other than this, topology optimization using a multiscale approach applied to other physics remains scarce and worth to exploration. An example the author proposed in this dissertation is the optimization of micropillar arrays. Current micropillar arrays commonly utilized in microfluidic devices in operations including cell sorting, bio-sensor detectors, microchannel heat sinks are cylindrical. However, the viscous fluid drag in cylindrical micropillar arrays remains large enough to

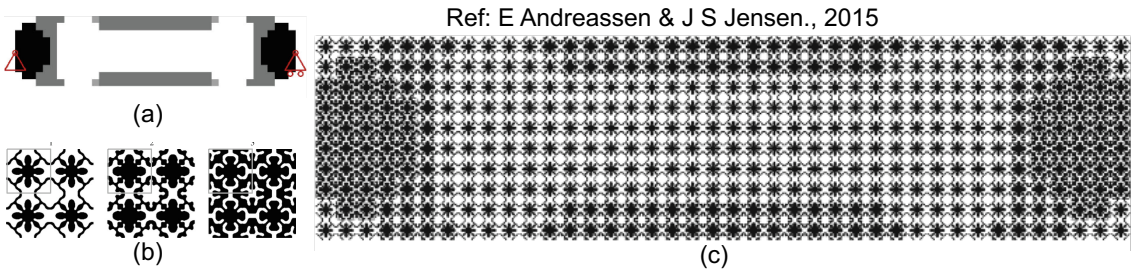

Figure 1.7.. A multiphase topology optimization of structural damping: (a) Macroscale topology optimization, (b) Topology optimization of meta-materials (meso-scale) (c) Multiscale model [59].

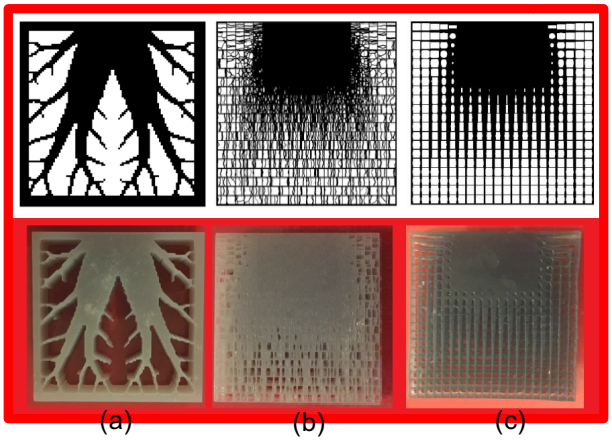

Figure 1.8.. A multiscale topology optimization approach applied to a heat sink with uniformly distributed heat source: (a) Topology optimization in macroscale, (b-c) Multiscale topology optimization using two different initial designs for meta-material scale.

cause flow separation. Although, the viscous drag force can be reduced by bio-inspired micropillar designs, the optimality can hardly be proved(Fig 1.9). The potential of optimizing the micropillar arrays using a multiscale approach will be exploited in Chapter Three.

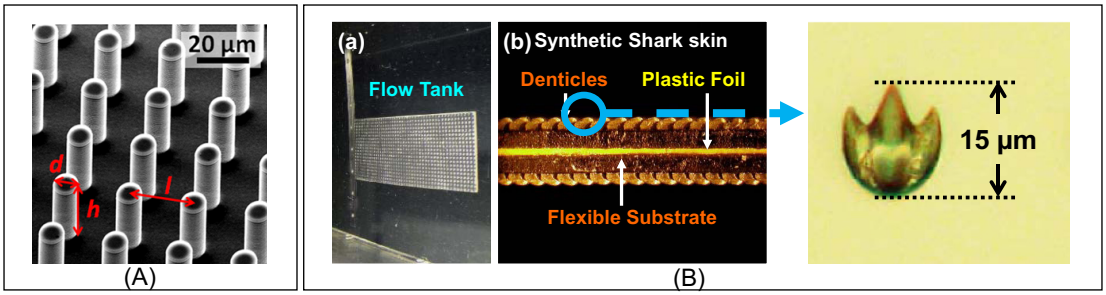

Figure 1.9.. (A) A scanning electron microscopy of the physical domain of a micropillar heat sink [113]. (B) A membrane composed of bio-inspired micropillar arrays composed of shark denticles shape micropillars [114].

1.2.3 Topology optimization coupling thermomechanical analysis

Structures for thermomechanical applications indicates those components resisting mechanical load and coupled thermo-elastic load caused by temperature variation, as well as transferring heat. These structures are widely applied in thermal management and protection system for electronic devices in turbine engine [115, 116], Micro-electro-mechanical system (MEMS) design [117], stability analysis for civil engineering, space structure as well as piping system [9, 118, 119], and injection molding industries.

Topology optimization allows the generation of lightweight, high-performance, and cost-effective thermo-mechanical structures.Several studies has been conducted to obtain optimal structures taking consideration of thermo-elastic load using topology optimization [10, 25, 26, 120]. These structures contain compliant mechanism microscopic mechnical system coupled with electrical circuits (MEMS) [25, 26], substrate of electronic devices [24], and structures containing thermo-elastic loads [10, 120] (Fig. 1.10). Structures involve with heat conduction have been discussed in the context of topology optimization in [14, 71, 83, 84, 121]. In addition, convection, and internal heat generation has been studied without explicitly accounting fluid motion (Fig. 1.12 (A)) [76–78, 121]. Multiobjective topology optimization that optimizing both thermal and mechanical performance in a thermomechanical structure have been studied in [93, 122].

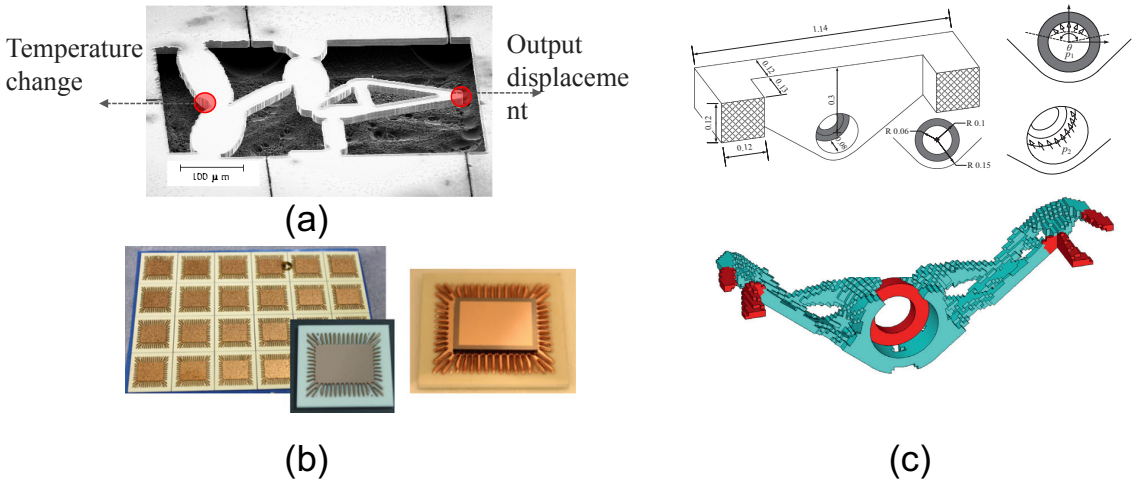

Figure 1.10.. Several thermomechanical strucutre (a) thermal actuator [25] (b) substrate of electronic devices [24] and (c) a beam containing thermo-elastic loads [10].

However, current multiobjective thermomechanical topology optimization does not consider convective heat transfer. In this dissertation, heat convection physics model will be incorporated to thermomechanical topology optimization. This effort aims to generate optimized multi-functional lattice, porous or foam heat sink [123–125]. These structures are desirable since they offer large surface-to-volume rate, which improves convective heat transfer [126], and on the other hand, they can withstand mechanical and thermomechanical load. Current AM technologies allows to manufacture porous metals having a having a unit cell size less than $4mm$ and a strut thickness less than $1mm$, offers us possibilities design manufacturable porous materials with enhanced thermomechanical performance [48, 127].

1.2.4 Topology optimization coupling thermal-fluid analysis

As another branch of multiphysics topology optimization, topology optimization coupling thermal-fluid analysis has been less studied compared to thermomechanical topology optimization. However, this study has a significant demand, since advanced microfluidic

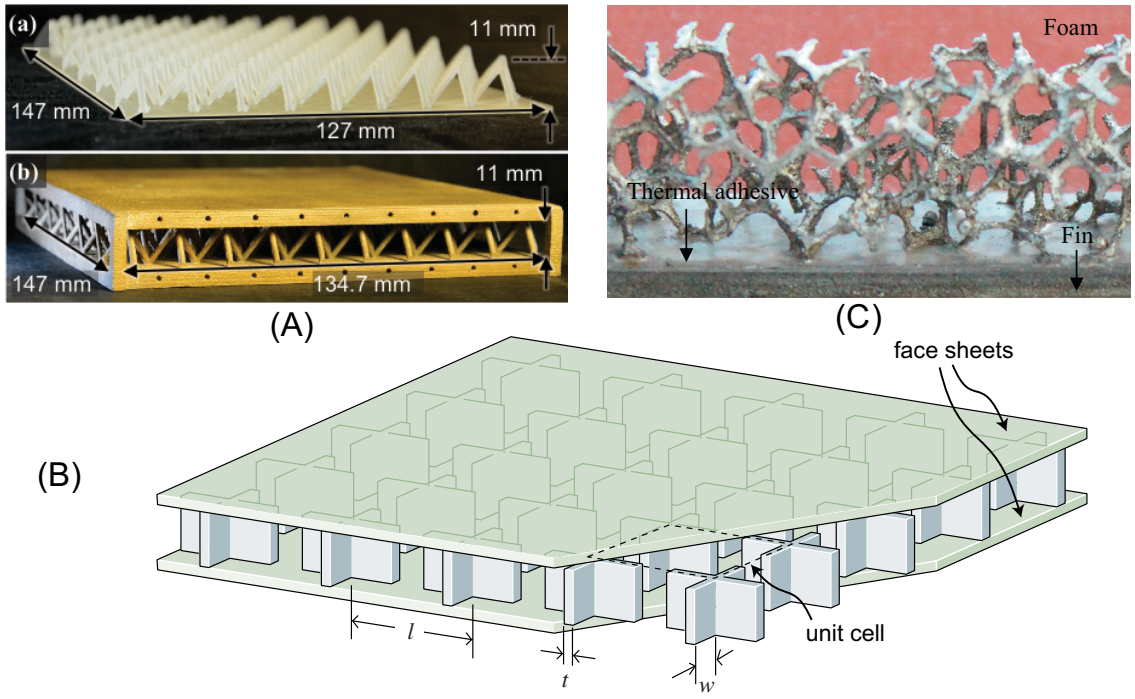

Figure 1.11.. Multifunctional lattice heat sink with (A) tetrahedral lattice [123] and (B) truncated square [124], and (C) metal foam [125].

heat sinks and battery group become more highly integrated, compact and powerful, it challenges heat exchanging capability to efficiently dissipate redundant heat, thus need for more optimized structures. A thermal-fluid model based topology optimization can reflect the effect of natural and forced convection due to the velocity field resulting from fluid mechanics model. Finite element models coupling thermal-fluid analysis have been incorporated to obtain heat sinks targeting heat transfer including natural convection [94, 95] (Fig. 1.12). To analyze the effect of forced convection, a topology optimization based on finite element model coupling Stokes flow and heat transfer has been proposed [96] . In this model, inertial force or advection in the fluid is not taken into account. To consider the inertial force without increasing the model compexity, a Darcy flow model has been employed as an approximate fluid flow model in the thermal-fluid analysis [128]. Some researchers have attempted to exploit the non-linear Navier-Stokes flow and convection-diffusion cou-

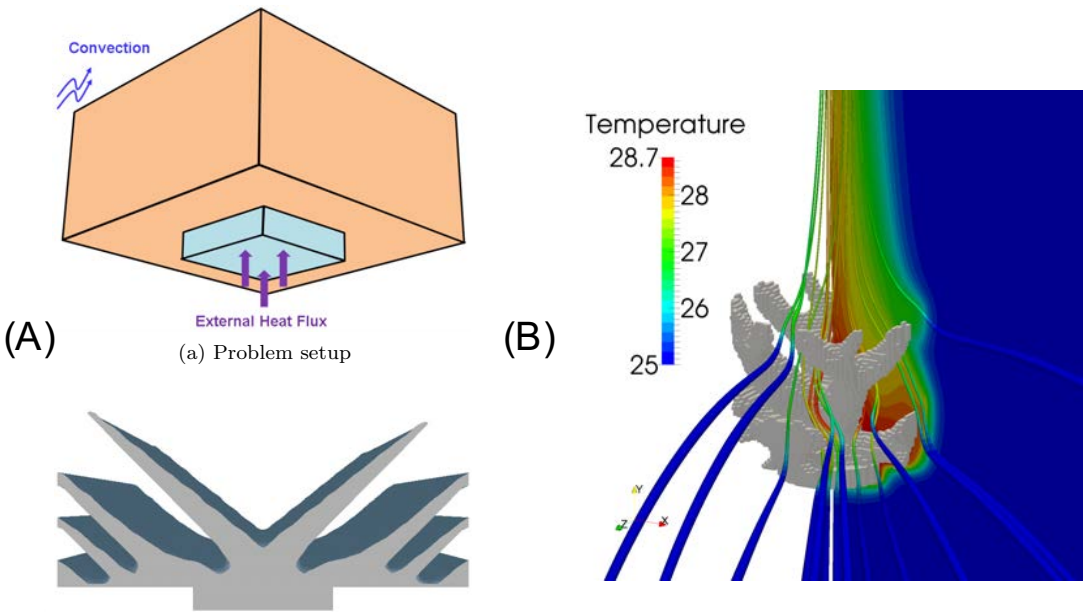

Figure 1.12.. (A) A topology optimization for convective heat transfer, without explicitly accounting fluid motion [121]. (B) A topology optimization for natural convection based on thermal-fluid (conjugate) heat transfer model [95].

pling FEA module in commercial software COMSOL Multiphysics® and make effort on secondary development [31,32,97]. The thermal-fluid physics model used in this approach is similar to advection-diffusion-reaction euqation for the toppology optimization of catalytic microfluidic reactors [129]. In this approach, heat transfer is evaluated by considering the internal heat exchange between fluid-solid boundary in the fixed design domain. In these studies, the resulting optimized topologies can be reflected by variation of Reynolds number values (Fig. 1.13). However, this approach would be inconvenient to customize the physics model such as imposing an external heat source. Several other studies taken account of external heat source [24, 98, 99] are formulated as multi-objectives problem statements, in which thermal and fluid performance are optimized by a weight-sum approach. Nevertheless, in this method, it has to keep a substantial weighting factor on the objective with respect to fluid flow performance. If this weighting factor is small, or the

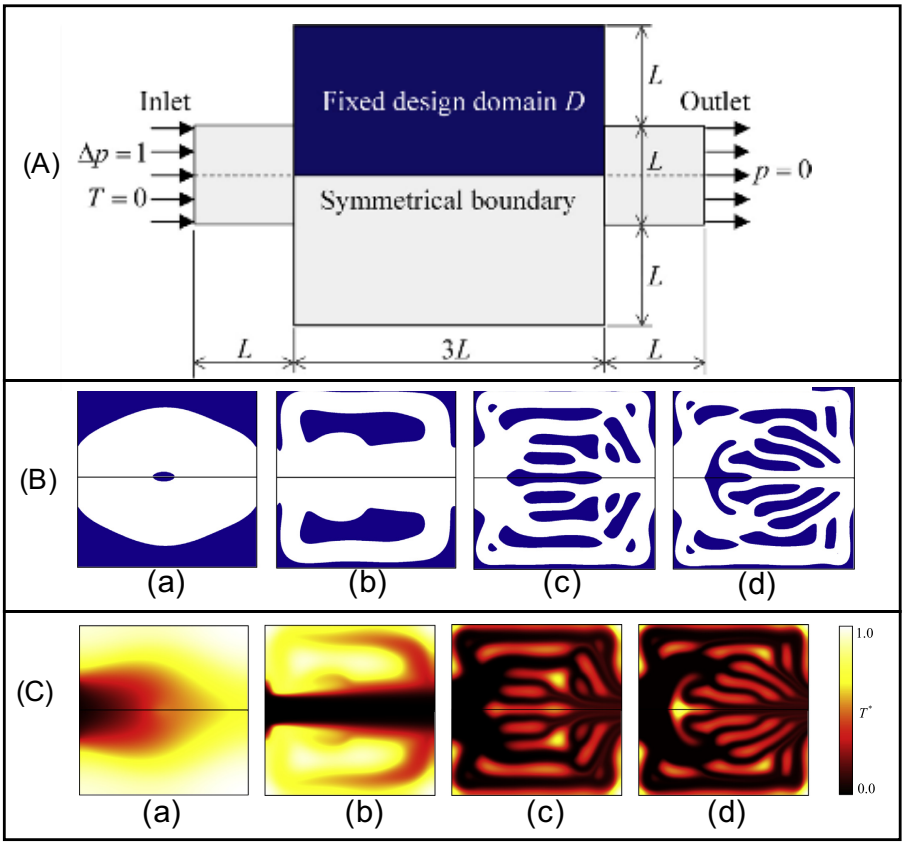

Figure 1.13.. This Figure shows how the resulting optimized topologies can be reflected by variation of Reynolds number values. In Fig. B and C, from (a) to (d) the Reynolds numbers are 1, 70, 170, 280 respectively. Fig. B shows the resulting topology, and Fig. C shows temperature distribution [31].

objective function is only related to thermal performance, the result may shows dead-end channels, where the fluid flow may be intersected by solid phase and unable to sucessfully pass from inlet to outlet (Fig. 1.14). Recently, other numerical model, such as Lattice-Boltzman method has been proposed as a substitution of finite element analysis [130] but they still need further development to fullfil the practical applications. Finally, in most of current studies, the investigation of how thermal-fluid parameters such as Prandtl number, Nusselt number and thermal diffusivity affect the resulting topologies remains scare.

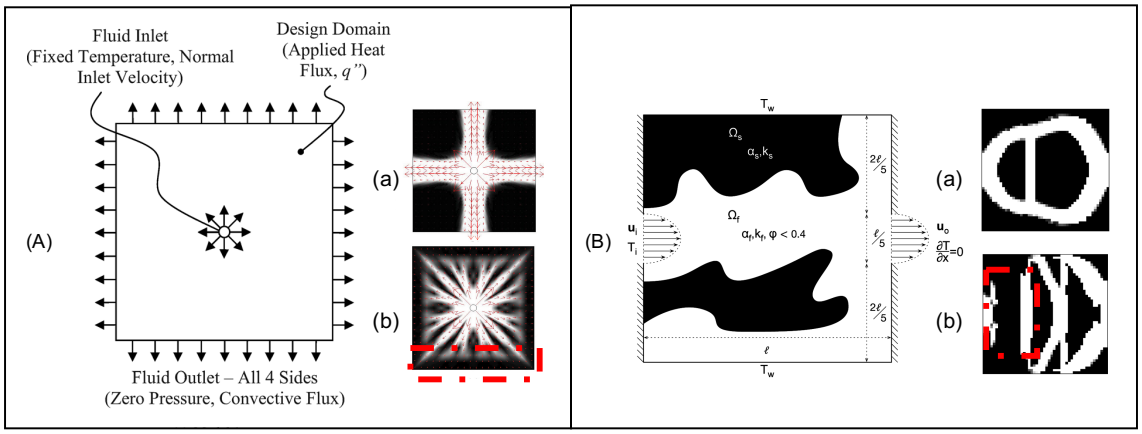

Figure 1.14.. This figure show how the weighting factors of fluid and thermal performance in a weighting sum approach affect the the resulting topology. In (A)-(b) [24] and (B)-(b) [98], with greater weighting factors for thermal-performance, it shows deadend channels may appeared at the location marked with red rectangulars.

1.3 Objective of this dissertation

The objective of this dissertation is to develop new approaches in the areas of multi-scale topology optimization, thermomechanical topology optimization including heat convection, and thermal-fluid topology optimization. The dissertation mainly focuses on developing five innovative topology optimization algorithms with respect to structure and multistructure coupling fluid, thermal and mechanical analysis, in order to solve customary design requirements. Most of algorithms are coded as in-house code in MATLAB. The contribution of this dissertation is presented in following five Chapters:

- **Chapter 2: Multiphase topology optimization of thermomechanical structures**

  In this Chapter, a topology optimization approach for lattice structures subjected to thermal and mechanical loads is presented. From the purposed mutiphase approach, the algorithm only requires computation in structural scale. In meta-materials scale, the interpolation functions of properties for the predifined lattice unit cells are determined using asymptotic homogenization. By incoporating these material interpo-

lation functions into structural scale toplogy optimization, the results can reflect an optimized structure composed of multiphase lattice unit cells.

- **Chapter 3: Multiscale thermomechanical topology optimization of self supporting cellular structures**

  In this Chapter, a multiscale topology optimization method is established. With a hierarchical approach, this method aims to create optimized design for non-periodic, self-supporting cellular structures subjected to thermo-mechanical loads. The proposed method seeks to maximize thermo-mechanical performance at the macroscale in a conceptual design while obtaining AM friendly structure for each unit cell at the mesoscale. Then the macroscale performance is re-estimated and the mesoscale design is updated until the macroscale performance is satisfied.

- **Chapter 4: Design of micropillar arrays for microfluidic devices using multiscale topology optimization for Navier-Stokes flow**

  This Chapter propose a new idea to utilize multiscale approach algorithm to design micropillar arrays in microfluidic devices. In the structural scale, velocity and viscous strain fields are obtained through Navier-Stokes-Brinkman finite element analysis. In the meta-metarials scale, the topology of each micropillar is obtained using inverse homogenization. The boundary conditions of the inverse homogenization problems are derived from finite element analysis of structural scale. The optimal micropillar topologies minimize flow separation and energy loss and maximize average velocity magnitude.

- **Chapter 5: Thermomechanical topology optimization of lattice heat transfer structure including natural convection and design-dependent heat source**

  In this Chapter, heat convection is involved in thermomechanical topology optimization representated by design-dependent heat source and natural convection. Utilizing this approximation method for convective heat transfer in the boundary surface, fluid mechanics model is not requried in this method. The method can be applied to gen-

erate multifunctional lattice heat transfer structure having better thermomechanical performance.

- **Chapter 6: Design of conformal cooling channels using a versatile thermal-fluid topology optimization**

  In this Chapter, an improved thermal-fluid topology optimization method is proposed. The method leads versatile topologies with regularities in terms of different combinations of thermal-fluid parameters such as Reynolds number, Prandtl number and thermal diffusivity. The method is applied to design a conformal cooling of an injection mold, which is produced through metal additive manufacturing.

2. MULTIPHASE TOPOLOGY OPTIMIZATION OF THERMOMECHANICAL STRUCTURES

This Chapter presents a topology optimization approach for lattice structures subjected to thermal and mechanical loads. The focus of this work is the design of injection molds. The proposed approach seeks to minimize the injection mold mass while satisfying constraints on mechanical and thermal performance. The optimal injection molds are characterized by a quasi-periodic distribution of lattice unit cells of variable relative density. The resulting lattice structures are suitable for additive manufacturing. The proposed structural optimization approach uses thermal and mechanical finite element analyses at two length scales: mesoscale and macroscale. At the mesoscale, lattice unit cells are utilized to obtain homogenized thermal and mechanical properties as a function of the lattice relative density. At the macroscale, the lattice unit cells are optimally distributed using the homogenized properties. The proposed design approach is demonstrated through 2D and 3D examples including the optimal design of an injection mold. The optimized injection mold is prototyped using additive manufacturing. The numerical model of the optimized mold shows that, with respect to a traditional solid mold design, a mass reduction of over 30% can be achieved with a small increase in nodal displacement (under 5 microns) and no difference in nodal temperature.

2.1 Background and motivation

During the injection molding cycle, injection molds are required to withstand pressure loads and thermal expansions while providing dimensional accuracy to the molded part. Molds are also required to uniformly transfer heat flux from the mold cavity, where the part is molded, to cooling channels filled with running coolant. While design guidelines are known to improve the thermal and mechanical performance of injection molds [131, 132],

the development of structural optimization methods such as topology optimization offers the potential to create novel and complex injection mold designs with higher performance [122].

With reference to heat conduction, topology optimization has been employed to minimize the temperature gradient magnitude distribution (heat dissipation) for thermal components including heat sinks for multichip modules [84] and thermal-fluid electronic microchannels [96]. Studies that consider coupled linear elasticity, heat conduction and the resulting thermoelastic load in topology optimization have been recently proposed for two-dimensional structures [93]. Thermal expansion has been considered in the topology optimization of micro-electro-mechanical-systems (MEMS) [10] and electronic packages [24]. Regardless of the numerical model, the result of the application of a traditional topology optimization algorithm is a solid-void structure in which intermediate densities are penalized. As an alternative to the solid-void structure, this work proposes the design of optimal injection molds with a lattice (porous) structure. The lattice structure uses intermediate densities, which relaxes the optimization problem, expands the design space, and, potentially, increases the performance of the final design [60]. In addition, a lattice injection mold opens possibilities for airflow assisted cooling and more complex heat exchanging design.

An optimal design of a lattice structure can be achieved through multiscale topology optimization. The multiscale topology optimization problem consists on finding the optimal lattice unit cell (LUC) designs (mesoscale structural optimization) as well as their optimal distribution in the structure (macroscale structural optimization). This method requires the application of asymptotic homogenization theory in order to derive the macroscale mechanical properties of the LUCs. The method has been effectively applied to 2D and 3D structures subjected to pure mechanical loads [67, 68, 133, 134]. Despite of their potential, multiscale topology optimization has two main drawbacks. First, it requires the execution of several optimization problems in parallel for each iteration, which makes it computationally expensive, especially for 3D designs. Second, the solutions do not necessarily converge to a manufacturable, connected design and time-consuming post-processing may

be needed. To alleviate the computational cost and to improve the connectivity of the LUCs, concurrent topology optimization strategies have been proposed [64, 135]. These strategies lead to the design of an optimal macroscale structure composed of a periodic (uniformly distributed) LUC. Despite of their manufacturability, the LUC periodicity produces a sub-optimal structure when compared to a non-periodic design.

An alternative approach is the use of multiphase topology optimization [58, 59]. This approach uses pre-defined LUCs with homogenized mechanical properties avoiding the mesoscale structural optimization. The geometry of the LUCs is controlled by a few geometric parameters that define their relative density or porosity. Material interpolation schemes are defined to map the LUC relative density to their homogenized mechanical properties. The (macroscale) structural optimization problem consists on finding the optimal relative density distribution, which ultimately provides the optimal LUC distribution within the structure. Multiphase topology optimization has been applied to two-dimensional structures subjected to pure mechanical load [58, 59]. The application of this approach to heat-transferring structures has been less reported in literature.

This work extends the use of multiphase topology optimization to three-dimensional structures composed quasi-periodic LUCs considering thermal and mechanical performance. Integral to the proposed multiphase topology optimization method for lattice injection molds is the use of a thermomechanical finite element model. In this model, the mechanical and thermal load analyses are coupled to predict the structure's thermoelastic response. Asymptotic homogenization theory is used to predict the isotropic thermal conductivity and the orthotropic linear elasticity of the LUCs.

The results are demonstrated with the topology optimization of lattice structures with minimum mass under elastic mechanical and thermal constraints, which include maximum nodal displacement and maximum nodal temperature on the mold cavity.

The remaining of the paper is organized as follows: The proposed design approach is presented in Sec. 2. The homogenization theory is explained in Sec. 3 and the macroscale structural optimization approach is explained in Sec. 4. Two numerical problems are presented to demonstrate the design approach in Sec. 5: (1) a 2D structure with thermal and

mechanical loads, (2) a core of a 3D injection mold design. Finally, summary and conclusion are provided in Sec. 6.

2.2 Proposed multiphase topology optimization approach

The proposed optimization approach involves finite element models in two length-scales: mesoscale and macroscale. The mesoscale finite element models correspond to the lattice unit cells (LUCs). These models are used to predict the homogenized LUC properties. As a result, homogenized elastic and thermal coefficients are expressed as functions of the LUC relative density. The macroscale finite element model corresponds to the injection mold. This model contains mechanical and thermal boundary conditions, which include external mechanical loads and supports as well as the heat sources (mold cavity) and sinks (cooling channels). The macroscale design problem addressed in this work is to find the optimal distribution of given number of LUCs that minimizes the injection mold mass while satisfying mechanical and thermal constraints. These constraints include mechanical and thermal compliance as well as maximum nodal displacement and maximum nodal temperature.

The macroscale design problem is solved in two steps: First, a relaxed convex problem is addressed so that the mass is minimized subject to constraints on mechanical compliance and a thermal compliance [14]. The result is a global optimum of a convex problem to be used as the initial design of a non-convex problem. Second, using this initial design, a structural optimization algorithm finds the optimal distribution of a discrete number of LUCs so that the maximum displacement and temperature are minimized in specific locations of the injection mold, e.g., mold cavity. The optimization approach is summarized in Fig. 2.1.

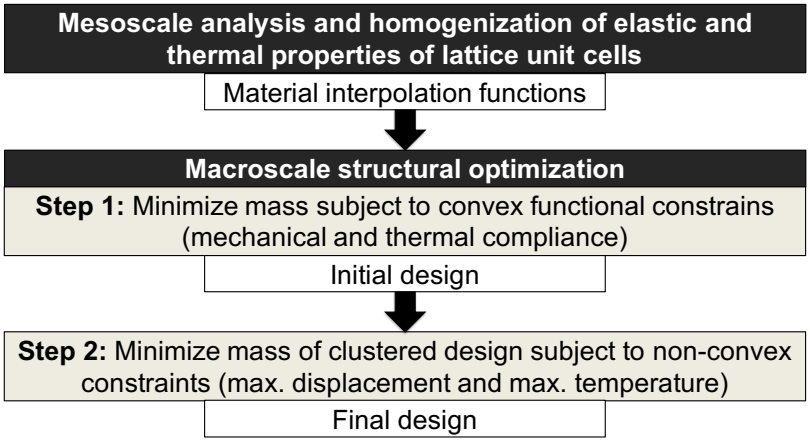

Figure 2.1.. Flowchart of proposed design approach.

2.3 Mesoscale analysis and homogenization of elastic and thermal properties of lattice unit cells

This section summarizes the numerical approaches used to derive the homogenized elasticity tensor $\mathbf{D}_c^H$ and the homogenized thermal conductivity tensor $\boldsymbol{\kappa}_c^H$ of an a-priori defined LUC. The theory presented in this section follows the principles of asymptotic homogenization [136–139].

2.3.1 Asymptotic homogenization of the elastic properties

Let a macroscale design domain Ω to be comprised of n_c LUCs, where $c = 1,\ldots,n_c$. Each of LUC is further discretized into n_e finite elements as illustrated in Fig. 2.2.

According to the homogenization theory for media with a periodic structure, the homogenized elasticity tensor $\mathbf{D}_c^H$ of a discretized periodic LUC is given by

$$\mathbf{D}_c^H = \frac{1}{|V_c|}\sum_{e=1}^{n_e}\int_{V_e}[\mathbf{I}-\mathbf{B}_e\boldsymbol{\chi}_e]^{\mathsf{T}}\mathbf{D}_e[\mathbf{I}-\mathbf{B}_e\boldsymbol{\chi}_e]\mathrm{d}V_e, \tag{2.1}$$

where n_e are the number of finite elements of the discretized LUC, $|V_c|$ is the LUC volume, $\mathbf{I}$ is the identity matrix, V_e is the volume of the finite element e, $\mathbf{B}_e$ is the element strain-displacement matrix, $\mathbf{D}_e$ is the element elasticity tensor, and $\boldsymbol{\chi}_e$ is the matrix containing the

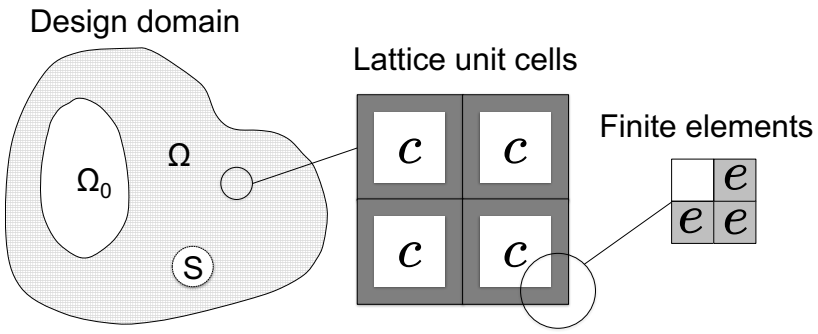

Figure 2.2.. Hierarchical organization of the design domain.

element displacement vectors χ_e^{ij} resulting from globally enforcing the unit test strains ε^{ij} (Fig. 2.3). For a 3D solid finite element, this is

$$\chi_e = [\chi_e^{11}, \chi_e^{22}, \chi_e^{33}, \chi_e^{12}, \chi_e^{23}, \chi_e^{13}], \tag{2.2}$$

where χ_e^{ij} are vectors of size 24×1. The element displacement vectors χ_e^{ij} are obtained from the global displacement vector of the LUC χ_c^{ij}, which is the solution of the equilibrium equation

$$\left[\sum_{e=1}^{n_e} \int_{V_e} \mathbf{B}_e^{\intercal} \mathbf{D}_e \mathbf{B}_e \mathrm{d}V_e\right] \chi_c^{ij} = \sum_{e=1}^{n_e} \int_{V_e} \mathbf{B}_e^{\intercal} \mathbf{D}_e \varepsilon^{ij} \mathrm{d}V_e. \tag{2.3}$$

The first term in the left hand side of Eq. (3.3) is the stiffness matrix of the LUC and the right hand side is the nodal force vector of the LUC.

It is convenient to define the element nodal displacement matrix χ_e^0 within a solid isotropic cell. This isotropic nodal displacement matrix is the solution of the equilibrium equation

$$\mathbf{B}_e \chi_e^0 = \mathbf{I}. \tag{2.4}$$

Since $\mathbf{I} = [\varepsilon^{11}, \varepsilon^{22}, \varepsilon^{33}, \varepsilon^{12}, \varepsilon^{23}, \varepsilon^{13}]$, then Eq. (2.4) can be written as

$$\left[\int_{V_e} \mathbf{B}_e^{\intercal} \mathbf{D}_e \mathbf{B}_e \mathrm{d}V_e\right] \chi_e^{0(ij)} = \int_{V_e} \mathbf{B}_e^{\intercal} \mathbf{D}_e \varepsilon^{ij} \mathrm{d}V_e. \tag{2.5}$$

Therefore, each component of the homogenized elasticity tensor $\mathbf{D}_c^H$ can be expressed as

$$D_{c,ijkl}^H = \frac{1}{|V|} \sum_{e=1}^{n_e} \int_{V_e} [\chi_e^{0(ij)} - \chi_e^{ij}]^{\intercal} \mathbf{k}_e [\chi_e^{0(kl)} - \chi_e^{kl}] \mathrm{d}V_e, \tag{2.6}$$

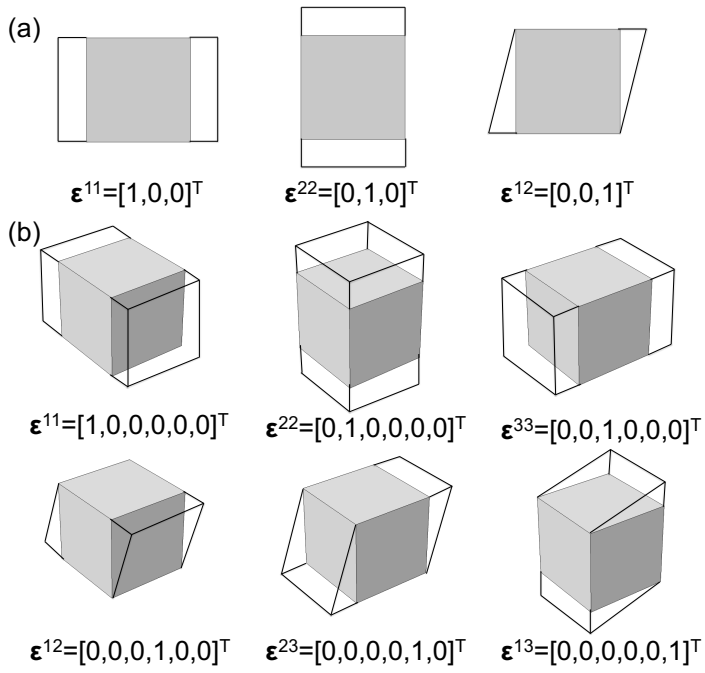

Figure 2.3.. The chosen unit strain tests imposed on (a) 2D representative LUCs and (b) 3D representative LUCs.

where $\mathbf{k}_e$ is the stiffness matrix for an element. The homogenized elasticity tensor is obtained based on periodic boundary conditions. For a 3D LUC, this tensor is a symmetric matrix of the form

$$\mathbf{D}_c^H = \begin{bmatrix} D^H_{c,1111} & D^H_{c,1122} & D^H_{c,1133} & D^H_{c,1112} & D^H_{c,1123} & D^H_{c,1113} \\ D^H_{c,2211} & D^H_{c,2222} & D^H_{c,2233} & D^H_{c,2212} & D^H_{c,2223} & D^H_{c,2213} \\ D^H_{c,3311} & D^H_{c,3322} & D^H_{c,3333} & D^H_{c,3312} & D^H_{c,3323} & D^H_{c,3313} \\ D^H_{c,1211} & D^H_{c,1222} & D^H_{c,1233} & D^H_{c,1212} & D^H_{c,1223} & D^H_{c,1213} \\ D^H_{c,2311} & D^H_{c,2322} & D^H_{c,2333} & D^H_{c,2312} & D^H_{c,2323} & D^H_{c,2313} \\ D^H_{c,1311} & D^H_{c,1322} & D^H_{c,1333} & D^H_{c,1312} & D^H_{c,1323} & D^H_{c,1313} \end{bmatrix}. \tag{2.7}$$

Each coefficient $D^H_{c,ijkl}$ can be expressed as a function of the density of the LUC as explained later in this paper.

2.3.2 Asymptotic homogenization of the thermal conductivity

Following the homogenization theory for thermal conductivity [139], the homogenized thermal conductivity tensor $\boldsymbol{\kappa}_c^H$ of a discretized periodic LUC is given by

$$\boldsymbol{\kappa}_c^H = \frac{1}{|V_c|}\sum_{e=1}^{n_e}\int_{V_e}[\mathbf{I}-\mathbf{B}_e^t\mathbf{T}_e]^\intercal\boldsymbol{\kappa}_e[\mathbf{I}-\mathbf{B}_e^t\mathbf{T}_e]\mathrm{d}V_e, \tag{2.8}$$

where n_e are the number of finite elements of the discretized LUC, $|V_c|$ is the LUC volume, $\mathbf{I}$ is the identity matrix, V_e is the volume of the finite element, $\mathbf{B}_e^t$ is the element "strain" (temperature gradient)-temperature matrix, $\boldsymbol{\kappa}_e$ is the element thermal conductivity tensor, and $\mathbf{T}_e$ is the matrix containing the element nodal temperature vectors $\mathbf{T}_e^{ij}$ resulting from globally enforcing the unit test temperature gradients $\mathbf{t}^i$ (Fig. 2.4). For a 3D solid finite element, this is

$$\mathbf{T}_e = [\mathbf{T}_e^1, \mathbf{T}_e^2, \mathbf{T}_e^3], \tag{2.9}$$

where the size of the vectors $\mathbf{T}_e^i$ is 8×1. As before, the element temperature vectors $\mathbf{T}_e^i$ are obtained from the global temperature vector of the LUC $\mathbf{T}_c^i$, which is the solution of the equilibrium equation

$$\left[\sum_{e=1}^{n_e}\int_{V_e}\mathbf{B}_e^{t\intercal}\boldsymbol{\kappa}_e\mathbf{B}_e^t\mathrm{d}V_e\right]\mathbf{T}_c^i = \sum_{e=1}^{n_e}\int_{V_e}\mathbf{B}_e^{t\intercal}\boldsymbol{\kappa}_e\mathbf{t}^i\mathrm{d}V_e. \tag{2.10}$$

The first term in the left hand side of Eq. (3.5) is the "stiffness" thermal matrix of the LUC and the right hand side is the nodal heat flux vector of the LUC.

The element nodal temperature matrix $\mathbf{T}_e^0$ within a solid isotropic (solid) cell is the solution of the equilibrium equation

$$\mathbf{B}_e^t\mathbf{T}_e^0 = \mathbf{I}. \tag{2.11}$$

Since $\mathbf{I} = [\mathbf{t}^1, \mathbf{t}^2, \mathbf{t}^3]$, then Eq. (2.11) can be written as

$$\left[\int_{V_e}\mathbf{B}_e^{t\intercal}\boldsymbol{\kappa}_e\mathbf{B}_e^t\mathrm{d}V_e\right]\mathbf{T}_e^{0(i)} = \int_{V_e}\mathbf{B}_e^{t\intercal}\boldsymbol{\kappa}_e\mathbf{t}^i\mathrm{d}V_e. \tag{2.12}$$

Therefore, each component of the homogenized stiffness thermal tensor $\boldsymbol{\kappa}_c^H$ can be expressed as

$$\kappa_{c,ij}^H = \frac{1}{|V_c|}\sum_{e=1}^{n_e}\int_{V_e}[\mathbf{T}_e^{0(i)}-\mathbf{T}_e^i]^\intercal\mathbf{k}_e^t[\mathbf{T}_e^{0(j)}-\mathbf{T}_e^j]\mathrm{d}V_e, \tag{2.13}$$

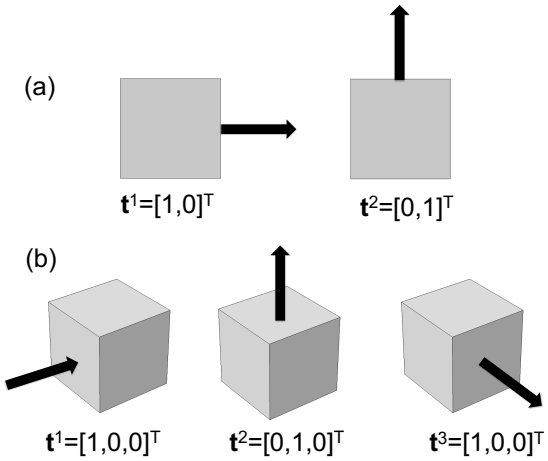

Figure 2.4.. Unit temperature gradients imposed on (a) 2D representative LUCs and (b) 3D representative LUCs.

where $\mathbf{k}_e$ is the stiffness thermal matrix for an element. For a 3D LUC, this tensor is a symmetric matrix of the form

$$\boldsymbol{\kappa}_c^H = \begin{bmatrix} \kappa_{c,11}^H & \kappa_{c,12}^H & \kappa_{c,13}^H \\ \kappa_{c,21}^H & \kappa_{c,22}^H & \kappa_{c,23}^H \\ \kappa_{c,31}^H & \kappa_{c,32}^H & \kappa_{c,33}^H \end{bmatrix}. \tag{2.14}$$

Here as well, each coefficient $\kappa_{c,ij}^H$ can be expressed as a function of the relative density of the LUC as explained in the following section.

2.3.3 Interpolation of homogenized thermomechanical properties

For a given set of lattice LUCs with known relative density values θ_c', the homogenized elasticity tensors $\mathbf{D}_c^H$ and the homogenized thermal conductivity tensors $\boldsymbol{\kappa}_c^H$ are obtained. Then, an interpolation function is derived to correlate the relative density θ_c of the LUC with its corresponding homogenized tensor coefficients. Using a polynomial approximation, the elasticity tensor coefficients are expressed as follows:

$$D_{c,ijkl}^H(\theta) = a_0 + \sum_{q=1}^{n_q} a_q \theta^q + \mathscr{O}(\theta^{n_q+1}), \tag{2.15}$$

where the coefficients a_q, for $q = 0, \ldots, n_q$, are determined by polynomial regression. Similarly, for the components of the homogenized thermal conductivity tensor, one obtains that

$$\kappa^H_{c,ij}(\theta) = b_0 + \sum_{q=1}^{n_q} b_q \theta^q + \mathscr{O}(\theta^{n_q+1}). \tag{2.16}$$

Polynomials of order one (linear interpolations) can also be obtained with $a_0 = 0$ and $a_1 = D^H_{c,ijkl}(\theta'_c = 1)$ for the elasticity tensor, and $b_0 = 0$ and $b_1 = \kappa^H_{c,ij}(\theta'_c = 1)$ for the thermal conductivity tensor. These interpolations are inaccurate but make the optimization problem convex; hence, they are utilized to generate the initial design (Step 1) (Sec. 2.4.1). Polynomials of order three are shown to provide sufficient accuracy and are used in the final stage of the optimization process (Step 2) (Sec. 2.4.2).

2.4 Macroscale structural optimization

The proposed multiphase structural optimization approach consists of two steps. During the first step, an initial optimal distribution of LUC relative densities θ^*_{1c}, $c = 1, \ldots, n_c$ is obtained. The initial design minimizes the mass of the structure subject to two functional constraints: mechanical compliance and thermal compliance. A linear interpolation of the elastic coefficients and thermal conductivity is used to make the problem convex. During the second step, the relative density values are optimally clustered using a set of predefined values θ'_p, $p = 1, \ldots, n_p$. The clustering process results in a design that can be easily fabricated using AM techniques. The final optimal design θ^*_{2c} minimizes the mass of the structure subject to constraints of the maximum displacement and temperature in specific regions of the design domain. The design domain Ω contains the cavities Ω_0 and heat sinks S of the injection tool to be optimized as well as the mechanical loads $\mathbf{f}$, supports, heat flux $\mathbf{q}$, and insulated boundaries. Also, let's define the boundaries Γ_W with target of the maximum displacement, and boundaries Γ_Q with target of the maximum temperature (Fig. 2.5).

In each step, the optimization is performed using the Globally Convergence Method of Moving Asymptotes (GCMMA) algorithm implemented in the FEA software COMSOL

Multiphysics (COMSOL, Stockholm, Sweden). The convergence ε in the GCMMA algorithm is given by the following condition:

$$\varepsilon = \left| \frac{\partial \psi(\boldsymbol{\lambda})}{\partial \lambda_i} \right| \leq \varepsilon_g, \tag{2.17}$$

where $\psi(\boldsymbol{\lambda})$ is the dual objective function, $\boldsymbol{\lambda}$ is the vector of Lagrange multipliers, and ε_g is a small positive number [37]. By default, $\varepsilon_g = 10^{-6}$ for the following 2D examples and $\varepsilon_g = 10^{-3}$ for the following 3D examples. Another convergence criterion is the number of maximum objective function evaluations N. By default, $N = 500$ for the following 2D examples and $N = 150$ for the following 3D examples.

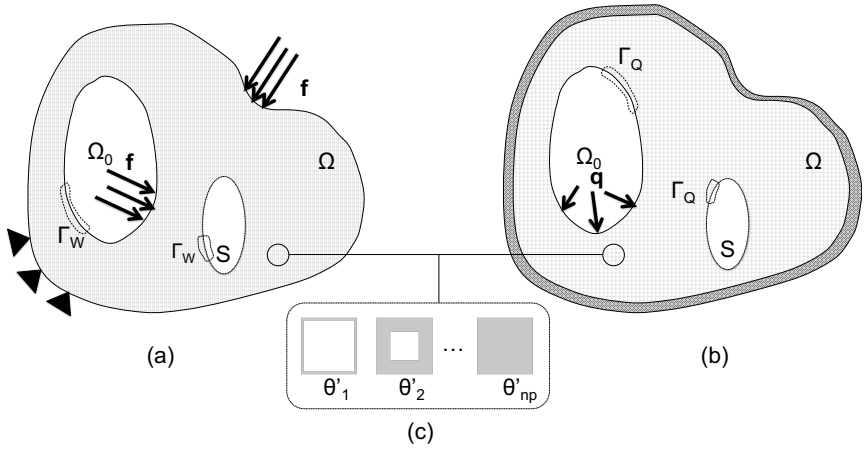

Figure 2.5.. The macroscale design domain: (a) mechanical boundary conditions, (b) thermal boundary conditions, and (c) finite number of lattice LUCs to be optimally distributed.

2.4.1 Step 1: Minimize mass subject to convex functional constrains

The first step aims to find the relative densities $\boldsymbol{\theta} \in \mathbb{R}^{n_c}$ that minimizes the structure's mass $m(\boldsymbol{\theta})$, subject to mechanical compliance and thermal compliance constraints of the design domain. The mass of the structure is defined by

$$m(\boldsymbol{\theta}) = \gamma_0 \sum_{c=1}^{n_c} v_c \theta_c, \tag{2.18}$$

where v_c is the element volume and γ_0 is the base material density. Mechanical compliance reflects the average displacement of the structure. In matrix notation, the mechanical compliance is defined as

$$W = \int_{\Omega} \boldsymbol{\epsilon}^{\intercal} \mathbf{D}^{H} \boldsymbol{\epsilon} \mathrm{d}\Omega, \tag{2.19}$$

where $\mathbf{D}^{H}$ is the homogenized elasticity tensor and $\boldsymbol{\epsilon}$ is the strain tensor. An appropriate mechanical compliance constraint ensures the structure deformation is small and the linear FEA is feasible. Similarly, the thermal compliance reflects the average temperature of the whole structure. It is defined as

$$Q = \int_{\Omega} \mathbf{t}^{\intercal} \boldsymbol{\kappa}^{H} \mathbf{t} \mathrm{d}\Omega, \tag{2.20}$$

where $\boldsymbol{\kappa}^{H}$ is the homogenized thermal conductivity tensor and $\mathbf{t}$ indicates temperature gradients. This constraint determines the compromise of heat conduction performance of the whole structure. With the discretization of the macroscale domain and the application of finite element analysis (FEA), the equation (2.19) yields the quadratic form

$$W(\boldsymbol{\theta}) = \mathbf{f}^{\intercal} \mathbf{u}(\boldsymbol{\theta}), \tag{2.21}$$

where $\mathbf{f}$ is the vector of external loads and $\mathbf{u}(\boldsymbol{\theta})$ is the vector of nodal displacements in the macroscale domain. The vector of nodal displacements satisfies the Hooke's law equilibrium equation:

$$\mathbf{K}(\boldsymbol{\theta}) \mathbf{u}(\boldsymbol{\theta}) = \mathbf{f}, \tag{2.22}$$

where

$$\mathbf{K}(\boldsymbol{\theta}) = \sum_{c=1}^{n_c} \int_{V_c} \mathbf{B}_c^{\intercal} \mathbf{D}_c^{H}(\theta_c) \mathbf{B}_c \mathrm{d}V_c. \tag{2.23}$$

In Eq. (2.23), $\mathbf{K}(\boldsymbol{\theta})$ is the stiffness matrix of the macroscale domain, $\mathbf{B}_c$ represents the strain-displacement relations of a LUC, and $\mathbf{D}_c^{H}(\theta_c)$ is the homogenized elasticity tensor of a LUC. In the same way, the thermal compliance (2.20) yields the quadratic form

$$Q(\boldsymbol{\theta}) = \mathbf{q}^{\intercal} \mathbf{T}(\boldsymbol{\theta}), \tag{2.24}$$

where $\mathbf{q}$ is the boundary heat flux and $\mathbf{T}(\boldsymbol{\theta})$ is the vector of nodal temperatures in the macroscale design domain. The vector of nodal temperatures satisfies the Fourier's law equilibrium equation:

$$\mathbf{K}_t(\boldsymbol{\theta})\mathbf{T}(\boldsymbol{\theta}) = \mathbf{q}, \tag{2.25}$$

where

$$\mathbf{K}_t(\boldsymbol{\theta}) = \sum_{c=1}^{n_c} \int_{V_c} \mathbf{B}_c^{t\,\mathsf{T}} \boldsymbol{\kappa}_c^H(\theta_c) \mathbf{B}_c^t \mathrm{d}V_c. \tag{2.26}$$

In Eq. (5.5), $\mathbf{K}_t(\boldsymbol{\theta})$ is the thermal stiffness matrix of the macroscale domain, $\mathbf{B}_c^t$ is the temperature and temperature gradient relations of a LUC, and $\boldsymbol{\kappa}_c^H(\theta_c)$ is the homogenized thermal conductivity tensor of a LUC.

Finally, the first optimization problem is stated as follows:

$$\begin{aligned}
\text{find} \quad & \boldsymbol{\theta}_1^* \in \mathbb{R}^{n_c} \\
\text{minimize} \quad & J_1(\boldsymbol{\theta}_1) = m(\boldsymbol{\theta}_1)/m(\boldsymbol{\theta}_0) \\
\text{subject to} \quad & W(\boldsymbol{\theta}_1) = \mathbf{f}^\mathsf{T}\mathbf{u}(\boldsymbol{\theta}_1) \leq C_W W(\boldsymbol{\theta}_0) \\
& Q(\boldsymbol{\theta}_1) = \mathbf{q}^\mathsf{T}\mathbf{T}(\boldsymbol{\theta}_1) \leq C_Q Q(\boldsymbol{\theta}_0) \\
& \boldsymbol{\theta}^{\min} \leq \boldsymbol{\theta}_1 \leq \mathbf{1} \\
\text{satisfying} \quad & \mathbf{u}(\boldsymbol{\theta}_1) = \mathbf{K}(\boldsymbol{\theta}_1)^{-1}\mathbf{f} \\
& \mathbf{T}(\boldsymbol{\theta}_1) = \mathbf{K}_t(\boldsymbol{\theta}_1)^{-1}\mathbf{q}
\end{aligned} \tag{2.27}$$

where $\boldsymbol{\theta}_0$ represents the initial solid structure, $\theta_{0c} = 1$ for $c = 1, \ldots, n_c$, $m(\boldsymbol{\theta}_0)$ is the initial mass, and $C_W \geq 1$ and $C_Q \geq 1$ are coefficients that degrade the mechanical compliance and thermal compliance of the initial design—by increasing these coefficients, the mass of the structure decreases and the performance of structure is sacrificed. The lower bound $\boldsymbol{\theta}^{\min}$ prevents the singularity of $\mathbf{K}(\boldsymbol{\theta}_1)$ and $\mathbf{K}_t(\boldsymbol{\theta}_1)$ and also prevents voids within the LUC structure. The value of the lower bound is also determined by the resolution of the AM system (3D printer). In this work, $\theta_c^{\min} = 0.259$ for 3D and $\theta_c^{\min} = 0.190$ for 2D, for $c = 1, \ldots, n_c$. Linear material interpolation functions connecting the homogenized properties of $\theta_c^{\min}$ and the solid material properties are used, in order to interpolate $\mathbf{D}_c^H(\theta_c)$ in $\mathbf{K}(\boldsymbol{\theta}_1)$ and $\boldsymbol{\kappa}_c^H(\theta_c)$ in $\mathbf{K}_t(\boldsymbol{\theta}_1)$. In this way, the material properties deviate from the real values, but

it ensures the problem is convex and the mass is the global minimum. The results of this design step can be used as the initial designs and the baselines of the second design step.

Notably, since the mechanical elasticity and thermal conductivity of the LUCs are homogenized independently, the thermal and the mechanical fields are decoupled to maintain a consistent analysis. While this may introduce an error in the calculation of the strain and stress fields, the thermo-elastic load in injection molds is considerably smaller than the injected pressure and clamping force; therefore, decoupling the two fields yields acceptable results as reported in literature [131].

2.4.2 Step 2: Minimize the mass of the clustered design subject to non-convex functional constraints

The objective of the second step is to minimize the structure's mass $m(\boldsymbol{\theta})$ subject to five constraints: the functional constraints used in the first step plus two additional non-convex functional constraints. The two additional functional constraints are the maximum nodal displacement $U(\boldsymbol{\theta}_2)$ and the maximum nodal temperature $T(\boldsymbol{\theta}_2)$ for each node j in specific locations of the design domain: Γ_W and Γ_Q, respectively. In vector form, $U_j(\boldsymbol{\theta}_2)$ can be written as $\mathbf{1}_j^\intercal \mathbf{u}(\boldsymbol{\theta}_2)$, and $T_j(\boldsymbol{\theta}_2)$ can be written as $\mathbf{1}_j^\intercal \mathbf{T}(\boldsymbol{\theta}_2)$, where $\mathbf{1}_j^\intercal$ is a vector with the value one at the location of node j and 0 at the other locations. With the implementation of this vector form, the sensitivities of $U_j(\boldsymbol{\theta}_2)$ and $T_j(\boldsymbol{\theta}_2)$ can be obtained using adjoint method. The constraint on the maximum nodal displacement and the maximum nodal temperature are

$$\begin{aligned} U(\boldsymbol{\theta}_2) &= \max_{u_j \in \Gamma_W} \{u_j(\boldsymbol{\theta}_2)\} \leq C_U U^{\max}(\boldsymbol{\theta}_0) \\ T(\boldsymbol{\theta}_2) &= \max_{T_j \in \Gamma_Q} \{T_j(\boldsymbol{\theta}_2)\} \leq C_T T^{\max}(\boldsymbol{\theta}_0), \end{aligned} \tag{2.28}$$

which can be written as

$$\begin{aligned} U_j(\boldsymbol{\theta}_2) &= \mathbf{1}_j^\intercal \mathbf{u}(\boldsymbol{\theta}_2) \leq C_U \mathbf{1}_j^\intercal \mathbf{u}^{\max}(\boldsymbol{\theta}_0), \quad j \in \Gamma_W, \\ T_j(\boldsymbol{\theta}_2) &= \mathbf{1}_j^\intercal \mathbf{T}(\boldsymbol{\theta}_2) \leq C_T \mathbf{1}_j^\intercal \mathbf{T}^{\max}(\boldsymbol{\theta}_0), \quad j \in \Gamma_Q. \end{aligned} \tag{2.29}$$

The locations Γ_W and Γ_Q include the surface of mold cavity (heat source) where the displacement and temperature need to be controlled within a strict threshold in order to guarantee the performance of the mold. Other locations may include the surface of the cooling channel, which is subjected to high stress [131]. The limit values of $U_j(\boldsymbol{\theta}_2)$ and $T_j(\boldsymbol{\theta}_2)$ are the values of the solid structure multiplied by the coefficients C_U and C_T, where $C_U \geq 1$ and $C_T \geq 1$. Since these two constraints are satisfied in a solid design, they will not be violated.

The objective function $J_1(\boldsymbol{\theta})$ is modified to avoid mesh dependency and limit the number of LUCs in the final design. A gradient control regularization function $R(\boldsymbol{\theta})$ is added to the objective to provide mesh-independent a result and improve the manufacturability [140]. This function is defined as follows:

$$R(\boldsymbol{\theta}) = \sum_{c=1}^{n_c} \nabla\theta_c{}^{\mathsf{T}} \nabla\theta_c, \tag{2.30}$$

where $\nabla\theta_c$ is the spatial gradient of the design variable field evaluated at the discrete location c. The intermediate densities caused by the addition of this regularization function are clustered using the following analytically differentiable penalization function:

$$\begin{aligned} P(\boldsymbol{\theta}, \boldsymbol{\theta}') &= \sum_{c=1}^{n_c} \prod_{p=1}^{n_p} \left[1 - \cos\left(\frac{\theta_c - \theta'_p}{A} \right) \right], \\ \theta^{\min} - 1 &\leq (\theta_c - \theta'_{n_p}) \leq 1 - \theta^{\min}, \end{aligned} \tag{2.31}$$

where θ'_p are predefined relative density values and A is a normalization factor, $A = 2(1 - \theta^{\min})/\pi$. A small value $P(\boldsymbol{\theta}, \boldsymbol{\theta}')$ ensures the design can be represented by a discrete number

n_p of LUCs phases. The penalization function in Eq. (2.31) is also added to the objective function. Finally, the optimization problem is defined as follows:

$$
\begin{aligned}
\text{find} \quad & \boldsymbol{\theta}_2^* \in \mathbb{R}^{n_c} \\
\text{minimize} \quad & J(\boldsymbol{\theta}_2) = \frac{m(\boldsymbol{\theta}_2)}{m(\boldsymbol{\theta}_1^*)} + C_R R(\boldsymbol{\theta}_2) + C_P \frac{P(\boldsymbol{\theta}_2, \boldsymbol{\theta}')}{P(\boldsymbol{\theta}_1^*, \boldsymbol{\theta}')} \\
\text{subject to} \quad & W(\boldsymbol{\theta}_2) = \mathbf{f}^\intercal \mathbf{u}(\boldsymbol{\theta}_2) \leq C_W W(\boldsymbol{\theta}_0) \\
& Q(\boldsymbol{\theta}_2) = \mathbf{q}^\intercal \mathbf{T}(\boldsymbol{\theta}_2) \leq C_Q Q(\boldsymbol{\theta}_0) \\
& U_j(\boldsymbol{\theta}_2) = \mathbf{1}_j^\intercal \mathbf{u}(\boldsymbol{\theta}_2) \leq C_U \mathbf{1}_j^\intercal \mathbf{u}^{\max}(\boldsymbol{\theta}_0), \quad j \in \Gamma_W \\
& T_j(\boldsymbol{\theta}_2) = \mathbf{1}_j^\intercal \mathbf{T}(\boldsymbol{\theta}_2) \leq C_T \mathbf{1}_j^\intercal \mathbf{T}^{\max}(\boldsymbol{\theta}_0), \quad j \in \Gamma_Q \\
& \boldsymbol{\theta}^{\min} \leq \boldsymbol{\theta}_2 \leq \mathbf{1} \\
\text{satisfying} \quad & \mathbf{u}(\boldsymbol{\theta}_2) = \mathbf{K}(\boldsymbol{\theta}_2)^{-1} \mathbf{f} \\
& \mathbf{T}(\boldsymbol{\theta}_2) = \mathbf{K}_t(\boldsymbol{\theta}_2)^{-1} \mathbf{q},
\end{aligned}
\tag{2.32}
$$

where the coefficients C_R and C_P are small positive numbers, $C_R < 1$ and $C_P < 1$. Polynomials material interpolation function of order three (Sec. 2.3.3) are used to interpolate $\mathbf{D}_c^H(\theta_c)$ in $\mathbf{K}(\boldsymbol{\theta}_2)$ and $\boldsymbol{\kappa}_c^H(\theta_c)$ in $\mathbf{K}_t(\boldsymbol{\theta}_2)$. The next section shows numerical examples of the proposed design approach.

2.5 Numerical examples

Two examples are presented to illustrate the design approach. The first example consists of the design of a multiphase 2D plate in cantilever thermo-mechanically loaded. The second example is the design of the cavity and core plates of a multiphase 3D plastic injection mold. In both examples, the properties of the base material are: density $\gamma_0 = 7850$ kg/m^3, Young's modulus $E_0 = 200$ GPa, Poisson's ratio $\nu_0 = 0.3$. In the first example, thermal conductivity $\kappa_0 = 44.5$ W/(m·K) is taken, but in the second example, $\kappa_0 = 17.8$ W/(m·K) is taken, which is the thermal conductivity of A286 stainless steel alloy at $573.15K$.

2.5.1 Design of a multiphase thermomechanically-loaded 2D plate

Let us consider a square plate of dimensions 1 m $\times$ 1 m and thickness 1 cm. The plate is rigidly fixed along its left lateral side as shown in Fig. 2.6(a). A downward force $F = 1$ kN is applied at the lower right corner. A heat sink with constant temperature 0°C (273.15 K) is located at the center of the left lateral side as shown in Fig. 2.6(b). All other sides of the plate are insulated. A heat flux $q = 10$ W is uniformly distributed on the plate's body. The plate is discretized into 2453 quadrilateral elements. The nodal displacement distributions under plane stress analysis and the nodal temperature distributions from FEA are shown in Figs. 2.6(c) and (d), respectively. In this example, the mechanical compliance $W(\boldsymbol{\theta})$, the thermal compliance $Q(\boldsymbol{\theta})$, the maximum nodal displacement $U(\boldsymbol{\theta})$ on the surface Γ_W, and the maximum nodal temperature $T(\boldsymbol{\theta})$ on the surface Γ_Q are listed in Table. 2.1 (a). Γ_W corresponds to the heat sink surface, and Γ_Q corresponds to the right free end of the plate.

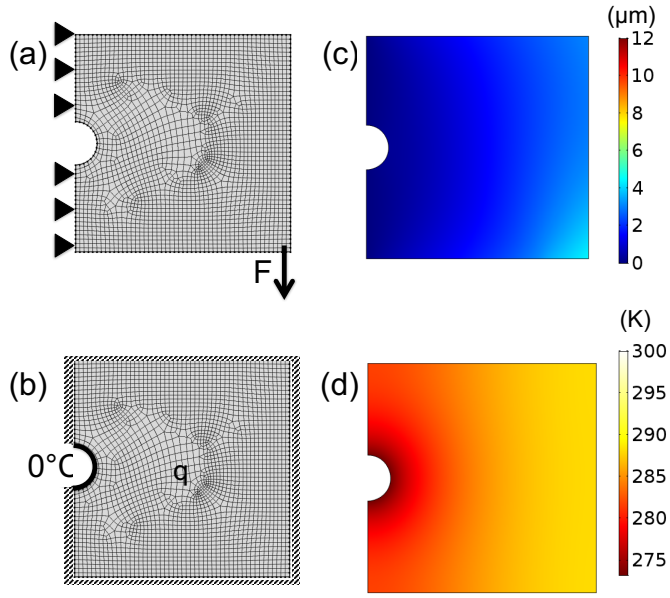

Figure 2.6.. Boundary conditions and results of the FEA for a plate: (a) mechanical load and supports; (b) thermal heat flux, sink, and insulation; (c) nodal displacement; and (d) nodal temperature distribution.

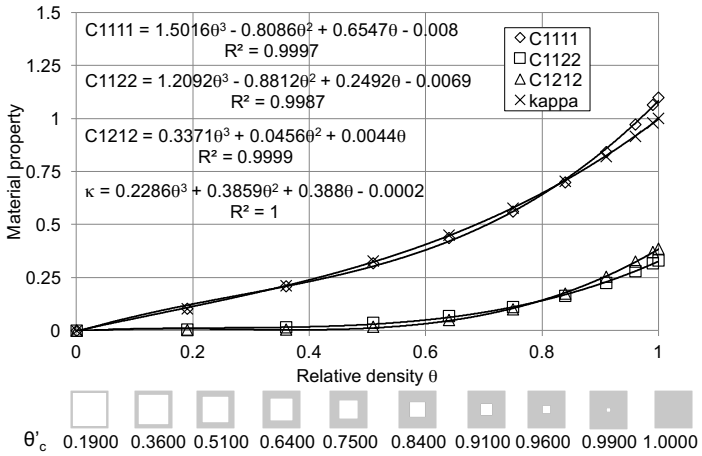

Figure 2.7.. Interpolation of elasticity coefficients and thermal conductivity for 2D LUCs.

Mesoscale analysis and homogenization

For the interpolation of the elastic and thermal properties, let us consider a sequence of square (2D) representative LUCs with known relative density values θ_c' (Fig. 2.7). The size of each 2D LUC is 20×20 (dimensionless length quantities). The finite element mesh is composed of Lagrange-type quadrialetral square (Q4) elements of size 1×1. Different sizes of rectangular holes are pre-defined in the center of the LUCs. While these are not optimized mesoscale structures, the shapes of the predefined LUCs are similar to those having maximum bulk modulus and maximum thermal conduction reported in literature [75, 141]. Due to the symmetry of their structure, only $D^H_{c,1111}$, $D^H_{c,1122}$, $D^H_{c,1212}$, and $\kappa^H_{c,11}$ need to be computed as shown by Eqs. (2.6) and (2.13). Third-order polynomial approximations for $D^H_{c,1111}$, $D^H_{c,1122}$, $D^H_{c,1212}$, and $\kappa^H_{c,11}$ are defined according to Eqs. (2.15) and (2.16). The results are shown for unit elements Young's modulus and unit thermal conductivity so the approximation can be easily scaled (Fig. 2.7). Notably, the interpolations of the homogenized elastic properties $D^H_{c,ijkl}(\theta)$ are scaled by a factor of E_0 and the interpolation of the homogenized thermal conductivity $\kappa^H_{c,ij}(\theta)$ is scaled by a factor of κ_0.

Macroscale structural optimization

The macroscale structural optimization involves the solution of two problems. The first problem is stated in Eq. (2.27) and the second problem is stated in Eq. (3.10). In this example, $\theta_c^{\min} = 0.19$, $C_W = 2.0$, and $C_Q = 1.2$ are utilized. Table 2.1 summarizes the performance and topologies of the solid design $\boldsymbol{\theta}_0$, the solution of the first problem $\boldsymbol{\theta}_1^*$, and several solutions to the second problem $\boldsymbol{\theta}_2^*$. The solid design (row a) depicts the highest mass m, the lowest (best) mechanical compliance W and thermal compliance Q as well as the lowest maximum surface nodal temperature $T(\boldsymbol{\theta}_0)$ and lowest maximum nodal displacement $U(\boldsymbol{\theta}_0)$.

The solution to the first problem (row b) has the lowest mass satisfying the mechanical and thermal compliance constraints. Since the material interpolation is linear, this design is conceptual but offers a reasonably good initial design for the second problem. Several solutions of the second problem are presented in Table 2.1 (rows c to k). Here, non-convex functional constraints associated with U and T are implemented using $C_U = 1$ and $C_T = 1.05$; this is, no allowed increase in displacement and a five percent increase in temperature with respect to the solid design.

Without regularization ($C_R = 0$) and without penalization ($C_P = 0$), the solution is binary (row c). This solution has the lowest mass $m(\boldsymbol{\theta}_2^*)$; however, it depicts thin-members that are difficult or impossible to capture in the additive manufacturing process. This drawback can be addressed with the use of the regularization function ($C_R = 0.001$) (row d). While the mass is increased with the respect to the previous design, the thin-members are no longer present. Unfortunately, there is a range of values of θ_c that cannot be captured in the additive manufacturing process due to the spatial material gradation.

Optimal manufacturable results (clustered designs) are achieved with the use of regularization ($C_R = 0.001$) and penalization ($C_P = 0.4$) functions. Table 2.1 includes solutions with two lattice phases (rows e to g), three lattice phases (rows h to j, and four lattice phases (row k). The predefined LUCs used in this problem are: $\theta_1' = 0.19$, $\theta_2' = 0.51$, $\theta_3' = 0.75$, and $\theta_4' = 1.00$ (solid phase). In these designs, W, Q, and $U(\boldsymbol{\theta})$ are active constraints. The

constraint associated with $T(\boldsymbol{\theta})$ is inactive, hence the maximum temperature of these designs have small differences. For the optimization problem considered, the optimal design is the two-phase structure (row e) which has the lowest mass and satisfies all constraints; however, the haviest two-phase design (row g) may also be considered as an alternative since it has the lowest maximum temperature. With respect to the solid design, the optimal design (row e) reduces the mass in about 31.1% without increasing the maximum displacement, and increasing the maximum temperature in only about 2.0%.

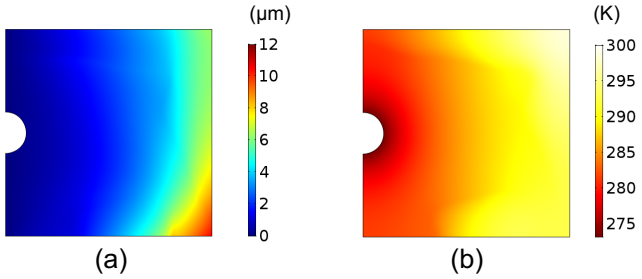

Figure 2.8.. Finite element analysis of the two-material, optimal design Table 2.1 (row e): (a) nodal displacement, and (b) nodal temperature distribution.

2.5.2 Design of a plastic injection mold

The proposed approach is applied to the optimal design of a multiphase, lattice plastic injection mold utilized for producing bump caps used in the car shock absorber. The injection mold consists of two main components: the cavity plate and the core plate. Each plate contains a solid volume comprising the surface in contact with the injected part. The mold is designed so that the injected part remains in the core plate and is ejected by ejection pins. The core plate is also referred to as the ejector mold. The geometries of the cavity and the core plates are shown in Fig. 2.9. During the optimization process the cooling channels and other orifices remain unchanged. The surfaces in contact with the cooling channels, orifices, and the injected part remain solid during the optimization process. The surfaces

Table 2.1.. Performance function values for the initial and final designs of the 2D plate.

Row	Design	$\boldsymbol{\theta}$	$m(\boldsymbol{\theta})$ [kg]	$W(\boldsymbol{\theta})$ [mJ]	$Q(\boldsymbol{\theta})$ [kg·m^2 ·K·s^{-3}]	$U(\boldsymbol{\theta})$ [μm]	$T(\boldsymbol{\theta})$ [K]
(a)	$\boldsymbol{\theta}_0 = \mathbf{1}$	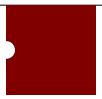	78.500	1.871	114.75	0.278	288.00
(b)	$\boldsymbol{\theta}_1^*$	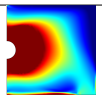	46.970	3.743	137.70	0.384	293.89
(c)	$\boldsymbol{\theta}_2^*(C_R = 0, C_P = 0)$		51.770	3.743	137.70	0.278	293.89
(d)	$\boldsymbol{\theta}_2^*(C_R = 0.001, C_P = 0)$		53.255	3.743	137.70	0.278	293.69
(e)	$\boldsymbol{\theta}_2^* \in \{\theta_1', \theta_4'\}(C_R = 0.001, C_P = 0.4)$		54.085	3.743	137.70	0.278	294.01
(f)	$\boldsymbol{\theta}_2^* \in \{\theta_2', \theta_4'\}(C_R = 0.001, C_P = 0.4)$		58.100	3.743	137.70	0.278	292.45
(g)	$\boldsymbol{\theta}_2^* \in \{\theta_3', \theta_4'\}(C_R = 0.001, C_P = 0.4)$		62.524	3.743	137.70	0.278	292.18
(h)	$\boldsymbol{\theta}_2^* \in \{\theta_1', \theta_2', \theta_4'\}(C_R = 0.001, C_P = 0.4)$	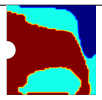	56.320	3.743	137.70	0.278	293.52
(i)	$\boldsymbol{\theta}_2^* \in \{\theta_1', \theta_3', \theta_4'\}(C_R = 0.001, C_P = 0.4)$		55.114	3.743	137.70	0.278	292.91
(j)	$\boldsymbol{\theta}_2^* \in \{\theta_2', \theta_3', \theta_4'\}(C_R = 0.001, C_P = 0.4)$		58.305	3.743	137.70	0.278	292.47
(k)	$\boldsymbol{\theta}_2^* \in \{\theta_1' \text{ to } \theta_4'\}(C_R = 0.001, C_P = 0.4)$	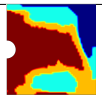	57.099	3.743	134.41	0.278	293.66

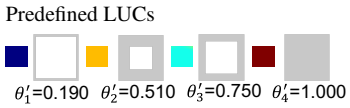

in contact with the injected part and the thread taps are simplified in order to improve the mesh quality of the finite element model and facilitate the numerical analysis.

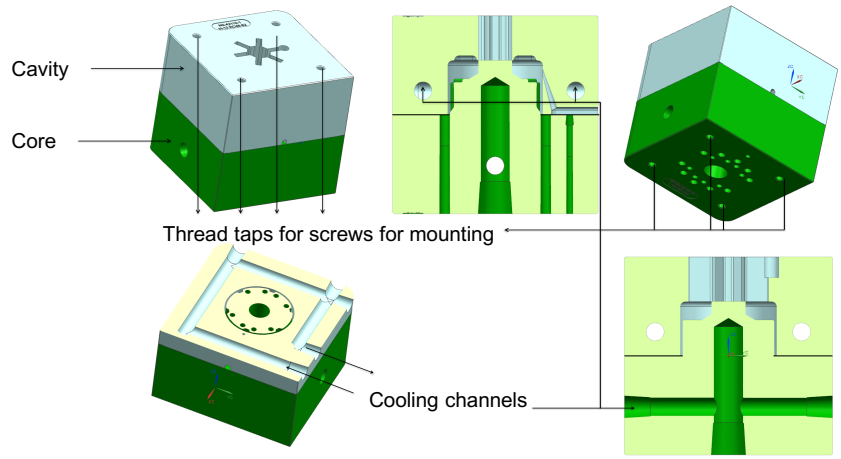

Figure 2.9.. The geometry of the original injection mold. Source: Hewitt Molding Company

Mesoscale analysis and homogenization

The homogenization of elastic and thermal properties makes use of cubic (3D) representative LUCs with relative densities θ_c' as shown in Fig. 2.10. For the analysis, each 3D LUC is discretized into $20 \times 20 \times 20$ Lagrange brick elements. Different sizes of rectangular holes are pre-defined along the three central, orthogonal axes of the LUCs. As before, while these are not optimized mesoscale structures, the shapes of the predefined LUCs are similar to those having maximum bulk modulus and maximum thermal conduction reported in literature [55, 75]. Due to the symmetry of the LUC structure, only $D^H_{c,1111}$, $D^H_{c,1122}$, $D^H_{c,1212}$, and $\kappa^H_{c,11}$ need to be computed. Third-order polynomial approximations are defined according to Eqs. (2.15) and (2.16). The results are shown for unit elements Young's modulus and unit thermal conductivity so the approximation can be easily scaled (Fig. 2.10). A verification with respect to Hashin-Shtrikman (H-S) bounds for two-phase materials is shown in the Appendix.

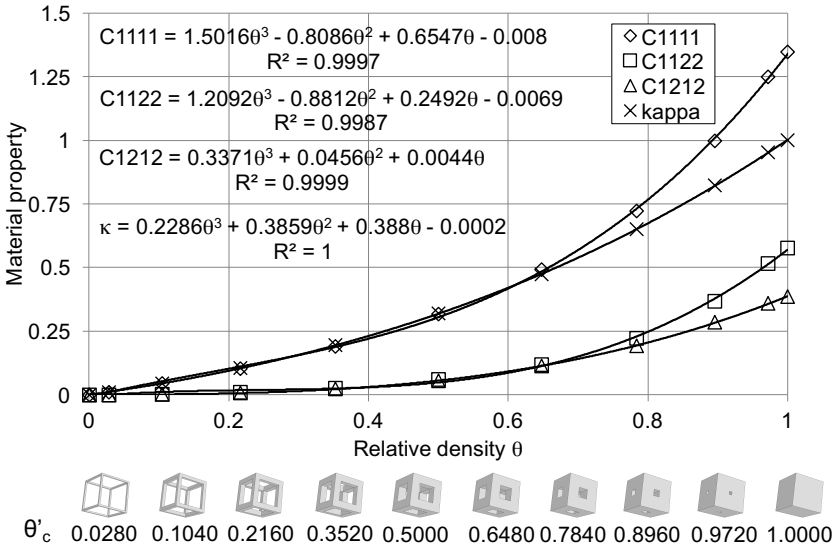

Figure 2.10.. Interpolation of elasticity coefficients and thermal conductivity for 3D LUCs.

Macroscale design of the cavity plate

The cavity plate is designed withing a design domain of dimensions 5.0 in $\times$ 5.0 in $\times$ 2.6 in (127 mm $\times$ 127 mm $\times$ 66 mm). This design domain is discretized into 97705 tetrahedral finite elements. The top surface of the cavity plate sustains a uniformly distributed load of 110 ton (1.08×10^6 N). Rollers are applied on the lateral surface nodes. The nodal displacement of the bottom surface is constrained in the z-direction. The injection pressure on the cavity is 131 MPa including the effect of thermal expansion. Straight cooling channels are enclosed the injected part, and the temperature of the cooling channel surfaces is assumed to be 26.7 °C (299.9 K). In steady state, a heat flux of 200 W is imposed on the cavity. All other surfaces of the core are insulated (Fig. 2.11). The boundaries Γ_W and Γ_Q are defined as the cavity's surface in contact with the injected part. The nodal displacement and temperature distributions of the initial solid mold are shown in Fig. 2.11.

The design $\boldsymbol{\theta}_1^*$ corresponding to the solution of the first optimization problem Eq. (2.27) is shown in Fig. 2.12 (a). The performance of this design is summarized in Table 2.2 (row

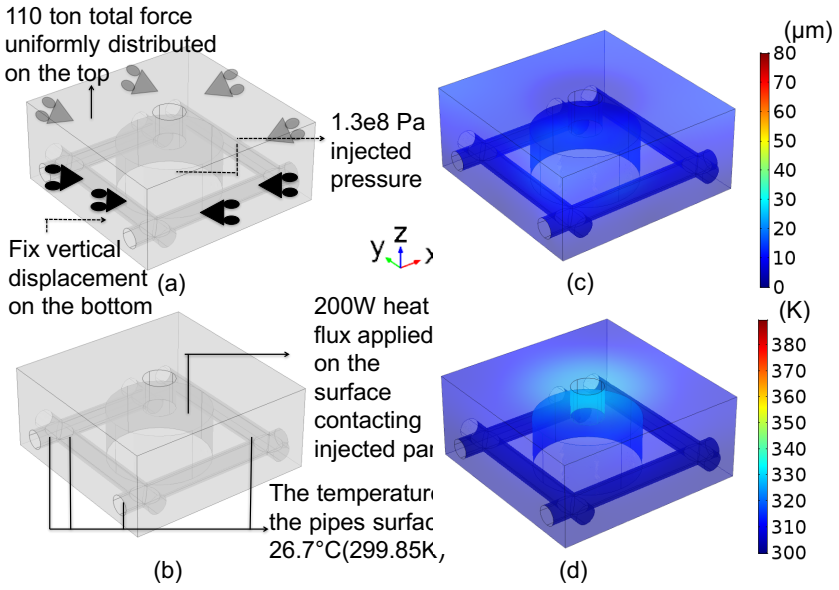

Figure 2.11.. Boundary conditions and results of the cavity plate's design domain with solid matrix: (a) mechanical loads and supports; (b) thermal heat flux and sink (cooling channel); (c) nodal displacement; and (d) nodal temperature distribution.

b). This initial design has the lowest mass m and satisfies the two functional constraints, i.e., mechanical compliance W and thermal compliance Q.

For the second problem Eq. (3.10), three predefined relative density values are used: $\theta_1' = 0.259$, $\theta_2' = 0.741$, and $\theta_3' = 1.000$ (solid phase). The parameters $C_P = 0.01$, $C_R = 0.03$, $C_U = 1$, and $C_T = 1.05$ are used in the optimization problem formulation. Here, two solutions $\boldsymbol{\theta}_2^*$ are presented Fig. 2.12 (b) and (c). These solutions consider two and three lattice phases, respectively. For these two designs, the constraints on W, Q, and $U(\boldsymbol{\theta})$ are activate, while the constraint on $T(\boldsymbol{\theta})$ is inactivate. The performance of each optimal design is summarized in Table 2.2 (rows c and d). The two-phase design shows a 23.8% mass reduction with respect to the solid design. For the surface in contact with injected part, the maximum displacement remains the same and the maximum temperature increases 3.1%. The three-phases design has an improved (inactive) mechanical compliance and higher mass. Based on the problem statement, the two-phase design is preferred.

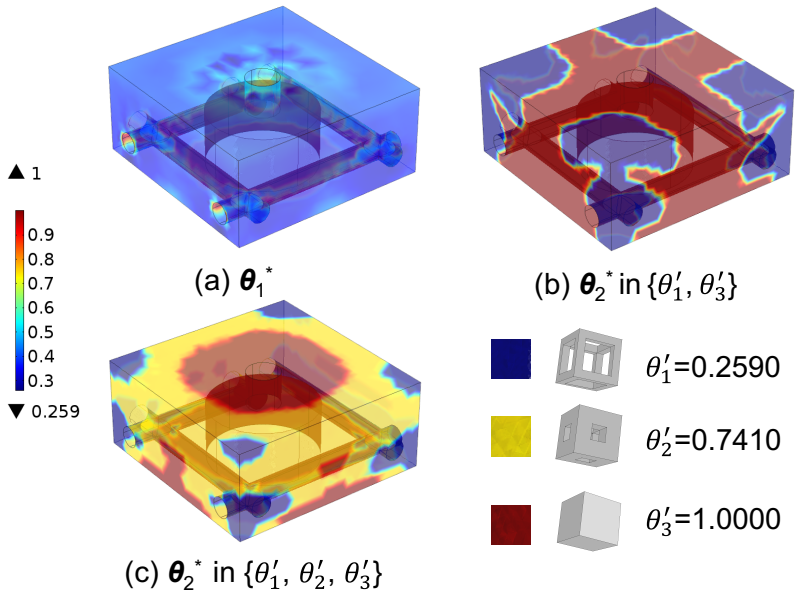

Figure 2.12.. The result optimal LUC phases distribution of the design domain for the cavity plate.

Table 2.2.. Performance function values of the initial and final designs of the cavity

Row	Design	$m(\boldsymbol{\theta})$ [kg]	$W(\boldsymbol{\theta})$ [J]	$Q(\boldsymbol{\theta})$ [kg·m^2 ·K·s^{-3}]	$U(\boldsymbol{\theta})$ [μm]	$T(\boldsymbol{\theta})$ [K]
(a)	$\boldsymbol{\theta}_0 = \mathbf{1}$	5.275	12.78	3992.8	22.18	337.52
(b)	$\boldsymbol{\theta}_1^*$	3.112	25.55	4791.4	30.25	348.25
(c)	$\boldsymbol{\theta}_2^* \in \{\theta_1', \theta_3'\}$	4.072	25.55	4791.4	22.18	348.00
(d)	$\boldsymbol{\theta}_2^* \in \{\theta_1', \theta_2', \theta_3'\}$	4.086	23.80	4792.0	22.18	347.90

Macroscale design of the core plate

The dimensions of the design domain for the core plate are 5.0 in $\times$ 5.0 in $\times$ 2.3 in (127 mm $\times$ 127 mm $\times$ 66 mm). The design domain is discretized into 113982 tetrahedral

finite elements. The bottom surface of the core sustains a uniformly distributed load of 110 ton (1.08×10^6 N). Rollers are applied on the lateral surfaces. The displacement of the top surface is constrained in the z-direction. As before, the injection pressure on the interface between the part and the core is 131 MPa. The temperature on the surface of the cooling channel is set to be 26.7 °C (299.9 K). At the steady state, a heat flux of 200 W is imposed on the interface between the part and the core. All other surfaces of the core are insulated. The boundaries Γ_W and Γ_Q are defined as the plate's surface in contact with the part. The nodal displacement and temperature distributions of the initial solid mold are shown in Fig. 2.13.

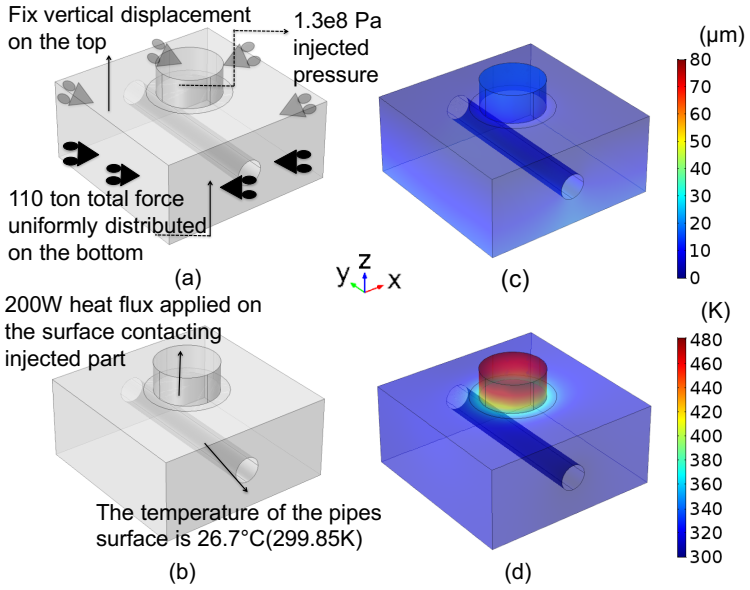

Figure 2.13.. Boundary conditions and FEA results of the core plate with solid matrix: (a) mechanical loads and supports; (b) thermal heat flux and sink (cooling channel); (c) nodal displacement; and (d) nodal temperature distribution.

The design $\boldsymbol{\theta}_1^*$ corresponding to the solution of the first optimization problem, Eq. (2.27), is shown in Fig. 2.14 (a). The performance of this design is summarized in Table 2.3 (row b). As expected, this initial design has the lowest mass m and satisfies the functional constraints on mechanical compliance W and thermal compliance Q.

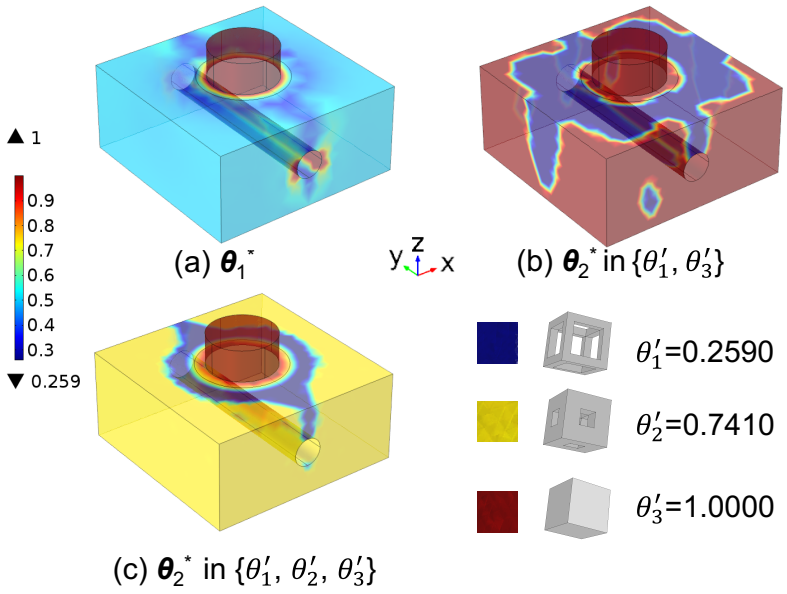

Figure 2.14.. The result optimal LUC phases distribution of the design domain for the core plate.

Table 2.3.. Performance function values of the initial and final designs of the core.

Row	Design	$m(\boldsymbol{\theta})$ [kg]	$W(\boldsymbol{\theta})$ [J]	$Q(\boldsymbol{\theta})$ [kg·m^2 ·K·s^{-3}]	$U(\boldsymbol{\theta})$ [μm]	$T(\boldsymbol{\theta})$ [K]
(a)	$\boldsymbol{\theta}_0 = \mathbf{1}$	6.971	11.20	27037.0	16.95	481.92
(b)	$\boldsymbol{\theta}_1^*$	3.830	22.40	32444.4	15.05	507.84
(c)	$\boldsymbol{\theta}_2^* \in \{\theta_1', \theta_3'\}$	4.771	22.40	32444.4	14.63	502.10
(d)	$\boldsymbol{\theta}_2^* \in \{\theta_1', \theta_2', \theta_3'\}$	5.150	20.85	31652.2	15.61	501.94

For the second problem, Eq. (3.10), the same three predefined relative density values are used, namely, $\theta_1' = 0.259$, $\theta_2' = 0.741$, and $\theta_3' = 1.000$ as well as the same parameters $C_P = 0.01$, $C_R = 0.03$, $C_U = 1$, and $C_T = 1.05$ in the optimization problem formulation.

Two solutions $\boldsymbol{\theta}_2^*$ are presented Fig. 2.14 (b) and (c). These solutions consider two and three lattice phases, respectively. For these two designs, the constraints on W and Q are activate, while the constraints on $U(\boldsymbol{\theta})$ and $T(\boldsymbol{\theta})$ are inactivate. The performance of each optimal design is summarized in Table 2.3 (rows c and d). The two-phase design shows a 31.6% mass reduction with respect to the solid design. For the surface in contact with injected part, the maximum displacement remains the same and the maximum temperature increases 4.2%.

Conformal cooling

In order to achieve better thermal performance, the proposed design approach can be applied to mold plates with conformal cooling channels. In this example, the straight cooling channel is replaced by a U-shaped cooling channel. This cooling channel conforms to the internal shape of the core plate as shown in Fig. 2.15. This modification significantly decreases the core plate's maximum temperature $T(\boldsymbol{\theta})$ and the thermal compliance Q without significantly change the maximum displacement $U(\boldsymbol{\theta})$. As in the previous example, the two-phases design is the optimal solution. The FEA results are shown in Fig. 2.15 and the performance of each optimal design n is summarized in Table 2.4.

Table 2.4.. Performance function values for the initial and final designs of the core plate with conformal cooling.

Row	Design	$m(\boldsymbol{\theta})$ [kg]	$W(\boldsymbol{\theta})$ [J]	$Q(\boldsymbol{\theta})$ [kg·m^2 ·K·s^{-3}]	$U(\boldsymbol{\theta})$ [μm]	$T(\boldsymbol{\theta})$ [K]
(a)	$\boldsymbol{\theta}_0 = \mathbf{1}$	6.874	11.63	10966.0	19.92	388.18
(b)	$\boldsymbol{\theta}_1^*$	3.673	23.26	11325.7	18.95	389.61
(c)	$\boldsymbol{\theta}_2^* \in \{\theta_1', \theta_3'\}$	4.612	23.26	11205.1	14.91	388.85
(d)	$\boldsymbol{\theta}_2^* \in \{\theta_1', \theta_2', \theta_3'\}$	4.978	23.26	11452.9	15.61	389.27

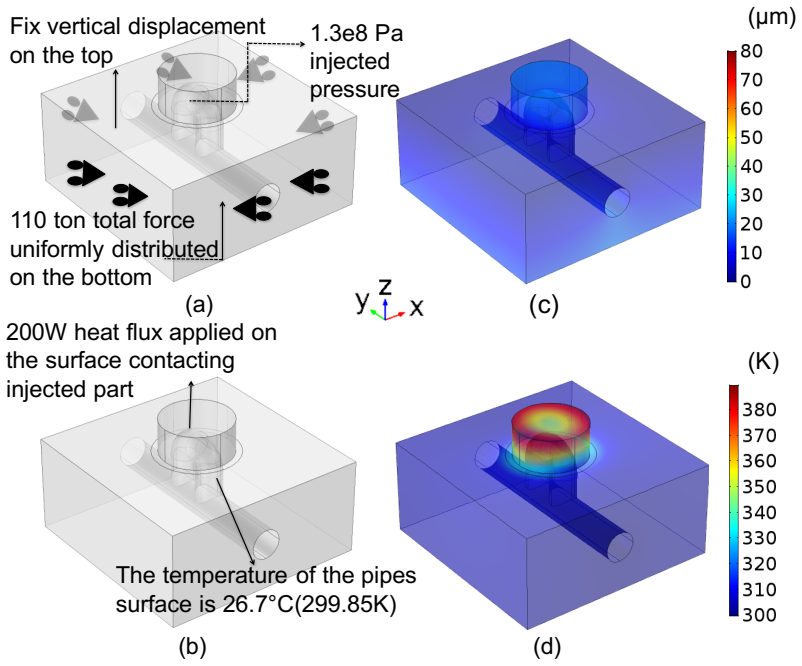

Figure 2.15.. Boundary conditions and FEA results of the core plate with solid matrix and conformal cooling channels: (a) mechanical loads and supports; (b) thermal heat flux, sink (cooling channel), and insulation; (c) nodal displacement; and (d) nodal temperature distribution.

Final design and additive manufacturing considerations

The optimized design domains for the core and cavity plates are defined by nodal density fields. These fields are interpolated in order to generate the final LUC rectangular grid. The rectangular LUC grid is merged to the initial mold design using boolean operations. The commercial software Netfabb® is used for this task. The merging operation eliminates hollow spaces in the interface and guarantees the quality of the final STL file used in additive manufacturing. The size and quality of the STL file depends on the number of triangles (or polygons) to tessellate the geometry. Generally, the STL file size and the number of triangles is limited by the 3D printer and also by the post-processing software. In work, Formlab Form 2 SLA printer (Formlabs, Somerville, MA) and the software

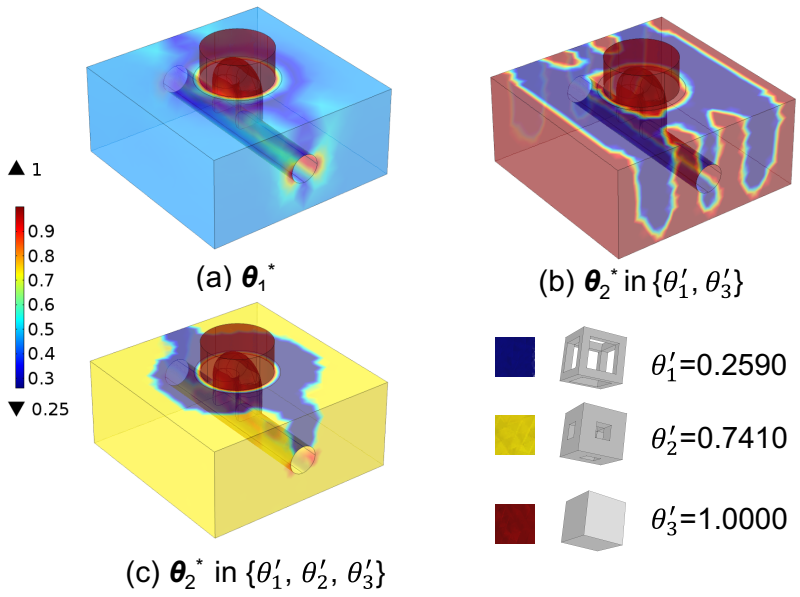

Figure 2.16.. The result optimal LUC phases distribution of the design domain for the core plate with conformal cooling.

Netfabb® (Autodesk, San Rafael, CA) are utilized. In order to keep the size of the STL small and tractable, only a two to four predefined LUCs are used in this work.

The final cavity and the core plate designs with conformal cooling channels are prototyped using a Formlabs Form 2 stereolithography (SLA) printer. Clear resin is used to visualize the internal lattice structure and the conformal cooling channels (Fig. 2.18). The lattice structure is embodied by cubic LUCs. The size of each cubic LUC is 0.2 in $\times$ 0.2 in $\times$ 0.2 in (5 mm $\times$ 5 mm $\times$ 5 mm). The minimum strut size and the minimum hole size within the LUC are 0.067 in (1.7 mm). The core plate is composed of 25 $\times$ 25 $\times$ 13 LUCs. The cavity plate is composed of 25 $\times$ 25 $\times$ 12 LUCs. Experimental verification in the SLA unit shows that there is no need for an internal support structure. The relative LUC size effect for homogenized properties of this structure is small [142].

In order to demonstrated the feasibility for metal additive manufacturing, a sample containing 125 functionally graded LUCs (5 $\times$ 5 $\times$ 5) is prototyped in a Direct Metal Laser Sintering (DMLS) unit (EOS M280, Hamburg, Germany) (Fig. 2.18 g). The test shows that

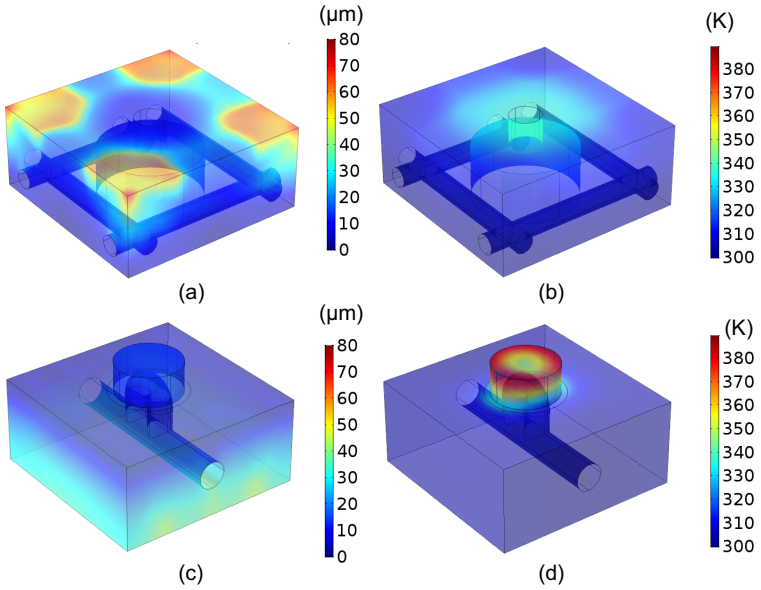

Figure 2.17.. Finite element analysis of the two-material optimal design: (a)The nodal displacement distribution of Table 2.2 (row c); (b) the nodal temperature distribution of Table 2.2 (row c); (c) the nodal displacement distribution of Table 2.4 (row c); and (d) the nodal temperature distribution of Table 2.4 (row c).

without internal support structure, the quality of any lattice cube with strut and hole size greater than 0.03 in (0.762 mm) is guaranteed: smaller strut members may curl during and smaller holes may be completely filled during the additive manufacturing process.

2.6 Conclusion

This Chapter presents a multiphase topology optimization approach to obtain lightweight lattice injection molds. The mesoscale LUC thermomehanical properties are derived using asymptotic homogenization. A polynomial fitting function is conveniently defined in order to conduct the macroscale structural optimization. The optimal macroscale design is obtained through thermomechanical, FEA-based structural optimization.

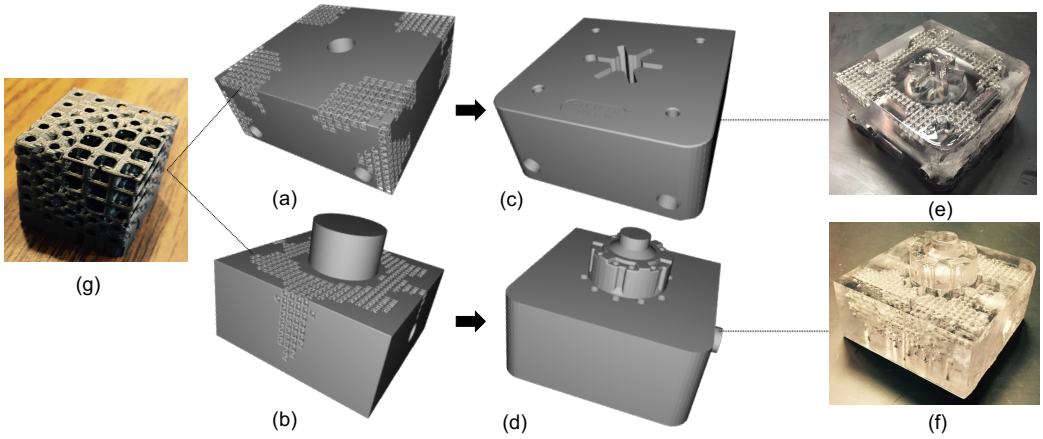

Figure 2.18.. (a) The lattice structure of the design domain of the cavity; (b) The lattice structure of the design domain of the core; (c) The final design of the cavity; (d) The final design of the core; (e) The final 3D-printed cavity in plastic resin; (f) The final 3D-printed core in plastic resin; (g) A lattice structure sample 3D-printed in stainless steel.

The proposed approach allows the systematic optimal design of lightweight lattice structures satisfying the global and local mechanical and thermal constraints. The optimal structure is defined by the optimal distribution of predefined lattice LUCs. In this study, homogenization is extended to three-dimensional structures and includes elastic properties as well as thermal properties. The numerical examples show that, with respect to a traditional solid design, a small change in nodal displacement (less than 5 μm) and no change in nodal temperature allows for significant mass reduction (over 30%). Since less material is used in the optimized designs, this translates into manufacturing cost savings. The resulting three-dimensional structures are manufacturable using additive manufacturing. With the development of additive manufacturing technologies for metallic tools (rapid tooling) it is expected that lattice molds become more popular in the near future.

Ongoing work focuses on the thermal and mechanical experimental tests. In addition, the influence of the lattice LUC's architecture on the additive manufacturing cost and fea-

sibility will be investigated. Finally, rather than assuming the constant temperature on the surface of the pipe, effort should be devoted on including heat convection and advection effects in pipe flows in the future design. To improve the steady state analysis, cooling cycles of the optimal design may be investigated. In addition, coupled thermo-elastic homogenization is being implemented so that the effect of thermo-elastic load will be consistently taken into account so this approach can be extended to general thermo-mechanical applications.

Appendix 1: Verification of the homogenization using Hashin-Shtrikman bounds

For verification of the homogenization and interpolation procedures, let us consider lattice LUCs using linear elasticity and thermal conductivity theories. The bulk modulus is given by

$$\begin{aligned} K(\theta) &= D^H_{c,1111}(\theta) - \tfrac{4}{3} D^H_{c,1212}(\theta) \\ &= D^H_{c,1122}(\theta) - \tfrac{2}{3} D^H_{c,1212}(\theta), \end{aligned} \tag{2.33}$$

the shear modulus is given by

$$\mu(\theta) = D^H_{c,1212}(\theta), \tag{2.34}$$

and thermal conductivity is given by

$$\kappa(\theta) = \kappa^H_{c,1}(\theta). \tag{2.35}$$

The bulk modulus, shear modulus, and thermal conductivity are compared with the Hashin-Shtrikman (H-S) bounds for two-phase materials [143, 144]. Figure 2.19 represents H-S bounds and functions corresponding to the 3D LUCs. As expected, the polynomial approximations falls within the H-S bound, closer to the upper bound.

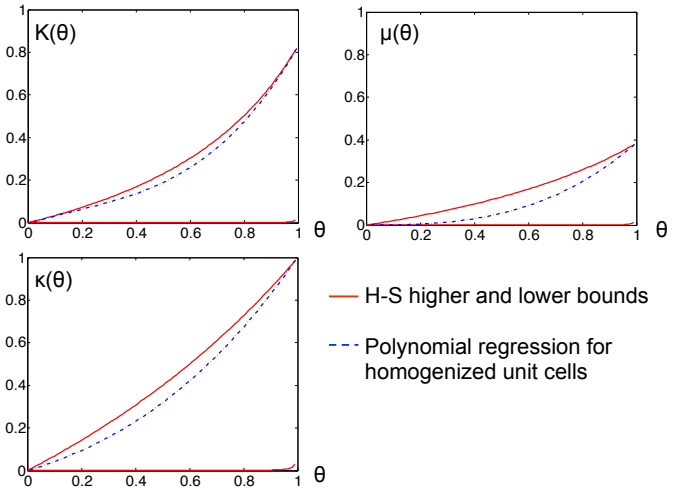

Figure 2.19.. The comparision between continuous 3D LUCs properties derived by polynomial regression and Hashin-Strikman bounds.

3. MULTISCALE, THERMOMECHANICAL TOPOLOGY OPTIMIZATION OF SELF-SUPPORTING CELLULAR STRUCTURES

This chapter aims to establish a multiscale topology optimization method for the optimal design of non-periodic, self-supporting cellular structures subjected to thermo-mechanical loads. The result is a hierarchically complex design that is thermally efficient, mechanically stable, and suitable for additive manufacturing. The proposed method seeks to maximize thermo-mechanical performance at the macroscale in a conceptual design while obtaining maximum shear modulus for each unit cell at the mesoscale. Then the macroscale performance is re-estimated and the mesoscale design is updated until the macroscale performance is satisfied. A two dimensional MBB beam withstanding thermo-mechanical load is presented to illustrate the proposed design method. Furthermore, the method is implemented to optimize a three-dimensional injection mold, which is successfully prototyped using 420 stainless steel infiltrated with bronze. By developing a computationally efficient and manufacturing friendly inverse homogenization approach, the novel multiscale design could generate porous molds which can save up to 30% material compared to their solid counterpart without decreasing thermo-mechanical performance. This study is a useful tool for the designer in molding industries to reduce the cost of the injection mold and take full advantage of additive manufacturing.

3.1 Background and motivation

Molds used in the plastic injection molding process must withstand extreme pressure loads and thermal expansion, while at the same time providing dimensional accuracy of the molded part. These molds are required to efficiently and uniformly transfer heat flux

from the molded part to cooling channels [131]. In conventional molds, the cooling system often consists of straight-line cooling channels, which can be manufactured using machining processes; however, they are thermally inefficient and unable to cool the injected part uniformly. The emergence of metal based Additive Manufacturing (AM) enables the design and production of intricate conformal cooling channels in molds, offering significant cost savings, particularly in designs having high geometric complexity. These AM technologies include Direct Metal Laser Sintering (DMLS), Electron Beam Melting (EBM) and Selective Laser Melting (SLM) [145]. The unique capabilities of AM technologies allow innovative design approachs that challenge traditional guidelines of the several major industries including plastics injection molding [146, 147].

These approaches, aiming to reduce the AM cost without decreasing the performance of design part, can be divided into three groups, namely macroscale (structural) design, mesoscale (meta-material) and multiscale design. In macroscale, structural optimization, including size optimization, shape optimization and topology optimization, are the most commonly used methods for parts design of additive manufacturing . Among them, topology optimization has the best design flexibility since it allows material distributed in terms of physics requirement, offering the potential to create novel and complex parts with high performance and reducing material cost [42, 148]. Some studies have been investigated to develop design frameworks of topology optimization for additive manufacturing for mechanical, thermal and thermo-mechanical structures [42, 122, 149]. In mesoscale, the solid phase meta-materials can be replaced with open cell lattice or porous materials, without changing the macroscale geometry contours [48, 146, 150]. Finally, in a multiscale design, both macroscale and mesoscale design method are simultaneously applied [58, 63, 65, 151]. The most computationally efficient and manufacturing friendly multiscale approach is called Topology Optimization with Functionally Graded Unit Cells [58, 151]. In this method, homogenized properties of a series of pre-defined lattice unit cells with functionally graded relative densities, from void to solid, are derived. The properties of these unit cells are synthesized and implemented in the macroscale topology optimization, leading optimal structures that composed of quasi-periodically distributed, functionally

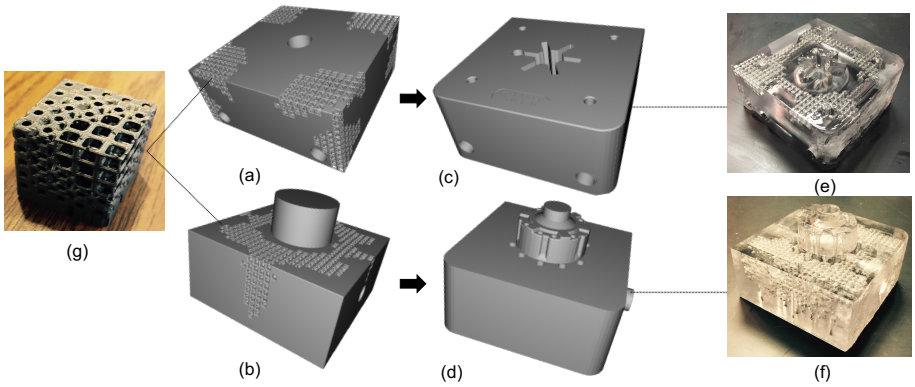

Figure 3.1.. (a) The lattice structure of the design domain of the cavity; (b) The lattice structure of the design domain of the core; (c) The final design of the cavity; (d) The final design of the core; (e) The final 3D-printed cavity in plastic resin; (f) The final 3D-printed core in plastic resin; (g) A lattice structure sample 3D-printed in stainless steel.

graded unit cells. As an example, in our previous work [151], injection molds designed using this method can ideally save 10% to 30% of material cost without compromising thermo-mechanical performance of the mold, as well as maintaining the geometry in contact with other mold assemblies (Fig.3.1).

Despite of the straightforward of this method, in such optimal design, the geometry complexity of the unit cells are limited since they are controlled by limmited functionally graded parameters. Furthermore, these lattice unit cells may consist of some undesirable long overhanging struts, which lead risks of deformation or sagging in the manufacture process. To support these unstable structures, additional material would be required during AM process. As a result, the actual material usage is more than anticipated. In addition, the removal of large amount of support materials for delicate lattice unit cell structures is time consuming and may breaking off small pieces of lattices. An efficient strategy to reduce support structure materials is to construct self-supporting lattice unit cells in mesoscale design. Self-supporting strucuture ensures that, during the manufacturing process of these cells, one building layer can be supported by its underneath layer without distorted too

much or even fail [48]. To obtain a self-supporting lattice structure, the fabrication angle between horizontal plane and downward face of the lattice unit cell should be more than some critical values between 40° to 45° [150]. Typical design strategies to design structures fulfilled this fabrication angle criterion include Computer Aided Design (CAD), biological architecture image data based design, and implicit surface design based on analytical mathematical equations. However, all of these strategies are developed by means of designers' intuition and experience, often requiring a tedious trial and error process to achieve the expected properties. Fortunately, the inverse homogenization method can complement this weakness [49]. With application of inverse homogenization, the optimum topologies of a lattice unit cell with maximum bulk modulus, shear modulus or heat conduction can be obtained [55, 75]. Among these topologies, the lattice unit cell having maximum shear modulus represents a diamond shape that benefit to reduce the support structure material in AM process.

However, inverse homogenization method is mainly implemented in a mesoscale design rather than in a multiscale design, probably due to the high computational cost to optimize each unit cell. In this study, a multiscale thermo-mechanical topology optimization algorithm involved a computationally efficient inverse homogenization method is proposed. A multiscale topology optimization specifies that, the optimized topologies are achieved in both macroscale structure and mesoscale unit cells. The two scales topologies can be optimized either concurrently or hierarchically. The concurrent approach is computationally efficient but it results in only one periodically distributed mesoscale topology [63], while the hierarchically approach can attain optimized properties for each lattice unit cell but it costs significant computational resource and time. Although this hierarchical approach has been an active research topic for many years [65], few of them are applied this approach in three dimensional design with consideration of manufacture issues. In our study, by implementing a computationally efficient inverse homogenization method to maximize shear modulus of each unit cell, the whole structure is self-supporting and easy to manufacture. Furthermore, a Hybrid Cellular Automata (HCA) [66] updating scheme is employed to guaranteed the thermo-mechanical performance of the macroscale structure. Also, com-

pared to our previous work [151], the method brings a manufacturing friendly design and the design accuracy is improved since each mesoscale unit cell is optimized.

The paper is organized as following: homogenization method, which is the foundation of the proposed approach, will be briefly reviewed in section 2. Then, the proposed multiscale thermo-mechanical topology optimization is presented in section 3. In section 4, the method is demonstrated by optimizing a solid mold to a porous injection mold. In Section 5, the issues with respect to final design, manufacturing as well as future experiment plan are described. Finally, conclusion is presented in section 6.

3.2 Representative volume element based homogenization

The material design is formulated as a structural optimization problem and be optimized using inverse homogenization method [152]. The objective function of this method contains effective properties of investigated material, which are found by numerical homogenization. Numerical homogenization can be implemented in asymptotic method (AH), mutual energy approach and represent volume element (RVE)-based approach. All of them can be used to derive homogenized elasticity tensor $\mathbf{D}_c^H$ and thermal conductivity tensor $\boldsymbol{\kappa}_c^H$ of an a-priori defined unit cell. In this section, these methods are briefly reviewed before presenting the proposed multiscale thermomechanical topology optimization approach.

3.2.1 Asymptotic homogenization and energy-based homogenization

Asymptotic homogenization (AH) assumes each mesoscale unit cell in a macroscale structure follows periodic boundary condition (PBC). The measurable quantity of a unit cell u is the superposition of macroscale quantity $u_0(x,y)$ and a small periodically fluctuated mesoscale quantity $u_1(x,y)$, which can be represented using first order asymptotic expansion:

$$u^{\varepsilon} = u_0(x,y) + \varepsilon u_1(x,y) + \mathscr{O}(\varepsilon^2), \quad y = x/\varepsilon, \quad \varepsilon \ll 1. \tag{3.1}$$

Asymptotic homogenization can be rewritten in an equivalent discretized form in terms of element mutual energies:

$$\mathbf{D}_c^H = \frac{1}{|V_c|}\sum_{e=1}^{n_e}\int_{V_e}[\mathbf{I}-\mathbf{B}_e\boldsymbol{\chi}_e]^\intercal\mathbf{D}_e[\mathbf{I}-\mathbf{B}_e\boldsymbol{\chi}_e]\mathrm{d}V_e, \tag{3.2}$$

where n_e are the number of finite elements of the discretized unit cell, $|V_c|$ is the unit cell volume, $\mathbf{I}$ is the identity matrix, V_e is the volume of the finite element e, $\mathbf{B}_e$ is the elemental strain-displacement matrix, $\mathbf{D}_e$ is the elemental elasticity tensor, and $\boldsymbol{\chi}_e$ is the matrix containing the element displacement vectors $\boldsymbol{\chi}_e^{ij}$ resulting from globally enforcing the unit test strain fields $\boldsymbol{\varepsilon}^{ij}$ ($[\boldsymbol{\chi}_e^{11},\boldsymbol{\chi}_e^{22},\boldsymbol{\chi}_e^{12}]$ for a 2D finite element). The elemental displacement vectors $\boldsymbol{\chi}_e^{ij}$ are obtained from the global displacement vector of the unit cell $\boldsymbol{\chi}_c^{ij}$, which is the solution of the equilibrium equation

$$\left[\sum_{e=1}^{n_e}\int_{V_e}\mathbf{B}_e^\intercal\mathbf{D}_e\mathbf{B}_e\mathrm{d}V_e\right]\boldsymbol{\chi}_c^{ij} = \sum_{e=1}^{n_e}\int_{V_e}\mathbf{B}_e^\intercal\mathbf{D}_e\boldsymbol{\varepsilon}^{ij}\mathrm{d}V_e. \tag{3.3}$$

The first term in the left hand side of Eq. (3.3) is the stiffness matrix of the unit cell and the right hand side is the nodal force vector of the unit cell.

In analogy to homogenization theory for elasticity tensor, homogenized thermal conductivity tensor $\boldsymbol{\kappa}_c^H$ of a discretized periodic unit cell is given by

$$\boldsymbol{\kappa}_c^H = \frac{1}{|V_c|}\sum_{e=1}^{n_e}\int_{V_e}[\mathbf{I}-\mathbf{B}_e^t\mathbf{T}_e]^\intercal\boldsymbol{\kappa}_e[\mathbf{I}-\mathbf{B}_e^t\mathbf{T}_e]\mathrm{d}V_e, \tag{3.4}$$

where n_e are the number of finite elements of the discretized unit cell, $|V_c|$ is the unit cell volume, $\mathbf{I}$ is the identity matrix, V_e is the volume of the finite element, $\mathbf{B}_e^t$ is the elemental (temperature gradient)-temperature matrix, $\boldsymbol{\kappa}_e$ is the element thermal conductivity tensor, and $\mathbf{T}_e$ is the matrix containing the element nodal temperature vectors $\mathbf{T}_e^{ij}$ resulting from globally enforcing the unit test temperature gradient fields ($[\mathbf{T}_e^1,\mathbf{T}_e^2]$ for a 2D solid finite element). As before, the element temperature vectors $\mathbf{T}_e^i$ are obtained from the global temperature vector of the unit cell $\mathbf{T}_c^i$, which is the solution of the equilibrium equation

$$\left[\sum_{e=1}^{n_e}\int_{V_e}\mathbf{B}_e^{t\,\intercal}\boldsymbol{\kappa}_e\mathbf{B}_e^t\mathrm{d}V_e\right]\mathbf{T}_c^i = \sum_{e=1}^{n_e}\int_{V_e}\mathbf{B}_e^{t\,\intercal}\boldsymbol{\kappa}_e\mathbf{t}^i\mathrm{d}V_e. \tag{3.5}$$

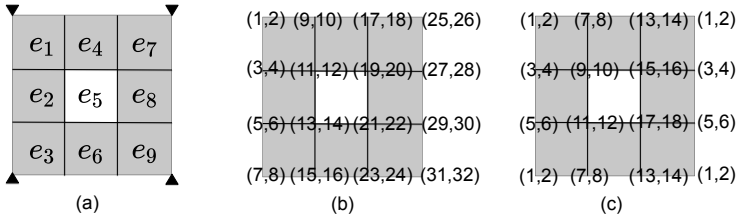

Figure 3.2.. Comparison of Dofs setting between energy-based homogenization and asymptotic homogenization.(a) The discretized unit cell. (b) Dofs used in energy-based homogenization.(c) Dofs used in asymptotic homogenization.

The first term in the left hand side of Eq. (3.5) is the "stiffness" thermal matrix of the unit cell and the right hand side is the nodal heat flux vector of the unit cell.

Energy-based homogenization is an equivalent approach to asymptotic homogenization. In this method, the mutual energy form (Eq. (3.2) or (3.4)) and PBC are adopted as well. The difference between these two methods are the implementation of PBC and test strains. In energy-based homogenization, nodal displacement constraints are imposed on each pair of opposites boundaries $k-$ and $k+$ to satisfy PBC:

$$\chi_i^{k+} - \chi_i^{k-} = \varepsilon_0^{ij} \Delta y, \tag{3.6}$$

where ε_0^{ij} is a given strain and Δy is the length of the unit cell [153]. In asymptotic homogenization, each pair of opposite boundaries share same Dofs (Fig.3.2) [154], and the test strains are imposed on the whole finite element.

3.2.2 Representative volume element method

Compared to above two methods, Representative volume element (RVE)-based method is straightforward. It is derived based on the assumption of constant strain fields are uni-

formly distributed over a RVE, thus homogenized elasticity tensor can be computed by average stress and strain using Hooke's law:

$$\langle \boldsymbol{\sigma} \rangle = \langle \boldsymbol{E} \rangle \langle \boldsymbol{\varepsilon} \rangle, \tag{3.7}$$

where $\langle \boldsymbol{\sigma} \rangle$ is average stress, and $\langle \boldsymbol{\varepsilon} \rangle$ is average strain of a RVE. In finite element analysis, by applying a group of prescribed unit test strain on the RVE's boundaries, the homogenized properties can be obtained through computation of average stress of the whole element. Using the strain and displacement relations (for 2D problem):

$$\varepsilon_x = \frac{\partial u}{\partial x}, \quad \varepsilon_y = \frac{\partial u}{\partial y}, \quad \gamma_{xy} = 0.5 \times (\frac{\partial u}{\partial y} + \frac{\partial v}{\partial x}), \tag{3.8}$$

applying prescribed displacement $[u = x \quad v = 0]$ on RVE's boundary yields an average stresses equal to E_{1111} and E_{2211}, applying prescribed displacement $[u = 0 \quad v = y]$ yields average stresses equal to E_{2222} and E_{1122}, and applying prescribed displacement $[u = 0.5 \times y \; v = 0.5 \times x]$ yields E_{1212}.

In analogy to this, homogenized thermal conductivity tensor can be computed by average heat flux and temperature gradient using Fourier's law:

$$\langle \boldsymbol{q} \rangle = \langle \boldsymbol{\kappa} \rangle \langle \nabla \boldsymbol{T} \rangle, \tag{3.9}$$

where $\langle \boldsymbol{q} \rangle$ is average heat flux. It can be obtained by applying prescribed temperature $T_1 = x$ and $T_2 = y$ on boundaries.

To compare RVE and AH methods, a test using a group of 3D cubes with rectangular holes are implemented as Fig.3.3 shown. The resulting values from RVE-based method are slightly higher than those derived from AH method and the equivalent energy-based approach, which implies using RVE-based approach may over-evaluate stiffness of the structure. However, RVE-based method has two main advantages over AH method. First, this method is appropriate to evaluate properties of non-periodic mesoscale material, because assumption of periodic boundary condition is not required. In addition, since prescribed displacements on the boundaries are linear functions of geometry coordinate, symmetry

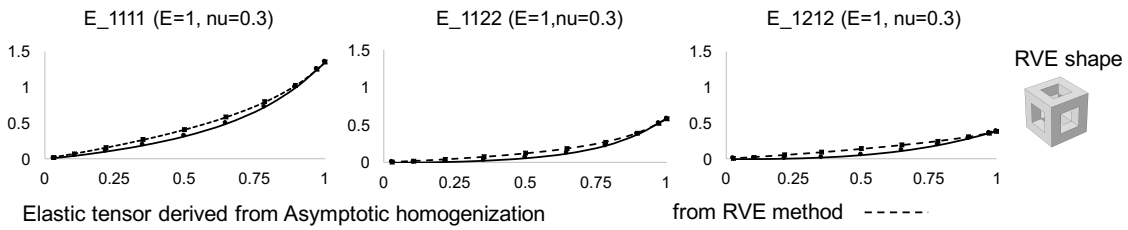

Figure 3.3.. A comparison between RVE-based method and asymptotic homogenization method.

condition can be used for finite element analysis, if RVE's center located on the coordinate $(0,0,0)$. The computation cost will thus be saved.

3.3 Multiscale thermomechanical topology optimization

In this section, proposed multiscale thermomechanical topology optimization is presented. A flow chart (Fig. 3.4) is shown to describe this approach. First, in terms of the force $\mathbf{f}$ and heat flux $\mathbf{f}_t$ applied to design domain Ω and surface Γ, a conceptual design having a density distribution $\boldsymbol{\theta}_c$ is generated, using macroscale thermo-mechanical topology optimization with a linear material interpolation. Elemental strains $\boldsymbol{\varepsilon}_1 \cdots \boldsymbol{\varepsilon}_{nel}$ and relative densities $\theta_1 \cdots \theta_{nel}$ of this conceptual design are evaluated. Based on these information, each unit cell is optimized through RVE-based inverse homogenization. Then, homogenized tensor $\left(\mathbf{D}^H_{C,1} \cdots \mathbf{D}^H_{C,nel}, \boldsymbol{\kappa}^H_{C,1} \cdots \boldsymbol{\kappa}^H_{C,nel}\right)$ and local stiffness matrix $\left(\mathbf{K}^H_1 \cdots \mathbf{K}^H_{nel}, \mathbf{K}^H_{t,1} \cdots \mathbf{K}^H_{t,nel}\right)$ of each optimal unit cells are computed through asymptotic homogenization (AH). With assembled global stiffness matrix $\left(\Sigma\mathbf{K}^H, \Sigma\mathbf{K}^H_t\right)$, the macroscale thermomechanical finite element analysis is performed to re-evaluated the objective. After these steps, the first iteration of multiscale optimization is finished. Since in the conceptual design, the linear interpolation represents a stiffer property than the actual material with same densities, the internal energy or compliance of resulting porous structure from the

first iteration would be underestimated. Hence, design variables are updated by enabling additional mass and next iteration is performed. The approach contains three key concepts, namely macroscale structural design, mesoscale material design, and design updating scheme, which will be described in following sections.

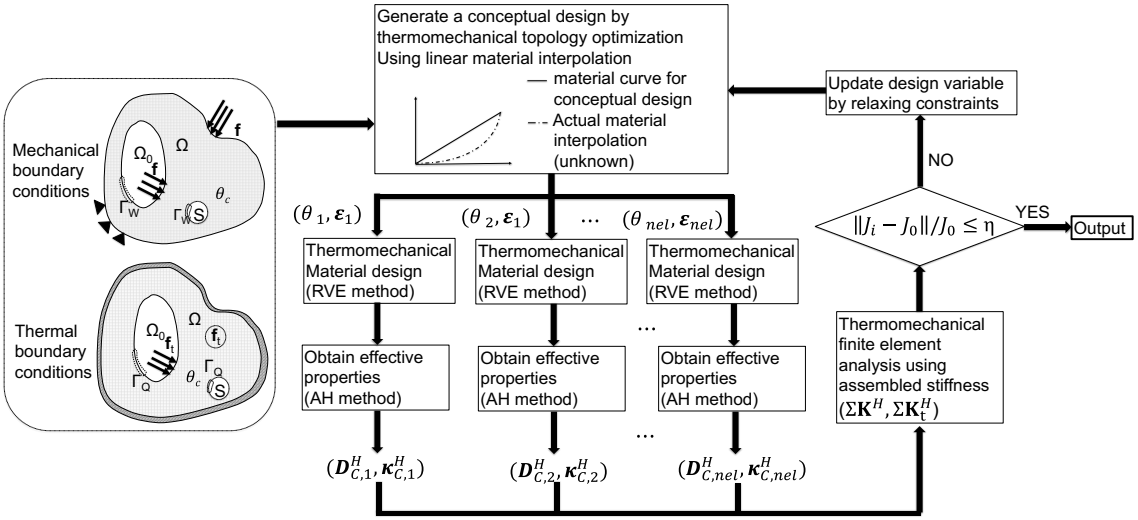

Figure 3.4.. Flow chart of multiscale thermomechanical topology optimization.

3.3.1 Macroscale structure design: topology optimization

The purpose of marcoscale optimization is to use given mass, minimize the internal energy or compliance arising from external load $\mathbf{f}^\intercal\mathbf{u}$ and thermal expansion $\mathbf{f}_{th}{}^\intercal\mathbf{u}$, while remaining thermal compliance $\mathbf{f}_t{}^\intercal\mathbf{T}$ that adopted as a measurement of heat conduction, employed as a constraint. The constraint aims to use relax factor C_Q to define an upper bound of thermal compliance, in order to ensure a small thermal compliance which indicating high thermal performance. Additionally, In the optimization process, Hooke's and Fourier's law

are served as physics constraints. Finally, macroscale thermomechanical topology optimization is stated as

$$\begin{aligned} \text{given} \quad & m(\boldsymbol{\theta}_1) \\ \text{minimize} \quad & \mathbf{f}^\intercal \mathbf{u}(\boldsymbol{\theta}_1) + \mathbf{f}_{th}(\mathbf{T})^\intercal \mathbf{u}(\boldsymbol{\theta}_1) \\ \text{subject to} \quad & \mathbf{f}_t{}^\intercal \mathbf{T}(\boldsymbol{\theta}_1) \leq C_Q \mathbf{f}_t{}^\intercal \mathbf{T}(\boldsymbol{\theta}_0) \\ & m(\boldsymbol{\theta}_{\min}) \leq m(\boldsymbol{\theta}_1) \leq m(\boldsymbol{\theta}_0) \\ & \boldsymbol{\theta}^{\min} \leq \boldsymbol{\theta}_1 \leq \mathbf{1} \\ \text{satisfying} \quad & \mathbf{K}(\boldsymbol{\theta}_1)\mathbf{u}(\boldsymbol{\theta}_1) = \mathbf{f} + \mathbf{f}_{th} \\ & \mathbf{K}_t(\boldsymbol{\theta}_1)\mathbf{f}_t = \mathbf{T}(\boldsymbol{\theta}_1), \end{aligned} \tag{3.10}$$

where $\boldsymbol{\theta}_1$ represents relative density distribution and $\boldsymbol{\theta}_0$ is the initial design; m is mass of macroscale structure; $\mathbf{f}$ is mechanical load and $\mathbf{f}_{th}$ is thermal expansion load; $\mathbf{u}$ is nodal displacement vector; $\mathbf{f}_t$ represents nodal heat flux and $\mathbf{T}$ nodal temperature. $\mathbf{K}$ is global stiffness matrix for mechanical; $\mathbf{K}_t$ is global stiffness for heat conduction. The sensitivity analysis of a coupled thermomechanical topology optimization is described in [25]. To analysis sensitivity of this problem, Eq. (3.10) can be rewritten as the form of Lagrangian function L:

$$\begin{aligned} \text{find} \quad & \boldsymbol{\theta}_1^* \in \mathbb{R}^{n_c} \\ \text{minimize} \quad & L(\boldsymbol{\theta}_1) = (\mathbf{f} + \mathbf{f}_{th})^\intercal \mathbf{u}(\boldsymbol{\theta}_1) + \omega \mathbf{f}_t{}^\intercal \mathbf{T}(\boldsymbol{\theta}_1) \\ & \boldsymbol{\lambda}_m{}^\intercal (\mathbf{K}(\boldsymbol{\theta}_1)\mathbf{u}(\boldsymbol{\theta}_1) - \mathbf{f} - \mathbf{f}_{th}) + \boldsymbol{\lambda}_t{}^\intercal (\mathbf{K}_t(\boldsymbol{\theta}_1)\mathbf{T}(\boldsymbol{\theta}_1) - \mathbf{f}_t) \\ \text{subject to} \quad & m(\boldsymbol{\theta}_{\min}) \leq m(\boldsymbol{\theta}_1) \leq m(\boldsymbol{\theta}_0) \\ & \theta^{\min} \leq \theta_1 \leq 1, \end{aligned} \tag{3.11}$$

where ω is a weighting factor, $\boldsymbol{\lambda_m}$ and $\boldsymbol{\lambda_t}$ are adjoint vectors. Notably, here the design dependent load $\mathbf{f}_{th}$ is not only a function of relative density $\boldsymbol{\theta}_1$, but also a function of

temperature $\mathbf{T}$. Indeed, $\mathbf{T}$ is a function of $\boldsymbol{\theta}_1$. Thus, by using chain rule, the derivatives of the Lagrangian for each element θ_c are written as

$$\begin{aligned}\frac{\partial L(\boldsymbol{\theta}_1)}{\partial \theta_c} =&\mathbf{u}(\boldsymbol{\theta}_1)^\intercal \frac{\partial \mathbf{f}_{th}}{\partial \theta_c} + \mathbf{u}(\boldsymbol{\theta}_1)^\intercal \frac{\partial \mathbf{f}_{th}}{\partial \mathbf{T}(\theta_1)} \frac{\partial \mathbf{T}(\theta_1)}{\partial \theta_c} + (\mathbf{f}+\mathbf{f}_{th})^\intercal \frac{\partial \mathbf{u}(\boldsymbol{\theta}_1)}{\partial \theta_c} + \omega \mathbf{f}_t{}^\intercal \frac{\partial \mathbf{T}(\boldsymbol{\theta}_1)}{\partial \theta_c} + \\ &\boldsymbol{\lambda}_m{}^\intercal \left(\frac{\partial \mathbf{K}(\theta_1)}{\partial \theta_c}\mathbf{u}(\boldsymbol{\theta}_1) + \mathbf{K}(\boldsymbol{\theta}_1)\frac{\partial \mathbf{u}(\boldsymbol{\theta}_1)}{\partial \theta_c} - \frac{\partial \mathbf{f}_{th}}{\partial \theta_c} - \frac{\partial \mathbf{f}_{th}}{\partial \mathbf{T}(\theta_1)}\frac{\partial \mathbf{T}(\boldsymbol{\theta}_1)}{\partial(\theta_c)} \right) + \\ &\boldsymbol{\lambda}_t{}^\intercal \left(\frac{\partial \mathbf{K}_t(\theta_1)}{\partial \theta_c}\mathbf{T}(\boldsymbol{\theta}_1) + \mathbf{K}_t(\boldsymbol{\theta}_1)\frac{\partial \mathbf{T}(\boldsymbol{\theta}_1)}{\partial \theta_c} \right)\end{aligned} \tag{3.12}$$

where $\boldsymbol{\lambda}_m{}^\intercal$ and $\boldsymbol{\lambda}_t{}^\intercal$ are the vectors of adjoint variables. In order to cancel $\frac{\partial \mathbf{u}(\boldsymbol{\theta}_1)}{\partial \theta_c}$term and $\frac{\partial \mathbf{T}(\boldsymbol{\theta}_1)}{\partial \theta_c}$, the value in adjoint vectors can be defined to satisfy

$$\begin{aligned}&\left((\mathbf{f}+\mathbf{f}_{th})^\intercal + \boldsymbol{\lambda}_m{}^\intercal \mathbf{K}(\boldsymbol{\theta}_1)\right)\frac{\partial \mathbf{u}(\boldsymbol{\theta}_1)}{\partial \theta_c} = \mathbf{0} \\ &\left(\mathbf{u}(\boldsymbol{\theta}_1)^\intercal \frac{\partial \mathbf{f}_{th}}{\partial \mathbf{T}(\theta_1)} + \boldsymbol{\lambda}_t{}^\intercal \mathbf{K}_t(\boldsymbol{\theta}_1) - \boldsymbol{\lambda}_m{}^\intercal \frac{\partial \mathbf{f}_{th}}{\partial \mathbf{T}(\theta_1)} + \omega \mathbf{f}_t{}^\intercal\right)\frac{\partial \mathbf{T}(\boldsymbol{\theta}_1)}{\partial \theta_c} = \mathbf{0},\end{aligned} \tag{3.13}$$

where

$$\frac{\partial \mathbf{f}_{th}}{\partial \mathbf{T}(\theta_1)} = \mathbf{K}_{mt}(\boldsymbol{\theta}_1), \tag{3.14}$$

where $\mathbf{K}_{mt}$ is the thermo-mechanical coupling matrix. By sequentially solving the above two equations, finally, the sensitivity is derived as

$$\frac{\partial L(\boldsymbol{\theta}_1)}{\partial \theta_c} = \mathbf{u}(\boldsymbol{\theta}_1)^\intercal \frac{\partial \mathbf{f}_{th}}{\partial \theta_c} + \boldsymbol{\lambda}_m{}^\intercal \left(\frac{\partial \mathbf{K}(\theta_1)}{\partial \theta_c}\mathbf{u}(\boldsymbol{\theta}_1) - \frac{\partial \mathbf{f}_{th}}{\partial \theta_c} \right) + \boldsymbol{\lambda}_t{}^\intercal \frac{\partial \mathbf{K}_t(\theta_1)}{\partial \theta_c}\mathbf{T}(\boldsymbol{\theta}_1) \tag{3.15}$$

In proposed multiscale approach, macroscale topology optimization is only called one time to generate a conceptual design. The design is generated using linear material interpolation, method of moving asymptotes (MMA) solver [**?**] and no filters.

3.3.2 Mesoscale material design: inverse homogenization

By using the information provided by macroscale conceptual design, maximum bulk modulus, shear modulus and heat conduction for each unit cell can be found through RVE-based inverse homogenization method. With application of elemental relative density

$m(\boldsymbol{\theta}_{ne})$, strain $\varepsilon(\boldsymbol{\theta}_{ne})$ and temperature gradient $\nabla\mathbf{T}(\boldsymbol{\theta}_{ne})$ derived from macroscale conceptual optimization, an inverse homogenization is written as a minimum compliance problem. It is stated as a displacement based, multiple-load cases topology optimization:

$$
\begin{aligned}
&\text{given} && m(\boldsymbol{\theta}_{ne}), \varepsilon(\boldsymbol{\theta}_{ne}), \nabla\mathbf{T}(\boldsymbol{\theta}_{ne}) \\
&\text{minimize} && \sum_{i=1}^{n} \mathbf{f}_i(\mathbf{u})^{\intercal}\mathbf{u}_i(m(\boldsymbol{\theta}_{ne}), \varepsilon(\boldsymbol{\theta}_{ne})) \quad \text{or} \quad \sum_{i=1}^{n} \mathbf{f}_{t,i}(\nabla\mathbf{T})^{\intercal}\mathbf{T}_i(m(\boldsymbol{\theta}_{ne}), \nabla\mathbf{T}(\theta_{ne})) \\
&\text{subject to} && m(\boldsymbol{\theta}_{\min}) \leq m(\boldsymbol{\theta}) \leq m(\boldsymbol{\theta}_{ne}) \\
& && \boldsymbol{\theta}^{\min} \leq \boldsymbol{\theta} \leq \boldsymbol{\theta}^{\max} \\
&\text{satisfying} && \mathbf{K}(\boldsymbol{\theta}_{ne})^{-1}\mathbf{u}(\boldsymbol{\theta}_{ne}) = \mathbf{f} \\
& && \mathbf{K}_t(\boldsymbol{\theta}_{ne})^{-1}\mathbf{T}(\boldsymbol{\theta}_{ne}) = \mathbf{f}_t,
\end{aligned}
\tag{3.16}
$$

where mechanical compliance (extreme elasticity property) or thermal compliance (extreme heat conduction) for each unit cell is stated as an objective. n is the number of load cases. For a 2D RVE, $n = 2$, and for a 3D RVE, $n = 6$. The loads in each load case are induced by prescribed displacement or temperature gradient, which are defined in Fig. 3.5 for a 2D RVE.

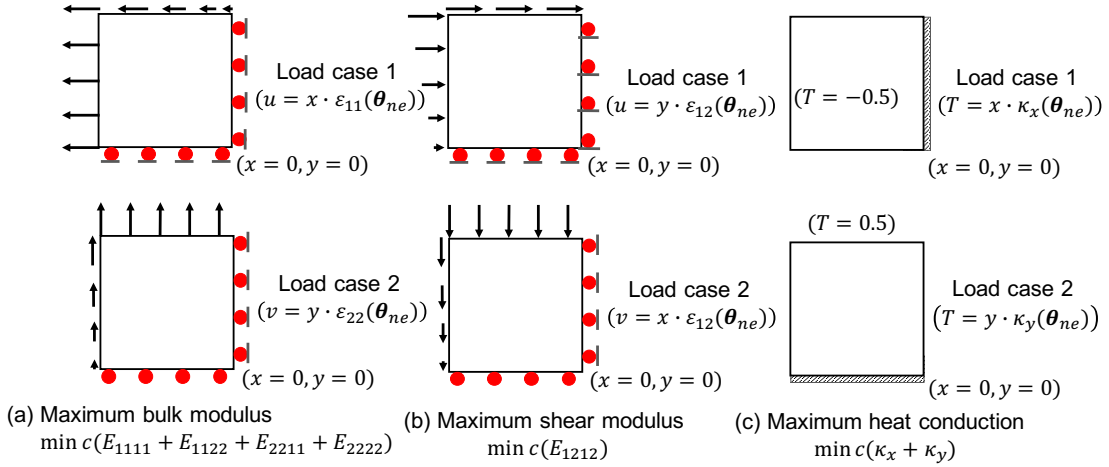

Figure 3.5.. Prescribed displacement (or temperature gradient) and supports (or insulated boundary) for the purpose of maximizing extreme properties.

The inverse homogenization problems for 2D RVEs are solved using in-house Matlab code, in which solid isotropic material penalization (SIMP) method [**?**] , MMA solver and density based filter are used. Fig. 3.6 shows resulting topologies using given relative density $m(\boldsymbol{\theta}_{ne})$=0.19, 0.5 and 0.81, prescribed strain $\boldsymbol{\varepsilon}(\boldsymbol{\theta}_{ne}) = (1,1,1)$, and prescribed temperature gradient $\nabla\boldsymbol{\kappa}(\theta_{ne}) = (1,1)$. Each unit cell is composed of 80 $\times$ 80 elements, but only a quarter of the structure (40×40 elements) is required to be analyzed. The results are consistent with reference ([54, 75, 107]). 3D extension is developed based

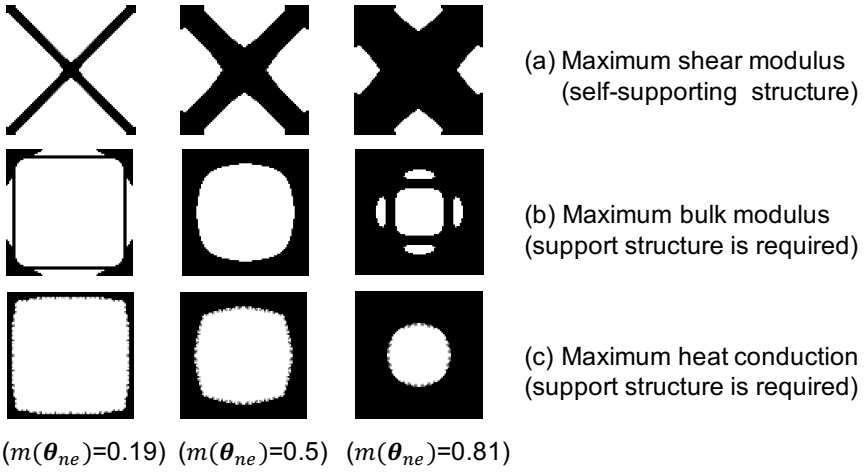

Figure 3.6.. 2D results from RVE-based inverse homogenization.

on Top3d program [155]. Similarly, the optimum topologies are obtained using SIMP method, MMA solver and density based filter with $m(\boldsymbol{\theta}_{ne})$=0.259, 0.5 and 0.74, prescribed strain $\boldsymbol{\varepsilon}(\boldsymbol{\theta}_{ne}) = (1,1,1,1,1,1)$, and prescribed temperature gradient $\nabla\boldsymbol{\kappa}(\theta_{ne}) = (1,1,1)$ (Fig. 3.7). The results are shown as a distribution of $2 \times 2 \times 2$ unit cells to illustrate the connectivity. Each unit cell is composed of (40 $\times$ 40 $\times$ 40) elements, but only 1/8 of the structure (20 $\times$ 20 $\times$ 20) is required to be analyzed. To facilitate the removal of extra material cost in AM process, open channels are defined as passive elements, making $m(\boldsymbol{\theta}_{\max})$=0.8.

As mentioned in the introduction, among the optimum topologies in Fig. 3.6 and Fig. 3.7, for the unit cells having maximum shear modulus (the first row), the angle between

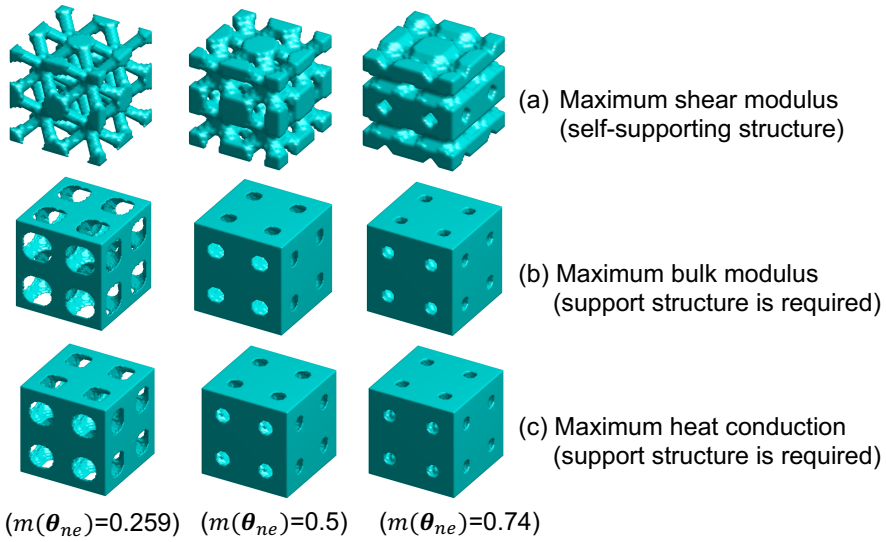

Figure 3.7.. 3D results from RVE-based inverse homogenization.

each tilt bar and horizontal plane is approximately 45°, obtaining a self-supporting structure. Compared to them, those unit cells having maximum bulk modulus and heat conduction contain overhangs that required additional support materials. In terms of maintaining a self-supporting structure, maximum shear modulus is a preferred objective function in material design. Notably, this objective function may not guarantee the overall material's thermo-mechanical properties, which will be achieved through design updating.

3.3.3 Updating rule of multiscale design

After macroscale topology optimization and mesoscale material design for each unit cell, one iteration is finished. Next, the homogenized properties of each unit cell are evaluated through asymptotic homogenization. Then global stiffness matrices are assembled and a new macroscale objective value can be evaluated by calling thermomechanical finite element analysis. This value may be a suboptimal value compared to conceptual design for two reasons: First, the material interpolation used in conceptual design is stiffer hence the thermomechanical performance would be overestimated; Second, the objective function in

the material design is maximizing shear modulus, which may not ensure the overall optimality of thermo-mechanical performance for each unit cell. A design update scheme is therefore required to revise the suboptimal macroscale objective value close to the anticipated value:

$$\eta_i = \| J_i - J_0 \| / J_0 \leq \eta, \tag{3.17}$$

where J_i is the objective evaluation of ith iteration, J_0 is objective of conceptual design, η is a small number. The following Hybrid Cellular Automata (HCA) [66] principle is employed to update elemental design variable x_i or its Moore neighborhood $\mathscr{N}_{\mathscr{M}}$, based on local objective value:

$$\begin{aligned}
&\text{if} \quad J_{i,ne} \geq J_{0,ne} \quad \text{and} \quad x_{i,ne} \leq x_{\max}, \quad x_{i+1,ne} = x_{i,ne} + \delta \\
&\text{elseif} \quad J_{i,ne} \leq J_{0,ne} \quad \text{and} \quad x_{i,ne} \geq x_{\min}, \quad x_{i+1,ne} = x_{i,ne} - \delta \\
&\text{elseif} \quad J_{i,ne} \geq J_{0,ne} \quad \text{and} \quad x_{i,ne} = x_{\max}, \quad x_{i+1,\mathscr{N}_{\mathscr{M}}} = x_{i,\mathscr{N}_{\mathscr{M}}} + \delta \\
&\text{elseif} \quad J_{i,ne} \leq J_{0,ne} \quad \text{and} \quad x_{i,ne} = x_{\min}, \quad x_{i+1,\mathscr{N}_{\mathscr{M}}} = x_{i,\mathscr{N}_{\mathscr{M}}} - \delta
\end{aligned} \tag{3.18}$$

These updated design variables are adopted to material design in next iteration.

3.4 Two dimensional numerical example

A 2D example is presented to illustrate the proposed multiscale approach. A $3cm \times 1cm$ MBB beam is meshed by 15×5 square voxels (Fig. 3.8). A downward mechanical load $F = 1N$ is located at the top left corner, and the fixed constraint is located at the bottom right corner. Meanwhile, a point-wise heat flux $q = 1W$ is located at the top left corner, and a boundary temperature $T = 0°C$ is located at the bottom right corner. The specified material is 420 stainless steel infiltrated with bronze, having density $7.86g/cm^3$, Young's stiffness $E = 147GPa$, heat conductivity $k = 22.6W/m \cdot K$, thermal expansion coefficient $\alpha = 7.4 \times 10^{-6}K^{-1}$. Assume in the conceptual design, the objective is minimizing the compliance due to the thermo-mechanical load within 50% volume fraction. The minimum relative density for each unit cell is $m(\boldsymbol{\theta}_{ne}) = 0.19$. The coefficient of thermal performance C_Q is equal to 3. The resulting topology is shown in Fig. 3.8 (a), having a normalized compliance equal to 1. Then in mesoscale, the shear modulus of each unit cell in this

15×5 frame is optimized based on the strain and relative density information derived from conceptual design.

After the first iteration, the topology of the MBB beam is shown as Fig. 3.8 (b). The homogenized properties of this structure is assembled to re-estimate the actual compliance and strain information via thermo-mechanical finite element analysis. In this example, the re-estimate compliance is about 61.4 % greater than the conceptual design. Thus the design updating allows unit cells having local compliance greater than conceptual design to add material, while in the unit cell having smaller local compliance compared to conceptual design, material would be partly removed. The material adding and removal rate δ is defined as

$$\delta = 0.05 \times \eta_i, \tag{3.19}$$

where $\eta_i = 0.05$. Based on the updated strain and relative density information, the topology of each unit cell is optimized in the second iteration. This iterative process is repeated 28 times before the convergence criteria satisfied. The final volume fraction to achieve the expected compliance is 65.5 %. The total computation time is 741.9 seconds, using Matlab in a Macbook Pro computer having 3.1 GHZ Intel Core i7 and 16 GB MHZ DDR3 memory. Finally, the optimal design is converted to a solid file with 0.1cm thickness, and verified

Table 3.1.. Comparison between the solid MBB beam, optimized porous MBB beam and the uniform porous MBB beam.

	Weight (g)	Max Von Mises stress (MPa)	Max temperature (°C)
Solid MBB beam	2.358	1.840	102.2
Optimized porous MBB beam	1.179	2.417	190.8
Uniform porous MBB beam	1.179	4.932	213.4

by thermo-mechanical finite element simulation using COMSOL Multiphysics. The results of stress and temperature fields are compared to the simulation results of a uniform porous

MBB beam having the same volume fraction, as well as a solid MBB beam (Fig. 3.9 and Table 3.1). It indicates that, an optimal porous structure, although compromising stiffness and heat transfer capability with respect to a solid counterpart, significantly improves thermo-mechanical performance compared to a uniform porous MBB beam with the same volume fraction.

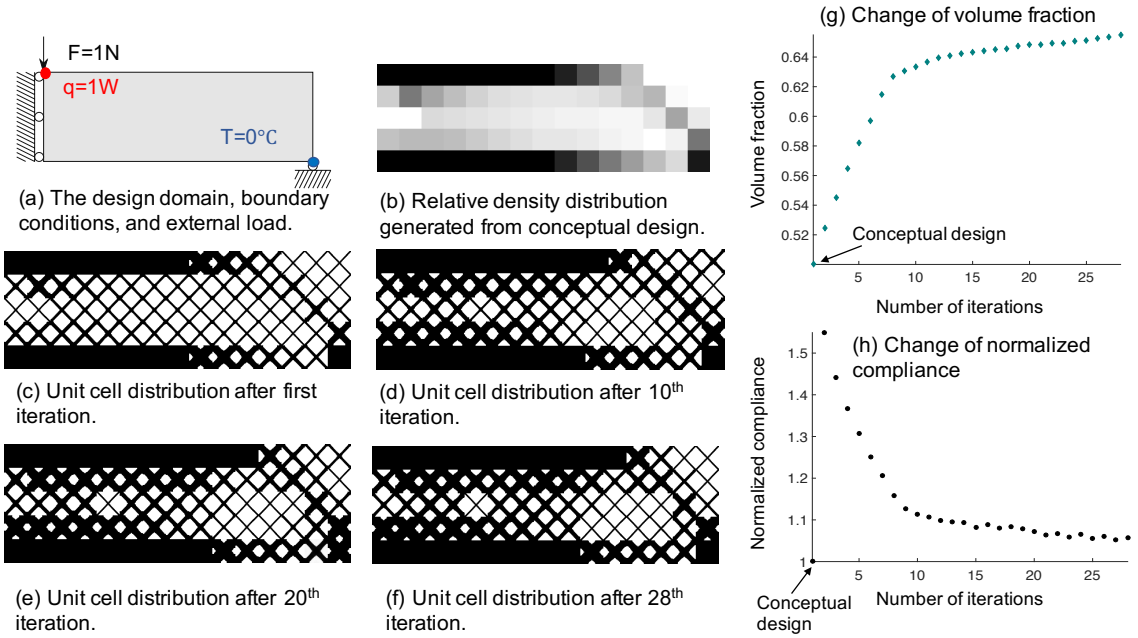

Figure 3.8.. A 2D MBB beam example presented to illustrate the proposed algorithm.

3.5 Application to porous injection mold

A 3D porous injection mold design is presented in this section. The mold is a 3 in $\times$ 3 in $\times$ 1.25 in core insert. Based on the geometry of the mold, a quarter of mold section is investigated. Besides, the top core of the mold is reserved as solid structure for conformal cooling design (Fig. 3.10 (a) to (e)). Injection load located at the injected part surface, clamping pressure at imposed on bottom, and press-fit load on lateral sides are served as mechanical force. For heat conduction, a heat flux imposed on the injected part surface,

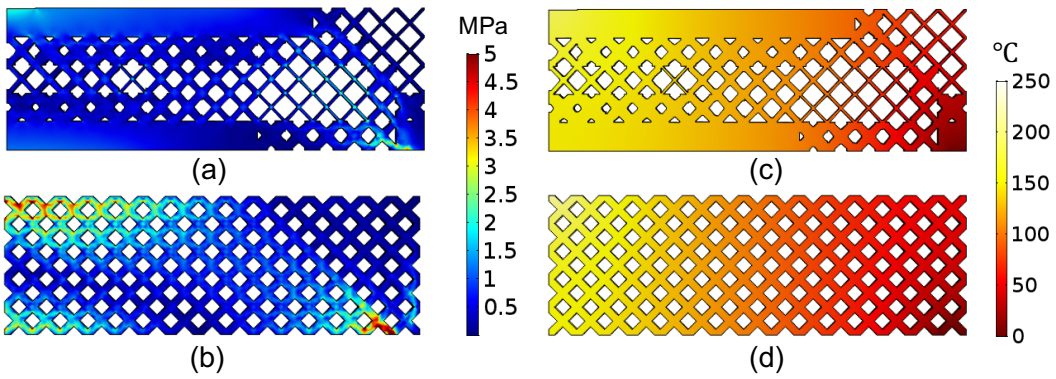

Figure 3.9.. Thermo-mechanical simulation of the optimized result ((a) stress field, and (c) temperature field), as well as the simulation results of a uniform MMB beam having same volume fraction ((b) stress field, and (d) temperature field)

.

and the temperature of cooling pipe is assumed as a constant value. All physics values are normalized in this problem.

In the problem statement, define given macroscale mass fraction $m(\theta)$=0.5, C_Q=1.1, η=0.2, $\delta = 0.05 \times \eta_i$. A $6 \times 6 \times 5$ cubic mesh is applied to the macroscale problem, while a $20 \times 20 \times 20$ cubic mesh is used for each of mesoscale voxel. However, in mesoscale, only 1/8 of each cubic is required to analyze. The convergence is satisfied after 15 iteration with $m(\theta)$=0.71 (Fig. 3.10 (f) and (g)). The total computation time is 61652 seconds (17.4 hours), using Matlab in a Macbook Pro computer having 3.1 GHZ Intel Core i7 and 16 GB MHZ DDR3 memory.

Finally, the optimal design is remeshed using 3-Matics and verified by thermo-mechanical finite element simulation using COMSOL Multiphysics. The results of stress field and temperature are compared to the simulation results of a uniform porous mold having the same volume fraction, as well as a solid mold (Fig. 3.11 and Table 3.2). It indicates that, unlike a uniform porous mold having the same volume fraction, though the weight of the optimal porous mold is 29% lighter than the solid counterpart, the maximum Von Mises stress is

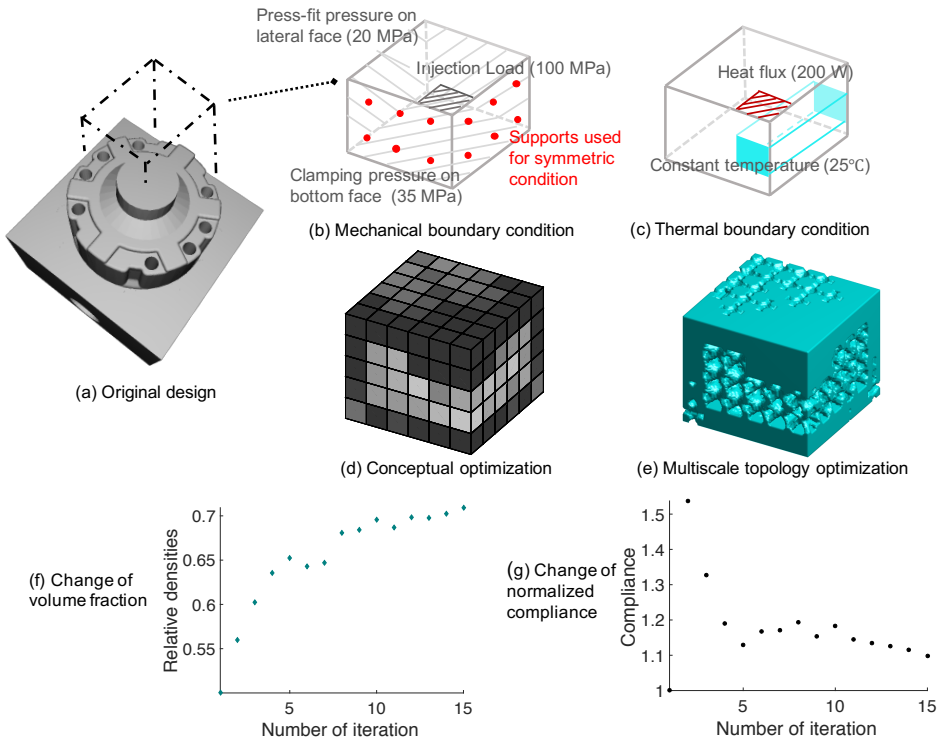

Figure 3.10.. Multiscale thermomechanical topology optimization of a porous injection mold.

below the yield strength of the material (427 MPa), and the maximum temperature in the mold doesn't have a significant change.

Table 3.2.. Comparison between the solid mold, optimized porous mold and the uniform porous mold.

	Weight (g)	Max Von Mises stress (MPa)	Max temperature (°C)
Solid mold	2.095	280.3	126.9
Optimized porous mold	1.487	325.5	127.1
Uniform porous mold	1.487	720.7	312.3

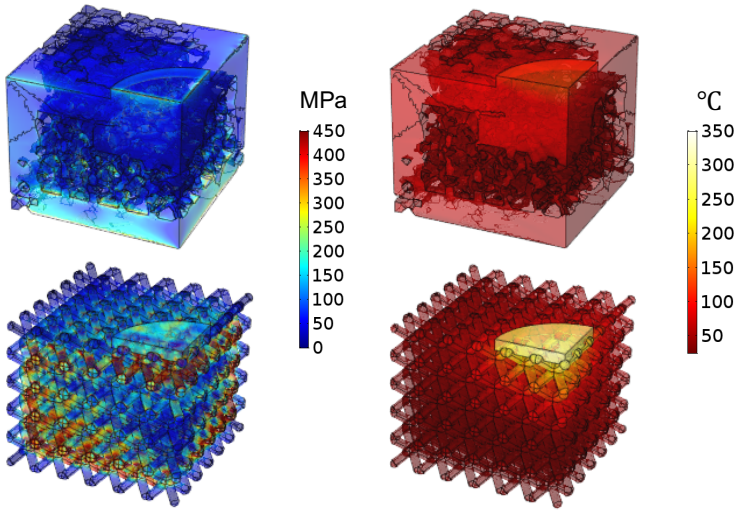

Figure 3.11.. Thermo-mechanical simulation of the optimized result ((a) stress field, and (c) temperature field), as well as the simulation results of a uniform MMB beam having same volume fraction ((b) stress field, and (d) temperature field)

.

The optimal structure is approximated to an iso-surface and meshed to a STL file. The file size is 125.7Mb, composed of 2511164 triangles. After modification in Netfabb, the triangle number is reduced to 374558, with a limit of deformation 0.01 in.

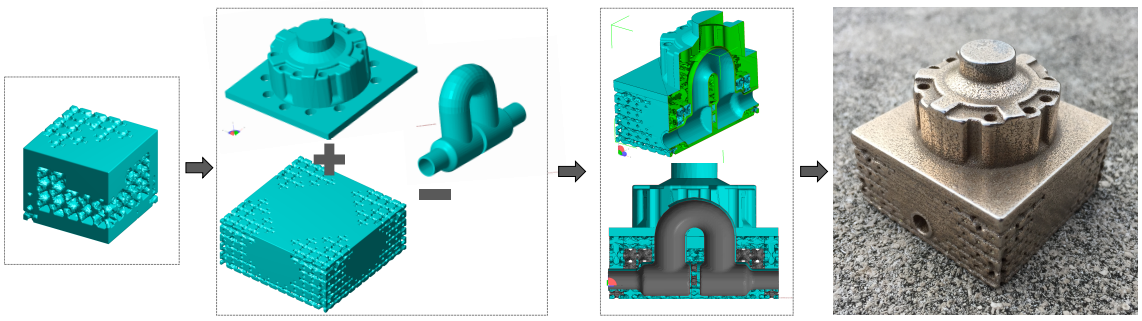

Figure 3.12.. Assemble and prototyping process of the injection mold.

3.6 Additive manufacturing and planning of experimental test

After mirroring the resulting section and performing Boolean operations to assemble the top core and conformal cooling channel, the porous injection mold is prototyped using Direct Metal Laser sintering (DMLS), with a scale factor 0.4 (Fig. 3.12). The scaled prototype was fabricated by an additive manufacturing service company (Shapeways, Newyork, U.S.). The printed steel is Stainless Steel Alloy 420 infiltrated with Bronze (90 %Cu / 10 % Sn). It is a matrix material composed of 60 % stainless steel and 40% bronze. The minimum wall thickness of this protocol is 1.0 mm, and the maximum length of hole allowing the materials to be removed is 2.0 mm. This scaled down prototype proves the internal lattice structure is self-supporting without the requirement to change the orientation of the mold. In the near future, the original size of the injection mold will be manufactured and experimental test will be employed. Before that, samples will be generated using the same machine and material, and experimental tests are planned to validate the mechanical and thermal properties (Fig. 3.13). These samples, composed of solid and porous materials, are designed based on ASTM E8, ASTM E9 and ASTM E1530 standards for the tensile, compression and thermal conductivity experiments, respectively. The experimental properties such as Young's modulus, Poisson's ratio, yield strength and thermal conductivity will be incorporated into the aforementioned examples to improve the accuracy of the solution.

3.7 Conclusion

In this Chapter, an innovative multiscale thermo-mechanical topology optimization method has been presented for generating injection molds. Compared to traditional studies, the proposed method is computationally efficient, and amiable to additive manufacturing by consisting of self-supporting lattice/porous structures. The thermo-mechanical performance of the injection mold is maximized with given volume fraction, and the self-supporting unit cells are formed by maximizing shear modulus with taking account of local relative densities and strains. The design is updated after comparing local objective value and the desired value after each iteration until the thermo-mechanical performance of the

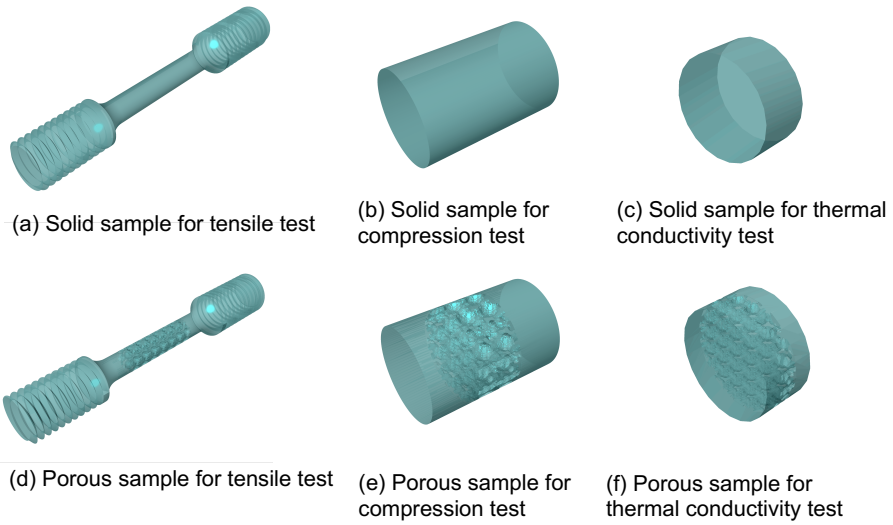

Figure 3.13.. Experimental samples to validate the thermal and mechanical properties.

mold is satisfied. The proposed design method is proved through the optimization of a solid mold insert. The optimized porous injection mold is about 30 % lighter than the solid counterpart, but the thermo-mechanical performance including Von Mises stress and surface temperature is approved. The resulting porous structure is tessellated in a stereolithography (STL) file. A scaled down physical prototype of the mold was fabricated using DMLS procedure without internal support structure to demonstrate the manufacturability of the optimal design.

Some limitations of this study should also be considered. First, since the macroscale design only provides a conceptual design by using a coarse mesh, the feasibility of the final design is required to be verified by simulation of entire structure involving both scales, or by experiments. In addition, the assembling process often requires a reduction of surface mesh to adapt the computer memory, which will slightly change the lattices' shape and compromise the accuracy. Furthermore, post processing CAD software such as Netfabb is still required in combination with the proposed algorithm, to assemble porous structure with mold pipes, ejector pins, injection gate, bolts and other detail geometries, which may

require high computer memory (more than 12GB RAM). In the future work, a more efficient assembling method is worth to investigate. Furthermore, the field testing for the optimized design will be implemented, in order to collect the experimental data and improve the design method.

4. DESIGN OF MICROPILLAR ARRAYS FOR MICROFLUIDIC DEVICES USING MULTISCALE TOPOLOGY OPTIMIZATION FOR NAVIER-STOKES FLOW

Micropillar arrays are frequently found in microfluidic devices. Applications involve heat exchange and mass transportation or mixing. Traditionally, micropillar arrays are composed of simple cylindrical structures. Advances in microscale additive manufacturing and topology optimization provide an opportunity to design complex, high-performance micropillar arrays. This Chapter introduces a novel multiscale topology optimization algorithm suitable for micropillar array design. In the macroscale, velocity and viscous strain fields are obtained through Navier-Stokes-Brinkman finite element analysis. In the microscale, the topology of each micropillar is obtained using inverse homogenization. The boundary conditions of the inverse homogenization problem are derived from the macroscale velocity and viscous strain fields. The optimal micropillar topologies minimize flow separation and energy loss and maximize average velocity magnitude. The numerical results show the performance of the simple cylindrical structures and the one optimized micropillar arrays.

4.1 Background and motivation

Micropillar arrays are composed of cylindrical, slender structures, which provide a large surface-area-to-volume ratio (Fig. 4.1A). The arrangement of the cylindrical structures can be tailored to make micropillar arrays suitable for microfluidic devices in operations including cell sorting [156–160], bio-sensor detectors [161, 162], microchannel heat sinks [113, 163, 164], and other microfluidic devices involving heat transfer and mass transportation/mixing mechanisms [165, 166]. The relatively simple micropillar architecture

can be fabricated with high accuracy—today's microscale 3D printers are able to manufacture cylindrical micropillar with diameters of under 20 μm [114]. However, the viscous fluid drag in cylindrical micropillar arrays remains large enough to cause flow separation [167]. It can be found from digital holographic microscopy technologies that, when laminar flow passing through cylindrical micropillar, flow separation may occur around cylinder, which causing energy loss [167]. The effects of flow separation include adverse pressure gradient and the formation of recirculation bubbles. This reduces the advective and convective heat and mass transfer rates, which leads to energy loss and energy efficiency reduction. Recently, bioinspired micropillar array designs have been proposed to reduce viscous fluid. These include shapes from fish skin, rice leaf, lotus leaf, and butterfly wing [114, 165, 166, 168] (Fig. 4.1B). While these designs are not proven to be optimal, their effectiveness has been demonstrated in laboratory settings.

An alternative approach is topology optimization. Topology optimization allows for changes in the connectivity of the fluid layout during optimization. With application of this method, flow passages having minimized energy loss can be found for multiple flow conditions [73, 80, 81, 85–87, 89, 90]. In existing researchs, these flow conditions include Stokes flow [80, 81], steady laminar flow [73, 85], and transient laminar flow [86, 87]. Topology optimization based on turbulent flow model is still a new research area, in which only a few of recent studies have been performed [89, 90]. Nevertheless, though current topology optimization method is useful in the design of a single micropillar or a small set of micropillars, this method is computationally expensive for the design of a micropillar array, which potentially contains hundreds of micropillars.

To mitigate the computation cost of a similar problem, which containing a macroscale design domain composed of artificial cellular materials, a multiscale topology optimization framework has been developed. In this method, the macroscale design domain is divided into multiple microscale domains. In each of microscale design domain, inverse homogenization can be applied to obtain its local optimal material distribution. The final macroscale topology is composed of all of these material designs in microscale [65]. Currently, the multiscale approach has been applied to optimize structures related to lin-

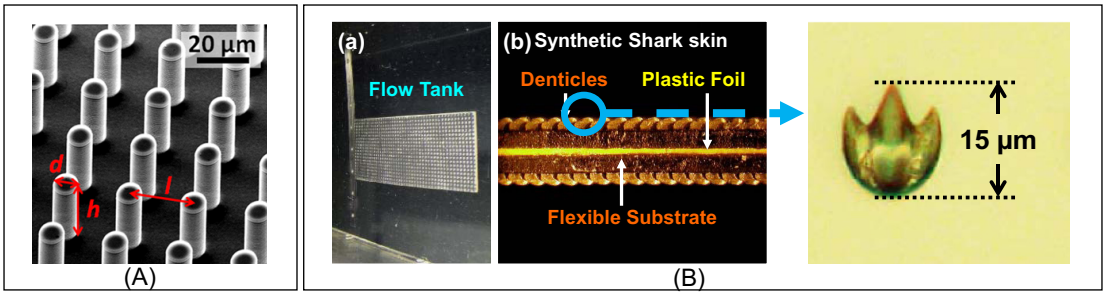

Figure 4.1.. (A) A scanning electron microscopy of the physical domain of a micropillar heat sink [113]. (B) A membrane composed of bio-inspired micropillar arrays composed of shark denticles shape micropillars [114].

ear [65, 169] and non-linear [170] solid mechanics, as well as thermomechanical [151] structures. For fluid problems, limited studies about material optimization are found in the [88, 103]. In these studies, the fluid permeability for material units are maximized under Stokes-Darcy flow. However, the research about multiscale topology optimization for fluid flow remains scarce.

In this study, a novel multiscale topology optimization algorithm for Navier-Stokes flow is proposed to achieve an optimal micropillar arrays that having maximum energy efficiency. The proposed method develops a represent volume element (RVE) based inverse homogenization approach to maximize the energy efficiency of each local micropillar. By applying the proposed method, each micropillar is optimal by means of the local velocity and viscous strain derived from macroscale finite element analysis, the optimal micropillar structure is thus formed in macroscale. The detailed methodology including finite element analysis and inverse homogenization, is described in Sec. 2. In both macroscale and microscale, finite element analysis model of Navier-Stokes flow is applied. In Sec. 3, the numerical results of individual micropillars with specified boundary conditions are illustrated, and the results of multiscale design are presented. The conclusion and future work is summarized in Sec. 4.

4.2 Fluid flow finite element model

A steady state Navier-Stokes equations without fluid body force can be described by the momentum and continuity equations

$$\begin{aligned} &\mathrm{Re}\,(\boldsymbol{u}\cdot\boldsymbol{\nabla})\,\boldsymbol{u} = -\boldsymbol{\nabla} p + \nabla^2\boldsymbol{u} - \alpha(\theta)\boldsymbol{u} \\ &\boldsymbol{\nabla}\cdot\boldsymbol{u} = 0, \end{aligned} \tag{4.1}$$

where Re is Reynolds number, which measures the relation of inertia-force-dominated flow and viscous-force-dominated flow:

$$\mathrm{Re} = \frac{\rho U L}{\mu}. \tag{4.2}$$

Here, U and L are the characteristic velocity and length, ρ is the fluid density, μ is the viscosity. The parameter $\alpha(\theta)$ is interpolation function of Brinkman Stiffness and is defined as

$$\alpha(\theta_e) = \rho\left(\theta_{\min} + (1-\theta_{\min})\frac{p_b(1-\theta_e)}{p_b+\theta_e}\right), \tag{4.3}$$

where θ_e is the proportion of fluid in an element, p_b is a positive penalty parameter used for tuning the function shape of $\alpha(\theta_e)$ (Fig. 6.3). This term can be interpreted as a large damping term that stops flow, which ensures the velocity in the solid domain ($\alpha(\theta_e)$=0) vanishes. The given governing equations of can be discretized using finite element analysis [171].

By applying Galerkin method and Green identity, Eq. (6.1) can be discretized to

$$\underbrace{\begin{bmatrix} \mathbf{K} & -\mathbf{G}^{\mathsf{T}} \\ -\mathbf{G} & \mathbf{0} \end{bmatrix}}_{\mathbf{K}_g} \underbrace{\begin{bmatrix} \mathbf{u} \\ \mathbf{p} \end{bmatrix}}_{\mathbf{U}} = \underbrace{\begin{bmatrix} \mathbf{f} \\ \mathbf{0} \end{bmatrix}}_{\mathbf{F}}, \tag{4.4}$$

where $\mathbf{u}$, $\mathbf{p}$ and $\mathbf{f}$ are nodal velocity, pressure and force, respectively. In a two dimensional problem, each node contains two directions of velocities: $\mathbf{u}_e$=$\{\mathbf{u}_e^x, \mathbf{u}_e^y\}$. The matrix $\mathbf{K}$ is constructed as

$$\mathbf{K} = \mathbf{K}_s + \mathbf{K}_b + \mathbf{K}_a. \tag{4.5}$$

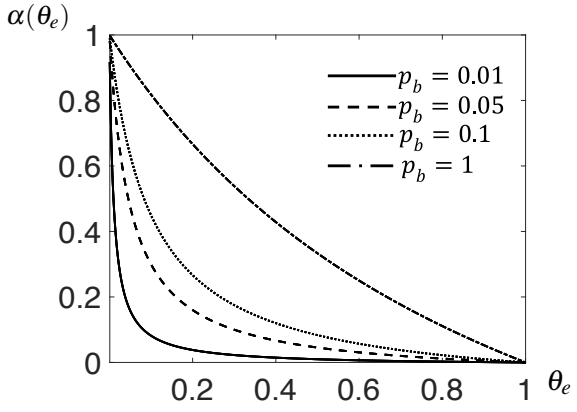

Figure 4.2.. The Shape of Interpolation Function $\alpha(\theta_e)$ is Influenced by Penalty Parameter p_b.

where $\mathbf{K}$ can be considered as a union of the matrices with respect to two directions of velocities $\mathbf{K}$=$\{\mathbf{K}^x, \mathbf{K}^y\}$. In this equation, the stiffness matrix of the Stokes flow is

$$\mathbf{K}_s = \sum_{e=1}^{n_e} \int_{V_e} \mu \nabla \mathbf{N_u}^\intercal \mathbf{I}_0 \nabla \mathbf{N_u} \mathrm{d}V_e, \tag{4.6}$$

where $\mathbf{N_u}$ is the matrix containing shape functions of the elemental velocity, and

$$\mathbf{I}_0 = \begin{bmatrix} 2 & 0 & 0 \\ 0 & 2 & 0 \\ 0 & 0 & 1 \end{bmatrix}. \tag{4.7}$$

For a two-dimensional element. $\mathbf{K}_b$ is the Brinkman damping matrix, which can be considered as a union of matrices with respect to two directions of velocities: $\mathbf{K}_b$=$\{\mathbf{K}_b^x, \mathbf{K}_b^y\}$. For both x and y directions, the matrix is constructed as:

$$\mathbf{K}_b^x = \mathbf{K}_b^y = \sum_{e=1}^{n_e} \int_{V_e} b\alpha(\theta_e) \mathbf{N_u}^\intercal \mathbf{N_u}, \mathrm{d}V_e, \tag{4.8}$$

where b is a constant reflecting resistance level. $\mathbf{K}_a$ is the advection matrix, which can be considered as a union of matrices with respect to two directions of velocities: $\mathbf{K}_a$=$\{\mathbf{K}_a^x$, $\mathbf{K}_a^y\}$. For both x and y directions, the matrix is constructed as:

$$\mathbf{K}_a^x = \mathbf{K}_a^y = \sum_{e=1}^{n_e} \int_{V_e} \mathrm{Re} \left(\underbrace{\mathbf{N_u}^\intercal \mathbf{N_u} \mathbf{u}_e^x \nabla \mathbf{N}_{\mathbf{u},x}}_{\mathbf{K}_a^{xx} \ \ and \ \ \mathbf{K}_a^{yx}} + \underbrace{\mathbf{N_u}^\intercal \mathbf{N_u} \mathbf{u}_e^y \nabla \mathbf{N}_{\mathbf{u},y}}_{\mathbf{K}_a^{xy} \ \ and \ \ \mathbf{K}_a^{yy}} \right) \mathrm{d}V_e. \tag{4.9}$$

In Eq. (6.4),$\mathbf{G}$ is the coupling matrix of the pressure and velocity of x and y directions : $\mathbf{G}$=$\{\mathbf{G}^x$, $\mathbf{G}^y\}$, where

$$\mathbf{G}^x = \sum_{e=1}^{n_e} \int_{V_e} \nabla \mathbf{N}_{\mathbf{u},x}^\intercal \mathbf{N_p} \mathrm{d}V_e, \tag{4.10}$$

and

$$\mathbf{G}^y = \sum_{e=1}^{n_e} \int_{V_e} \nabla \mathbf{N}_{\mathbf{u},y}^\intercal \mathbf{N_p} \mathrm{d}V_e. \tag{4.11}$$

Since nodal velocity is presented in both left hand side $\mathbf{K}_g$ and right hand side $\mathbf{U}$ of Eq. (6.4), an iterative method is required to solve this equation. In this study, a Newton's iterative method is used. Assume in k th iteration, the residual of Eq. (6.4) is

$$\mathbf{K}_g^k \mathbf{U}^k - \mathbf{F}^k = \mathbf{R}(\mathbf{U}^k) \tag{4.12}$$

which can be rewritten using Taylor expansion:

$$\mathbf{R}(\mathbf{U}^k) + \frac{\partial \mathbf{R}}{\partial \mathbf{U}} \mid_{\mathbf{U}^k} \delta \mathbf{U} + \mathscr{O}(\delta \mathbf{U})^2 = \mathbf{0} \tag{4.13}$$

where

$$\delta \mathbf{U} = \mathbf{U}^{k+1} - \mathbf{U}^k. \tag{4.14}$$

Omitting the terms of order two and higher, the following equation is obtained:

$$\mathbf{U}^{k+1} = \mathbf{U}^k - \mathbf{J}^{-1,k}(\mathbf{U}^k) \mathbf{R}(\mathbf{U}^k) \tag{4.15}$$

where

$$\mathbf{J}^k = \frac{\partial \mathbf{R}^k}{\partial \mathbf{U}^k} \tag{4.16}$$

is the Jacobian matrix (also known as tangent matrix) of kth iteration, that can be derived analytically for this problem. The detailed procedures of its derivation refers to [171], the result is

$$\mathbf{J}^k = \mathbf{K}^k + \hat{\mathbf{J}}^k \tag{4.17}$$

where $\hat{\mathbf{J}}^k$ assembles $\{\mathbf{N}_{xx}^k, \mathbf{N}_{xy}^k, \mathbf{N}_{yx}^k, \mathbf{N}_{yy}^k\}$ and

$$\begin{aligned}
\mathbf{N}_{xx}{}^k &= \sum_{e=1}^{n_e} \int_{V_e} \nabla \mathbf{N}_{\mathbf{u},x} \mathbf{u}_e^{x,k} \left(\mathbf{N}_{\mathbf{u}}{}^{\intercal} \mathbf{N}_{\mathbf{u}} \right) \mathrm{d}V_e, \\
\mathbf{N}_{xy}{}^k &= \sum_{e=1}^{n_e} \int_{V_e} \nabla \mathbf{N}_{\mathbf{u},y} \mathbf{u}_e^{x,k} \left(\mathbf{N}_{\mathbf{u}}{}^{\intercal} \mathbf{N}_{\mathbf{u}} \right) \mathrm{d}V_e, \\
\mathbf{N}_{yx}{}^k &= \sum_{e=1}^{n_e} \int_{V_e} \nabla \mathbf{N}_{\mathbf{u},x} \mathbf{u}_e^{y,k} \left(\mathbf{N}_{\mathbf{u}}{}^{\intercal} \mathbf{N}_{\mathbf{u}} \right) \mathrm{d}V_e, \\
\mathbf{N}_{yy}{}^k &= \sum_{e=1}^{n_e} \int_{V_e} \nabla \mathbf{N}_{\mathbf{u},y} \mathbf{u}_e^{y,k} \left(\mathbf{N}_{\mathbf{u}}{}^{\intercal} \mathbf{N}_{\mathbf{u}} \right) \mathrm{d}V_e.
\end{aligned} \tag{4.18}$$

Finally, in k th iteration, a SUPG stabilization matrix $\mathbf{S}$ is applied to improve the stability of advection and the algorithm convergence:

$$\mathbf{S}^k = \{\mathbf{S}^{k,x}, \mathbf{S}^{k,y}\} \tag{4.19}$$

where

$$\mathbf{S}^{k,x} = \mathbf{S}^{k,y} = \mathbf{S}_{xx}^k + \mathbf{S}_{xy}^k + \mathbf{S}_{yx}^k + \mathbf{S}_{yy}^k \tag{4.20}$$

and

$$\begin{aligned}
\mathbf{S}_{xx}{}^k &= \sum_{e=1}^{n_e} \int_{V_e} \left(\mathbf{u}_e^{x,k} \mathbf{N}_{\mathbf{u}}{}^{\intercal} \right) \nabla \mathbf{N}_{\mathbf{u},x} \left(\mathbf{u}_e^{x,k} \mathbf{N}_{\mathbf{u}}{}^{\intercal} \right) \nabla \mathbf{N}_{\mathbf{u},x} \mathrm{d}V_e, \\
\mathbf{S}_{yx}{}^k &= \sum_{e=1}^{n_e} \int_{V_e} \left(\mathbf{u}_e^{x,k} \mathbf{N}_{\mathbf{u}}{}^{\intercal} \right) \nabla \mathbf{N}_{\mathbf{u},x} \left(\mathbf{u}_e^{y,k} \mathbf{N}_{\mathbf{u}}{}^{\intercal} \right) \nabla \mathbf{N}_{\mathbf{u},y} \mathrm{d}V_e, \\
\mathbf{S}_{yx}{}^k &= \sum_{e=1}^{n_e} \int_{V_e} \left(\mathbf{u}_e^{y,k} \mathbf{N}_{\mathbf{u}}{}^{\intercal} \right) \nabla \mathbf{N}_{\mathbf{u},y} \left(\mathbf{u}_e^{x,k} \mathbf{N}_{\mathbf{u}}{}^{\intercal} \right) \nabla \mathbf{N}_{\mathbf{u},x} \mathrm{d}V_e, \\
\mathbf{S}_{yy}{}^k &= \sum_{e=1}^{n_e} \int_{V_e} \left(\mathbf{u}_e^{y,k} \mathbf{N}_{\mathbf{u}}{}^{\intercal} \right) \nabla \mathbf{N}_{\mathbf{u},y} \left(\mathbf{u}_e^{y,k} \mathbf{N}_{\mathbf{u}}{}^{\intercal} \right) \nabla \mathbf{N}_{\mathbf{u},y} \mathrm{d}V_e.
\end{aligned} \tag{4.21}$$

As a result, the updated advection matrix for the next iteration is

$$\mathbf{K}_a^{k+1} = \mathbf{K}_a^k + \mathbf{S}^k \tag{4.22}$$

Using the updated advection matrix, the updated nonlinear residual can be written as

$$\mathbf{K}_g^{k+1}\mathbf{U}^{k+1} - \mathbf{F}^{k+1} = \mathbf{R}(\mathbf{U}^{k+1}). \tag{4.23}$$

The algorithm is converged if the norm of the nonlinear residual is small enough. The finite element model is programming in MATLAB and connected with the following presented multiscale topology optimization method.

4.3 Proposed multiscale topology optimization method

In proposed multiscale topology optimization method, macroscale and microscale design domain are defined in Fig. 6.2. The macroscale domain Ω can be considered as a substrate composed of a group of micropillar arrays. In macroscale design domain, the fluid flow passes from inlet Γ_{inflow} to outlet $\Gamma_{outflow}$ driven by a pressure difference between p_1 and p_0. The flow velocity at the edges of macroscale design domain Γ_{wall} is assumed as zero, which also called no-slip boundaries. Each finite element in the macroscale design domain is defined as a microscale design domin ω_j. The initial design of each microscale design domain is defined as a unit cell containing a cylindrical micropillar at the center. Therefore, the initial design of macroscale design domain is an assembling of all of the cylindrical micropillars.

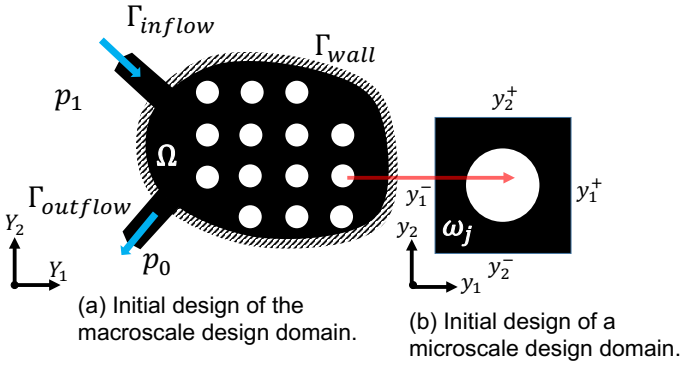

Figure 4.3.. The macroscale and microscale design domains of the proposed methodology.

To implement the method, the macroscale finite element analysis dominated by Navier-Stokes equation with Brinkman penalization term is employed. From this step, the velocity and viscous strain fields required for optimization of each micropillar are required. Utilizing this information, a set of inverse homogenization problems from $\mathbf{P_1}$ to $\mathbf{P_{ne}}$ are created to optimize each micropillars. The number of problem statements is equal to the number of macroscale element *ne*. These optimized micropillars are assembled as the final design of micropillar arrays.

$$\Omega = \Sigma_{j=1}^{ne} \omega_j. \tag{4.24}$$

Next, the details of inverse homogenization method are illustrated.

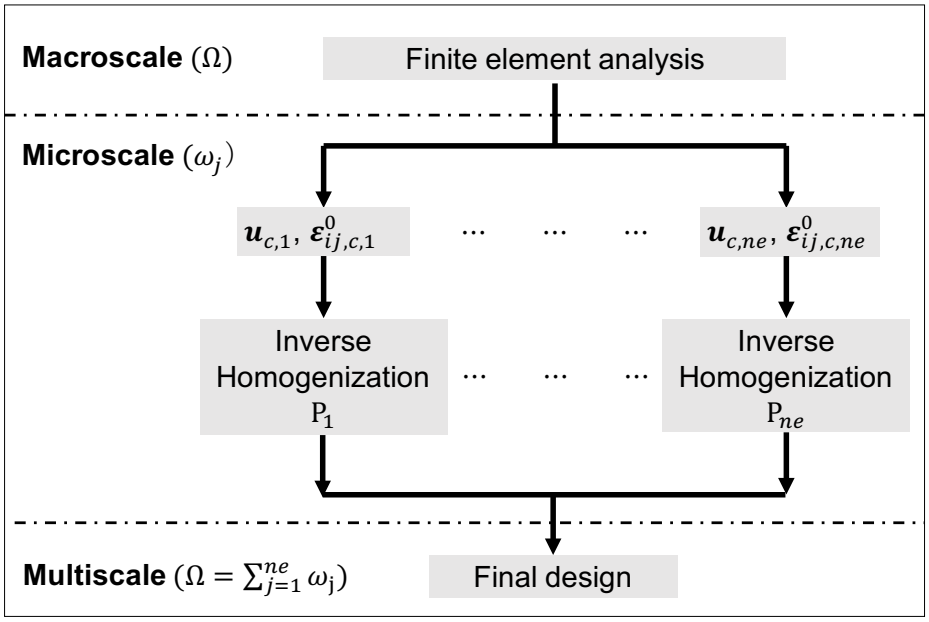

Figure 4.4.. Proposed multiscale topology optimization.

4.3.1 Inverse homogenization for fluid flow models

Following the assumption of periodicity, the velocity field of the unit cell subject to a given rate ε_{ij}^0 can be accounted for the sum of a macroscale velocity field and a fluctuate velocity $u_i^\star$

$$u_i = \varepsilon_{ij}^0 y_j + u_i^\star \tag{4.25}$$

In practice, for each unit cell the velocity imposed on the boundaries $\boldsymbol{u}_c \in u_i$ can be obtained from macroscale finite element results through

$$\boldsymbol{u}_c = \mathbf{N_u}^\intercal \mathbf{u}_c \tag{4.26}$$

where $\boldsymbol{u}_c$ is the sum of $\boldsymbol{u}_{X,c}$ and $\boldsymbol{u}_{Y,c}$ (Fig. 4.5), and $\mathbf{u}_c$ denotes discretized corresponding nodal velocity in the finite element model. Further,a local velocity boundary condition due

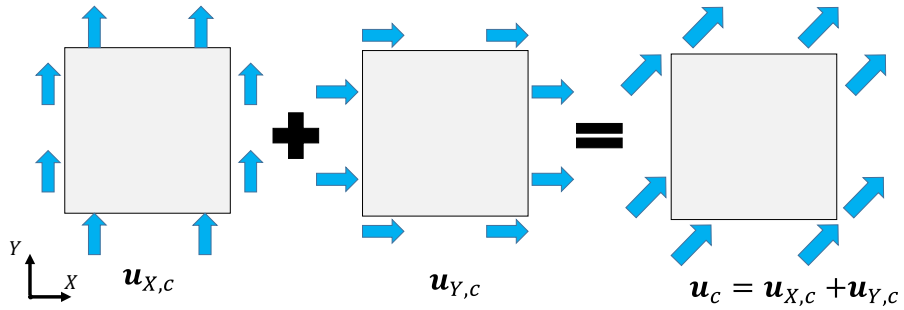

Figure 4.5.. The local velocity boundary condition imposed on a unit cell due to velocity field obtained from macroscale finite element analysis.

to local strain $\epsilon_{ij,c}^0 \in \varepsilon_{ij}^0$ for each unit cell is derived as follows. In Eq. (4.25), the velocity on a pair of opposite boundaries have the relations:

$$\begin{aligned} u_i^{k+} &= \varepsilon_{ij}^0 y_j^{k+} + u_i^\star \\ u_i^{k-} &= \varepsilon_{ij}^0 y_j^{k-} + u_i^\star, \end{aligned} \tag{4.27}$$

where the superscripts $k+$ and $k-$ denotes the pair of opposite parallel boundary surfaces that are oriented perpendicular to the k_{th} direction. Taking the difference of these two equation derives

$$u_i^{k+} - u_i^{k-} = \varepsilon_{ij}^0 \left(y_j^{k+} - y_j^{k-} \right) = \varepsilon_{ij}^0 \Delta y_j^k. \tag{4.28}$$

For a two dimensional unit cell, Δy_j^k, $j,k = 1,2$. In particular,

$$\begin{aligned} \Delta y_1^1 = y_1^0, \;\; \Delta y_2^1 = 0 \\ \Delta y_1^1 = 0, \;\; \Delta y_2^1 = y_2^0 \end{aligned} \tag{4.29}$$

Therefore, local strain $\epsilon_{ij,c}^0$ for a unit cell can be translated to a group of velocity vectors applied to the edges of the unit cell $\boldsymbol{u}(\epsilon_{ij,c}^0)$ that satisfying

$$\begin{aligned} \frac{\partial \boldsymbol{u}_{y_1}(\epsilon_{11,c}^0)}{\partial y_1} &= \epsilon_{11,c}^0 \\ \frac{\partial \boldsymbol{u}_{y_2}(\epsilon_{22,c}^0)}{\partial y_2} &= \epsilon_{22,c}^0 \\ \frac{\partial \boldsymbol{u}_{y_1}(\epsilon_{12,c}^0)}{\partial y_2} + \frac{\partial \boldsymbol{u}_{y_2}(\epsilon_{12,c}^0)}{\partial y_1} &= 2\epsilon_{12,c}^0 \end{aligned} \tag{4.30}$$

As an example, Fig. 4.6 shows how this velocity boundary condition imposed on a unit cell when the strain fields obtained from macroscale finite element analysis are $\epsilon_{11,c}^0 = \{1,0,0\}$, $\epsilon_{22,c}^0 = \{0,1,0\}$ and $\epsilon_{12,c}^0 = \{0,0,1\}$ respectively. In general cases, the strain field is derived

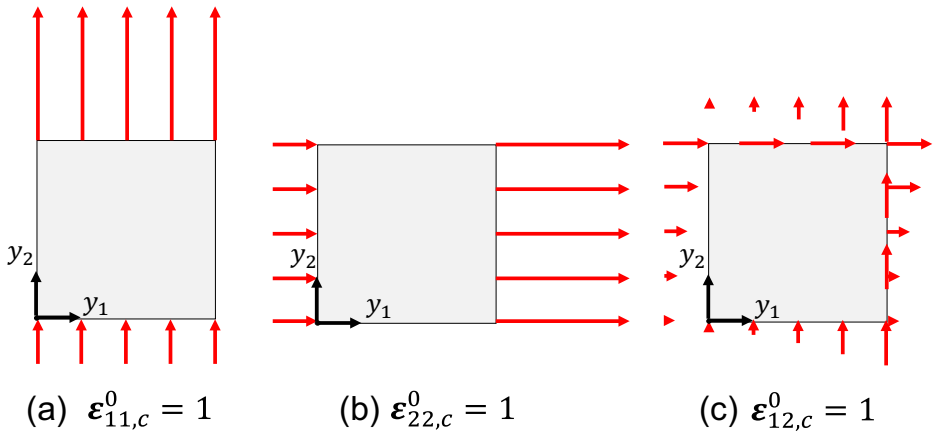

Figure 4.6.. The local velocity boundary condition imposed on a unit cell when the strain fields obtained from macroscale finite element analysis are $\epsilon_{11,c}^0 = \{1,0,0\}$, $\epsilon_{22,c}^0 = \{0,1,0\}$ and $\epsilon_{12,c}^0 = \{0,0,1\}$ respectively.

from macroscale finite element analysis as:

$$\epsilon_{11,c}^0 = \nabla \mathbf{N}_{\mathbf{u}}{}^{\mathsf{T}} \mathbf{u}_c \tag{4.31}$$

Finally, the total local velocity imposed on the periodic boundaries of a unit cell is:

$$\boldsymbol{u}_{c,\Gamma_c} = \boldsymbol{u}_c + \boldsymbol{u}(\boldsymbol{\epsilon}^0_{ij,c}) \tag{4.32}$$

Consequently, with incorporation of the periodic boundary condition, the fluctuate velocity field for the unit cell $\mathbf{v} \in u^\star$ can be solved through the finite element analysis:

$$\underbrace{\begin{bmatrix} \mathbf{K} & -\mathbf{G}^\intercal \\ -\mathbf{G} & \mathbf{0} \end{bmatrix}}_{\mathbf{K}_g} \underbrace{\begin{bmatrix} \mathbf{v} \\ \mathbf{p} \end{bmatrix}}_{\mathbf{U}} = \underbrace{\begin{bmatrix} \mathbf{f_c} \\ \mathbf{0} \end{bmatrix}}_{\mathbf{F}}, \tag{4.33}$$

where $\mathbf{f_c}$ is the boundary fluid drag force interpolated from $\boldsymbol{u}_{c,\Gamma_c}$. Notably, to ensure the non-singularity, the nodal pressure $\mathbf{p}$ of the four corner nodes are fixed in solving this equation.

The proposed inverse homogenization method aims to optimally distribute limited channels within a design domain, i.e.:

$$\sum_{e=1}^{n_e} v_e \theta_e \leq V_\Omega, \tag{4.34}$$

in order to obtain a structure having minimum energy loss Q_c caused by fluid drag force in terms of boundary velocity $\boldsymbol{u}_{c,\Gamma_c}$:

$$Q_c = \frac{1}{2}\mathbf{v}^\intercal \mathbf{K}\mathbf{v} - \mathbf{f_c}^\intercal \mathbf{v}. \tag{4.35}$$

Where V_Ω equal to the porosity assigned in finite element analysis, v defines the nodal velocity of the specific unit cell. Therefore, the objective is to find a structure consisting of optimal micropillar shape $\boldsymbol{\theta}^*_c$ that minimizes energy loss Q_c per unit cell, under physics

constraint Eq. (6.4), periodic boundary condition defined in Eq. (4.32), as well as volume constraint Eq. (6.35) :

$$\begin{aligned}
&\text{find} \quad \boldsymbol{\theta}_c^* \in \Omega^{n_e} \\
&\min \quad Q_c = \frac{1}{2}\mathbf{v}^\intercal \mathbf{K}\mathbf{v} - \mathbf{f_c}^\intercal \mathbf{v} \\
&\text{s.t.} \quad \underbrace{\begin{bmatrix} \mathbf{K} & -\mathbf{G}^\intercal \\ -\mathbf{G} & \mathbf{0} \end{bmatrix}}_{\mathbf{K}_g} \underbrace{\begin{bmatrix} \mathbf{v} \\ \mathbf{p} \end{bmatrix}}_{\mathbf{U}} = \underbrace{\begin{bmatrix} \mathbf{f_c} \\ \mathbf{0} \end{bmatrix}}_{\mathbf{F}}, \\
&\boldsymbol{u}_{c,\Gamma_c} = \boldsymbol{u}_c + \boldsymbol{u}(\boldsymbol{\epsilon}^0_{ij,c}) \\
&\sum_{e=1}^{n_e} v_e \theta_e \leq V_\Omega,
\end{aligned} \tag{4.36}$$

4.3.2 Sensitivity analysis

The sensitivity analysis is performed using the adjoint method. The evaluation of the sensitivity coefficients is demonstrated for a general objective function $Q_c(\boldsymbol{\theta}, \mathbf{v}(\boldsymbol{\theta}))$. Nodal velocity $\mathbf{v}(\boldsymbol{\theta})$ is required to satisfy the constraint governed by finite element analysis equation

$$\mathbf{R}(\boldsymbol{\theta}, \mathbf{v}(\boldsymbol{\theta})) = \mathbf{K}_g\mathbf{U} - \mathbf{F}. \tag{4.37}$$

The objective function is augmented in terms of a Lagrange multiplier vector $\boldsymbol{\lambda}$ and the Lagrangian function Ł is written as

$$Ł = Q_c(\boldsymbol{\theta}, \mathbf{v}(\boldsymbol{\theta})) + \boldsymbol{\lambda}^\intercal \mathbf{R}(\boldsymbol{\theta}, \mathbf{v}(\boldsymbol{\theta})) \tag{4.38}$$

The sensitivity of this Lagrangian function is

$$\begin{aligned}
\frac{\mathrm{d}Ł}{\mathrm{d}\theta_e} &= \frac{\partial Q_c}{\partial \theta_e} + \frac{\partial Q_c}{\partial \mathbf{U}}\frac{\partial \mathbf{U}}{\partial \theta_e} + \boldsymbol{\lambda}^\intercal\left(\frac{\partial \mathbf{R}}{\partial \theta_e} + \frac{\partial \mathbf{R}}{\partial \mathbf{U}}\frac{\partial \mathbf{U}}{\partial \theta_e}\right) \\
&= \frac{\partial Q_c}{\partial \theta_e} + \boldsymbol{\lambda}^\intercal\frac{\partial \mathbf{R}}{\partial \theta_e} + \left(\frac{\partial Q_c}{\partial \mathbf{U}} + \boldsymbol{\lambda}^\intercal\frac{\partial \mathbf{R}}{\partial \theta_e}\right)\frac{\mathrm{d}\mathbf{U}}{\mathrm{d}\theta_e}
\end{aligned} \tag{4.39}$$

To avoid the computation of $\frac{\mathrm{d}\mathbf{U}}{\mathrm{d}\theta_e}$, define

$$\frac{\partial Q_c}{\partial \mathbf{U}} + \boldsymbol{\lambda}^\intercal\frac{\partial \mathbf{R}}{\partial \mathbf{U}} = \mathbf{0} \tag{4.40}$$

From Eq. (6.44), adjoint vector $\boldsymbol{\lambda}$ can be solved. Hence, the analytical sensitivity of Lagrangian is

$$\frac{\mathrm{d}Ł}{\mathrm{d}\theta_e} = \frac{\partial Q_c}{\partial \theta_e} + \frac{\partial \mathbf{R}^\intercal}{\partial \theta_e}\boldsymbol{\lambda}. \tag{4.41}$$

To solve Eq. (6.44), let's rewrite global stiffness $\mathbf{K}_g$ as

$$\mathbf{K}_g = \mathbf{K}_u + \mathbf{K}_p, \tag{4.42}$$

where

$$\mathbf{K}_u = \begin{bmatrix} \mathbf{K} & \mathbf{0} \\ \mathbf{0} & \mathbf{0} \end{bmatrix}, \tag{4.43}$$

and

$$\mathbf{K}_p = \begin{bmatrix} \mathbf{0} & -\mathbf{G}^\intercal \\ -\mathbf{G} & \mathbf{0} \end{bmatrix}. \tag{4.44}$$

Using this definition accompanied with global force $\mathbf{F}$ and assembling vector of velocity and pressure $\mathbf{U}$ remarked in Eq. (6.4), the energy loss Q_c can be rewritten as

$$Q_c = \frac{1}{2}\mathbf{U}^\intercal \mathbf{K}_u \mathbf{U} - \mathbf{F}^\intercal \mathbf{U}, \tag{4.45}$$

and the partial derivative of Q_c is

$$\frac{\partial Q_c}{\partial \mathbf{U}} = \mathbf{K}_u \mathbf{U} + \frac{1}{2}\mathbf{U}^\intercal \frac{\partial \mathbf{K}_u}{\partial \mathbf{U}}\mathbf{U} - \mathbf{F}^\intercal \tag{4.46}$$

From Eq. (6.18), the above equation is equivalent to

$$\frac{\partial Q_c}{\partial \mathbf{U}} = \mathbf{K}_u \mathbf{U} + \frac{1}{2}\hat{\mathbf{J}}\mathbf{U} - \mathbf{F}^\intercal. \tag{4.47}$$

Then, recall $\frac{\partial \mathbf{R}}{\partial \mathbf{U}}$ in (6.43) and (6.44) is Jacobian matrix $\mathbf{J}$ from Eq. (6.16) and (6.17). Therefore, $\boldsymbol{\lambda}$ in Eq. (6.44) is obtained and the sensitivity $\frac{\mathrm{d}Ł}{\mathrm{d}\theta_e}$ in Eq. (6.45) is derived.

Specifically, for a Stokes flow model, $\hat{\mathbf{J}}$ is zero, the adjoint vector $\boldsymbol{\lambda}$ becomes

$$\boldsymbol{\lambda} = \begin{bmatrix} \mathbf{0} \\ \mathbf{p} \end{bmatrix} \tag{4.48}$$

and the sensitivity is

$$\frac{\partial Ł}{\partial \theta_e} = \frac{1}{2}\mathbf{U}^\intercal \frac{\partial \mathbf{K}_u}{\partial \theta_e}\mathbf{U} = \frac{1}{2}\mathbf{u}^\intercal \frac{\partial \mathbf{K}_b}{\partial \theta_e}\mathbf{u}. \tag{4.49}$$

4.4 Numerical examples

Let us consider a macroscale design domain Ω (Fig. 4.7a) defined by a rectangular substrate composed of 20×60 unit cells. In this example, dimensionless variables are used. The initial design of each unit cell is a cylinder that occupies 25% of the microscale design domain (Fig. 4.7b). A fixed pressure $P_0 = 1$ is applied to the surface Γ_{in}. A no slip boundary condition (zero velocity, $u_0 = 0$) is applied to the surface Γ_{wall}.

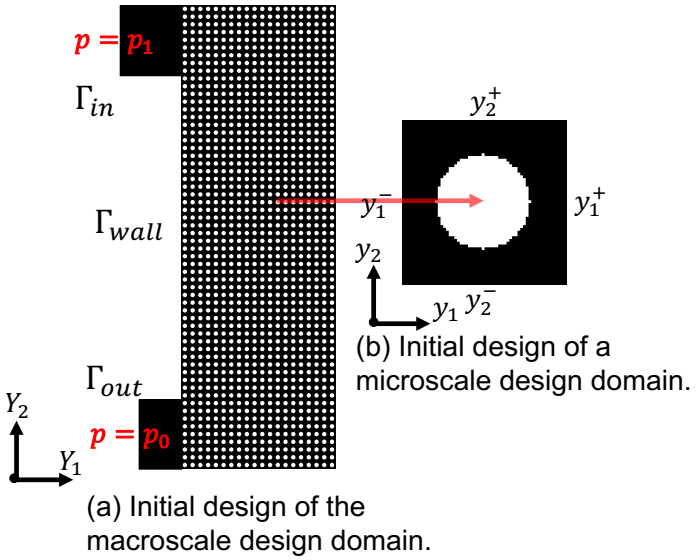

Figure 4.7.. A macroscale design domain contains 60×20 mesoscale square elements.

Two notifications with respected to this numerical example is remarked. First, the Reynolds numbers of the macroscale and microscale design domains are different, since characteristic length of macroscale L_Y is about 60 times of the microscale L_y, makes the Reynolds numbers of macroscale 60 times of the microscale. Two scenarios having different Reynolds numbers are analyzed (Table 4.1). In scenario A, the Reynolds number for the macroscale is 50, therefore the Reynolds number in the microscale becomes 0.83, which is approximated to zero. In scenario B, the Reynolds number is 900 for the macroscale and 15 for the microscale. Second, in this numerical example, Q2Q1 element is applied. Each

of element contains eighteen degrees of freedom for velocity and four degrees of freedom for pressure (Fig. 6.4). In the following paragraphs, firstly, the results of microscale op-

Table 4.1.. Two analyzed scenarios and their relevant Reynolds numbers.

Scenario	Re for L_Y	Re for L_y
A	50	0.83($\approx$0)
B	900	15

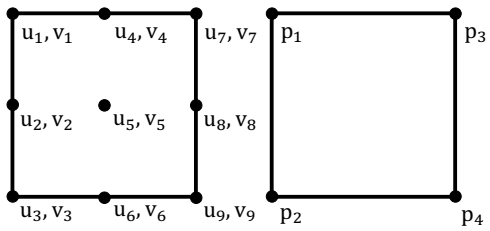

Figure 4.8.. An Illustration of A Quadratic Velocity/Linear Pressure (Q2Q1) Element.

timization problems for selected typical boundary conditions are presented to illustrate the proposed inverse homogenization method. Then, the multiscale approach is implemented to generate final designs of optimal micropillar arrays. For each scenarios, in microscale, twenty-one typical boundary conditions are employed. Each of these boundary conditions consists of an superposition of a local velocity vector and a unit strain (Fig. 4.9a).

4.4.1 Scenario A for microscale: Reynolds number Re=0

In Scenario A, when $\boldsymbol{u}$= $\{1,0\}$ and ε= $\{0,0,0\}$, the resulting topology verifies the example shown in literature [80, 81]. The rest of topologies in Scenario A indicate how the optimal topology changing with variation of the boundary velocity and strain fields (Fig. 4.9b). The optimal topologies have shapes coinciding to fish bodies. Each of them has

reduced flow seperation compared to their counterparts, when same boundary conditions applied to the initial design (Fig. 4.9a and b). In this figure, the reduced flow seperation can be observed by comparing variation of the velocity magnitudes between each pair of corresponding unit cells (Fig. 4.9a and b). Further, the optimal designs have lower energy loss (Table 4.2) and higher average velocity magnitude (Table 4.3) that could benefit the convective heat and mass transfer.

Table 4.2.. Energy loss of the initial design (Init.) and optimal designs (Opt.) under selected boundary conditions for Scenario A (Re=0, Stokes flow).

	(a) $\boldsymbol{u}=\{1,0\}$		(b) $\boldsymbol{u}=\{0,1\}$		(c) $\boldsymbol{u}=\{1,1\}$	
	Init.	Opt.	Init.	Opt.	Init.	Opt.
(1) $\varepsilon=\{0,0,0\}$	1142.1	594.9	1142.1	594.9	2280.7	1184.7
(2) $\varepsilon=\{1,0,0\}$	3634.9	2423.2	2491.1	1822.6	4758.9	2996.4
(3) $\varepsilon=\{0,1,0\}$	2529.8	1822.6	3673.7	2423.2	4823.4	2996.4
(4) $\varepsilon=\{0,0,1\}$	2995.4	1405.4	2928.0	1405.4	5240.7	2584.6
(5) $\varepsilon=\{-1,0,0\}$	1376.6	1218.6	2520.3	1822.6	2529.8	1822.6
(6) $\varepsilon=\{0,-1,0\}$	2507.5	1822.6	1363.6	1218.6	2491.1	1822.6
(7) $\varepsilon=\{0,0,-1\}$	647.3	209.6	714.7	209.6	674.3	209.6

4.4.2 Scenario B for microscale: Reynolds number Re=15.

Similar to Scenario A, in Scenario B, optimal designs shown in Fig. 4.10 b also have lower flow seperation, lower energy loss (Table. 4.4) and higher average velocity magnitude (Table. 4.5) compared to the initial cylinder micropillars (Fig. 4.10 a and b) . Compared Scenario B to A, it indicates a higher Reynolds number leads additional energy loss. However, since in the microscale the Reynolds number difference is small, this additional energy loss is less than 10 %, and their optimal shapes are resemblance. On the other hand,

Table 4.3.. Average velocity magnitude of the original design (Init.) and optimal designs (Opt.) under selected boundary conditions for Scenario A (Re=0, Stokes flow)

	(a) $\boldsymbol{u}=\{1,0\}$		(b) $\boldsymbol{u}=\{0,1\}$		(c) $\boldsymbol{u}=\{1,1\}$	
	Init.	Opt.	Init.	Opt.	Init.	Opt.
(1) $\varepsilon=\{0,0,0\}$	0.8440	0.9289	0.8440	0.9289	1.1812	1.2644
(2) $\varepsilon=\{1,0,0\}$	1.2696	1.3964	0.9455	1.0239	1.5135	1.6323
(3) $\varepsilon=\{0,1,0\}$	0.9509	1.0239	1.2676	1.3964	1.5213	1.6323
(4) $\varepsilon=\{0,0,1\}$	1.3627	1.4705	1.3523	1.4705	1.7811	1.9064
(5) $\varepsilon=\{-1,0,0\}$	0.4303	0.4763	0.9453	1.0239	0.9509	1.0239
(6) $\varepsilon=\{0,-1,0\}$	0.9483	1.0239	0.4321	0.4763	0.9455	1.0239
(7) $\varepsilon=\{0,0,-1\}$	0.6235	0.6959	0.6117	0.6959	0.6202	0.6959

in Scenario B, Newton solver is called twenty times to obtain the convergence of the nonlinear finite element analysis, hence the computational time of Scenario B is twenty times compared to Scenario A. To balance the accuracy and computational cost, in the following multiscale design, Stokes flow is assumed for both Scenario A and B in microscale.

4.4.3 Scenario A for multiscale: Reynolds number Re=50.

In order to obtain an optimal multiscale design, as mentioned, a macroscale finite element analysis should be required before inverse homogenization. The porosity for Brinkman damping term is defined as 0.25, which indicates the volume fraction of cylinder micropillar in an initial design:

$$1-\theta_e = 0.25 \tag{4.50}$$

In Scenario A, Reynolds number Re=50 is employed. From the macroscale finite element analysis, the velocity and strain fields data is obtained (Fig. 4.11a).The data is incoporated

Table 4.4.. Energy loss of the original design (Init.) and optimal designs (Opt.) under selected boundary conditions for Scenario B (Re=15).

	(a) $\boldsymbol{u}=\{1,0\}$		(b) $\boldsymbol{u}=\{0,1\}$		(c) $\boldsymbol{u}=\{1,1\}$	
	Init.	Opt.	Init.	Opt.	Init.	Opt.
(1) $\varepsilon=\{0,0,0\}$	1149.3	606.2	1149.2	606.2	2329.9	1288.8
(2) $\varepsilon=\{1,0,0\}$	3683.4	2451.6	2511.1	1897.2	4896.3	3002.7
(3) $\varepsilon=\{0,1,0\}$	2549.7	2224.8	3710.7	2457.8	4942.1	3098.2
(4) $\varepsilon=\{0,0,1\}$	3054.2	1550.6	2989.1	1460.1	5486.1	2778.6
(5) $\varepsilon=\{-1,0,0\}$	1377.6	1221.7	2541.7	1897.2	2548.9	1896.4
(6) $\varepsilon=\{0,-1,0\}$	2525.7	1880.9	1364.9	1219.7	2510.9	1803.3
(7) $\varepsilon=\{0,0,-1\}$	651.6	229.4	719.1	229.4	683.5	229.5

Table 4.5.. Average velocity magnitude of the original design (Orig.) and optimal designs (Opt.) under selected boundary conditions for Scenario B (Re=15).

	(a) $\boldsymbol{u}=\{1,0\}$		(b) $\boldsymbol{u}=\{0,1\}$		(c) $\boldsymbol{u}=\{1,1\}$	
	Orig.	Opt.	Orig.	Opt.	Orig.	Opt.
(1) $\varepsilon=\{0,0,0\}$	0.8428	0.9297	0.8426	0.9296	1.1809	1.2767
(2) $\varepsilon=\{1,0,0\}$	1.2816	1.4112	0.9521	1.0346	1.5221	1.7496
(3) $\varepsilon=\{0,1,0\}$	0.9455	1.1344	1.2519	1.3877	1.5096	1.7332
(4) $\varepsilon=\{0,0,1\}$	1.3659	1.4824	1.3432	1.5066	1.7752	2.0752
(5) $\varepsilon=\{-1,0,0\}$	0.4251	0.4763	0.9362	1.0346	0.9431	1.0344
(6) $\varepsilon=\{0,-1,0\}$	0.9513	1.0465	0.4356	0.4838	0.9501	1.0465
(7) $\varepsilon=\{0,0,-1\}$	0.6236	0.7023	0.6115	0.7022	0.6212	0.7020

to microscale inverse homogenization problem statements, consequently the optimal micropillar arrays are generated (Fig. 4.11b and c). The resulting optimal micropillar arrays should in coordinate with macroscale velocity and strain fields.

4.4.4 Scenario B for multiscale: Reynolds number Re=900.

Following the same procedure, the final design of optimal micropillar arrays for Scenario B is obtained. With Reynolds number Re=900, the velocity and strain data derived from finite element analysis is shown in Fig. 4.12a. Since the Reynolds number is increased, the velocity and strain magnitudes of Scenario B are siginificantly higher than Scenario A. Remarkably, a zone containing high strain value is existed in the upper side of the marcoscale design domain, due to dramatical velocity variation caused by the fluid jetting from the inflow and impinging to the right side boundary. The resulting optimal micropillar arrays in coordinate with the velocity and strain fields are shown in (Fig. 4.11b and c). These two panels can be converted to STL format and printed by micro and nano-scribe 3D printer.

4.5 Conclusion

In this Chapter, multiscale topology optimization has been applied to the design of micropillar arrays in microfluidic devices, using non-linear Navier-Stokes flow model. A novel approach of inverse homogenization for fluid flow is proposed. The resulting micropillars are in fish-body alike shapes and in coordinate with the macroscale velocity and strain fields. In contrast to common utilized micropillar arrays, the optimal micropillar arrays leading a design with lower flow separation, lower energy loss and higher average velocity magnitude. Furthermore, compared with the common utilized micropillar arrays, the proposed method is customized to specific geometric boundary conditions and physics features.

Two simplifications are assumed in the proposed model. First, the laminar flow model is assumed. Second, the proposed microscale design model assume each micropillar is

composed of Brinkman penalization term, which reduces fluid-structural interaction of the fluid around the micropillar. To calibrate the method and analysis the errors, we are planing to produce the design using microscale additive manufacturing, and implementing experimental studies. In addition, further update of this method includes application to three-dimensional elements, parallel compuation, as well as extention to transient and turbulent problems.

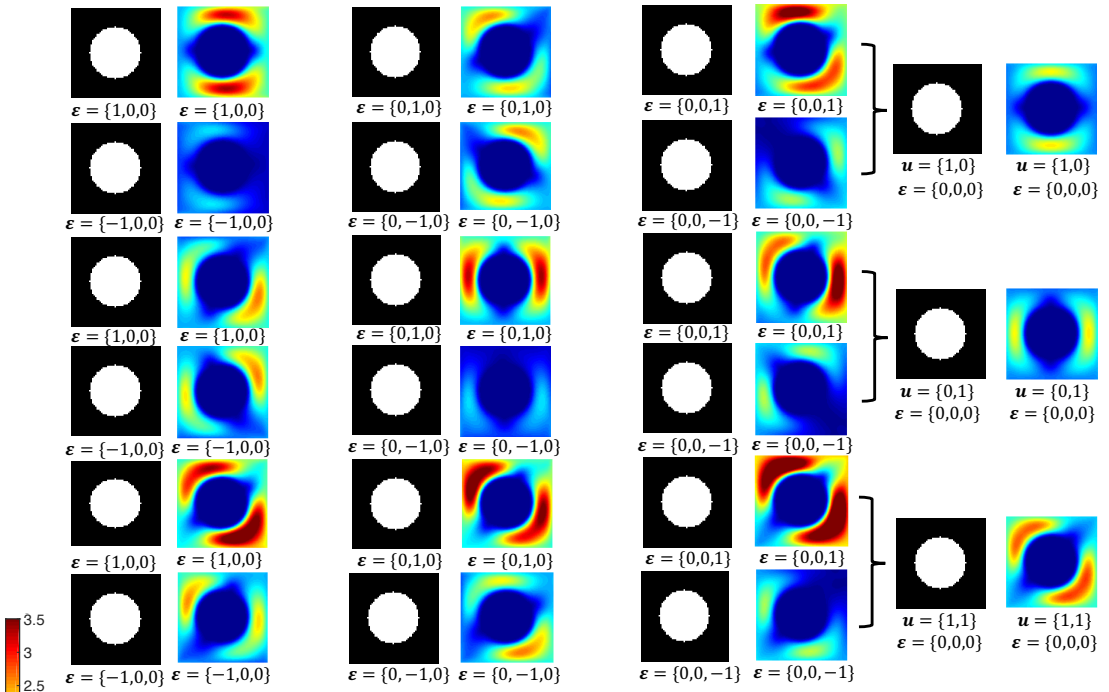

(a) The initial micropillar design with specific boundary conditions and their velocity magnitude plots (Re=0).

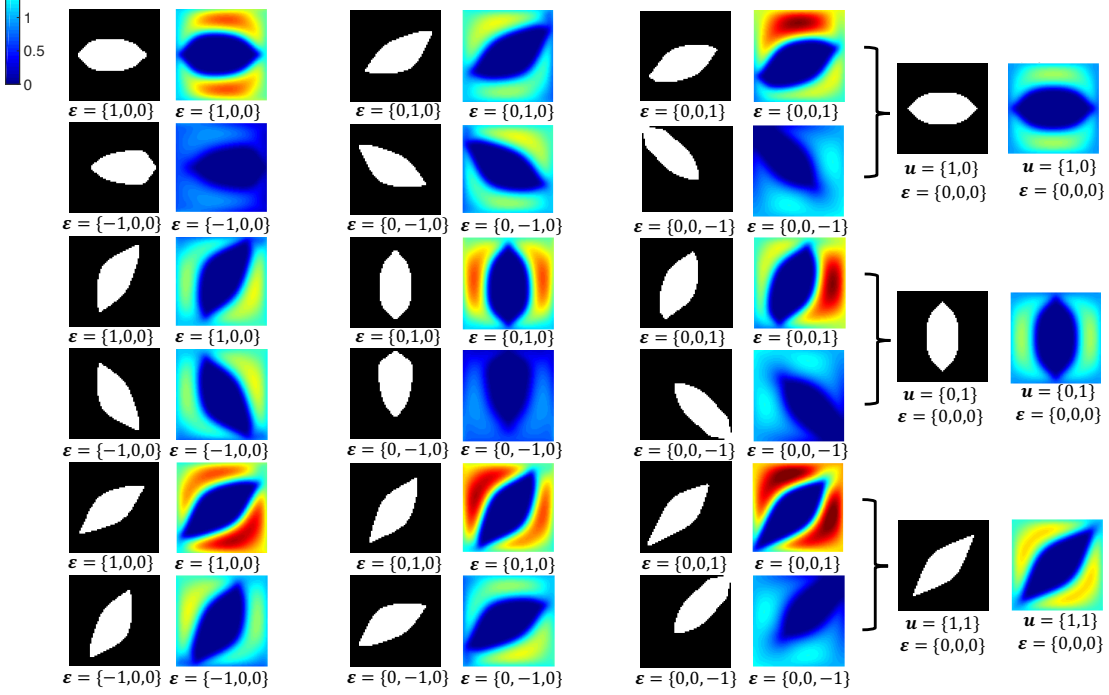

(b) The optimal micropillar designs with specific boundary conditions and their velocity magnitude plots (Re=0).

Figure 4.9.. The optimal micropillars and the resulting velocity magnitude plots under specific boundary conditions for Scenario A (Re=0, Stokes flow).

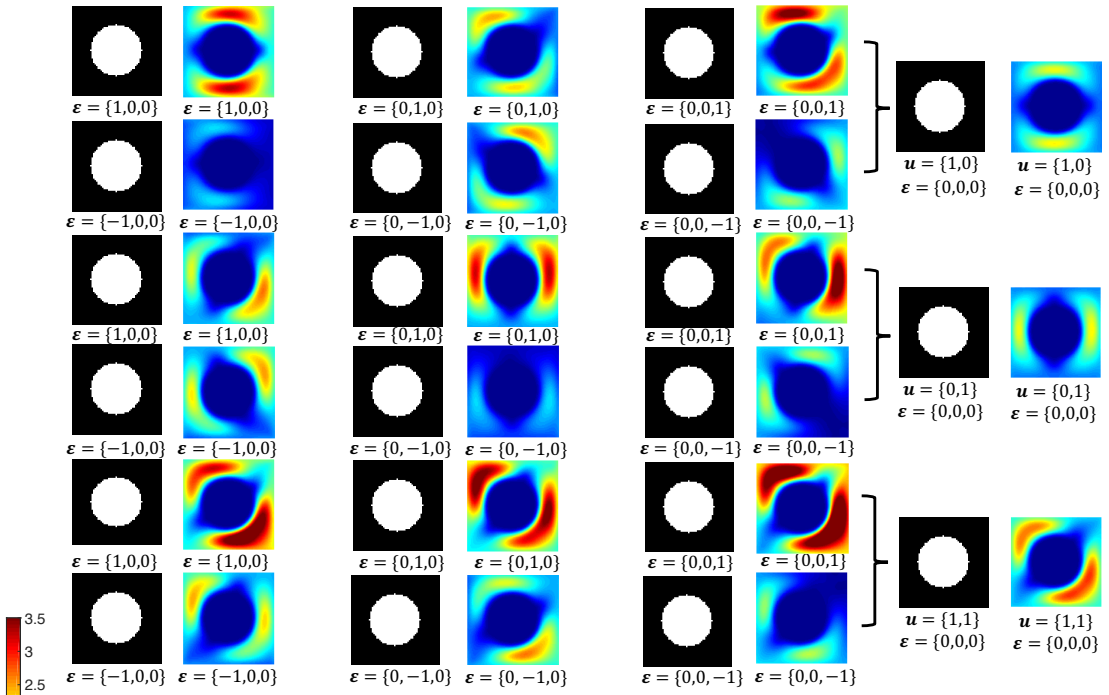

(a) The initial micropillar design with specific boundary conditions and their velocity magnitude plots (Re=15).

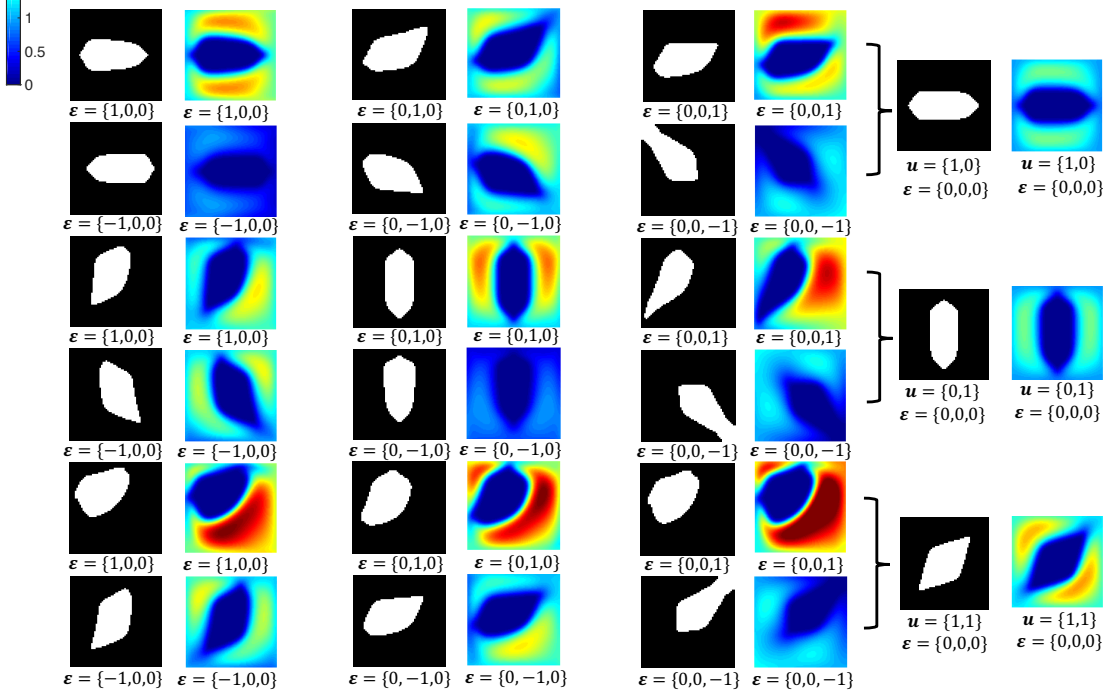

(b) The optimal micropillar designs with specific boundary conditions and their velocity magnitude plots (Re=15).

Figure 4.10.. The optimal micropillars and the resulting velocity magnitude plots under specific boundary conditions for Scenario B (Re=15).

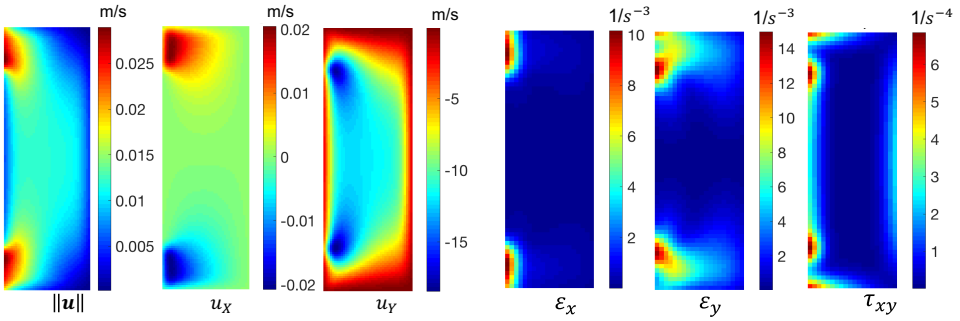

(a) Velocity and strain field derived from macroscale finite element analysis

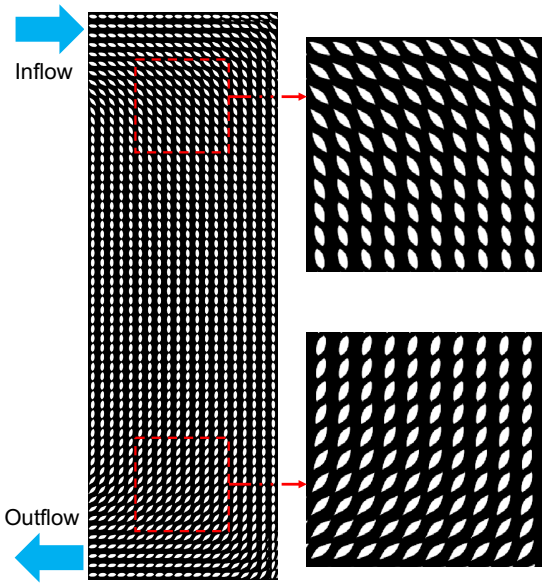

(b) Top view of multiscale design of micropillar arrays

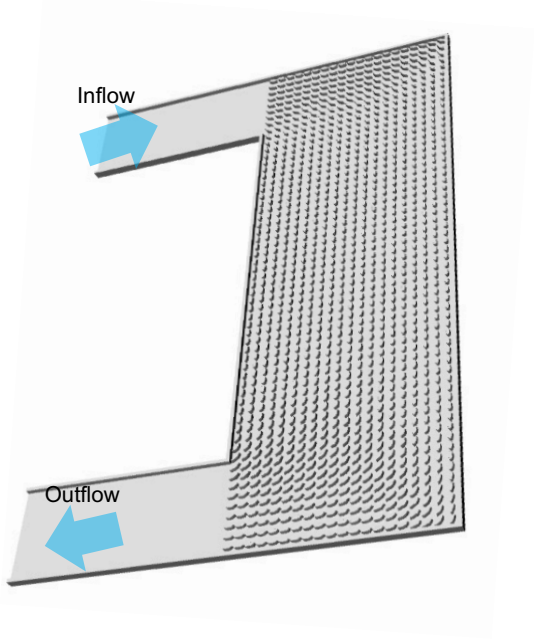

(c) STL file of the multiscale design

Figure 4.11.. Final design of micropillar arrays for Scenario A(Re=50).

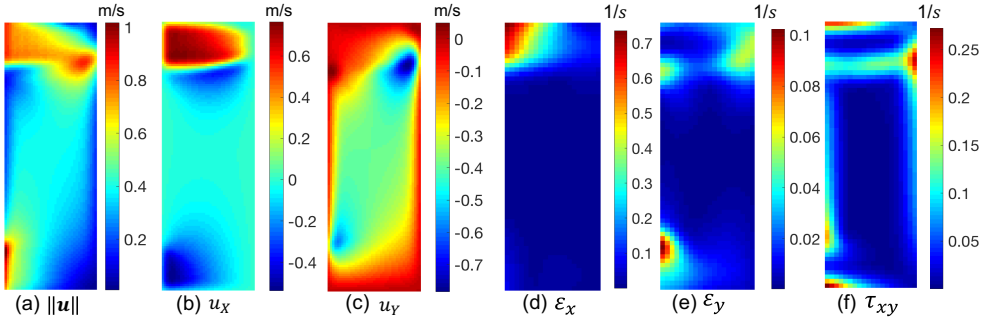

(a) Velocity and strain field derived from macroscale finite element analysis

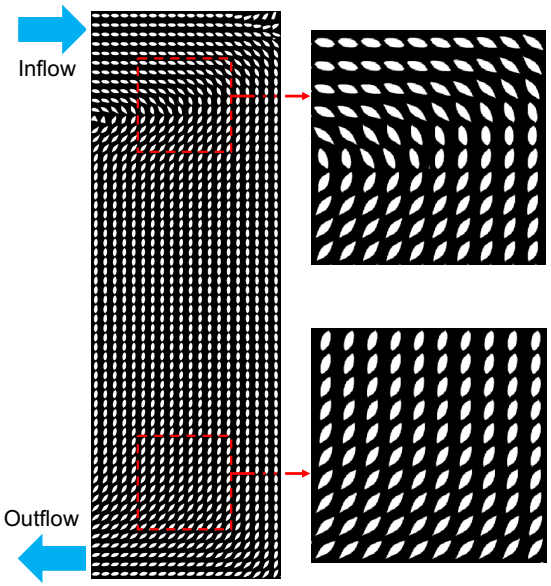

(b) Top view of multiscale design of micropillar arrays

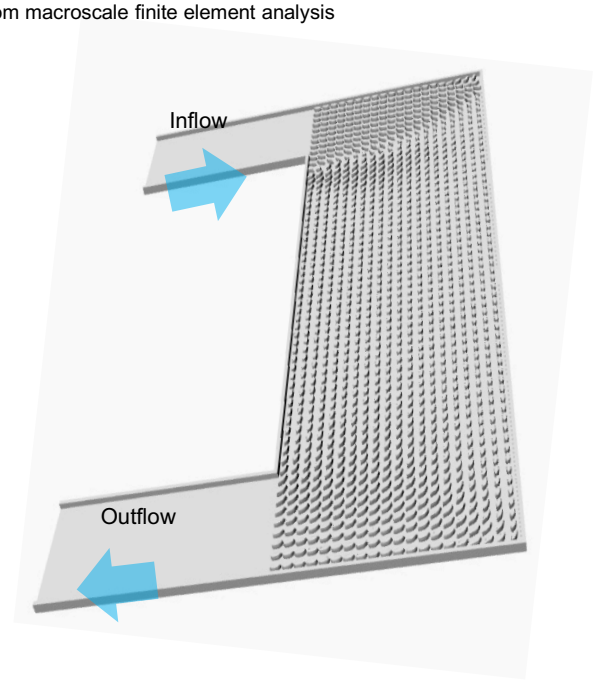

(c) STL file of the multiscale design

Figure 4.12.. Final design of micropillar arrays for Scenario B(Re=900).

5. THERMOMECHANICAL TOPOLOGY OPTIMIZATION OF LATTICE HEAT TRANSFER STRUCTURE INCLUDING NATURAL CONVECTION AND DESIGN DEPENDENT HEAT SOURCE

Lattice Heat Transfer (LHT) structures provide superior structural support whilst improving the heat transfer coefficient by means of their high surface-to-volume ratio. By using current Additive Manufacturing (AM) technologies, LHT with highly complex structures is possible. In this Chapter, the design concept of LHT is further improved by implementing a thermomechanical topology optimization method. With utilization of design-dependent heat source, the method can be applied to generate stiffer LHT structure under mechanical and thermomechanical load, without decreasing its thermal performance, compared to a design made of uniform LTH having the same mass fraction. Two numerical examples are presented to illustrate how to use the proposed approach to design LHT sections. The result shows, by applying the proposed approach, the mechanical performance can be improved more than 50% compared to a uniform LTH with the same mass fraction, without decreasing the thermal performance. The method does not require fluid mechanics model thus it is computational effective and particularly suitable for the conceptual design stage. The resulting optimized lattice made possible by utilizing additive manufacturing technologies.

5.1 Background and motivation

Lattice Heat Transfer (LHT) structures provide superior structural support whilst improving the heat transfer coefficient by means of their high surface-to-volume ratio [125, 172, 173]. Especially, the accelerated development of additive Manufacturing (AM/3D Printing) technologies enables the design and production of intricate lattice structure, of-

fering significant cost savings, particularly in designs having high geometric complexity [48, 174, 175]. In terms of this multifunctional advantages, lattice structure recently attracted great research interests in the applications which simultaneously requiring mechanical high strength and heat transfer rate [123, 124]. These application includes e.g. gas turbine blade and cooling system of injection molds. In gas turbine blades, inserting lattice structure as cooling layer provides the sufficient structural strength of the blade and an overall heat transfer rate two to three times compared to those of a smooth channel [176–178]. Lattice layers have been implemented as cooling system for injection mold, leading a 20% reduction in cooling time, compared to the design having non-lattice conformal cooling [179–181].

Current lattice heat transfer structures are mainly composed of uniformly distributed unit cells each having the same porosity, randomly generated foam-like porous media, as well as structures similar to fins and pillar arrays. The common way to find the optimised LHT structures is carrying out analysis based on simulation data collected after designs are generated, and experimental data recorded after the structures are produced [123–125, 172, 173]. However, the limited design freedom and collected data could hardly prove the satisfied optimality of the structure. To overcome these drawbacks, in this research, a topology optimization approach is proposed to attain flexible and complex lattice structures that significantly improve the design optimality. As a LHT structure concurrently requires transfering heat, and withstanding pure mechanical load as well as thermal stress induced by the temperature gradient, a thermomechanical topology optimization could be incorporated to optimize a LHT structure. Traditional thermomechanical topology optimization has been employed to create thermal actuator [91, 182, 183], thermal management device for spacecraft [10, 92], and injection mold [151]. However, in these approaches, the investigation involve convective heat transfer on the structure's boundary surfaces remains scarce in iterature and is explored in this work.

Convective heat transfer that have been discussed in the context of topology optimization theory are mainly composed of either a thermal-fluid (conjugate) heat transfer model, or a heat transfer model only consisting of solid structure. In a thermal-fluid model based

topology optimization, the natrual and forced convective heat transfer are affected by fluid field resulting from Navier-Stokes equation or Darcy equation [32, 94, 128], which maybe time-consuming to couple with thermomechanical model, and unattractive for early stage conceptual design studies. An alternative approach is to employ design-dependent heat source in the topology optimization of heat transfer problem without a fluid model. The design-dependent heat source means that the heat source varies with the element states or material itself, and it was initially tackled topology optimization of heat conduction problem [84]. Further, design-dependent heat source has been incorporated to analyze heat transfer model taking into account heat conduction, convection, and internal heat generation [77, 78, 121].

In this study, convective heat transfer and design-dependent heat source is coupled with thermomechanical model, resulting in a novel topology optimization method. The method is espcially tailored to the design of multifunctional lattice heat transfer (LHT) structures requiring adequate thermal, mechanical and thermomechanical performance. In this method, it is assumed the design-dependent heat source is only located at fluid phase, and the optimised fluid and solid phase distribution is available as a result of thermomechanical topology optimization. The paper is organized as follows: In Section two, the finite element analysis of thermomechanical model is briefly presented; In Section three, the proposed thermomechanical topology optimization including sensitivity analysis is illustrated; Two numerical examples are shown in Section Four. Finally, the summary of this work is presented in Section Five.

5.2 Finite element analysis of thermomechanical model

In a coupled thermomechanical model, both pure mechanical load and thermomechanical load caused by non-uniform temperature field should be considered. The overall thermal and mechanical performance is significantly influenced by the heat source distribution. In this study, it is assumed that the heat source is only applied to areas containing fluid. With the application of the proposed method, the optimized shape, location and numbers

of areas are obtained. Before the illustration of the method, procedures of thermomechanical finite element analysis (FEA) is briefly described as follows, where natural convection and design-dependent heat source is incorporated.

5.2.1 Thermal model with convection and design-dependent heat load

In a thermal model, the energy dissipation can be written as

$$\mathrm{Q} = \frac{1}{2}\int_{\Omega} \nabla \mathrm{T}^{\intercal} \boldsymbol{\kappa}(\boldsymbol{\theta}) \nabla \mathrm{T} \mathrm{d}\Omega - \mathrm{W}_{\mathrm{q}}, \tag{5.1}$$

where $\boldsymbol{\kappa}$ is the thermal conductivity tensor, $\nabla \mathrm{T}$ indicates temperature gradients, and W is the external work. Discretize Eq. (5.1) yields

$$\mathbf{Q} = \mathbf{T}(\boldsymbol{\theta})^{\intercal} \mathbf{K}_{\mathrm{t}}(\boldsymbol{\theta}) \mathbf{T}(\boldsymbol{\theta}) - \mathbf{q}^{\intercal} \mathbf{T}(\boldsymbol{\theta}), \tag{5.2}$$

In a static equilibrium state $\frac{\partial \mathbf{Q}}{\partial \mathbf{T}} = \mathbf{0}$, Fourier equation in Matrix form is formulated:

$$\mathbf{K}_{\mathrm{t}}(\boldsymbol{\theta}) \mathbf{T}(\boldsymbol{\theta}) = \mathbf{q}(\boldsymbol{\theta}) \tag{5.3}$$

where the global stiffness of heat transfer $\mathbf{K}_t$ is composed of stiffness matrix of thermal conduction $\mathbf{K}_{\mathrm{cond}}$ and natural convection $\mathbf{K}_{\mathrm{conv}}$:

$$\mathbf{K}_{\mathrm{t}}(\boldsymbol{\theta}) = \mathbf{K}_{\mathrm{cond}}(\boldsymbol{\theta}) + \mathbf{K}_{\mathrm{conv}}(\boldsymbol{\theta}). \tag{5.4}$$

In Eq. (5.4),

$$\mathbf{K}_{\mathrm{cond}}(\boldsymbol{\theta}) = \sum_{e=1}^{n_e} \int_{\Omega} \nabla \mathbf{N}^{\intercal} \boldsymbol{\kappa}(\boldsymbol{\theta}) \nabla \mathbf{N} \mathrm{dV}, \tag{5.5}$$

where

$$\boldsymbol{\kappa}(\boldsymbol{\theta}) = \boldsymbol{\kappa}_{\min} + (\boldsymbol{\kappa}_s - \boldsymbol{\kappa}_{\min}) \theta^{p_1}, \tag{5.6}$$

where p_1 is a penalty number. This material interpolation scheme indicates the thermal conductivity is higher when the solid material containing more volume in an element.Notably, $\boldsymbol{\kappa}_{\min}$ is the minimum thermal conductivity for an element to avoid singularity in matrix computation. The stiffness of natural convection is formulated as

$$\mathbf{K}_{\mathrm{conv}} = \sum_{e=1}^{n_e} h \int_{\mathrm{V}} \mathbf{N}^{\intercal} \mathbf{N} \mathrm{dV}, \tag{5.7}$$

where h is convective heat transfer coefficient. In Eq. (5.3), $\mathbf{q}$ is the boundary heat source vector which composed of constant heat source $\mathbf{q}_0$ and a design-dependent heat source $\mathbf{q}_0(\boldsymbol{\theta})$.

$$\mathbf{q}(\boldsymbol{\theta}) = \mathbf{q}_0 + \mathbf{q}_0(\boldsymbol{\theta}), \tag{5.8}$$

In this equation,

$$\mathbf{q}_0(\boldsymbol{\theta}) = \sum_{e=1}^{n_e} h_1(\theta) \int_V \mathbf{N} \mathrm{dV}. \tag{5.9}$$

The design-dependency is represented by the following material interpolation function

$$h_1(\theta) = h_f(1 - \theta^{p_2}) \tag{5.10}$$

In terms Eq. (5.10), the design-dependent heat source is provided by voids containing fluid. This material interpolation scheme assumes there is a maximum design-dependent heat source h_f when the element V is filled with fluid, and zero when the element is filled with solid. When the element is filled with fluid, the design dependent heat source $\mathbf{q}_0$ reaches its maximum value $\overline{\mathrm{q}_0}$.

5.2.2 Thermomechanical model with convection and design-dependent heat load

Solving the heat transfer model, it will result in a non-uniform temperature field, which induce thermo-elastic strain and stress fields. For a thermomechanical structure, the strain and stress relations can be described as

$$\mathbf{D}\big(\boldsymbol{\epsilon} - \boldsymbol{\epsilon}_{\mathrm{T}}\big) = \boldsymbol{\sigma} \tag{5.11}$$

In Eq. (5.11), $\mathbf{D}$ is elasticity tensor, and $\boldsymbol{\epsilon}$ is strain due to mechanical load. $\boldsymbol{\epsilon}_{\mathrm{T}}$ is strain due to thermal-elastic load coupling the temperature field derived from thermal model. The elementwise thermal-elastic strain $\boldsymbol{\epsilon}_{\mathrm{T}}$ is formulated as

$$\boldsymbol{\epsilon}_{\mathrm{T}e} = \alpha(\theta)\big(\mathbf{N}\mathbf{T}_e(\theta) - \mathrm{T}_0\big)\mathbf{1} \tag{5.12}$$

where α is thermal expansion coefficient related to proportion of solid phase in the an element θ and penalty number p_3:

$$\alpha(\theta) = \alpha_{\min} + (\alpha_0 - \alpha_{\min})\,\theta^{p_3}. \tag{5.13}$$

$\mathbf{T}_e(\theta)$ is the elemental temperature obtained from thermal model. The strain energy density is

$$\Phi = \frac{1}{2}\int_{\Omega}\left(\boldsymbol{\epsilon}-\boldsymbol{\epsilon}_{\mathrm{T}}\right)^{\intercal}\mathbf{D}(\boldsymbol{\theta})\left(\boldsymbol{\epsilon}-\boldsymbol{\epsilon}_{\mathrm{T}}\right)\mathrm{d}\Omega - \mathrm{W}, \tag{5.14}$$

Discretize Eq. (5.14) yields

$$\Phi = \frac{1}{2}\mathbf{u}^{\intercal}\mathbf{K}_{\mathrm{elast}}(\boldsymbol{\theta})\mathbf{u} - \mathbf{f}_{\mathrm{th}}{}^{\intercal}\left(\boldsymbol{\theta},\mathbf{T}(\boldsymbol{\theta})\right)\mathbf{u} - \mathbf{f}^{\intercal}\mathbf{u}, \tag{5.15}$$

In Eq. (5.15), the thermo-elastic load $\mathbf{f}_{th}$ is represented as

$$\mathbf{f}_{\mathrm{th}}\left(\boldsymbol{\theta},\mathbf{T}(\boldsymbol{\theta})\right) = \mathbf{K}_{\mathrm{mt}}(\boldsymbol{\theta})\mathbf{T}(\boldsymbol{\theta}), \tag{5.16}$$

where $\mathbf{K}_{\mathrm{mt}}$ is thermo-mechanical coupling stiffness matrix

$$\mathbf{K}_{\mathrm{mt}}(\boldsymbol{\theta}) = \sum_{e=1}^{n_e}\int_{\mathrm{V}}\mathbf{B}^{\intercal}\mathbf{D}(\theta_e)\alpha\mathbf{N}\mathrm{dV}, \tag{5.17}$$

and nodel temperature $\mathbf{T}(\boldsymbol{\theta})$ is derived from Eq. (5.15) assocaited to the thermal model. $\mathbf{B}$ is the matrix representing strain-displacement relation. The stiffness matrix of elasticity $\mathbf{K}_{\mathrm{elast}}$ is

$$\mathbf{K}_{\mathrm{elast}}(\boldsymbol{\theta}) = \sum_{e=1}^{n_e}\int_{\mathrm{V}}\mathbf{B}^{\intercal}\mathbf{D}(\theta_e)\mathbf{B}\mathrm{dV}. \tag{5.18}$$

$\mathbf{u}$ is the nodal displacement, and $\mathbf{f}$ is the external force.

In a static equilibrium state $\frac{\partial\Phi}{\partial\mathbf{u}} = \mathbf{0}$, Hook's law in matrix form is formulated:

$$\mathbf{K}_{\mathrm{elast}}(\boldsymbol{\theta})\mathbf{u}(\boldsymbol{\theta}) = \left(\mathbf{f}_{\mathrm{th}}\left(\boldsymbol{\theta},\mathbf{T}(\boldsymbol{\theta})\right) + \mathbf{f}\right)^{\intercal}\mathbf{u}(\boldsymbol{\theta}) \tag{5.19}$$

5.3 Proposed thermomechanical topology optimization

As aforementioned, the heat source can be divided to constant heat source $\mathbf{q}_0$ and design-dependent heat source $\mathbf{q}_0^i(\boldsymbol{\theta})$. In this problem, we assume constant heat source is applied to the boundary surface Γ in Figure. 5.1. As described in Eq. (5.9) and Eq. (5.10), the heat source is applied to the cavities ω_1 to ω_n in Figure. 5.1. The shape, location, area, and numbers of these cavities are unknown. which will be defined from the proposed algorithm. However, the two equations show, the sum of these design-dependent

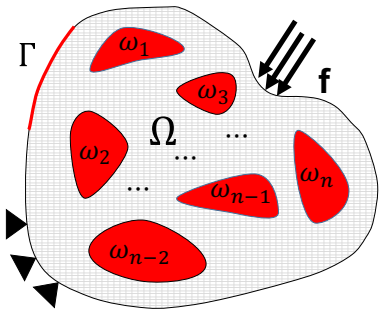

Figure 5.1.. An Illustration of design domain, constant and design-dependent heat source for proposed method.

heat source should have an upper bound $\bar{\mathrm{q}}$, if the volume fraction of all the cavities have an upper bound. These heat source conditions can be formulated as:

$$\begin{aligned} &\mathbf{q}_0 \in \Gamma, \quad \mathbf{q}_0^i(\boldsymbol{\theta}) \in \omega_i \quad (i = 1 \dots n), \\ &\sum_{i=1}^{n} \mathbf{q}_0^i = \bar{\mathrm{q}} \end{aligned} \tag{5.20}$$

The heat load could induce a non-uniform temperature field, thus a thermal load field $\mathbf{f}_{\mathrm{th}}\big(\boldsymbol{\theta}, \mathbf{T}(\boldsymbol{\theta})\big)$ is obtained. A superposition of the intermal thermal load and external mechanical load $\mathbf{f}$ is applied as the total load to formulate the load of thermomechanical problem.

In a thermomechanical topology optimization problem, it is desire to obtain high thermal and mechanical performance. A common used measurement for thermal perforamance is heat compliance

$$J_{\mathrm{t}} = \mathbf{q}(\boldsymbol{\theta})^{\mathsf{T}} \mathbf{T}(\boldsymbol{\theta}). \tag{5.21}$$

For mechanical performance, the mechanical compliance is adopted as

$$J_{\mathrm{m}} = \Big(\mathbf{f}_{\mathrm{th}}\big(\boldsymbol{\theta}, \mathbf{T}(\boldsymbol{\theta})\big) + \mathbf{f}\Big)^{\mathsf{T}} \mathbf{u}(\boldsymbol{\theta}). \tag{5.22}$$

In this article, mechanical compliance is utilized as objective function of thermomechanical topology optimization, while the thermal compliance is defined as a constraint that should be smaller than the reference value of the initial design J_{t}^0:

$$\begin{aligned} &\text{minimize} \quad J_{\mathrm{m}}(\boldsymbol{\theta}) \\ &\text{subject to} \quad J_{\mathrm{t}}(\boldsymbol{\theta}) \leq J_{\mathrm{t}}^0(\boldsymbol{\theta}) \end{aligned} \tag{5.23}$$

At the same time, the mass constraints for the structure and each elements

$$\begin{aligned} & m(\boldsymbol{\theta}) \leq m(\boldsymbol{\theta}_0) \\ & \theta^{\min} \leq \theta \leq \theta^{\text{solid}}, \end{aligned} \tag{5.24}$$

where m is the mass of the structure, and $m(\theta)_0$ is a given constant. $\theta^{\min}$ is the minimum allowable density for each element, which is the relative density of fluid phase in this study. θ^{solid} is the relative density of solid phase, equal to 1. Finally, Fourier's law Eq. (5.3) and Hook's law Eq. (5.19) are required to be satisfied. Finally, the problem statement of proposed thermomechanical topology optimization is

$$\begin{aligned} \text{find} \quad & \boldsymbol{\theta}^* \in \mathbb{R}^{n_c} \\ \text{minimize} \quad & J_{\text{m}}(\boldsymbol{\theta}) \\ \text{subject to} \quad & J_{\text{t}}(\boldsymbol{\theta}) \leq J_{\text{t}}^0(\boldsymbol{\theta}) \\ & m(\boldsymbol{\theta}) \leq m(\boldsymbol{\theta}_0) \\ & \theta^{\min} \leq \theta \leq \theta^{\text{solid}} \\ & \mathbf{q}_0 \in \Gamma, \quad \mathbf{q}_0^i(\boldsymbol{\theta}) \in \omega_i \quad (i = 1 \ldots n), \\ & \sum_{i=1}^{n} \mathbf{q}_0^i = \overline{\text{q}} \\ \text{satisfying} \quad & \mathbf{q}(\boldsymbol{\theta}) = \mathbf{K}_{\text{t}}(\boldsymbol{\theta})\mathbf{T}(\boldsymbol{\theta}) \\ & \mathbf{f}_{\text{th}}\big(\boldsymbol{\theta}, \mathbf{T}(\boldsymbol{\theta})\big) + \mathbf{f} = \mathbf{K}_{\text{elast}}(\boldsymbol{\theta})\mathbf{u}(\boldsymbol{\theta}). \end{aligned} \tag{5.25}$$

To analysis sensitivity of this problem Eq. (5.25) can be rewritten as the form of Lagrangian function Ł:

$$\begin{aligned} \text{Ł} = & \Big(\mathbf{f}_{\text{th}}\big(\boldsymbol{\theta}, \mathbf{T}(\boldsymbol{\theta})\big) + \mathbf{f}\Big)^{\intercal} \mathbf{u}(\boldsymbol{\theta}) + \lambda_J \Big(\mathbf{q}(\boldsymbol{\theta})^{\intercal} \mathbf{T}(\boldsymbol{\theta}) - \beta J_{\text{t}}^0(\boldsymbol{\theta})\Big) + \\ & \boldsymbol{\lambda}_m{}^{\intercal} \Big(\mathbf{K}_{\text{elast}}(\boldsymbol{\theta})\mathbf{u}(\boldsymbol{\theta}) - \mathbf{f} - \mathbf{f}_{\text{th}}\big(\boldsymbol{\theta}, \mathbf{T}(\boldsymbol{\theta})\big)\Big) + \\ & \boldsymbol{\lambda}_t{}^{\intercal} \left(\mathbf{K}_t(\boldsymbol{\theta})\mathbf{T}(\boldsymbol{\theta}) - \mathbf{q}(\boldsymbol{\theta})\right) \end{aligned} \tag{5.26}$$

Where $\boldsymbol{\lambda}_m{}^\intercal$ and $\boldsymbol{\lambda}_t{}^\intercal$ are adjoint vectors, and λ_J is a penalty which is activated when the thermal compliance is greater than the initial design value, β is a relaxation factor equal to 1.1:

$$\begin{aligned} &\text{if} \quad J_{\mathrm{t}}(\boldsymbol{\theta}) \leq \beta J_{\mathrm{t}}^0(\boldsymbol{\theta}), \quad \lambda_J = 0 \\ &\text{otherwise} \quad \lambda_J = 1 \end{aligned} \tag{5.27}$$

Since $\mathbf{f_{th}}$ a function of relative density $\boldsymbol{\theta}$ and temperature $\mathbf{T}(\boldsymbol{\theta})$, $\mathbf{T}(\boldsymbol{\theta})$ is a function of $\boldsymbol{\theta}$, and $\mathbf{q}(\boldsymbol{\theta})$ is a function of $\boldsymbol{\theta}$, the derivatives of the Lagrangian for each element θ are written as

$$\begin{aligned} \frac{\partial Ł(\boldsymbol{\theta})}{\partial \theta} =& \mathbf{u}(\boldsymbol{\theta})^\intercal \frac{\partial \mathbf{f}_{\mathrm{th}}}{\partial \theta} + \mathbf{u}(\boldsymbol{\theta})^\intercal \frac{\partial \mathbf{f}_{\mathrm{th}}}{\partial \mathbf{T}(\theta)} \frac{\partial \mathbf{T}(\theta)}{\partial \theta} + (\mathbf{f} + \mathbf{f}_{\mathrm{th}})^\intercal \frac{\partial \mathbf{u}(\boldsymbol{\theta})}{\partial \theta} + \\ & \lambda_J \mathbf{T}(\boldsymbol{\theta})^\intercal \frac{\partial \mathbf{q}}{\partial \theta} + \lambda_J \mathbf{q}^\intercal \frac{\partial \mathbf{T}(\boldsymbol{\theta})}{\partial \theta} + \\ & \boldsymbol{\lambda}_m{}^\intercal \left(\frac{\partial \mathbf{K}_{\mathrm{elast}}(\theta)}{\partial \theta} \mathbf{u}(\boldsymbol{\theta}) + \mathbf{K}_{\mathrm{elast}}(\theta) \frac{\partial \mathbf{u}(\boldsymbol{\theta})}{\partial \theta} - \frac{\partial \mathbf{f}_{\mathrm{th}}}{\partial \theta} - \frac{\partial \mathbf{f}_{\mathrm{th}}}{\partial \mathbf{T}(\theta)} \frac{\partial \mathbf{T}(\boldsymbol{\theta})}{\partial \theta} \right) + \\ & \boldsymbol{\lambda}_t^\intercal \left(\frac{\partial \mathbf{K}_t(\boldsymbol{\theta})}{\partial \theta} \mathbf{T}(\theta) + \mathbf{K}_t \frac{\partial \mathbf{T}(\boldsymbol{\theta})}{\partial \theta} - \frac{\partial \mathbf{q}(\boldsymbol{\theta})}{\partial \theta} \right) \end{aligned} \tag{5.28}$$

In order to cancel $\frac{\partial \mathbf{u}(\boldsymbol{\theta})}{\partial \theta}$term and $\frac{\partial \mathbf{T}(\boldsymbol{\theta})}{\partial \theta}$, the value in adjoint vectors can be defined to satisfy

$$\begin{aligned} &\left((\mathbf{f} + \mathbf{f}_{\mathrm{th}})^\intercal + \boldsymbol{\lambda}_m{}^\intercal \mathbf{K}_{\mathrm{elast}}(\boldsymbol{\theta}) \right) \frac{\partial \mathbf{u}(\boldsymbol{\theta})}{\partial \theta} = \mathbf{0} \\ &\left(\mathbf{u}(\boldsymbol{\theta})^\intercal \frac{\partial \mathbf{f}_{\mathrm{th}}}{\partial \mathbf{T}(\theta)} + \boldsymbol{\lambda}_t{}^\intercal \mathbf{K}_t(\boldsymbol{\theta}) - \boldsymbol{\lambda}_m{}^\intercal \frac{\partial \mathbf{f}_{\mathrm{th}}}{\partial \mathbf{T}(\theta)} + \lambda_J \mathbf{q}(\boldsymbol{\theta})^\intercal \right) \frac{\partial \mathbf{T}(\boldsymbol{\theta})}{\partial \theta} = \mathbf{0}, \end{aligned} \tag{5.29}$$

By sequentially solving the above two equations, finally, the sensitivity is derived as

$$\begin{aligned} \frac{\partial L(\boldsymbol{\theta})}{\partial \theta_c} =& \mathbf{u}(\boldsymbol{\theta})^\intercal \frac{\partial \mathbf{f}_{\mathrm{th}}}{\partial \theta} + \lambda_J \mathbf{T}(\boldsymbol{\theta})^\intercal \frac{\partial \mathbf{q}(\boldsymbol{\theta})}{\partial \theta} + \boldsymbol{\lambda}_m{}^\intercal \left(\frac{\partial \mathbf{K}_{\mathrm{elast}}(\boldsymbol{\theta})}{\partial \theta} \mathbf{u}(\boldsymbol{\theta}) - \frac{\partial \mathbf{f}_{\mathrm{th}}}{\partial \theta} \right) \\ & + \boldsymbol{\lambda}_t{}^\intercal \left(\frac{\partial \mathbf{K}_t(\boldsymbol{\theta})}{\partial \theta} \mathbf{T}(\boldsymbol{\theta}) - \frac{\partial \mathbf{q}(\boldsymbol{\theta})}{\partial \theta} \right). \end{aligned} \tag{5.30}$$

5.4 Numerical examples

Two numerical examples are shown in this section, namely Design 1 and Design 2. Both of these two designs share the same boudary conditions associated to heat transfer, but their boundary condition for thermomechanical models are different. In Design 1, the

bottom edge is fixed, and compressive pressure is imposed on the top edge. In Design 2, the boundary condition and mechanical load locations are following a typical Messerschmitt-Bölkow-Blohm (MBB) beam example. Assume the initial design domain is composed of X-bracing lattice structure having a mass fraction of $m(\boldsymbol{\theta}_0)$=0.5. X-bracing lattice structure is adopted since it can be produced without requiring additional materials for supporting structure in additive manufacturing.

To reveal the capability of the proposed method, for each design, four scenarios (A-D) are examined. The results of initial design for each four scenarios are listed as Scenarios *a* to *d*. In Scenario A and *a*, only thermal boundary conditions and supports for thermo-mechanical model are applied. All the mechanical loads are induced from non-uniform temperature field derived from heat transfer model. In Scenario B and *b*, an additional external constant heat flux is applied. Then, in Scenario C and *c*, an external pressure or force is imposed on the boundary. Finally, in Scenario D and *d*, the convective heat transfer coefficient is doubled. The penalization numbers values are p_1=5, p_2=3, and p_3=1.2. The relative density of fluid phase $\theta^{\min}$ is equal to 0.15. For all of these examples, non-dimensional parameters are used.

5.4.1 Example 1:A lattice heat transfer section withstanding compressive mecahanical load

In the first example, a rectangular design domain having 120×240 elements are fixed at the bottom edge. In the thermal model, design-dependent heat source is imposed on the entire design domain. The maximum value of the heat source value per element $\overline{q_0}$ is 0.01, convective heat transfer coefficient h is equal to 0.005. The thermal model results in a non-uniform temperature field, inducing thermomechanical loads. In Scenario A and *a*, only the induced thermomechanical loads are considered in the mechanical model. In Scenario B and *b*, apply boudary heat source q_2=0.1 to each node on the bottom edge (Fig. 5.3). Then, in Scenario C and *c*, compressive pressure p=0.005 is applied to the each node on

Table 5.1.. A summary of boundary condition for Scenarios

Scenario	Boundary condition of thermal problem	Boundary condition of thermomechanical problem
a and A	Volumetric design-dependent	Thermomechanical
a and A	heat source	load
b and B	In addition to volumetric design-dependent heat source, apply a constant heat source to the bottom edge	Thermomechanical l load
b and B	In addition to volumetric design-dependent heat source, apply a constant heat source to the bottom edge	In addition toThermomechanical l load, apply external mechanical load to the boundary edges
b and B	In addition to volumetric design-dependent heat source, apply a constant heat source to the bottom edge, increasing convective heat transfer coefficient	In addition toThermomechanical l load, apply external mechanical load to the boundary edges

the top edge (Fig. 5.4). Then, in Scenario D and *d*, the convective heat transfer h is doubled from 0.005 to 0.01 (Fig. 5.5).

The topology, temperature distribution and displacement magnitude plot of the first example are shown in Fig. 5.2 to Fig. 5.5, and the key results are listed in Table 5.2. The mechanical compliance of optimal designs are only 40% to 52% of the initial designs, while thermal compliance are maintained 95% to 102% of the initial designs. In addition, it is interest to observe some key results such as mean displacement magnitude $\widehat{\| u \|}$, maximum displacement magnitude $\overline{\| u \|}$, maximum temperature $\widehat{\mathrm{T}}$ and mean temperature $\overline{\mathrm{T}}$. The mean displacement magnitudes of the optimal designs are 56% to 77% of the initial designs, and the maximum displacements of the optimal designs are only 21% to 27% of the initial designs. The mean temperature of the optimal designs are 91% to 94% of ini-

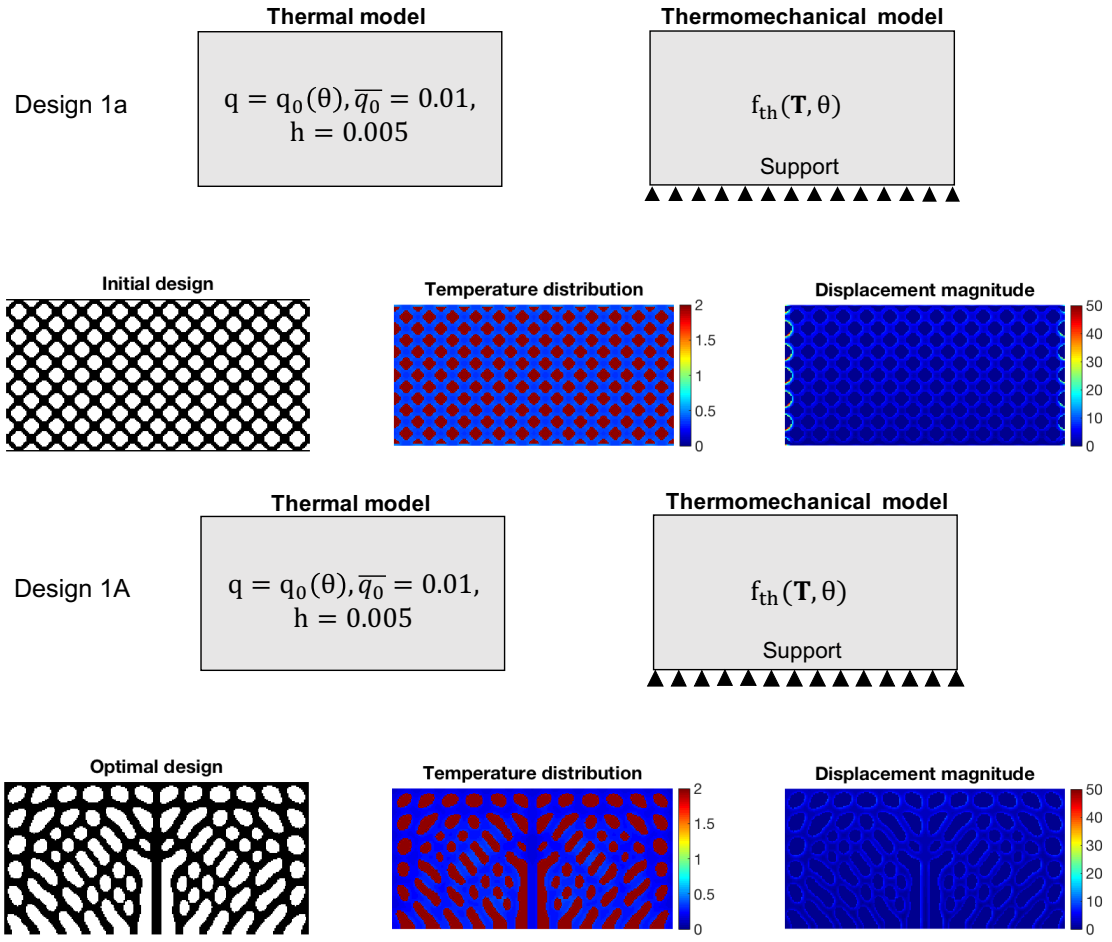

Figure 5.2.. Topology, temperature distribution, and displacement magnitude distribution of initial and optimal design for scenario 1A and 1a.

tial designs, which implies a limited compromising of thermal performance to ensure the significant mechanical performance. The maximum temperature of the optimal designs are 72% to 102% of the initial designs, implies though the overall heat transfer performance is generally maintained, the local heat transfer performance may not be guaranteed.

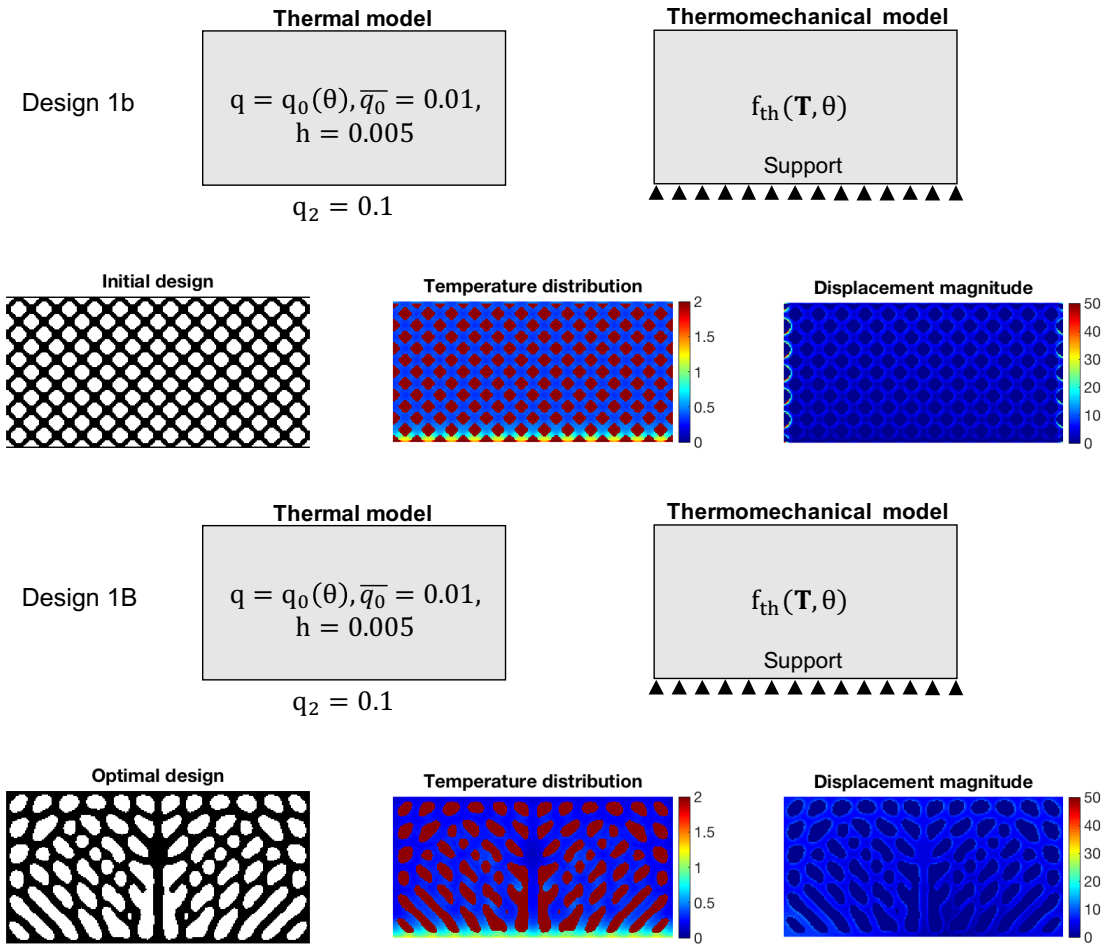

Figure 5.3.. Topology, temperature distribution, and displacement magnitude distribution of initial and optimal design for scenario 1B and 1b.

5.4.2 Example 2: A lattice heat transfer section with boundary conditions of a MBB beam

In the second example, the thermal model remains the same as the first example, and the supports are located at left edge and the right bottom corner, in terms of a half MBB beam. In Scenario A and *a*, only the induced thermomechanical loads are considered in the mechanical model (Fig. 5.6). In Scenario B and *b*, apply boudary heat source q_2=0.1 to each node on the bottom edge (Fig. 5.7). Then, in Scenario C and *c*, an external load *p*=1.2

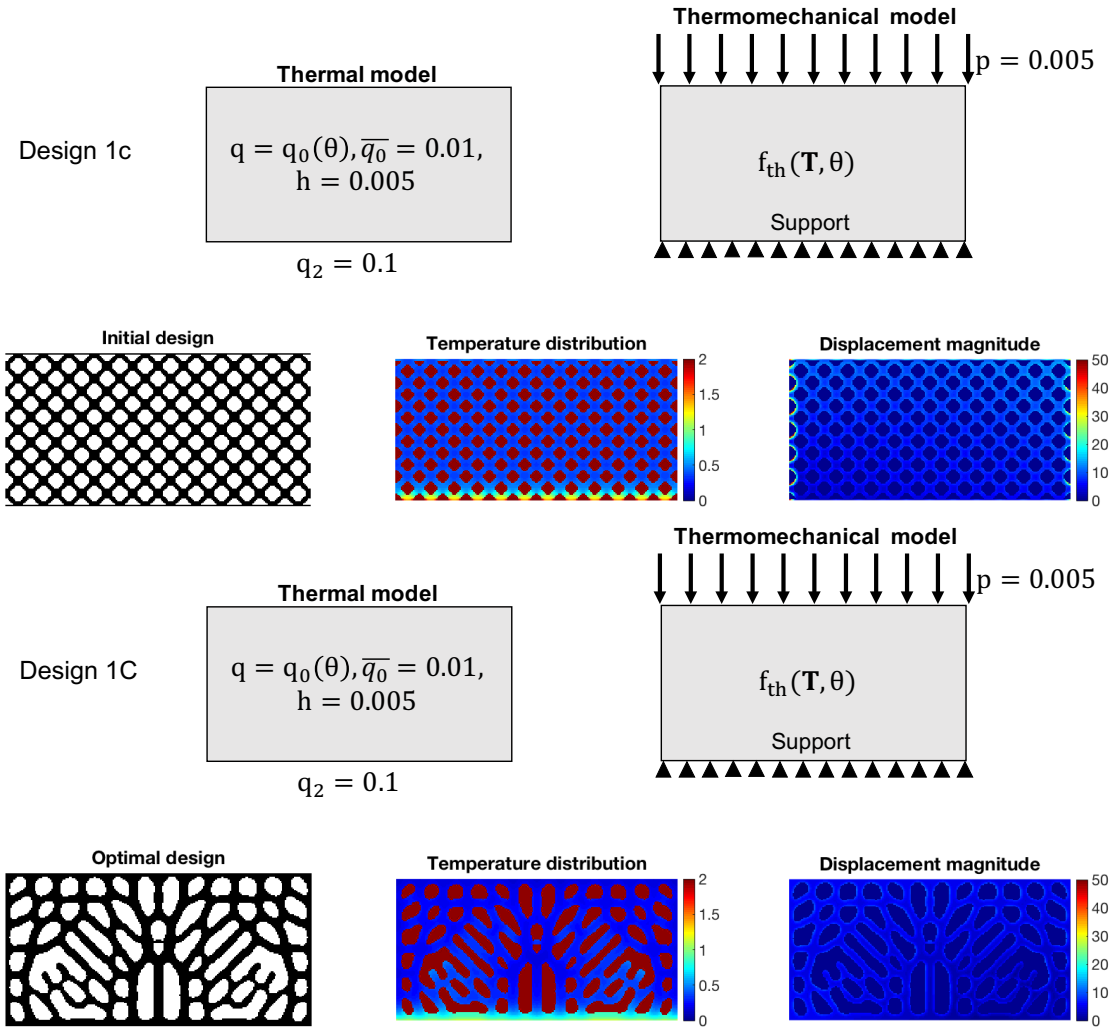

Figure 5.4.. Topology, temperature distribution, and displacement magnitude distribution of initial and optimal design for scenario 1C and 1c.

is applied to the left top corner (Fig. 5.8). Then, in Scenario D and *d*, the convective heat transfer *h* is doubled from 0.005 to 0.01 (Fig. 5.9).

The topology, temperature distribution and displacement magnitude plot of the second example are shown in Fig. 5.2 to Fig. 5.5, and the key results are listed in Table 5.3. The results show trends similar to the first example: The mechanical compliance of optimal designs are only 27% to 46% of the initial designs, while thermal compliance are maintained 94% to 110% of the initial designs. The mean displacement magnitudes of the optimal

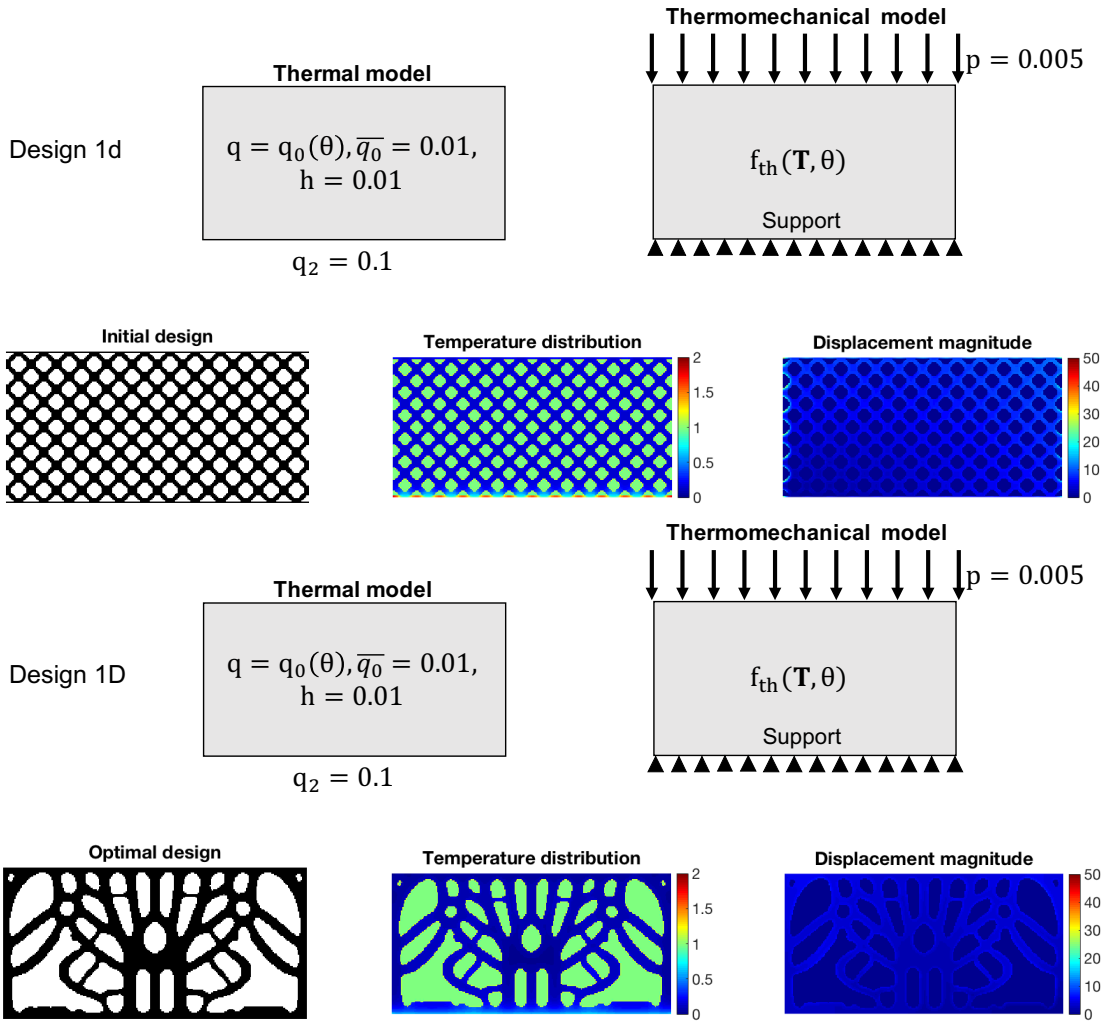

Figure 5.5.. Topology, temperature distribution, and displacement magnitude distribution of initial and optimal design for scenario 1D and 1d.

designs are 26% to 79% of the initial designs, and the maximum displacements of the optimal designs are only 22% to 46% of the initial designs. The mean temperature of the optimal designs are 91% to 100% of initial designs, which implies a limited compromising of thermal performance to ensure the significant mechanical performance. The maximum temperature of the optimal designs are 73% to 103% of the initial designs, which shows though the overall heat transfer performance is generally maintained, the local heat transfer performance may not be guaranteed.

Table 5.2.. Key results of example 1: A LHT section withstanding compressive mecahanical load

Case	$J_m(\boldsymbol{\theta})$	$J_t(\boldsymbol{\theta})$	$\widehat{\parallel u \parallel}$	$\overline{\parallel u \parallel}$	$\widehat{\mathrm{T}}$	$\overline{\mathrm{T}}$
Design 1a	285.90	1843.1	2.3133	47.617	0.9331	2.1032
Design 1A	160.38	1736.4	1.7944	10.006	0.9027	2.1518
Design 1b	282.53	1863.1	2.3755	47.718	1.0408	2.7952
Design 1B	152.36	1758.1	1.8206	10.172	0.9477	2.153
Design 1c	301.76	1863.1	4.2062	50.115	1.0408	2.7952
Design 1C	158.8	1798.4	2.672	11.392	0.9571	2.164
Design 1d	83.613	958.25	3.1024	27.8121	0.5212	1.8108
Design 1D	33.704	984.42	1.7487	7.5790	0.4945	1.3121

Table 5.3.. Key results of example 2: A LHT section with boundary conditions of a MBB beam

Case	$J_m(\boldsymbol{\theta})$	$J_t(\boldsymbol{\theta})$	$\widehat{\parallel u \parallel}$	$\overline{\parallel u \parallel}$	$\widehat{\mathrm{T}}$	$\overline{\mathrm{T}}$
Design 2a *a*	350.86	1855.4	3.5224	53.560	0.9981	2.109
Design 2A	164.04	1753.6	2.2592	12.1389	0.9049	2.1697
Design 2*b*	347.32	1874.7	3.8300	52.242	1.0457	2.7952
Design 2B	156.20	1886.1	3.0133	15.246	0.9923	2.1489
Design 2*c*	814.94	1874.7	127.36	416.61	1.0457	2.7952
Design 2C	327.53	2032.2	55.0129	192.24	1.0517	2.1649
Design 2*d*	551.70	963.79	126.97	394.31	0.5236	1.8108
Design 2D	152.30	1058.7	32.516	111.15	0.5128	1.3163

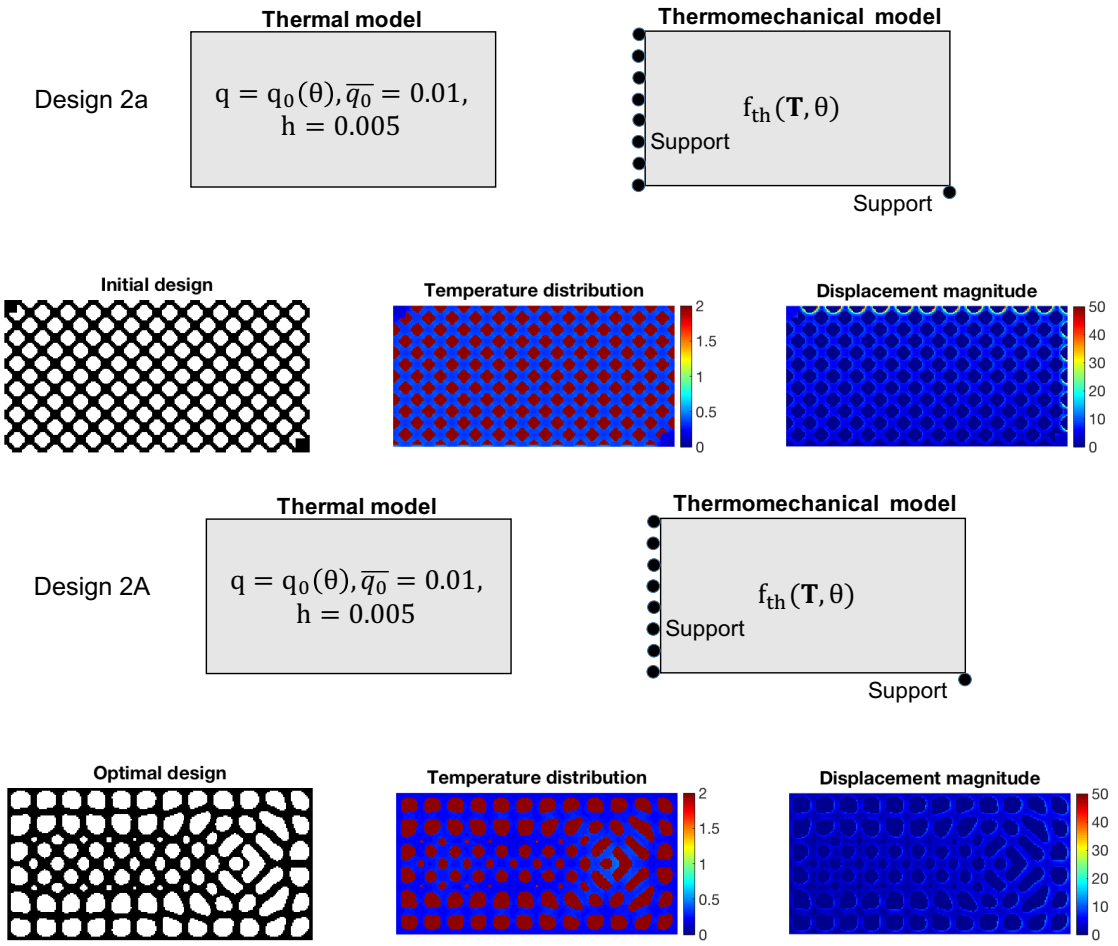

Figure 5.6.. Topology, temperature distribution, and displacement magnitude distribution of initial and optimal design for scenario 2A and 2a.

5.5 Conclusion

This Chapter presents a novel thermomechanical topology optimization method with consideration of convective heat transfer and design-dependent heat source, that exploits the benefits of multifunctional lattice heat transfer structure. The heat source is dependent on if the material is solid or fluid, thus the optimised solid-fluid interface and heat source distribution can be obtained through the method. Since the method does not require a fluid mechanics model, it is computationally efficient and especially appropriate to be applied in

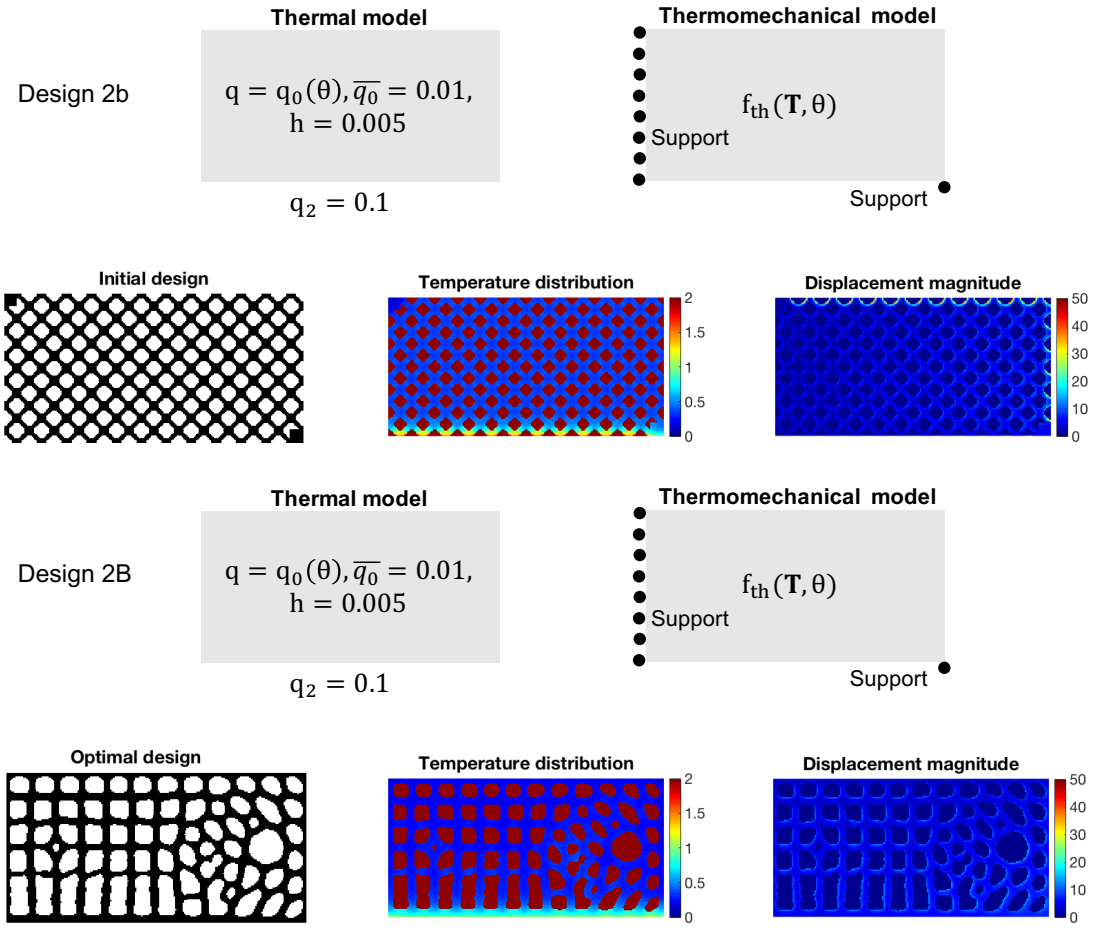

Figure 5.7.. Topology, temperature distribution, and displacement magnitude distribution of initial and optimal design for scenario 1Band 1b.

the conceptual design stage. With the application of this method, the mechanical stiffness of the lattice heat trasnfer structure due to mechanical and thermomechanical loads is significantly improved, while the overall heat transfer performance is maintained. The final design shows complex lattice structures that can augment current additive manufacturing technologies.

Finally, limitations of this method and future work are addressed. First, the method use design-dependent heat source to replace accurate fluid mechanics model, it could not reflect velocity field, therefore it could not reflect the temperature gradient caused by forced con-

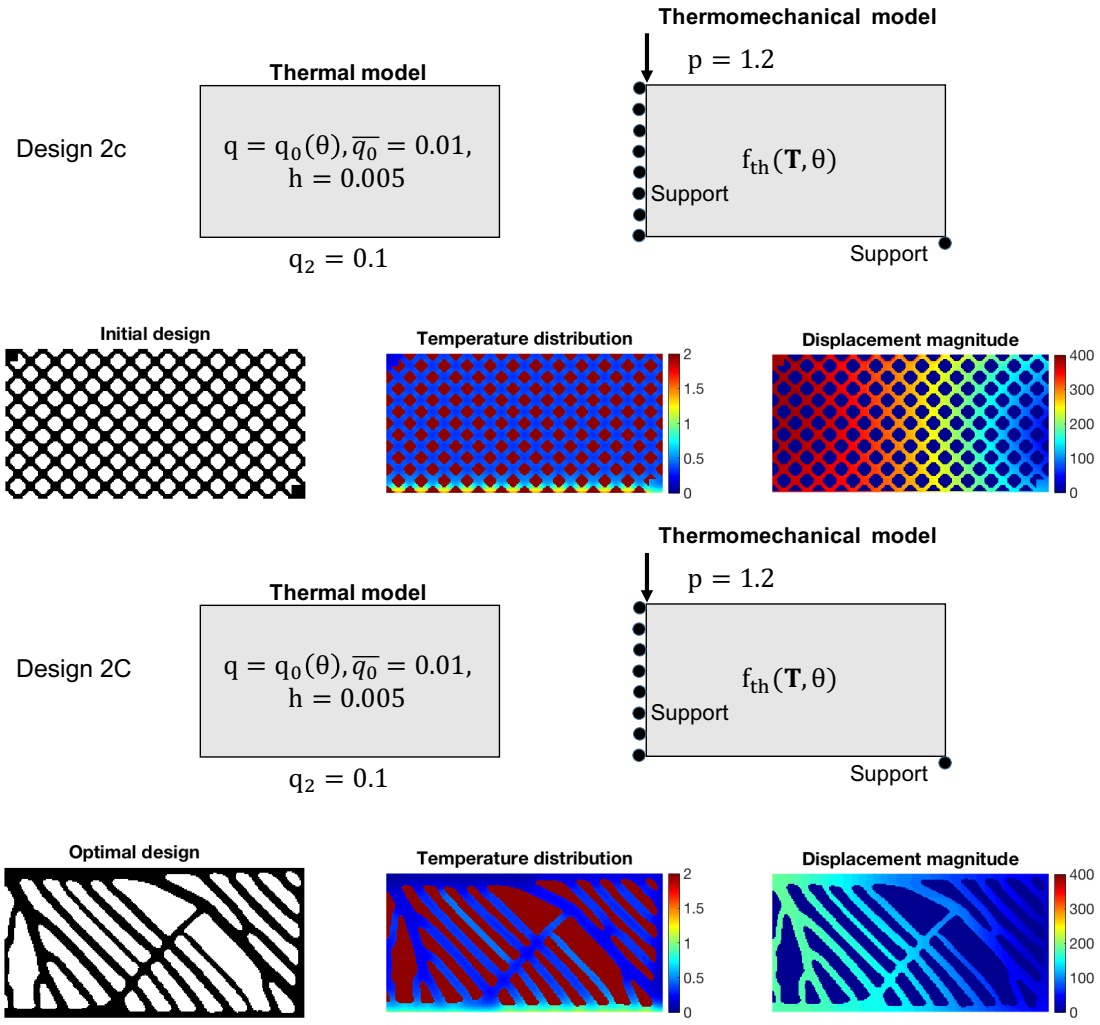

Figure 5.8.. Topology, temperature distribution, and displacement magnitude distribution of initial and optimal design for scenario 1C and 1c.

vection in the fluid. Therefore, it implies the method is limited to investigate the problem that the velocity difference in the fluid is small. Second, the results of numerical example show the method may not ensure to maintain the local heat transfer performance. For a detailed design, thermal-fluid-structure coupled simulation and experimental study is also required.

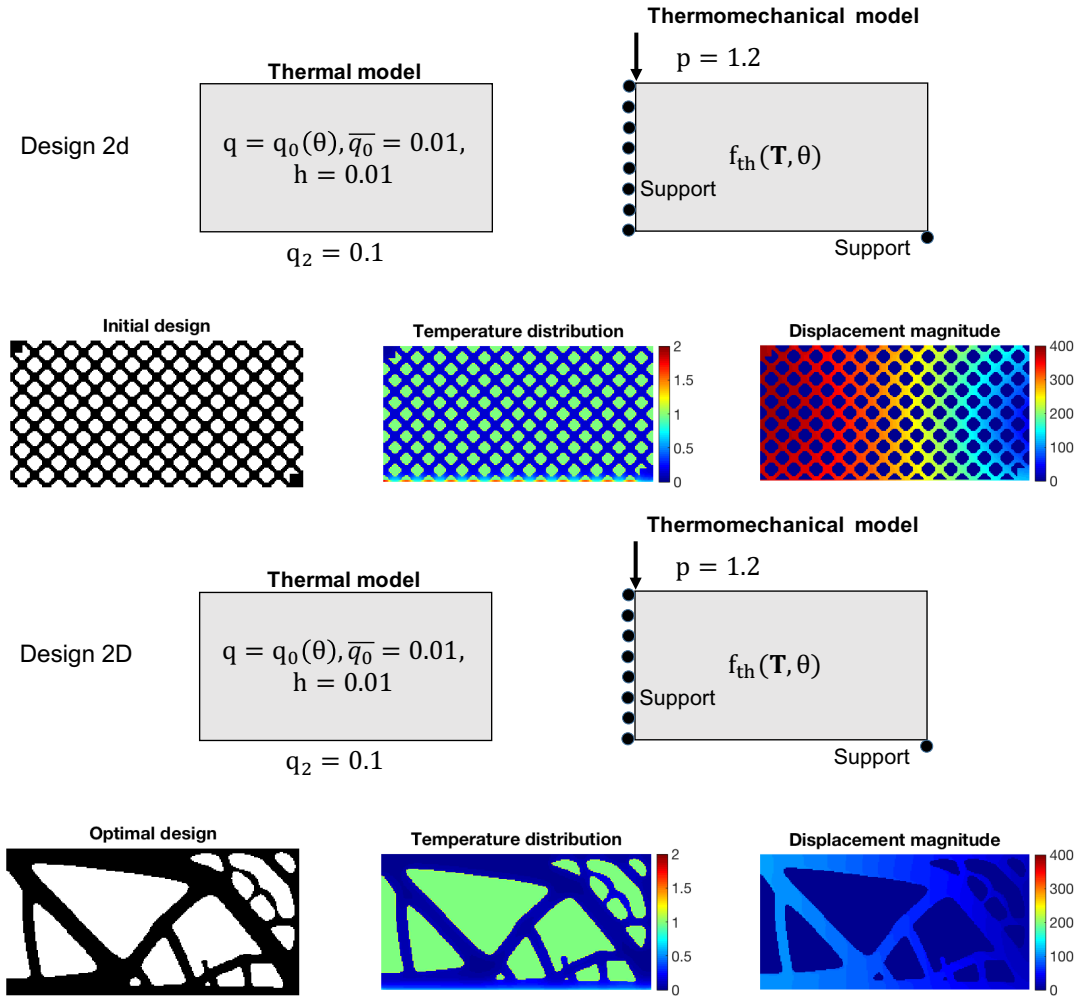

Figure 5.9.. Topology, temperature distribution, and displacement magnitude distribution of initial and optimal design for scenario 1D and 1d.

6. DESIGN OF CONFORMAL COOLING CHANNELS USING A VERSATILE THERMAL-FLUID TOPOLOGY OPTIMIZATION

Current design methods of conformal cooling systems are either intuitive or parametric optimization based that lack of optimally and complexity. Thermal-fluid topology optimization has the potential to generate free-form, complex and optimal channels distribution. However, existing research about thermal-fluid topology optimization remain scarce and they have restricted flexibility to allow thermal-fluid parameters changing in a wide range, or unable to involve external heat source in analysis. To solve these issues, we code a novel thermal-fluid topology optimization algorithm in this study. The proposed method contains a Navier-Stokes flow and heat transfer coupled finite element analysis with a Newton iterative solver. Further, the sensitivity analysis of the coupled thermal-fluid field is analytically derived using adjoint method, which avoids the appearance of dead-end channels. Applying this method leads versatile topologies with regularities in terms of different combinations of thermal-fluid parameters such as Reynolds number, Prandtl number and thermal diffusivity. Finally, the method is applied to design a conformal cooling of an injection mold, which is produced through Direct Metal Laser Sintering additive manufacturing.

6.1 Background and motivation

Additive manufacturing allows the fabrication of highly complex parts and tools, extending the design possibilities of conformal cooling systems in heat exchangers and components that require heat dissipation. In particular, increasing the complexity and optimally of the cooling system in an injection mold offers the potential to increase the heat transfer rate in a uniform manner across the surface of the injected part, which improves the efficiency of the injection process, enhances the quality of the part, and significantly reduces the production cost [145]. The optimization methods of conformal cooling systems have

been extensively investigated [184, 185]. In these studies, conformal cooling systems were optimized in terms of parametrized geometric control points, and their optimal shapes were obtained through parameters optimization with surrogate models. Unfortunately, these design methods are limited by the constraints of their simple architecture. To attain an architecture with a higher geometric complexity, a morphological surface based cooling network has been proposed. In this method, a surface conformal to the heat source is pre-defined to allow cooling channels positioning, hence the channels have equal distance to the heat source and a uniform cooling is expected to achieve [186]. The cooling channels can be located with regard to thermal performance results from steady-state finite-element analysis (FEA) (Fig. 6.1a) [187]. The channels also can be designed based on a Centroid Voronoi diagram to generate a complex flow network thoroughly covering the entire morphology surface, which reminds the capillary network in nature [188] (Fig. 6.1b). However, these intuitive driven design methods cannot ensure the thermal-fluid optimally of the system.

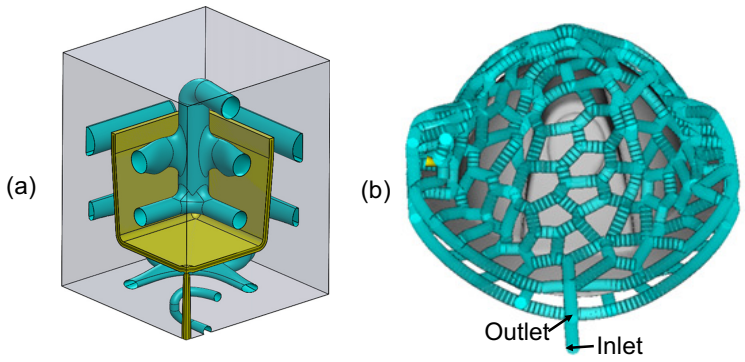

Figure 6.1.. (a) Conformal Cooling Designs Positioned on Morphological Surfaces [187]. (b) A Centroid Voronoi Diagram Based Flow Network Located on Morphological Surfaces. [188].

An innovative and potentially transformational alternative is a freeform conformal cooling design, characterized by its complexity and optimally. One of the most potentially effective way to generate an optimal freeform channel distribution is via finite element analysis (FEA)-based thermal-fluid topology optimization. Studies associated to un-coupled

heat transfer and fluid flow topology optimization can be found in many literature. A topology optimization focused on heat transfer problem aims to obtain optimal structure with respect to thermal conduction [14, 83, 84], natural convection [76, 77] and forced convection [78, 79]. In these studies, surrogate material models are adopted to approximating the characteristic of fluid field and convective heat transfer. On the other hand, the objective of a topology optimization focused on fluid is to find channels that minimizing energy dissipation due to drag force under certain flow categories such as Stokes [73, 80] and laminar flow [86, 87].Topology optimization of turbulent flow is still a new research area, in which only a few of recent studies have been published [89, 90].

Comparatively, less studies in connection with a coupled thermal-fluid FEA based topology optimization can be found. A thermal-fluid FEA has been incorporated to obtain heat sinks targeting optimal thermal conduction and natural convection [94, 95]. To investigate optimal channel shapes under forced convection, a thermal-fluid topology optimization algorithm is proposed with incorporation of FEA coupling Stokes flow and heat transfer [96]. However, a linear Stokes flow model is limited in application since the non-linear advection term is neglected. To substitute the effect of non-linear advection term, in a latest study, a Darcy flow FEA is employed as an approximate fluid flow model in the thermal-fluid analysis [128]. Some researchers have attempted to exploit the non-linear Navier-Stokes flow and convection-diffusion coupling FEA module in commercial software COMSOL Multiphysics® and make effort on secondary development [31, 32, 97]. In this approach, heat transfer is evaluated by considering the internal heat exchange between fluid-solid boundary in the fixed design domain. However, a topology optimization utilizing commercial software would be inconvenient to customize the physics model such as impose an external heat source. Another studies consider the external heat source [24, 98, 99], and formulate multi-objectives problem statements, in which thermal and fluid performance are optimized as a weight-sum approach. However, in this method, it has to remain a substantial weighting factor on the objective with respect to fluid flow performance. When this weighting factor is small, or the objective function is pure thermal performance, the result may shows dead-end channels, where the fluid flow may be intersected by solid phase

and not be able to sucessfully pass from inlet to outlet. Additionally, these models has a restricted flexibility to allow thermal-fluid parameters such as Reynolds number, Prandtl number and thermal diffusivity changing in a wide range, and unable to properly reflect how different combinations of these thermal-fluid parameters influence the resulting optimal topologies.

To solve these issues, in this study, a novel thermal-fluid topology optimization algorithm is developed. An in-house finite element code is created in MATLAB to solve coupled nonlinear Navier-Stokes flow and heat transfer problem. This code consists of an external heat source term, and it allows thermal-fluid parameters shifting in a wide range and leads versatile solutions. With incorporation of non-linear FEA code with a Newton iterative solver, a coupled thermal-fluid topology optimization is formulated. Further, the sensitivity analysis of the coupled thermal-fluid field is analytically derived using adjoint method, which avoids the appearance of dead-end channels. It intriguingly shows, in terms of different combinations of thermal-fluid parameters, the algorithm results in diverse optimal shapes with regularities. Further, the proposed method is applied to design an optimal conformal cooling channels for our industries partner. Several efforts in order to achieve an applicable industrial product from a conceptual design are presented, which including generation of a symmetric and flow-balanced design, parametric computer-aided final design and additive manufacturing.

This Chapter is organized as follows. In Section Two, the procedure to develop the coupled thermal-fluid finite element model is described, and numerical results are presented. In Section Three, the topology optimization algorithm is formulated and sensitivity analysis is explained. Also, the numerical example of the proposed topology optimization is presented in Section Three. The procedure of design optimization of the conformal cooling of injection mold by means of proposed algorithm is described in Section Four. Finally, the conclusion and future work are signified in Section Five.

6.2 Derivation of the thermal-fluid finite element analysis

The governing equations and their discretized form of thermal-fluid finite analysis required in the proposed method, including fluid-flow model and heat transfer model are briefly described in this section. The details of these methods are illustrated in [171]. The schematic figure of the design domain Ω in this study is shown in Fig. 6.2. The following components are included in the boundary conditions: A prescribed heat source q, inflow and outflow locations (Γ_{in} and Γ_{out}), inflow and outflow properties such as inflow pressure p_1, temperature T and outflow pressure p_0, and no slip and insulated boundary Γ_{wall}.

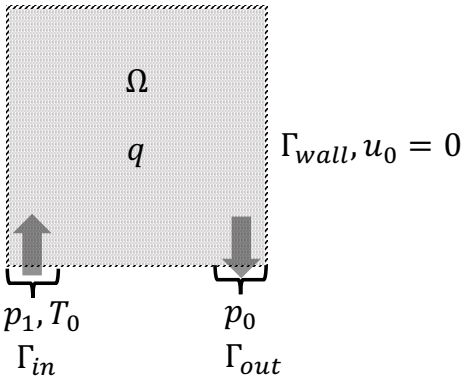

Figure 6.2.. Problem Description of The Proposed Finite Element Analysis Model.

In this thermal-fluid analysis, assume there is no temperature field induced buoyancy force field involved in Navier-Stokes equation, hence the fluid and thermal problem can be solved segregately as explained in the next section.

6.2.1 Fluid-flow model

[1] A fluid finite element model is based on Navier-Stokes equations. A steady state Navier-Stokes equations without fluid body force can be described by momentum and continuity equations are presented as follows:

$$\begin{aligned} &\mathrm{Re}\,(\boldsymbol{u}\cdot\boldsymbol{\nabla})\,\boldsymbol{u} = -\boldsymbol{\nabla} p + \nabla^2\boldsymbol{u} - \alpha(\theta)\boldsymbol{u} \\ &\boldsymbol{\nabla}\cdot\boldsymbol{u} = 0, \end{aligned} \tag{6.1}$$

where *Re* is Reynolds number which measures the relation of inertia force dominated flow and viscous force dominated flow:,

$$\mathrm{Re} = \frac{\rho U L}{\mu}, \tag{6.2}$$

here U and L are the characteristic length and velocity, ρ is the fluid density, μ is the viscosity, $\boldsymbol{u}$ is the velocity field, p is the pressure field. $\alpha(\theta)$ is interpolation function of Brinkman Stiffness:

$$\alpha(\theta_e) = \rho\left(\theta_{\min} + (1-\theta_{\min})\frac{p_b(1-\theta_e)}{p_b+\theta_e}\right), \tag{6.3}$$

where θ_e is the proportion of fluid in an element, p_b is a positive penalty parameter used for tuning the function shape of $\alpha(\theta_e)$ (Fig. 6.3). This term can be interpreted as a large damping term that stops flow, which ensures the velocity in the solid domain ($\alpha(\theta_e)$=0) vanishes.

By applying Galerkin method and Green identity, Eq. (6.1) can be discretized as

$$\underbrace{\begin{bmatrix} \mathbf{K} & -\mathbf{G}^{\mathsf{T}} \\ -\mathbf{G} & \mathbf{0} \end{bmatrix}}_{\mathbf{K}_g} \underbrace{\begin{bmatrix} \mathbf{u} \\ \mathbf{p} \end{bmatrix}}_{\mathbf{U}} = \underbrace{\begin{bmatrix} \mathbf{f} \\ \mathbf{0} \end{bmatrix}}_{\mathbf{F}}, \tag{6.4}$$

where **u**, **p** and **f** are nodal velocity, pressure and force, respectively. In a two dimensional problem, each node contains two directions of velocities: $\mathbf{u}_e$=$\{\mathbf{u}_e^x, \mathbf{u}_e^y\}$. The matrix **K** is constructed as

$$\mathbf{K} = \mathbf{K}_s + \mathbf{K}_b + \mathbf{K}_a. \tag{6.5}$$

[1]The context of Section 6.2.1 is the same as Chapter 4, Section 4.2. It is repeated here for the convenience of reading.

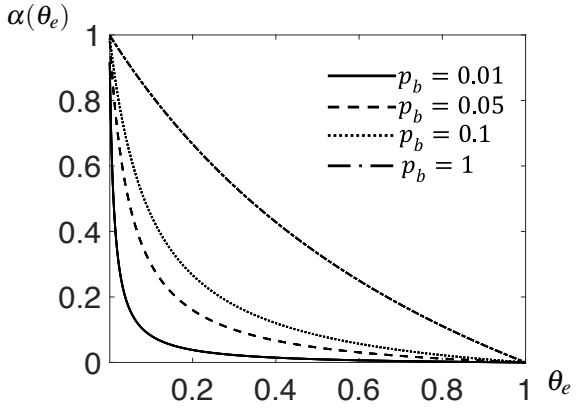

Figure 6.3.. The Shape of Interpolation Function $\alpha(\theta_e)$ is Influenced by Penalty Parameter p_b.

$\mathbf{K}$ can be considered as a union of the matrices with respect to two directions of velocities $\mathbf{K}$=$\{\mathbf{K}^x, \mathbf{K}^y\}$. In this equation, the stiffness matrix of Stokes flow

$$\mathbf{K}_s = \sum_{e=1}^{n_e} \int_{V_e} \mu \nabla \mathbf{N_u}^\intercal \mathbf{I}_0 \nabla \mathbf{N_u} \mathrm{d}V_e, \tag{6.6}$$

where $\mathbf{N_u}$ is the matrix containing shape functions of the elemental velocity, and

$$\mathbf{I}_0 = \begin{bmatrix} 2 & 0 & 0 \\ 0 & 2 & 0 \\ 0 & 0 & 1 \end{bmatrix}. \tag{6.7}$$

for a two dimensional element. $\mathbf{K}_b$ is the Brinkman damping matrix, which can be considered as a union of matrices with respect to two directions of velocities: $\mathbf{K}_b$=$\{\mathbf{K}_b^x, \mathbf{K}_b^y\}$. For both x and y directions, the matrix is constructed as:

$$\mathbf{K}_b^x = \mathbf{K}_b^y = \sum_{e=1}^{n_e} \int_{V_e} b\alpha(\theta_e) \mathbf{N_u}^\intercal \mathbf{N_u}, \mathrm{d}V_e, \tag{6.8}$$

where b is a constant reflecting resistance level. $\mathbf{K}_a$ is the advection matrix, which can be considered as a union of matrices with respect to two directions of velocities: $\mathbf{K}_a$=$\{\mathbf{K}_a^x$, $\mathbf{K}_a^y\}$. For both x and y directions, the matrix is constructed as:

$$\mathbf{K}_a^x = \mathbf{K}_a^y = \sum_{e=1}^{n_e} \int_{V_e} \mathrm{Re} \left(\underbrace{\mathbf{N_u}^\intercal \mathbf{N_u} \mathbf{u}_e^x \nabla \mathbf{N}_{\mathbf{u},x}}_{\mathbf{K}_a^{xx} \ \ and \ \ \mathbf{K}_a^{yx}} + \underbrace{\mathbf{N_u}^\intercal \mathbf{N_u} \mathbf{u}_e^y \nabla \mathbf{N}_{\mathbf{u},y}}_{\mathbf{K}_a^{xy} \ \ and \ \ \mathbf{K}_a^{yy}} \right) \mathrm{d}V_e. \tag{6.9}$$

$\mathbf{G}$ is the coupling matrix of the pressure and velocity of x and y directions : $\mathbf{G}$=$\{\mathbf{G}^x$, $\mathbf{G}^y\}$, where

$$\mathbf{G}^x = \sum_{e=1}^{n_e} \int_{V_e} \nabla \mathbf{N}_{\mathbf{u},x}^\intercal \mathbf{N_p} \mathrm{d}V_e, \tag{6.10}$$

and

$$\mathbf{G}^y = \sum_{e=1}^{n_e} \int_{V_e} \nabla \mathbf{N}_{\mathbf{u},y}^\intercal \mathbf{N_p} \mathrm{d}V_e. \tag{6.11}$$

Since nodal velocity is presented in both left hand side $\mathbf{K}_g$ and right hand side $\mathbf{U}$ of Eq. (6.4), an iterative method is required to solve this equation.

In this work, a Newton's iterative method is used. Assume in k-th iteration, the residual of Eq. (6.4) is

$$\mathbf{K}_g^k \mathbf{U}^k - \mathbf{F}^k = \mathbf{R}(\mathbf{U}^k) \tag{6.12}$$

which can be rewritten using Taylor expansion:

$$\mathbf{R}(\mathbf{U}^k) + \frac{\partial \mathbf{R}}{\partial \mathbf{U}} \mid_{\mathbf{U}^k} \delta \mathbf{U} + \mathscr{O}(\delta \mathbf{U})^2 = \mathbf{0} \tag{6.13}$$

where

$$\delta \mathbf{U} = \mathbf{U}^{k+1} - \mathbf{U}^k. \tag{6.14}$$

Omitting the terms of order two and higher, the following equation is obtained:

$$\mathbf{U}^{k+1} = \mathbf{U}^k - \mathbf{J}^{-1,k}(\mathbf{U}^k) \mathbf{R}(\mathbf{U}^k) \tag{6.15}$$

where

$$\mathbf{J}^k = \frac{\partial \mathbf{R}^k}{\partial \mathbf{U}^k} \tag{6.16}$$

is the Jacobian matrix (also known as tangent matrix) of k-th iteration, that can be derived analytically for this problem. The detailed procedures of its derivation refers to [171], the result is

$$\mathbf{J}^k = \mathbf{K}^k + \hat{\mathbf{J}}^k \tag{6.17}$$

where $\hat{\mathbf{J}}^k$ assembles $\{\mathbf{N}_{xx}^k, \mathbf{N}_{xy}^k, \mathbf{N}_{yx}^k, \mathbf{N}_{yy}^k\}$ and

$$\begin{aligned}
\mathbf{N}_{xx}{}^k &= \sum_{e=1}^{n_e} \int_{V_e} \nabla \mathbf{N}_{\mathbf{u},x} \mathbf{u}_e^{x,k} \left(\mathbf{N}_{\mathbf{u}}{}^{\intercal} \mathbf{N}_{\mathbf{u}} \right) \mathrm{d}V_e, \\
\mathbf{N}_{xy}{}^k &= \sum_{e=1}^{n_e} \int_{V_e} \nabla \mathbf{N}_{\mathbf{u},y} \mathbf{u}_e^{x,k} \left(\mathbf{N}_{\mathbf{u}}{}^{\intercal} \mathbf{N}_{\mathbf{u}} \right) \mathrm{d}V_e, \\
\mathbf{N}_{yx}{}^k &= \sum_{e=1}^{n_e} \int_{V_e} \nabla \mathbf{N}_{\mathbf{u},x} \mathbf{u}_e^{y,k} \left(\mathbf{N}_{\mathbf{u}}{}^{\intercal} \mathbf{N}_{\mathbf{u}} \right) \mathrm{d}V_e, \\
\mathbf{N}_{yy}{}^k &= \sum_{e=1}^{n_e} \int_{V_e} \nabla \mathbf{N}_{\mathbf{u},y} \mathbf{u}_e^{y,k} \left(\mathbf{N}_{\mathbf{u}}{}^{\intercal} \mathbf{N}_{\mathbf{u}} \right) \mathrm{d}V_e.
\end{aligned} \tag{6.18}$$

Finally, in k th iteration, a SUPG stabilization matrix $\mathbf{S}$ is applied to improve the stability of advection and the algorithm convergence:

$$\mathbf{S}^k = \{\mathbf{S}^{k,x}, \mathbf{S}^{k,y}\} \tag{6.19}$$

where

$$\mathbf{S}^{k,x} = \mathbf{S}^{k,y} = \mathbf{S}_{xx}^k + \mathbf{S}_{xy}^k + \mathbf{S}_{yx}^k + \mathbf{S}_{yy}^k \tag{6.20}$$

and

$$\begin{aligned}
\mathbf{S}_{xx}{}^k &= \sum_{e=1}^{n_e} \int_{V_e} \left(\mathbf{u}_e^{x,k} \mathbf{N}_{\mathbf{u}}{}^{\intercal} \right) \nabla \mathbf{N}_{\mathbf{u},x} \left(\mathbf{u}_e^{x,k} \mathbf{N}_{\mathbf{u}}{}^{\intercal} \right) \nabla \mathbf{N}_{\mathbf{u},x} \mathrm{d}V_e, \\
\mathbf{S}_{yx}{}^k &= \sum_{e=1}^{n_e} \int_{V_e} \left(\mathbf{u}_e^{x,k} \mathbf{N}_{\mathbf{u}}{}^{\intercal} \right) \nabla \mathbf{N}_{\mathbf{u},x} \left(\mathbf{u}_e^{y,k} \mathbf{N}_{\mathbf{u}}{}^{\intercal} \right) \nabla \mathbf{N}_{\mathbf{u},y} \mathrm{d}V_e, \\
\mathbf{S}_{yx}{}^k &= \sum_{e=1}^{n_e} \int_{V_e} \left(\mathbf{u}_e^{y,k} \mathbf{N}_{\mathbf{u}}{}^{\intercal} \right) \nabla \mathbf{N}_{\mathbf{u},y} \left(\mathbf{u}_e^{x,k} \mathbf{N}_{\mathbf{u}}{}^{\intercal} \right) \nabla \mathbf{N}_{\mathbf{u},x} \mathrm{d}V_e, \\
\mathbf{S}_{yy}{}^k &= \sum_{e=1}^{n_e} \int_{V_e} \left(\mathbf{u}_e^{y,k} \mathbf{N}_{\mathbf{u}}{}^{\intercal} \right) \nabla \mathbf{N}_{\mathbf{u},y} \left(\mathbf{u}_e^{y,k} \mathbf{N}_{\mathbf{u}}{}^{\intercal} \right) \nabla \mathbf{N}_{\mathbf{u},y} \mathrm{d}V_e.
\end{aligned} \tag{6.21}$$

As a result, the updated advection matrix for the next iteration is

$$\mathbf{K}_a^{k+1} = \mathbf{K}_a^k + \mathbf{S}^k \tag{6.22}$$

Finally, the updated nonlinear residual is

$$\mathbf{K}_g^{k+1}\mathbf{U}^{k+1} - \mathbf{F}^{k+1} = \mathbf{R}(\mathbf{U}^{k+1}). \tag{6.23}$$

The algorithm is converged if the norm of the nonlinear residual is small enough.

6.2.2 Heat transfer model

On the other hand, a steady state heat transfer equation (convection-diffusion equation) is also required in a coupled thermal-fluid finite element analysis:

$$\mathrm{Re}\,\mathrm{Pr}(\theta)\,[\boldsymbol{u}(\theta)\cdot\boldsymbol{\nabla}]\,T = \boldsymbol{\nabla}^2 T - hT - q. \tag{6.24}$$

where $\boldsymbol{u}(\theta)$ is the fluid velocity derived from the Navier-Stokes finite element analysis. $Pr(\theta)$ is Prandtl number reflecting to fluid fraction:

$$\mathrm{Pr}(\theta) = \mathrm{Pr}_0\left(\theta_{\min} + (1-\theta_{\min})\theta_e^{p_v}\right), \tag{6.25}$$

and Pr_0 is the Prandtl number of the fluid, which represents the relation of momentum and thermal diffusivities:

$$\mathrm{Pr}_0 = \frac{c_p\mu}{\kappa}, \tag{6.26}$$

where c_p is thermal capacity, κ is thermal diffusivity. The term $\mathrm{Re}\,\mathrm{Pr}(\theta)$ is Nusselt number $Nu(\theta)$ providing a measure of convection heat transfer.

$$\mathrm{Nu}(\theta) = \mathrm{Re}\,\mathrm{Pr}(\theta). \tag{6.27}$$

Besides, in Eq. (6.24), h is natural convective coefficient, q is external heat source. With the application of Galerkin method and Green identity, Eq. (6.24) can be discretized to

$$\mathbf{K}_t\mathbf{T} = \mathbf{q}, \tag{6.28}$$

where $\mathbf{q}$ is external heat source, and $\mathbf{T}$ is the vector of nodal temperatures. The matrix $\mathbf{K}_t$ is constructed as

$$\mathbf{K}_t = \mathbf{K}_c + \mathbf{K}_n + \mathbf{K}_v + \mathbf{S}. \tag{6.29}$$

In this equation, the stiffness matrix of thermal conduction is

$$\mathbf{K}_c = \sum_{e=1}^{n_e} \int_{V_e} \nabla \mathbf{N_T}^\intercal \mathbf{I} \nabla \mathbf{N_T} \mathrm{d}V_e, \tag{6.30}$$

where $\mathbf{N_T}$ is the matrix containing shape functions of the elemental temperature, and

$$\mathbf{I} = \begin{bmatrix} 1 & 0 \\ 0 & 1 \end{bmatrix}. \tag{6.31}$$

for a two dimensional element. $\mathbf{K}_n$ is the natural convection matrix, which is constructed as

$$\mathbf{K}_n = \sum_{e=1}^{n_e} \int_{V_e} h \mathbf{N_T}^\intercal \mathbf{N_T} \mathrm{d}V_e. \tag{6.32}$$

$\mathbf{K}_v$ is the convection matrix, which is constructed as:

$$\begin{aligned} \mathbf{K}_v = \sum_{e=1}^{n_e} \int_{V_e} \mathrm{Nu}(\theta) \Bigg(& \underbrace{\mathbf{N_u}^\intercal \mathbf{N_u} \mathbf{u}_e^x \nabla \mathbf{N_T}_{,x}}_{\mathbf{N}_v^x} + \\ & \underbrace{\mathbf{N_u}^\intercal \mathbf{N_u} \mathbf{u}_e^y \nabla \mathbf{N_T}_{,y}}_{\mathbf{N}_v^y} \Bigg) \mathrm{d}V_e. \end{aligned} \tag{6.33}$$

Finally, $\mathbf{S}$ is the stabilization matrix:

$$\mathbf{S} = \mathbf{S}_{xx} + \mathbf{S}_{xy} + \mathbf{S}_{yx} + \mathbf{S}_{yy}. \tag{6.34}$$

Since in Eq. (6.28), the global stiffness matrix $\mathbf{K}_t$ includes velocity field $\mathbf{u}$ derived from fluid model, the resulting temperature field $\mathbf{T}$ is influenced by thermal fluid parameters. In the following numerical example, the influence of three parameters, namely Reynolds number Re, Prandtl number Pr_0 and thermal diffusivity κ are illustrated.

6.3 Numerical implementation of thermal-fluid finite element analysis

Let us consider the rectangular design domain Ω shown in Fig. 6.2 is 60 mm $\times$ 60mm and meshed by 60 $\times$ 60 quadratic velocity/linear pressure Q2Q1 elements. Each element contains eighteen degrees of freedom (dofs) for velocity, four dofs for pressure and nine dofs for temperature.

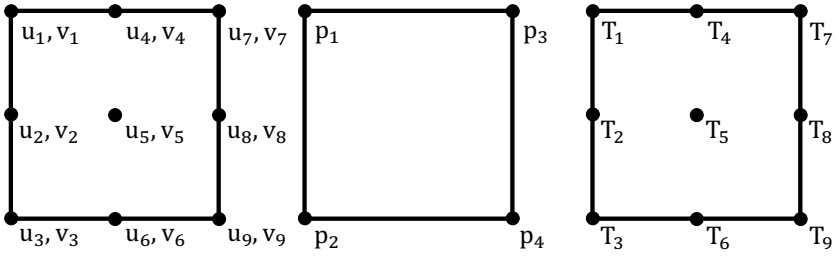

Figure 6.4.. An Illustration of A Quadratic Velocity/Linear Pressure (Q2Q1) Element.

The entire system consists of 3600 elements, 29282 dofs for velocity, 3721 dofs for pressure, and 14641 dofs for temperature. Apply fixed pressure $P_0 = 1Pa$ and fixed temperature $T_0 = 0$ to Γ_{in}, and fixed pressure $P_0 = 0Pa$ to Γ_{out}, zero velocity $u_0 = 0$ to no slip boundary Γ_{wall}, and external heat source $q = 1kW$ uniformly distributed in the design domain Ω.

The results of finite element analysis could be effected by thermal-fluid parameters associated with fluid advection, thermal convection as well as thermal conduction. In this example, the fluid advection is characterized by Reynolds number Re, the thermal convection is determined by Prandtl number Pr_0, and thermal conduction is measured by thermal diffusivity κ. First, the effect of Reynolds numbers Re to the resulting velocity magnitude distribution is depicted in Fig. 6.5. Three cases are compared using Reynolds numbers $\mathrm{Re} = 100$, $\mathrm{Re} = 500$ and $\mathrm{Re} = 1000$, while other parameters of these three cases are the same. It shows, along with a higher Reynolds number, the velocity magnitudes are higher, and the flow driven by inertia force is capable to cover a broader region of design domain. For instance, in Fig. 6.5(a), a U-shape flow path with low velocity magnitude is emerged, in terms of high relative significant viscous resistance. In constrast, in Fig. 6.5(c), high velocity flow is jetted from the inlet, impinged the right top edge because of high advection.

Then, Fig. 6.6 illustrates the common effect of Reynolds number, Prandtl number and thermal diffusivity to the temperature distribution in a fluid design domain. In addition to

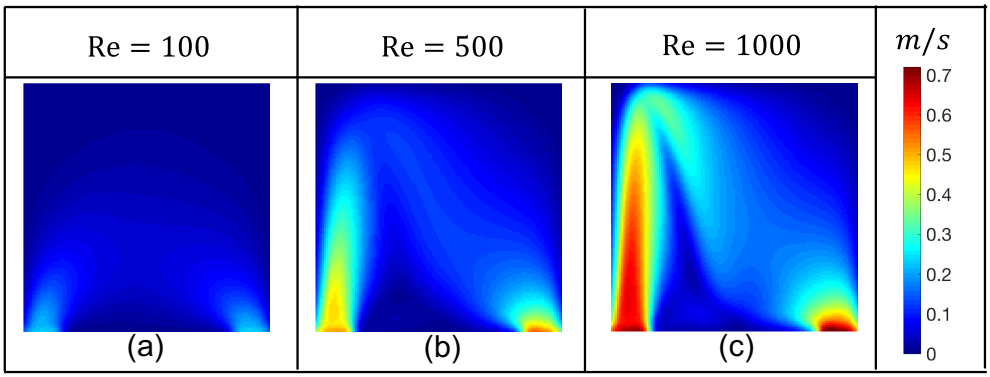

Figure 6.5.. The Velocity Magnitude Plot Associated with Reynolds Number Equal to 100, 500 and 1000 in a Fluid Design Domain.

applying three different Reynolds numbers, three Prandtl numbers Pr_0=7.56 that equal to the value of 16.85°C liquid water, Pr_0=1.53 that equal to the value of 111.85°C liquid water and Pr_0=0.024 that equal to liquid metal are applied to the thermal-fluid model. Besides, two thermal diffusivities κ=3.35 $\times 10^{-6}\ m^2/s$ that equal to the value of stainless steel 310) and κ=1.88 $\times 10^{-5}\ m^2/s$ that equal to the value of steel AISI 1010 are applied. The resulting temperature distribution associated to these parameter combinations are summarized in a 3×3 matrix (Fig. 6.6). The effect of Reynolds numbers can be seen by comparing three columns (C1 to C3). It indicates when Reynolds number changes, the convective heat transfer are improved at locations that velocity magnitude increase, and reduced at where velocity magnitude decrease. The effect of Prandtl numbers is presented by observing the first and second row (R1 and R2). It shows a higher Prandtl number provides better heat transfer performance while thermal diffusivity is unchanged. However, a high Prandtl number does not ensure better heat transfer performance when thermal diffusivities of two cases are different. For example, the comparison of second and third row (R2 and R3) indicates that, a higher thermal diffusivity leads a better heat transfer performance even with a smaller Prandtl number.

In terms of this example, it clearly shows, with a same external heat source, different combinations of thermal-fluid parameters may resulting in versatile results such as velocity

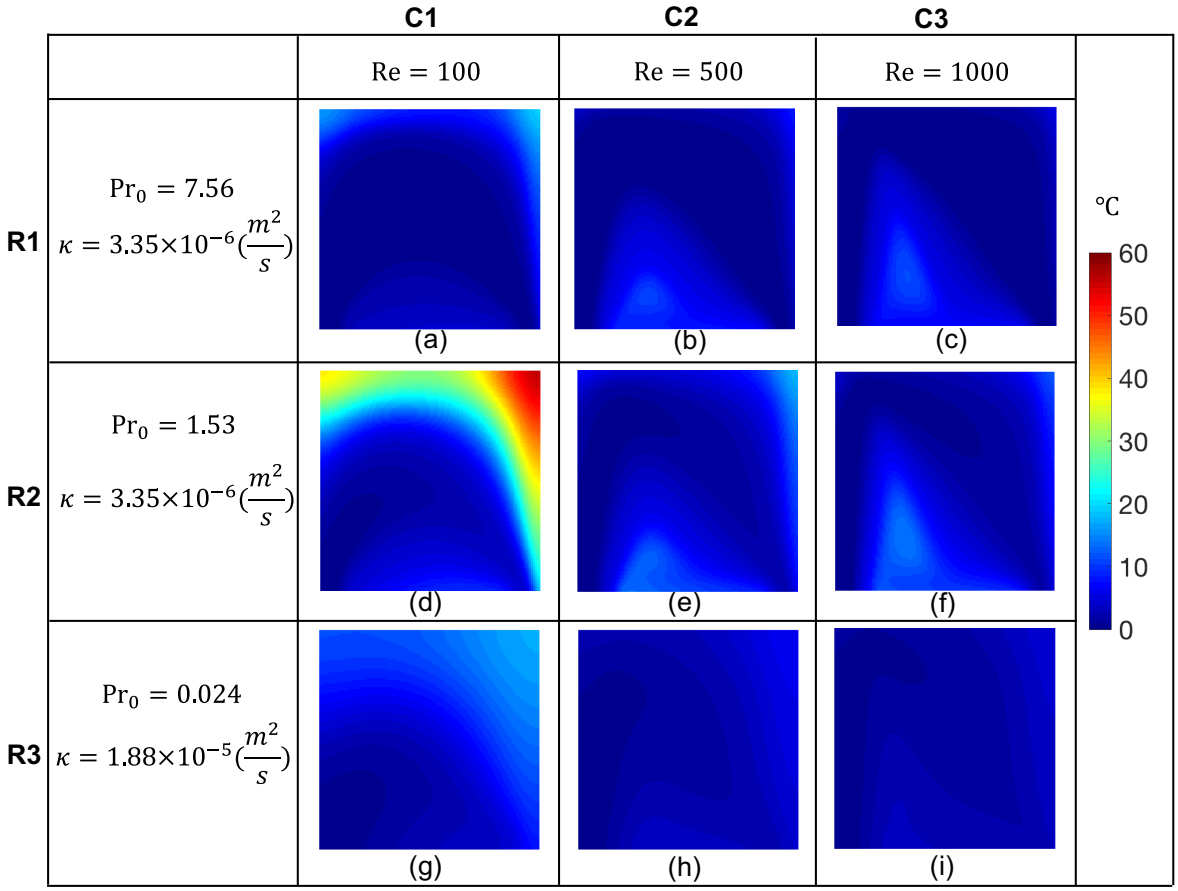

Figure 6.6.. The Temperature Field Plot Associated with Different Combinations of Reynolds Numbers, Prandtl Numbers, and Thermal Diffusivities. In this figure, **C** is the abbreviation of Column, and **R** is the abbreviation of Row.

magnitude and temperature, for this finite element model. This thermal-fluid FEA acts as a substantial role in the following presented topology optimization method, since it is served as sources of objectives as well as constraints, and the FEA module is called in each iteration during the optimization process.

6.4 Proposed thermal-fluid topology optimization method

With incorporation of the finite element analysis, the proposed thermal-fluid topology optimization method aims to optimally distribute limited channels within a design domain, i.e.,

$$\sum_{e=1}^{n_e} v_e \theta_e \leq V_\Omega, \tag{6.35}$$

in order to obtain a structure having minimum energy dissipation caused by fluid drag force and thermal resistance. For a pure Navier-Stokes flow problem, the energy dissipation caused by drag force takes the form

$$Q_1 = \frac{1}{2}\mathbf{u}^\intercal \mathbf{K}_u \mathbf{u} - \mathbf{f}^\intercal \mathbf{u}. \tag{6.36}$$

Therefore, the objective is to find a structure consisting of channel distribution $\boldsymbol{\theta}_1^*$ that minimizes energy dissipation Q_1 under physics constraint Eq. (6.4) and volume constraint Eq. (6.35) :

$$\begin{aligned} \text{find} \quad & \boldsymbol{\theta}_1^* \in \Omega^{n_e} \\ \min \quad & Q_1 = \frac{1}{2}\mathbf{u}^\intercal \mathbf{K}_u \mathbf{u} - \mathbf{f}^\intercal \mathbf{u} \\ \text{s.t.} \quad & \begin{bmatrix} \mathbf{K} & -\mathbf{G}^\intercal \\ -\mathbf{G} & \mathbf{0} \end{bmatrix} \begin{bmatrix} \mathbf{u} \\ \mathbf{p} \end{bmatrix} = \begin{bmatrix} \mathbf{f} \\ \mathbf{0} \end{bmatrix} \\ & \sum_{e=1}^{n_e} v_e \theta_e \leq V_\Omega, \end{aligned} \tag{6.37}$$

For a pure thermal problem, the energy dissipation caused by thermal resistance is defined as thermal compliance:

$$Q_2 = \mathbf{q}^\intercal \mathbf{T}, \tag{6.38}$$

Similarly, the objective of a pure thermal problem is to find a structure consisting of channel distribution $\boldsymbol{\theta}_2^*$ that minimizes thermal compliance Q_2 under physics constraint Eq. (6.28) and volume constraint Eq. (6.35) :

$$\begin{aligned} \text{find} \quad & \boldsymbol{\theta}_2^* \in \Omega^{n_e} \\ \min \quad & Q_2 = \mathbf{T}^\intercal \mathbf{K}_t \mathbf{T} \\ \text{s.t.} \quad & \mathbf{K}_t \mathbf{T} = \mathbf{q} \\ & \sum_{e=1}^{n_e} v_e \theta_e \leq V_\Omega, \end{aligned} \tag{6.39}$$

Compared to a pure thermal problem, in the proposed thermal-fluid topology optimization the fluid and heat transfer physics constraints are required to simultaneously satisfied, and a upper bound of energy dissipation caused by fluid drag force $\bar{Q}_1$ is determined. Finally, the problem statement of thermal-fluid topology optimization is defined as

$$\begin{aligned} \text{find} \quad & \boldsymbol{\theta}_3^{c*} \in \Omega^{n_e} \\ \min \quad & Q_3 = \mathbf{T}^\intercal \mathbf{K}_t \mathbf{T} \\ \text{s.t.} \quad & \begin{bmatrix} \mathbf{K} & -\mathbf{G}^\intercal \\ -\mathbf{G} & \mathbf{0} \end{bmatrix} \begin{bmatrix} \mathbf{u} \\ \mathbf{p} \end{bmatrix} = \begin{bmatrix} \mathbf{f} \\ \mathbf{0} \end{bmatrix} \\ & \mathbf{K}_t(\mathbf{u})\,\mathbf{T} = \mathbf{q} \\ & \sum_{e=1}^{n_e} v_e \theta_e \leq V_\Omega. \end{aligned} \tag{6.40}$$

In this study, a gradient-based sequential convex programming algorithm called Method of Moving Asymptotes (MMA) [36] is used to solve these constrained optimization problems. The analytic gradients of the problems Eq. (6.37) to (6.40) are derived in the following sensitivity analysis procedure.

6.4.1 Sensitivity analysis

In this work, the sensitivities of these three problems are derived using the adjoint method. For a fluid problemThe evaluation of gradients is demonstrated for a generic

objective $Q_1(\boldsymbol{\theta}, \mathbf{u}(\boldsymbol{\theta}))$. Nodal velocity $\mathbf{u}(\boldsymbol{\theta})$ is required to satisfy the constraint governed by finite element analysis equation

$$\mathbf{R}(\boldsymbol{\theta}, \mathbf{u}(\boldsymbol{\theta})) = \mathbf{K}_g \mathbf{U} - \mathbf{F}, \tag{6.41}$$

where $\mathbf{R}$ is the residual. The objective function is augmented in terms of a Lagrange multiplier vector $\boldsymbol{\lambda_f}$ and the Lagrangian function $Ł_1$ is written as

$$Ł_1 = Q_1(\boldsymbol{\theta}, \mathbf{u}(\boldsymbol{\theta})) + \boldsymbol{\lambda_f}^\intercal \mathbf{R}(\boldsymbol{\theta}, \mathbf{u}(\boldsymbol{\theta})) \tag{6.42}$$

The sensitivity of this Lagrangian function is

$$\begin{aligned} \frac{\mathrm{d}Ł_1}{\mathrm{d}\theta_e} &= \frac{\mathrm{d}Q_1}{\mathrm{d}\theta_e} + \boldsymbol{\lambda_f}^\intercal \frac{\mathrm{d}\mathbf{R}}{\mathrm{d}\theta_e} \\ &= \frac{\partial Q_1}{\partial \theta_e} + \frac{\partial Q_1}{\partial \mathbf{U}} \frac{\partial \mathbf{U}}{\partial \theta_e} + \boldsymbol{\lambda_f}^\intercal \left(\frac{\partial \mathbf{R}}{\partial \theta_e} + \frac{\partial \mathbf{R}}{\partial \mathbf{U}} \frac{\partial \mathbf{U}}{\partial \theta_e} \right) \\ &= \frac{\partial Q_1}{\partial \theta_e} + \boldsymbol{\lambda_f}^\intercal \frac{\partial \mathbf{R}}{\partial \theta_e} + \left(\frac{\partial Q_1}{\partial \mathbf{U}} + \boldsymbol{\lambda_f}^\intercal \frac{\partial \mathbf{R}}{\partial \theta_e} \right) \frac{\mathrm{d}\mathbf{U}}{\mathrm{d}\theta_e} \end{aligned} \tag{6.43}$$

To avoid the computation of $\frac{\mathrm{d}\mathbf{U}}{\mathrm{d}\theta_e}$, define

$$\frac{\partial Q_1}{\partial \mathbf{U}} + \boldsymbol{\lambda_f}^\intercal \frac{\partial \mathbf{R}}{\partial \mathbf{U}} = \mathbf{0} \tag{6.44}$$

and $\boldsymbol{\lambda_f}$ can be solved. Hence, the analytical sensitivity of Lagrangian is

$$\frac{\mathrm{d}Ł_1}{\mathrm{d}\theta_e} = \frac{\partial Q_1}{\partial \theta_e} + \frac{\partial \mathbf{R}^\intercal}{\partial \theta_e} \boldsymbol{\lambda_f}. \tag{6.45}$$

To solve Eq. (6.44), let's rewrite global stiffness $\mathbf{K}_g$ as

$$\mathbf{K}_g = \mathbf{K}_u + \mathbf{K}_p, \tag{6.46}$$

where

$$\mathbf{K}_u = \begin{bmatrix} \mathbf{K} & \mathbf{0} \\ \mathbf{0} & \mathbf{0} \end{bmatrix}, \tag{6.47}$$

and

$$\mathbf{K}_p = \begin{bmatrix} \mathbf{0} & -\mathbf{G}^\intercal \\ -\mathbf{G} & \mathbf{0} \end{bmatrix}. \tag{6.48}$$

Using this definition accompanied with global force $\mathbf{F}$ and assembling vector of velocity and pressure $\mathbf{U}$ remarked in Eq. (6.4), the energy dissipation Q_1 can be rewritten as

$$Q_1 = \frac{1}{2}\mathbf{U}^\intercal \mathbf{K}_u \mathbf{U} - \mathbf{F}^\intercal \mathbf{U}, \tag{6.49}$$

and the partial derivative of Q_1 is

$$\frac{\partial Q_1}{\partial \mathbf{U}} = \mathbf{K}_u \mathbf{U} + \frac{1}{2}\mathbf{U}^\intercal \frac{\partial \mathbf{K}_u}{\partial \mathbf{U}}\mathbf{U} - \mathbf{F}^\intercal \tag{6.50}$$

Then, remind $\frac{\partial \mathbf{R}}{\partial \mathbf{U}}$ in (6.43) and (6.44) is Jacobian matrix $\hat{\mathbf{J}}$ from Eq. (6.16) to (6.18). Incorporate Eq. (6.18), the above equation is equivalent to

$$\frac{\partial Q_1}{\partial \mathbf{U}} = \mathbf{K}_u \mathbf{U} + \frac{1}{2}\hat{\mathbf{J}}\mathbf{U} - \mathbf{F}^\intercal. \tag{6.51}$$

Therefore, $\boldsymbol{\lambda_f}$ in Eq. (6.44) is obtained and the sensitivity $\frac{\mathrm{d}Ł_1}{\mathrm{d}\theta_e}$ in Eq. (6.45) is derived. Similarly, the Lagrangian function of the pure thermal problem is

$$Ł_2 = Q_2 + \boldsymbol{\lambda}_t^\intercal \left(\mathbf{K}_t \mathbf{T} - \mathbf{q}\right). \tag{6.52}$$

The sensitivity of this augmented expression is

$$\frac{\mathrm{d}Ł_2}{\mathrm{d}\theta_e} = \mathbf{q}^\intercal \frac{\partial \mathbf{T}}{\partial \theta_e} + \boldsymbol{\lambda}_t^\intercal \left(\frac{\partial \mathbf{K}_t}{\partial \theta_e}\mathbf{T} + \mathbf{K}_t \frac{\partial \mathbf{T}}{\partial \theta_e}\right). \tag{6.53}$$

To remove the field of sensitivity of $\frac{\partial \mathbf{T}}{\partial \theta_e}$, the following expression should be zero:

$$\left(\boldsymbol{\lambda}_t^\intercal \mathbf{K}_t + \mathbf{q}^\intercal\right) \frac{\partial \mathbf{T}}{\partial \theta_e} = \mathbf{0}. \tag{6.54}$$

The adjoint vector $\boldsymbol{\lambda}_t$ can be obtained by solving Eq. (6.54) and it is equal to $-\mathbf{T}$, so that the sensitivity of a fluid problem can be written as

$$\frac{\mathrm{d}Ł_2}{\mathrm{d}\theta_e} = -\mathbf{T}^\intercal \frac{\partial \mathbf{K}_t}{\partial \theta_e}\mathbf{T}. \tag{6.55}$$

In the proposed thermal-fluid coupled topology optimization, to begin with, define the augumented residual $\mathfrak{R}$ including heat transfer is composed of the residual of both fluid and thermal problems:

$$\mathfrak{R} = \{\mathfrak{R}_\mathrm{U}, \mathfrak{R}_\mathrm{T}\}. \tag{6.56}$$

Without consideration of buoyancy term, $\mathfrak{R}_{\mathrm{U}}$ is equal to $\mathbf{R}$, and $\mathfrak{R}_{\mathrm{T}}$ is equal to $(\mathbf{K}_t\mathbf{T}-\mathbf{q})$. The Lagrangian function of the coupled thermal-fluid problem becomes

$$Ł_{\mathbf{3}} = Q_3 + \boldsymbol{\lambda}_{tf}{}^{\mathsf{T}}\mathfrak{R}\left(\boldsymbol{\theta}, \mathbf{u}\left(\boldsymbol{\theta}\right), \mathbf{T}\left(\boldsymbol{\theta}\right)\right). \tag{6.57}$$

The sensitivity of this Lagrangian function is

$$\frac{\mathrm{d}Ł_3}{\mathrm{d}\theta_e} = \frac{\mathrm{d}Q_3}{\mathrm{d}\theta_e} + \boldsymbol{\lambda}_{tf}{}^{\mathsf{T}}\frac{\mathrm{d}\mathfrak{R}}{\mathrm{d}\theta_e}, \tag{6.58}$$

where the differetiation of the objective function is

$$\frac{\mathrm{d}Q_3}{\mathrm{d}\theta_e} = \frac{\partial Q_3}{\partial \theta_e} + \begin{bmatrix} \frac{\partial Q_3}{\partial \mathbf{U}} & \frac{\partial Q_3}{\partial \mathbf{T}} \end{bmatrix} \begin{bmatrix} \frac{\partial \mathbf{U}}{\partial \theta_e} \\ \\ \frac{\partial \mathbf{T}}{\partial \theta_e} \end{bmatrix}, \tag{6.59}$$

and the differentiation of coupled residual is

$$\frac{\mathrm{d}\mathfrak{R}}{\mathrm{d}\theta_e} = \begin{bmatrix} \frac{\partial \mathfrak{R}_{\mathrm{U}}}{\partial \mathbf{U}} & \frac{\partial \mathfrak{R}_{\mathrm{U}}}{\partial \mathbf{T}} \\ \\ \frac{\partial \mathfrak{R}_{\mathrm{T}}}{\partial \mathbf{U}} & \frac{\partial \mathfrak{R}_{\mathrm{T}}}{\partial \mathbf{T}} \end{bmatrix} \begin{bmatrix} \frac{\partial \mathbf{U}}{\partial \theta_e} \\ \\ \frac{\partial \mathbf{T}}{\partial \theta_e} \end{bmatrix}. \tag{6.60}$$

The adjoint vector $\boldsymbol{\lambda}_{tf}$ can be written as

$$\boldsymbol{\lambda}_{tf} = \begin{bmatrix} \boldsymbol{\lambda}_{tf}^{\mathbf{U}} \\ \\ \boldsymbol{\lambda}_{tf}^{\mathbf{T}} \end{bmatrix}. \tag{6.61}$$

To cancel the adjoint vectors, solving following equations:

$$\begin{aligned} \frac{\partial \mathfrak{R}_{\mathrm{U}}}{\partial \mathbf{U}}\boldsymbol{\lambda}_{tf}^{\mathbf{U}} + \frac{\partial Q_3}{\partial \mathbf{U}} &= \mathbf{0} \\ \frac{\partial \mathfrak{R}_{\mathrm{T}}}{\partial \mathbf{U}}\boldsymbol{\lambda}_{tf}^{\mathbf{U}} + \frac{\partial \mathfrak{R}_{\mathrm{T}}}{\partial \mathbf{T}}\boldsymbol{\lambda}_{tf}^{\mathbf{T}} + \frac{\partial Q_3}{\partial \mathbf{T}} &= \mathbf{0} \end{aligned} \tag{6.62}$$

can yield the value of adjoint vector $\boldsymbol{\lambda}_{tf}$ and the sensitivity of coupling thermal-fluid field.

6.5 Versatile topologies resulted from thermal-fluid parameters

Let us apply proposed topology optimization algorithm to find the optimal channel distributions of the presented in Sec. 6.3. A same 3×3 matrix having thermal-fluid

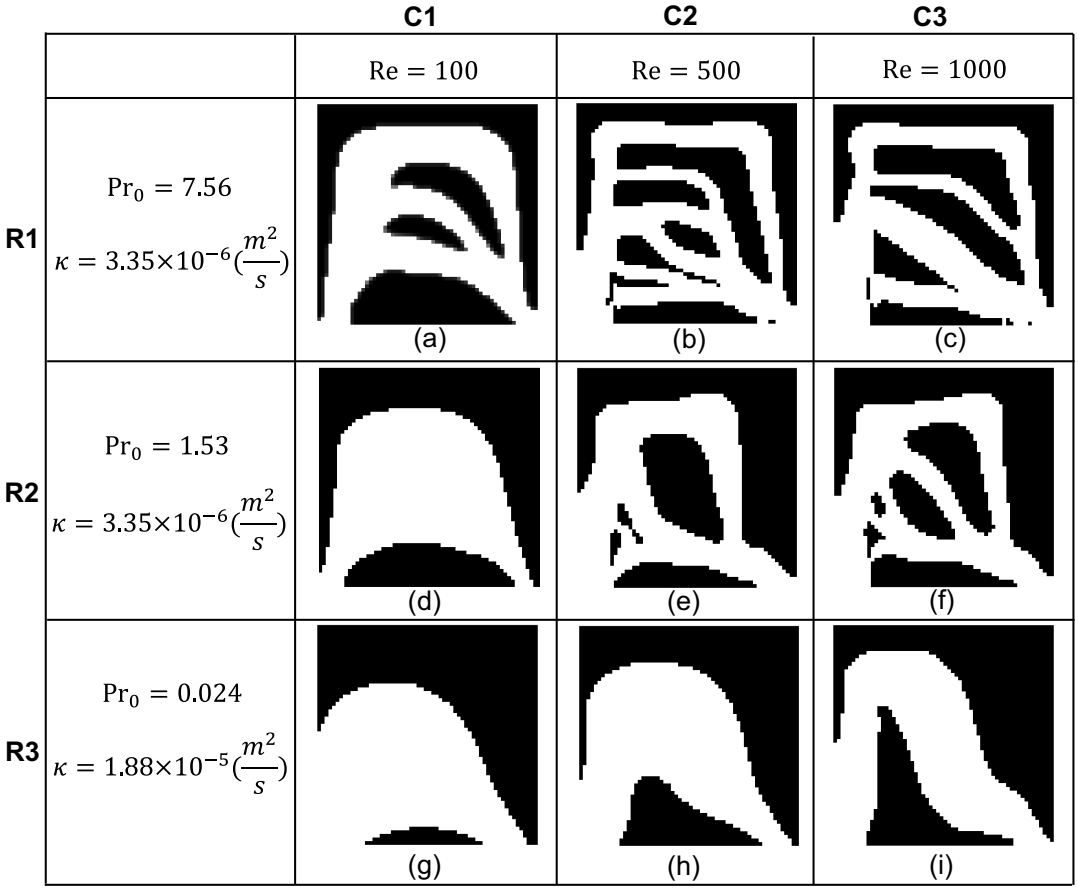

Figure 6.7.. Resulting Topologies Under Specific Combinations of Reynolds Number, Prandtl Number and Thermal Diffusivity. In this figure, **C** is the abbreviation of Column, and **R** is the abbreviation of Row.

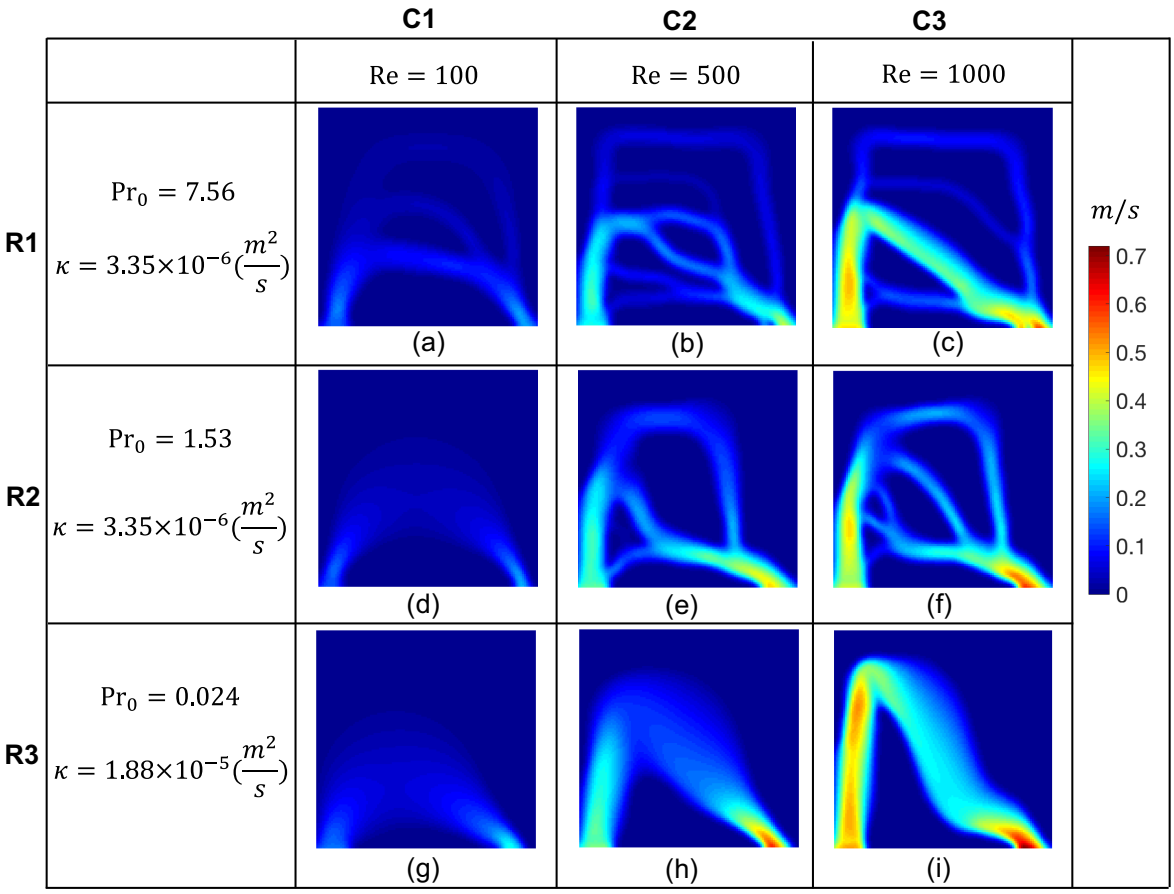

Figure 6.8.. Resulting Velocity Magnitude Plots Under Specific Combinations of Reynolds Number, Prandtl Number and Thermal Diffusivity.

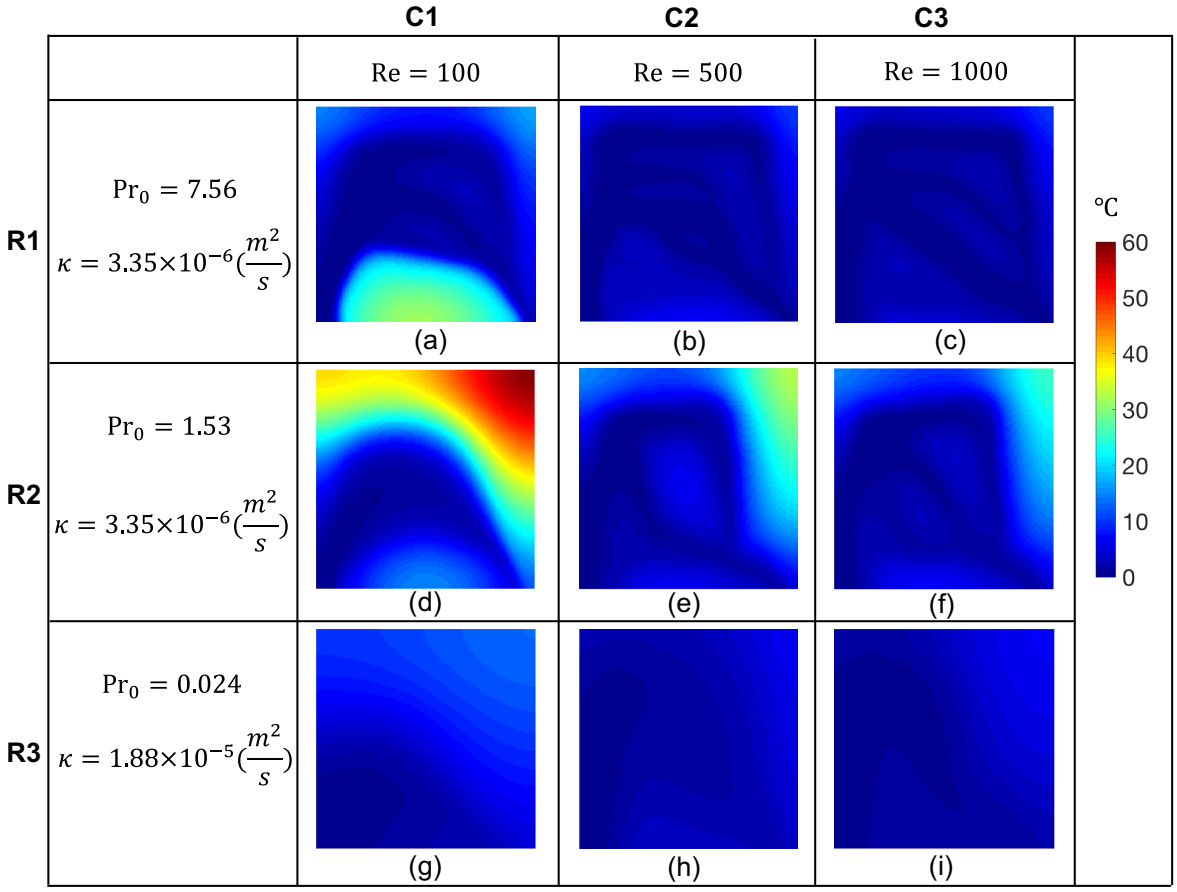

Figure 6.9.. Resulting Temperature Field Plots Under Specific Combinations of Reynolds number, Prandtl Number and Thermal Diffusivity.

parameter combination of Reynolds number Re, Prandtl number Pr_0 and thermal diffusivity κ same as Section 3 is used to analyze the resulting topologies (Fig. 6.6). Notably, in the algorithm, the constant b reflecting Brinkman resistance level in Eq. (6.8) is defined to be linked with Prandtl number Pr_0 as

$$b = 0.001 \times \mathrm{Pr}_0. \tag{6.63}$$

This assumption aims to modeling the fact that high porosity simultaneously leads more contact surface areas and flow resistance, the parameter 0.001 is adopted based on author's experience. Other comparable parameters associated with these implementations are same. In each implementation, the outer loop of MMA solver contains 200 iterations, and in each outer iteration, the inner loop of Newton solver contains 20 iterations.

The resulting topology in Fig. 6.7 shows versatile shapes under the specific combinations of thermal-fluid parameters (Reynolds numbers, Prandtl numbers and Thermal diffusivity). with the sensitivity analysis of coupling thermal-fluid fields, In all of these results, most of channels can passing flow from inlet to outlet without be intersected by solid phase. The influence of Reynolds number is analyzed by observation of three columns (C1 to C3) in Fig. 6.7, it shows, with increasing of Reynolds number, the effort of reducing energy dissipation of fluid becomes more critical to affect the final topologies. This can be verified by examing Fig. 6.8, which shows the average velocity magintude would be significantly increased with higher Reynolds number. This fact implies that, compared to thermal dissipation, a larger part of fluid energy dissipation would be required to mitigate. As a result, in first and second rows (R1 and R2), the diameter of the longest channel would be narrowed with a higher Reynolds number, which preserves sufficient velocity for offering efficient convective heat transfer capability to reduce the temperature (Fig. 6.9). To achieve this, in the third row (R3), the only channel covers broader region accompanying with the Reynolds number rising, and the diameter becomes narrow in averge. The influence of Prandtl number is investigated by comparing the first and second row (R1 and R2) in Fig. 6.7. It can be discovered that, the higher Prandtl number yields channel distributions having more geometric complexity and covering broader region of design domain. Not surprisingly, the topologies resulted from higher Prandtl number in R1 are cooled down better than their

counterparts in R2 (Fig. 6.9). Finally, to investigate the differences of channel distribution resulted from a thermal convection governed design domain in contrast to a conduction dominated design domain, the second and third rows (R2 and R3) in Fig. 6.7 are compared. The result clearly shows a convection governed design domain leads a channel distribution with higher geometric complexity compared to a conduction dominated design domain. In addition, it can be found that a higher convection may not guarantee a better thermal performance when conduction is low (Fig. 6.9).

6.6 Application in an injection mold

In this section, the proposed method is applied to design an optimal conformal cooling system of a core insert, which is used for manufacturing containers utilized in automated pharmacy compounding system (Fig. 6.10). Our task is to replace the baffle array cooling to optimal conformal cooling. The cylinder close to the injected part is determined as the morphological surface, half of the this cylinder is flattened and considered as the design domain (length: 80 mm, width: 60 mm). Both the inlet and outlet have a diameter of 4 cm.

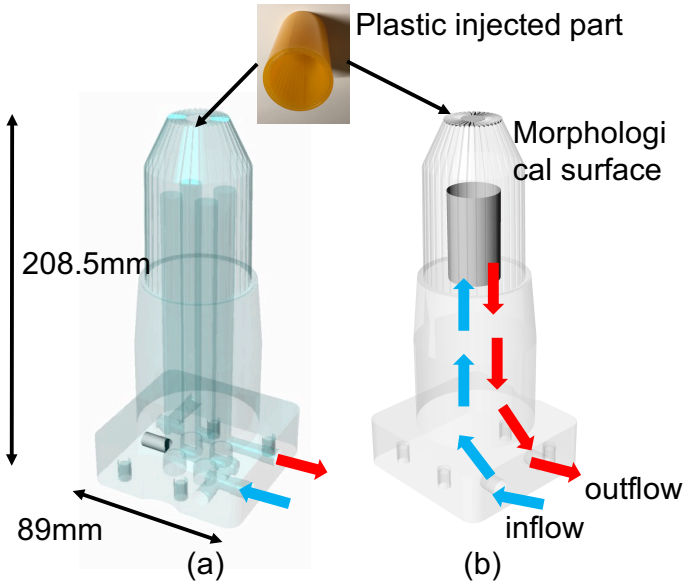

Figure 6.10.. Original Design of the Injection Mold and Design Domain Selection.

This specific design requires an interchangeable inlet and outlet, to attain this, a symmetric design is considered. First, the problem statement $\mathbf{P}_1$ is defined as Eq. (6.40) with aforementioned boundary condition. For the thermal-fluid parameters, Reynolds number Re=500, Prandtl number for 16°C water Pr_0=7.56, and thermal diffusivity for stainless steel 310, κ=3.35$\times m^2/s$ is applied. Then, an additional problem statement $\mathbf{P}_2$ is defined, in which the outlet and inlet is reversed (Fig.6.11). The final symmetric FEA problem $\mathbf{P}_{sym}$ is defined as

$$\mathbf{P}_{sym} = \frac{\mathbf{P}_1 + \mathbf{P}_2}{2}. \tag{6.64}$$

This modification of problem statement leads a symmetric design $\boldsymbol{\theta}_4^{c*}$ (Fig.6.12)

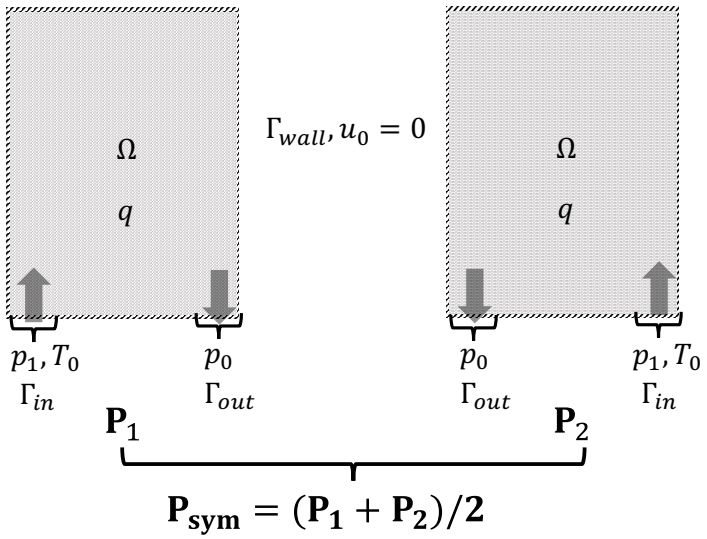

Figure 6.11.. The Statement of A Symmetric Design.

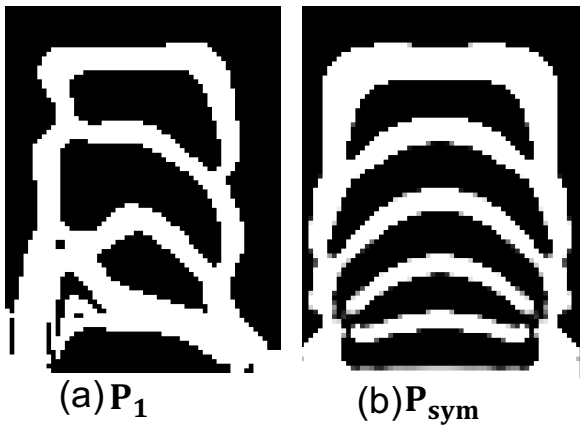

Figure 6.12.. Modification from (a) An Asymmetric Design to (b) A Symmetric Design.

Further, in practical operation of the cooling system, it is necessary to guarantee the channel network is flow balanced, which enable sufficient flow rate through each channel even in the worst case. To accomplish a flow balanced system, an additional optimization problem is formulated. For the derived symmetric design, a section Γ_i containing number

n of flow channels is selected. Same velocities $\bar{u}_1^i = \cdots \bar{u}_n^i$ are distributed on each of the pipe sections $\mathbf{d}_1^i = \cdots \mathbf{d}_n^i$. With this specific boundary condition, a topology optimization aiming to minimize energy dissipation of fluid is stated:

$$
\begin{aligned}
\text{given} \quad & \boldsymbol{\theta}_4^{c*} \in \Omega^{n_e} \\
& \boldsymbol{u}_1^i = \boldsymbol{u}_2^i = \cdots \boldsymbol{u}_n^i \\
& \in \{\boldsymbol{d}_1^i = \boldsymbol{d}_2^i = \cdots \boldsymbol{d}_n^i\} \in \Gamma^i \\
\min \quad & Q_1^c = \frac{1}{2}\mathbf{u}^\intercal \mathbf{K}_u \mathbf{u} - \mathbf{f}^\intercal \mathbf{u} \\
\text{find} \quad & \boldsymbol{\theta}_5^{c*} \in \mathbb{R}^{n_e} \\
\text{s.t.} \quad & \begin{bmatrix} \mathbf{K} & -\mathbf{G}^\intercal \\ -\mathbf{G} & \mathbf{0} \end{bmatrix} \begin{bmatrix} \mathbf{u} \\ \mathbf{p} \end{bmatrix} = \begin{bmatrix} \mathbf{f} \\ \mathbf{0} \end{bmatrix} \\
& \mathbf{K}_t(\mathbf{u})\,\mathbf{T} = \mathbf{q} \\
& \sum_{e=1}^{n_e} v_e \theta_e \leq V_\Omega,
\end{aligned}
\tag{6.65}
$$

and the resulting topology $\boldsymbol{\theta}_5^{c*}$ is shown in Fig. 6.13.

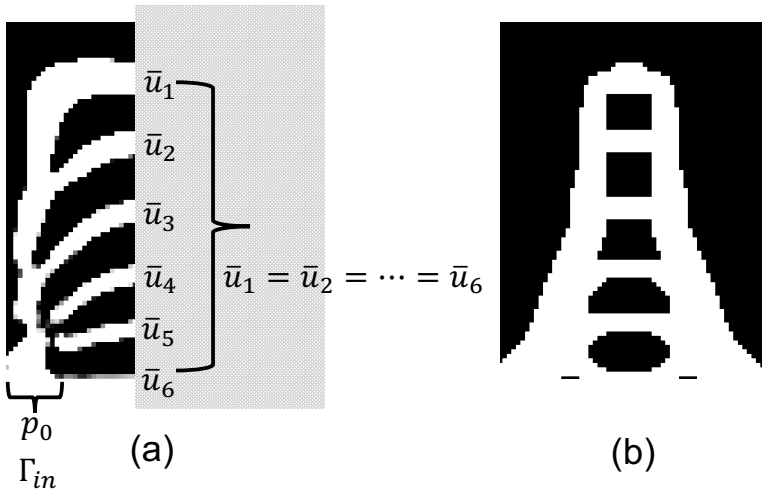

Figure 6.13.. Modification from (a) Symmetric Design to (b) A Flow-balanced Design.

The next effort is to convert a Bitmap format file to a CAD format file. In order to finish this, several procedures are implemented in Grasshopper®, a graphical algorithm editor tightly integrated with Rhinoceros® 3D modeling software. First, the interface between solid and fluid phases is captured by using *Image sampler* component, and the central lines of the pipes are found. Based on these central lines, *Pipe variable* component is used to create pipe geometries that fitted the interface (Fig. 6.14 (a)). Then, a *Surface Morph* component is used to make the geometries conform to the morphological surface (Fig. 6.14 (b)). The resulting geometries are in *.stp* format and can be volumetric meshed and validated through three dimensional thermal-fluid simulation. The simulation in COMSOL Multiphysics® shows sufficient flow rates is guaranteed for entire channels with uniform fluid temperature under worst case (Fig. 6.15).

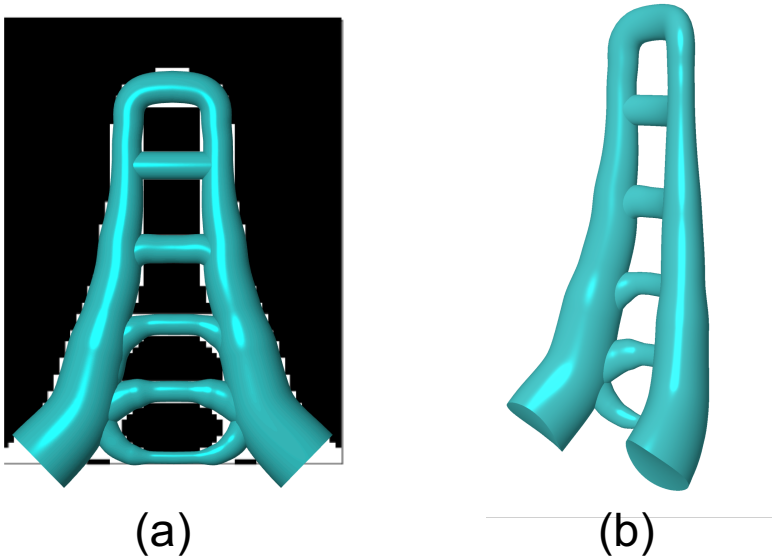

Figure 6.14.. Conversion from A Bitmap Format File to A CAD Format File.

The final conformal cooling design contains a pair of optimal channels, which are smoothly merged and in connection with inflow and outflow. The final modification is finished in Rhinoceros®. The design is successfully produced using Direct Metal Laser

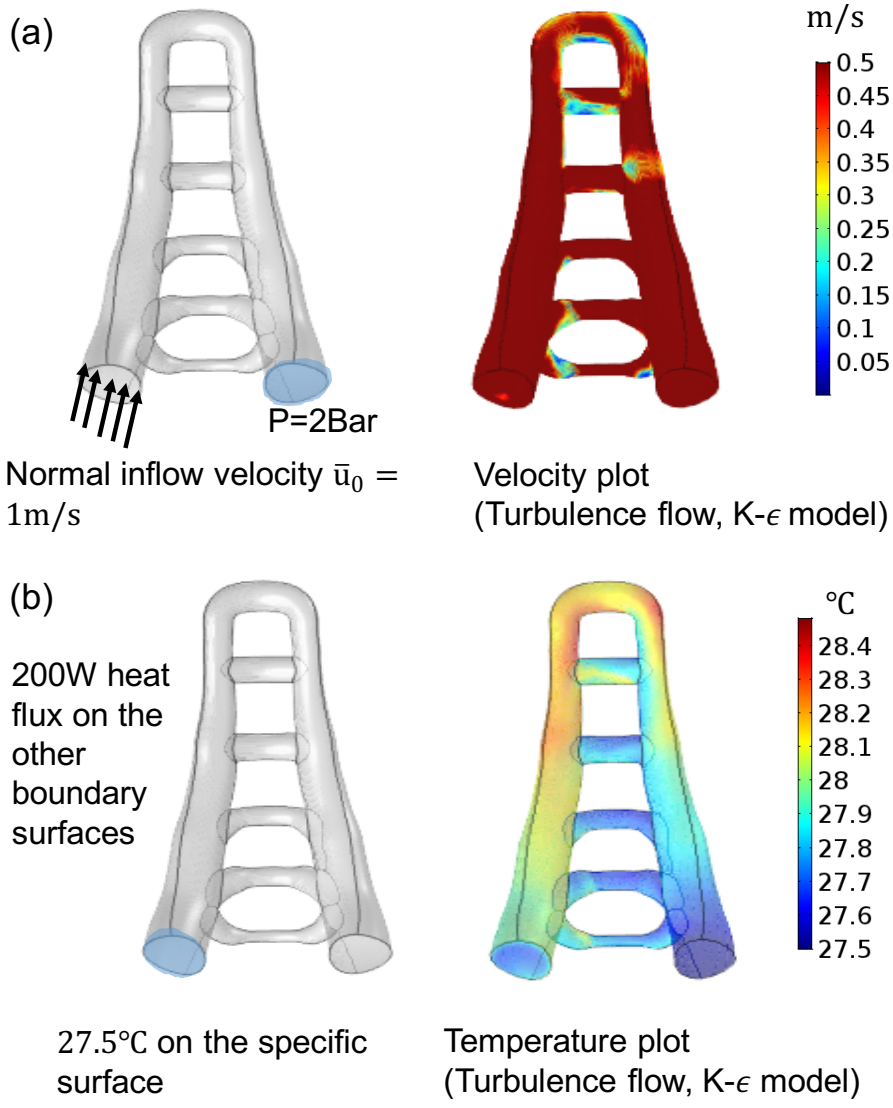

Figure 6.15.. Verification of Final Design by Three Dimensional Thermal-fluid Coupled Simulation for Cooling System under $k-\varepsilon$ Turbulence Model.

Sintering additive manufacturing technology (Fig. 6.16), and experimental study is under preparation.

6.7 Conclusion

In this Chapter, an innovative thermal-fluid topology optimization method is proposed. The method incorporates an in-house finite element code that coupling non-linear Navier-Stokes flow and heat transfer. It allows thermal-fluid parameters associated to fluid advection, as well as thermal convection and conduction shifting in a wide range. An external heat source term is included in the algorithm. Versatile channel distributions are derived from gradient-based optimizer under different combinations of the thermal-fluid parameters. Further, a symmetric and flow-balanced design is finished for optimal designing the conformal cooling of an injection mold.

We remark that some assumptions are made in this article to simplify the problem. First, in finite element analysis the temperature field induced buoyancy force field is not incorporated in Navier-Stokes equation. A fully coupled finite element model and sensitivity analysis including buoyancy driven force is expected be included in the future work. Second, the topology optimization considering transient thermal-fluid analysis will be investigated. Finally, thermal-fluid topology optimization with turbulence flow is anticipated to be involved in our future work.

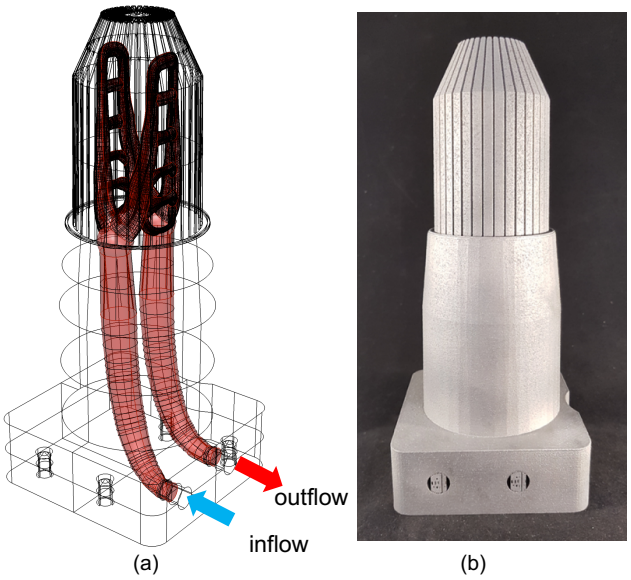

Figure 6.16.. Final Design of Injection Mold with Conformal Cooling and the Product obtained from Additive Manufacturing.

7. SUMMARY

In this dissertation, several innovative methods associated to multiscale topology optimization, thermomechanical topology optimization, and thermal fluid topology optimization are proposed. These methods are presented in Chapter Two to Six. From Chapter Two to Four, the methods with respect to multiscale approach are presented, and Chapter Five and Six aims to contribute further research associated with topology optimization considering heat convection.

Chapter Two and Three aims to apply two different multiscale topology optimization frameworks to design optimised lattice thermomechanical structures. In Section Two, a multiphase approach is applied, where homogenized properties of prescribed lattice unit cells are incorporated as polynomial fitting functions of tensor properties, in order to conduct the macroscale structural optimization. Using a clustering approach, the final structure is composed of several phases of prescribed lattice unit cells. In Chapter Three, A hierarchical approach is proposed, which is amiable to additive manufacturing by consisting of self-supporting lattice/porous structures. A scaled down physical prototype of the mold was fabricated using DMLS procedure without internal support structure to demonstrate the manufacturability of the optimal design. In Chapter Four, the concept of multiscale approach is extended as a new idea to design micropillar arrays in microfluidic devices, using non-linear Navier-Stokes flow model. A novel approach of inverse homogenization for fluid flow is proposed. In contrast to common utilized micropillar arrays, the optimal micropillar arrays leading a design with lower flow separation, lower energy loss and higher average velocity magnitude, in terms of specific geometric and physics boundary conditions.

In Chapter Five, a new thermomechanical topology optimization method with consideration of convective heat transfer is presented. The method involves with heat convection without fluid mechanics model. It utilizes design-dependent heat source to determine

whether the local element is fluid or solid phase. The model is computationally efficient and suitable for the conceptual design strategy. The final design shows complex lattice structures that can augment current additive manufacturing technologies. In Chapter Six, an improved thermal-fluid topology optimization method is developed. The methods allows flexible change of thermal-fluid parameters associated to heat source, fluid advection, as well as thermal convection and conduction, with generation of versatile channel distributions. A symmetric and flow-balanced design is finished for optimal designing the conformal cooling of an injection mold.

REFERENCES

[1] Peter W Christensen and Anders Klarbring. *An introduction to structural optimization*, volume 153. Springer Science & Business Media, 2008.

[2] Martin P Bendsøe. Topology optimization. In *Encyclopedia of Optimization*, pages 2636–2638. Springer, 2001.

[3] Martin Philip Bendsøe and Noboru Kikuchi. Generating optimal topologies in structural design using a homogenization method. *Computer methods in applied mechanics and engineering*, 71(2):197–224, 1988.

[4] Jose Miranda Guedes and Noboru Kikuchi. Preprocessing and postprocessing for materials based on the homogenization method with adaptive finite element methods. *Computer Methods in Applied Mechanics and Engineering*, 83(2):143 – 198, 1990.

[5] M Zhou and GIN Rozvany. The coc algorithm, part ii: topological, geometrical and generalized shape optimization. *Computer Methods in Applied Mechanics and Engineering*, 89(1-3):309–336, 1991.

[6] George IN Rozvany, Ming Zhou, and Torben Birker. Generalized shape optimization without homogenization. *Structural optimization*, 4(3-4):250–252, 1992.

[7] Mathias Stolpe and Krister Svanberg. An alternative interpolation scheme for minimum compliance topology optimization. *Structural and Multidisciplinary Optimization*, 22(2):116–124, 2001.

[8] O. Sigmund and S. Torquato. Composites with extremal thermal expansion coefficients. *Applied Physics Letters*, 69(21):3203 – 3203, 1996.

[9] Ole Sigmund and Salvatore Torquato. Design of materials with extreme thermal expansion using a three-phase topology optimization method. *Journal of the Mechanics and Physics of Solids*, 45(6):1037–1067, 1997.

[10] Tong Gao, Pengli Xu, and Weihong Zhang. Topology optimization of thermo-elastic structures with multiple materials under mass constraint. *Computers & Structures*, 173:150–160, 2016.

[11] Tong Gao and Weihong Zhang. A mass constraint formulation for structural topology optimization with multiphase materials. *International Journal for Numerical Methods in Engineering*, 88(8):774–796, 2011.

[12] Rouhollah Tavakoli and Seyyed Mohammad Mohseni. Alternating active-phase algorithm for multimaterial topology optimization problems: a 115-line matlab implementation. *Structural and Multidisciplinary Optimization*, 49(4):621–642, 2014.

[13] Kai Liu, Duane Detwiler, and Andres Tovar. Cluster-based optimization of cellular materials and structures for crashworthiness. *Journal of Mechanical Design*, 140(11):111412, 2018.

[14] Allan Gersborg-Hansen, Martin P Bendsøe, and Ole Sigmund. Topology optimization of heat conduction problems using the finite volume method. *Structural and multidisciplinary optimization*, 31(4):251–259, 2006.

[15] Anders Klarbring and Niclas Strömberg. Topology optimization of hyperelastic bodies including non-zero prescribed displacements. *Structural and Multidisciplinary Optimization*, 47(1):37–48, 2013.

[16] Fengwen Wang, Boyan Stefanov Lazarov, Ole Sigmund, and Jakob Søndergaard Jensen. Interpolation scheme for fictitious domain techniques and topology optimization of finite strain elastic problems. *Computer Methods in Applied Mechanics and Engineering*, 276:453–472, 2014.

[17] Yangjun Luo, Michael Yu Wang, and Zhan Kang. Topology optimization of geometrically nonlinear structures based on an additive hyperelasticity technique. *Computer methods in applied mechanics and engineering*, 286:422–441, 2015.

[18] Yangjun Luo and Zhan Kang. Topology optimization of continuum structures with drucker–prager yield stress constraints. *Computers & Structures*, 90:65–75, 2012.

[19] Yangjun Luo and Zhan Kang. Layout design of reinforced concrete structures using two-material topology optimization with drucker–prager yield constraints. *Structural and Multidisciplinary Optimization*, 47(1):95–110, 2013.

[20] Oded Amir. Stress-constrained continuum topology optimization: a new approach based on elasto-plasticity. *Structural and Multidisciplinary Optimization*, 55(5):1797–1818, 2017.

[21] Jimmy Forsberg and Larsgunnar Nilsson. Topology optimization in crashworthiness design. *Structural and Multidisciplinary Optimization*, 33(1):1–12, 2007.

[22] Neal M Patel, Byung-Soo Kang, John E Renaud, and Andrés Tovar. Crashworthiness design using topology optimization. *Journal of Mechanical Design*, 131(6):061013, 2009.

[23] Kai Liu, Duane Detwiler, and Andres Tovar. Optimal design of nonlinear multimaterial structures for crashworthiness using cluster analysis. *Journal of Mechanical Design*, 139(10):101401, 2017.

[24] Ercan M Dede. Optimization and design of a multipass branching microchannel heat sink for electronics cooling. *Journal of Electronic Packaging*, 134(4):041001, 2012.

[25] O. Sigmund. Design of multiphysics actuators using topology optimization. i. one-material structures. *Computer Methods in Applied Mechanics and Engineering*, 190(49-50):6577 – 604, 2001/10/12.

[26] O. Sigmund. Design of multiphysics actuators using topology optimization. ii. two-material structures. *Computer Methods in Applied Mechanics and Engineering*, 190(49-50):6605 – 27, 2001/10/12.

[27] Grégoire Allaire, François Jouve, and Anca-Maria Toader. A level-set method for shape optimization. *Comptes Rendus Mathematique*, 334(12):1125–1130, 2002.

[28] Grégoire Allaire, François Jouve, and Anca-Maria Toader. Structural optimization using sensitivity analysis and a level-set method. *Journal of computational physics*, 194(1):363–393, 2004.

[29] Grégoire Allaire, Frédéric De Gournay, François Jouve, and A-M Toader. Structural optimization using topological and shape sensitivity via a level set method. *Control and cybernetics*, 34(1):59, 2005.

[30] ChunGang Zhuang, ZhenHua Xiong, and Han Ding. A level set method for topology optimization of heat conduction problem under multiple load cases. *Computer methods in applied mechanics and engineering*, 196(4-6):1074–1084, 2007.

[31] Kentaro Yaji, Takayuki Yamada, Seiji Kubo, Kazuhiro Izui, and Shinji Nishiwaki. A topology optimization method for a coupled thermal–fluid problem using level set boundary expressions. *International Journal of Heat and Mass Transfer*, 81:878–888, 2015.

[32] Yuki Sato, Kentaro Yaji, Kazuhiro Izui, Takayuki Yamada, and Shinji Nishiwaki. An optimum design method for a thermal-fluid device incorporating multiobjective topology optimization with an adaptive weighting scheme. *Journal of Mechanical Design*, 2017.

[33] RJ Yang and CH Chuang. Optimal topology design using linear programming. *Computers & structures*, 52(2):265–275, 1994.

[34] Claude Fleury. Conlin: an efficient dual optimizer based on convex approximation concepts. *Structural optimization*, 1(2):81–89, 1989.

[35] RN Kaul and Surjeet Kaur. Optimality criteria in nonlinear programming involving nonconvex functions. *Journal of Mathematical Analysis and Applications*, 105(1):104–112, 1985.

[36] Krister Svanberg. The method of moving asymptotes-a new method for structural optimzation. *International Journal for Numerical Methods in Engineering*, 24:359–373, 1987.

[37] Krister Svanberg. Mma and gcmma-two methods for nonlinear optimization. Technical report, Technical report, 2007.

[38] Andrés Tovar, Neal M Patel, Glen L Niebur, Mihir Sen, and John E Renaud. Topology optimization using a hybrid cellular automaton method with local control rules. *Journal of Mechanical Design*, 128(6):1205–1216, 2006.

[39] XY Yang, YM Xei, GP Steven, and OM Querin. Bidirectional evolutionary method for stiffness optimization. *AIAA journal*, 37(11):1483–1488, 1999.

[40] X Huang and YM Xie. Bi-directional evolutionary topology optimization of continuum structures with one or multiple materials. *Computational Mechanics*, 43(3):393, 2009.

[41] Martin Leary, Mohammad Babaee, Milan Brandt, and Aleksandar Subic. Feasible build orientations for self-supporting fused deposition manufacture: a novel approach to space-filling tesselated geometries. In *Advanced Materials Research*, volume 633, pages 148–168. Trans Tech Publ, 2013.

[42] Tomás Zegard and Glaucio H Paulino. Bridging topology optimization and additive manufacturing. *Structural and Multidisciplinary Optimization*, 53(1):175–192, 2016.

[43] Martin Leary, Luigi Merli, Federico Torti, Maciej Mazur, and Milan Brandt. Optimal topology for additive manufacture: a method for enabling additive manufacture of support-free optimal structures. *Materials & Design*, 63:678–690, 2014.

[44] Quhao Li, Wenjiong Chen, Shutian Liu, and Liyong Tong. Structural topology optimization considering connectivity constraint. *Structural and Multidisciplinary Optimization*, 54(4):971–984, 2016.

[45] Shanglong Zhang, Julián A Norato, Arun L Gain, and Naesung Lyu. A geometry projection method for the topology optimization of plate structures. *Structural and Multidisciplinary Optimization*, 54(5):1173–1190, 2016.

[46] Weisheng Zhang, Jie Yuan, Jian Zhang, and Xu Guo. A new topology optimization approach based on moving morphable components (mmc) and the ersatz material model. *Structural and Multidisciplinary Optimization*, 53(6):1243–1260, 2016.

[47] Xu Guo, Jianhua Zhou, Weisheng Zhang, Zongliang Du, Chang Liu, and Ying Liu. Self-supporting structure design in additive manufacturing through explicit topology optimization. *Computer Methods in Applied Mechanics and Engineering*, 323:27–63, 2017.

[48] Ahmed Hussein, Liang Hao, Chunze Yan, Richard Everson, and Philippe Young. Advanced lattice support structures for metal additive manufacturing. *Journal of Materials Processing Technology*, 213(7):1019–1026, 2013.

[49] Xiaojian Wang, Shanqing Xu, Shiwei Zhou, Wei Xu, Martin Leary, Peter Choong, M Qian, Milan Brandt, and Yi Min Xie. Topological design and additive manufacturing of porous metals for bone scaffolds and orthopaedic implants: a review. *Biomaterials*, 83:127–141, 2016.

[50] Jun Wu, Niels Aage, Rüdiger Westermann, and Ole Sigmund. Infill optimization for additive manufacturing—approaching bone-like porous structures. *IEEE transactions on visualization and computer graphics*, 24(2):1127–1140, 2018.

[51] Martin P Bendsøe, JM Guedes, Robert B Haber, P Pedersen, and JE Taylor. An analytical model to predict optimal material properties in the context of optimal structural design. *Journal of Applied Mechanics*, 61(4):930–937, 1994.

[52] O. Sigmund. Tailoring materials for specific needs. *Journal of Intelligent Material Systems and Structures*, 5(6):736 – 742, 1994.

[53] Martin P Bendsøe and Ole Sigmund. Material interpolation schemes in topology optimization. *Archive of applied mechanics*, 69(9-10):635–654, 1999.

[54] Ole Sigmund. A new class of extremal composites. *Journal of the Mechanics and Physics of Solids*, 48(2):397–428, 2000.

[55] X Huang, A Radman, and YM Xie. Topological design of microstructures of cellular materials for maximum bulk or shear modulus. *Computational Materials Science*, 50(6):1861–1870, 2011.

[56] Yiqiang Wang, Zhen Luo, Nong Zhang, and Zhan Kang. Topological shape optimization of microstructural metamaterials using a level set method. *Computational Materials Science*, 87:178–186, 2014.

[57] Sajad Arabnejad Khanoki and Damiano Pasini. Multiscale design and multiobjective optimization of orthopedic hip implants with functionally graded cellular material. *Journal of biomechanical engineering*, 134(3):031004, 2012.

[58] Pu Zhang, Jakub Toman, Yiqi Yu, Emre Biyikli, Mesut Kirca, Markus Chmielus, and Albert C To. Efficient design-optimization of variable-density hexagonal cellular structure by additive manufacturing: Theory and validation. *Journal of Manufacturing Science and Engineering*, 137(2):021004, 2015.

[59] Erik Andreassen and Jakob Søndergaard Jensen. A practical multiscale approach for optimization of structural damping. *Structural and Multidisciplinary Optimization*, pages 1–10, 2015.

[60] Tong Wu, Kai Liu, and Andres Tovar. Multiphase thermomechanical topology optimization of functionally graded lattice injection molds. In *ASME 2016 International Design Engineering Technical Conferences and Computers and Information in Engineering Conference*, pages V02AT03A036–V02AT03A036. American Society of Mechanical Engineers, 2016.

[61] J Robbins, SJ Owen, BW Clark, and TE Voth. An efficient and scalable approach for generating topologically optimized cellular structures for additive manufacturing. *Additive Manufacturing*, 12:296–304, 2016.

[62] Ling Liu, Jun Yan, and Gengdong Cheng. Optimum structure with homogeneous optimum truss-like material. *Computers & Structures*, 86(13):1417–1425, 2008.

[63] Jiadong Deng, Jun Yan, and Gengdong Cheng. Multi-objective concurrent topology optimization of thermoelastic structures composed of homogeneous porous material. *Structural and Multidisciplinary Optimization*, 47(4):583–597, 2013.

[64] X Yan, X Huang, Y Zha, and YM Xie. Concurrent topology optimization of structures and their composite microstructures. *Computers & Structures*, 133:103–110, 2014.

[65] H Rodrigues, Jose M Guedes, and MP Bendsoe. Hierarchical optimization of material and structure. *Structural and Multidisciplinary Optimization*, 24(1):1–10, 2002.

[66] Charles L Penninger, Neal M Patel, Glen L Niebur, Andrés Tovar, and John E Renaud. A fully anisotropic hierarchical hybrid cellular automaton algorithm to simulate bone remodeling. *Mechanics Research Communications*, 35(1):32–42, 2008.

[67] P.G. Coelho, P.R. Fernandes, H.C. Rodrigues, J.B. Cardoso, and J.M. Guedes. Numerical modeling of bone tissue adaptation-a hierarchical approach for bone apparent density and trabecular structure. *Journal of Biomechanics*, 42(7):830 – 837, 2009.

[68] Pedro G Coelho, João B Cardoso, Paulo R Fernandes, and Hélder C Rodrigues. Parallel computing techniques applied to the simultaneous design of structure and material. *Advances in Engineering Software*, 42(5):219–227, 2011.

[69] Ole Sigmund and S Torquato. Design of smart composite materials using topology optimization. *Smart Materials and Structures*, 8(3):365, 1999.

[70] Yeong-Moo Yi, Sang-Hoon Park, and Sung-Kie Youn. Design of microstructures of viscoelastic composites for optimal damping characteristics. *International Journal of Solids and Structures*, 37(35):4791–4810, 2000.

[71] Qing Li, Grant P Steven, Osvaldo M Querin, and YM Xie. Shape and topology design for heat conduction by evolutionary structural optimization. *International Journal of Heat and Mass Transfer*, 42(17):3361–3371, 1999.

[72] Alberto Donoso. Numerical simulations in 3d heat conduction: minimizing the quadratic mean temperature gradient by an optimality criteria method. *SIAM Journal on Scientific Computing*, 28(3):929–941, 2006.

[73] Allan Gersborg-Hansen, Ole Sigmund, and Robert B Haber. Topology optimization of channel flow problems. *Structural and Multidisciplinary Optimization*, 30(3):181–192, 2005.

[74] Francois H Burger, Jaco Dirker, and Josua P Meyer. Three-dimensional conductive heat transfer topology optimisation in a cubic domain for the volume-to-surface problem. *International Journal of Heat and Mass Transfer*, 67:214–224, 2013.

[75] Shiwei Zhou, Joseph Cadman, Yuhang Chen, Wei Li, Yi Min Xie, Xiaodong Huang, Richard Appleyard, Guangyong Sun, and Qing Li. Design and fabrication of biphasic cellular materials with transport properties–a modified bidirectional evolutionary structural optimization procedure and matlab program. *International Journal of Heat and Mass Transfer*, 55(25):8149–8162, 2012.

[76] Tyler E Bruns. Topology optimization of convection-dominated, steady-state heat transfer problems. *International Journal of Heat and Mass Transfer*, 50(15):2859–2873, 2007.

[77] Younghwan Joo, Ikjin Lee, and Sung Jin Kim. Topology optimization of heat sinks in natural convection considering the effect of shape-dependent heat transfer coefficient. *International Journal of Heat and Mass Transfer*, 109:123–133, 2017.

[78] A Iga, S Nishiwaki, K Izui, and M Yoshimura. Topology optimization for thermal conductors considering design-dependent effects, including heat conduction and convection. *International Journal of Heat and Mass Transfer*, 52(11):2721–2732, 2009.

[79] Tong Wu, Namrata Upadhyaya, Douglas Acheson, and Andres Tovar. Structural optimization of injection molds with lattice cooling. In *ASME 2017 International Design Engineering Technical Conferences and Computers and Information in Engineering Conference*, pages V02BT03A008–V02BT03A008. American Society of Mechanical Engineers, 2017.

[80] Thomas Borrvall and Joakim Petersson. Topology optimization of fluids in stokes flow. *International journal for numerical methods in fluids*, 41(1):77–107, 2003.

[81] James K Guest and Jean H Prévost. Topology optimization of creeping fluid flows using a darcy–stokes finite element. *International Journal for Numerical Methods in Engineering*, 66(3):461–484, 2006.

[82] Vivien J Challis and James K Guest. Level set topology optimization of fluids in stokes flow. *International journal for numerical methods in engineering*, 79(10):1284–1308, 2009.

[83] Seung-Hyun Ha and Seonho Cho. Topological shape optimization of heat conduction problems using level set approach. *Numerical Heat Transfer, Part B: Fundamentals*, 48(1):67–88, 2005.

[84] T Gao, WH Zhang, JH Zhu, YJ Xu, and DH Bassir. Topology optimization of heat conduction problem involving design-dependent heat load effect. *Finite Elements in Analysis and Design*, 44(14):805–813, 2008.

[85] Laurits Højgaard Olesen, Fridolin Okkels, and Henrik Bruus. A high-level programming-language implementation of topology optimization applied to steady-state navier–stokes flow. *International Journal for Numerical Methods in Engineering*, 65(7):975–1001, 2006.

[86] Sebastian Kreissl, Georg Pingen, and Kurt Maute. Topology optimization for unsteady flow. *International Journal for Numerical Methods in Engineering*, 87(13):1229–1253, 2011.

[87] Yongbo Deng, Zhenyu Liu, Ping Zhang, Yongshun Liu, and Yihui Wu. Topology optimization of unsteady incompressible navier–stokes flows. *Journal of Computational Physics*, 230(17):6688–6708, 2011.

[88] James K Guest and Jean H Prévost. Design of maximum permeability material structures. *Computer Methods in Applied Mechanics and Engineering*, 196(4-6):1006–1017, 2007.

[89] Gil Ho Yoon. Topology optimization for turbulent flow with spalart–allmaras model. *Computer Methods in Applied Mechanics and Engineering*, 303:288–311, 2016.

[90] Cetin B Dilgen, Sumer B Dilgen, David R Fuhrman, Ole Sigmund, and Boyan S Lazarov. Topology optimization of turbulent flows. *Computer Methods in Applied Mechanics and Engineering*, 331:363–393, 2018.

[91] Yixian Du, Zhen Luo, Qihua Tian, and Liping Chen. Topology optimization for thermo-mechanical compliant actuators using mesh-free methods. *Engineering Optimization*, 41(8):753–772, 2009.

[92] Weihong Zhang, Jungang Yang, Yingjie Xu, and Tong Gao. Topology optimization of thermoelastic structures: mean compliance minimization or elastic strain energy minimization. *Structural and Multidisciplinary Optimization*, 49(3):417–429, 2014.

[93] Akihiro Takezawa, Gil Ho Yoon, Seung Hyun Jeong, Makoto Kobashi, and Mitsuru Kitamura. Structural topology optimization with strength and heat conduction constraints. *Computer Methods in Applied Mechanics and Engineering*, 276:341–361, 2014.

[94] Joe Alexandersen, Niels Aage, Casper Schousboe Andreasen, and Ole Sigmund. Topology optimisation for natural convection problems. *International Journal for Numerical Methods in Fluids*, 76(10):699–721, 2014.

[95] Joe Alexandersen, Ole Sigmund, and Niels Aage. Large scale three-dimensional topology optimisation of heat sinks cooled by natural convection. *International Journal of Heat and Mass Transfer*, 100:876–891, 2016.

[96] Adriano A Koga, Edson Comini C Lopes, Helcio F Villa Nova, Cicero R de Lima, and Emílio Carlos Nelli Silva. Development of heat sink device by using topology optimization. *International Journal of Heat and Mass Transfer*, 64:759–772, 2013.

[97] Tadayoshi Matsumori, Tsuguo Kondoh, Atsushi Kawamoto, and Tsuyoshi Nomura. Topology optimization for fluid–thermal interaction problems under constant input power. *Structural and Multidisciplinary Optimization*, 47(4):571–581, 2013.

[98] Gilles Marck, Maroun Nemer, and Jean-Luc Harion. Topology optimization of heat and mass transfer problems: laminar flow. *Numerical Heat Transfer, Part B: Fundamentals*, 63(6):508–539, 2013.

[99] Xiaoping Qian and Ercan M Dede. Topology optimization of a coupled thermal-fluid system under a tangential thermal gradient constraint. *Structural and Multidisciplinary Optimization*, 54(3):531–551, 2016.

[100] Casper Schousboe Andreasen and Ole Sigmund. Topology optimization of fluid–structure-interaction problems in poroelasticity. *Computer Methods in Applied Mechanics and Engineering*, 258:55–62, 2013.

[101] Christian Lundgaard, Joe Alexandersen, Mingdong Zhou, Casper Schousboe Andreasen, and Ole Sigmund. Revisiting density-based topology optimization for fluid-structure-interaction problems. *Structural and Multidisciplinary Optimization*, pages 1–27, 2018.

[102] Gil Ho Yoon. Stress-based topology optimization method for steady-state fluid–structure interaction problems. *Computer Methods in Applied Mechanics and Engineering*, 278:499–523, 2014.

[103] James K Guest and Jean H Prévost. Optimizing multifunctional materials: design of microstructures for maximized stiffness and fluid permeability. *International Journal of Solids and Structures*, 43(22-23):7028–7047, 2006.

[104] Vivien J Challis, James K Guest, Joseph F Grotowski, and Anthony P Roberts. Computationally generated cross-property bounds for stiffness and fluid permeability using topology optimization. *International Journal of Solids and Structures*, 49(23-24):3397–3408, 2012.

[105] Haydn NG Wadley. Multifunctional periodic cellular metals. *Philosophical Transactions of the Royal Society A: Mathematical, Physical and Engineering Sciences*, 364(1838):31–68, 2005.

[106] O. Sigmund. Materials with prescribed constitutive parameters: an inverse homogenization problem. *International Journal of Solids and Structures*, 31(17):2313 – 29, Sept. 1994.

[107] MM Neves, H Rodrigues, and J Miranda Guedes. Optimal design of periodic linear elastic microstructures. *Computers & Structures*, 76(1):421–429, 2000.

[108] S Amstutz, SM Giusti, AA Novotny, and EA de Souza Neto. Topological derivative for multi-scale linear elasticity models applied to the synthesis of microstructures. *International Journal for Numerical Methods in Engineering*, 84(6):733–756, 2010.

[109] Erik Andreassen, Boyan S Lazarov, and Ole Sigmund. Design of manufacturable 3d extremal elastic microstructure. *Mechanics of Materials*, 69(1):1–10, 2014.

[110] C.S. Andreasen and O Sigmund. Multiscale modeling and topology optimization of poroelastic actuators. *Smart Mater. Struct.*, 21, 2012.

[111] Felix Fritzen, Liang Xia, Matthias Leuschner, and Piotr Breitkopf. Topology optimization of multiscale elastoviscoplastic structures. *International Journal for Numerical Methods in Engineering*, 106(6):430–453, 2016.

[112] Joe Alexandersen and Boyan S Lazarov. Topology optimisation of manufacturable microstructural details without length scale separation using a spectral coarse basis preconditioner. *Computer Methods in Applied Mechanics and Engineering*, 290:156–182, 2015.

[113] Yangying Zhu, Dion S Antao, Zhengmao Lu, Sivanand Somasundaram, Tiejun Zhang, and Evelyn N Wang. Prediction and characterization of dry-out heat flux in micropillar wick structures. *Langmuir*, 32(7):1920–1927, 2016.

[114] George V Lauder, Dylan K Wainwright, August G Domel, James C Weaver, Li Wen, and Katia Bertoldi. Structure, biomimetics, and fluid dynamics of fish skin surfaces. *Physical Review Fluids*, 1(6):060502, 2016.

[115] Sabuj Mallik, Ndy Ekere, Chris Best, and Raj Bhatti. Investigation of thermal management materials for automotive electronic control units. *Applied Thermal Engineering*, 31(2):355–362, 2011.

[116] John R Wagner, Mrudula C Ghone, Darren W Dawson, and Egidio E Marotta. Coolant flow control strategies for automotive thermal management systems. Technical report, SAE Technical Paper, 2002.

[117] Jack W Judy. Microelectromechanical systems (mems): fabrication, design and applications. *Smart materials and Structures*, 10(6):1115, 2001.

[118] Emmanuel G Collins and Stephen Richter. Linear-quadratic-gaussian-based controller design for hubble space telescope. *Journal of Guidance, Control, and Dynamics*, 18(2):208–213, 1995.

[119] Matteo Bruggi and Alberto Taliercio. Design of masonry blocks with enhanced thermomechanical performances by topology optimization. *Construction and Building Materials*, 48:424–433, 2013.

[120] Tong Gao and Weihong Zhang. Topology optimization involving thermo-elastic stress loads. *Structural and Multidisciplinary Optimization*, 42(5):725–738, 2010.

[121] Mingdong Zhou, Joe Alexandersen, Ole Sigmund, and Claus BW Pedersen. Industrial application of topology optimization for combined conductive and convective heat transfer problems. *Structural and Multidisciplinary Optimization*, 54(4):1045–1060, 2016.

[122] Tong Wu, Suchana A Jahan, Praveen Kumaar, Andres Tovar, Hazim El-Mounayri, Yi Zhang, Jing Zhang, Doug Acheson, Kim Brand, and Razi Nalim. A framework for optimizing the design of injection molds with conformal cooling for additive manufacturing. *Procedia Manufacturing*, 1:404–415, 2015.

[123] Karen N Son, Justin A Weibel, Vellaisamy Kumaresan, and Suresh V Garimella. Design of multifunctional lattice-frame materials for compact heat exchangers. *International Journal of Heat and Mass Transfer*, 115:619–629, 2017.

[124] Douglas T Queheillalt, Gerardo Carbajal, GP Peterson, and Haydn NG Wadley. A multifunctional heat pipe sandwich panel structure. *International Journal of Heat and Mass Transfer*, 51(1-2):312–326, 2008.

[125] SS Feng, JJ Kuang, T Wen, TJ Lu, and K Ichimiya. An experimental and numerical study of finned metal foam heat sinks under impinging air jet cooling. *International Journal of Heat and Mass Transfer*, 77:1063–1074, 2014.

[126] L-P Lefebvre, John Banhart, and David C Dunand. Porous metals and metallic foams: current status and recent developments. *Advanced engineering materials*, 10(9):775–787, 2008.

[127] Gianni Campoli, MS Borleffs, S Amin Yavari, R Wauthle, Harrie Weinans, and Amir Abbas Zadpoor. Mechanical properties of open-cell metallic biomaterials manufactured using additive manufacturing. *Materials & Design*, 49:957–965, 2013.

[128] Xi Zhao, Mingdong Zhou, Ole Sigmund, and Casper Schousboe Andreasen. A "poor man's approach" to topology optimization of cooling channels based on a darcy flow model. *International Journal of Heat and Mass Transfer*, 116:1108–1123, 2018.

[129] Fridolin Okkels and Henrik Bruus. Scaling behavior of optimally structured catalytic microfluidic reactors. *Physical Review E*, 75(1):016301, 2007.

[130] Kentaro Yaji, Takayuki Yamada, Masato Yoshino, Toshiro Matsumoto, Kazuhiro Izui, and Shinji Nishiwaki. Topology optimization in thermal-fluid flow using the lattice boltzmann method. *Journal of Computational Physics*, 307:355–377, 2016.

[131] David O. Kazmer. Injection mold design engineering. In David O. Kazmer, editor, *Injection Mold Design Engineering (Second Edition)*, pages I – XXIV. Hanser, second edition edition, 2016.

[132] Júlio C Viana, Noelle Billon, and António M Cunha. The thermomechanical environment and the mechanical properties of injection moldings. *Polymer Engineering & Science*, 44(8):1522–1533, 2004.

[133] H. Rodrigues, J.M. Guedes, and M. P. Bendsøe. Hierarchical optimization of material and structure. *Structural and Multidisciplinary Optimization*, 24(1):1–10, 2002.

[134] P.G. Coelho, P.R. Fernandes, J.M. Guedes, and H.C. Rodrigues. A hierarchical model for concurrent material and topology optimisation of three-dimensional structures. *Structural and Multidisciplinary Optimization*, 35(2):107 – 115, 2008.

[135] Ling Liu, Jun Yan, and GengDong Cheng. Optimum structure with homogeneous optimum truss-like material. *Computers and Structures*, 86(13-14):1417–1425, 2008.

[136] B. Hassani and E. Hinton. A review of homogenization and topology optimization. i. homogenization theory for media with periodic structure. *Computers and Structures*, 69(6):707 – 17, 1998.

[137] B. Hassani and E. Hinton. A review of homogenization and topology optimization. ii. analytical and numerical solution of homogenization equations. *Computers and Structures*, 69(6):719 – 38, 1998.

[138] E. Andreassen and C.S. Andreasen. How to determine composite material properties using numerical homogenization. *Computational Materials Science*, 83:488 – 95, 2014.

[139] Young Seok Song and Jae Ryoun Youn. Evaluation of effective thermal conductivity for carbon nanotube/polymer composites using control volume finite element method. *Carbon*, 44(4):710–717, 2006.

[140] Thomas Borrvall. Topology optimization of elastic continua using restriction. *Archives of Computational Methods in Engineering*, 8(4):351–385, 2001.

[141] Katsuyuki Suzuki and Noboru Kikuchi. A homogenization method for shape and topology optimization. *Computer methods in applied mechanics and engineering*, 93(3):291–318, 1991.

[142] Kenjiro Terada, Muneo Hori, Takashi Kyoya, and Noboru Kikuchi. Simulation of the multi-scale convergence in computational homogenization approaches. *International Journal of Solids and Structures*, 37(16):2285–2311, 2000.

[143] Zvi Hashin and Shmuel Shtrikman. A variational approach to the theory of the effective magnetic permeability of multiphase materials. *Journal of applied Physics*, 33(10):3125–3131, 1962.

[144] Zvi Hashin and Shmuel Shtrikman. A variational approach to the theory of the elastic behaviour of multiphase materials. *Journal of the Mechanics and Physics of Solids*, 11(2):127–140, 1963.

[145] Lars-Erik Rännar, Anders Glad, and Claes-Göran Gustafson. Efficient cooling with tool inserts manufactured by electron beam melting. *Rapid Prototyping Journal*, 13(3):128–135, 2007.

[146] Yunlong Tang, Yunlong Tang, Yaoyao Fiona Zhao, and Yaoyao Fiona Zhao. A survey of the design methods for additive manufacturing to improve functional performance. *Rapid Prototyping Journal*, 22(3):569–590, 2016.

[147] Gabriel Antonio Mendible, Gabriel Antonio Mendible, Jack A Rulander, Jack A Rulander, Stephen P Johnston, and Stephen P Johnston. Comparative study of rapid and conventional tooling for plastics injection molding. *Rapid Prototyping Journal*, 23(2):344–352, 2017.

[148] Jikai Liu and Yongsheng Ma. A survey of manufacturing oriented topology optimization methods. *Advances in Engineering Software*, 100:161–175, 2016.

[149] E.M. Dede. Optimization and design of a multipass branching microchannel heat sink for electronics cooling. *Journal of Electronic Packaging*, 134(4):041001 (10 pp.), 2012.

[150] F Calignano. Design optimization of supports for overhanging structures in aluminum and titanium alloys by selective laser melting. *Materials & Design*, 64:203–213, 2014.

[151] Tong Wu, Kai Liu, and Andres Tovar. Multiphase topology optimization of lattice injection molds. *Computers & Structures*, 192:71–82, 2017.

[152] Ole Sigmund. Materials with prescribed constitutive parameters: an inverse homogenization problem. *International Journal of Solids and Structures*, 31(17):2313–2329, 1994.

[153] Liang Xia and Piotr Breitkopf. Design of materials using topology optimization and energy-based homogenization approach in matlab. *Structural and multidisciplinary optimization*, 52(6):1229–1241, 2015.

[154] Erik Andreassen and Casper Schousboe Andreasen. How to determine composite material properties using numerical homogenization. *Computational Materials Science*, 83:488–495, 2014.

[155] Kai Liu and Andrés Tovar. An efficient 3d topology optimization code written in matlab. *Structural and Multidisciplinary Optimization*, 50(6):1175–1196, 2014.

[156] Z Hugh Fan, Shakuntala Mangru, Russ Granzow, Paul Heaney, Wen Ho, Qianping Dong, and Rajan Kumar. Dynamic dna hybridization on a chip using paramagnetic beads. *Analytical chemistry*, 71(21):4851–4859, 1999.

[157] Mark A Hayes, Nolan A Polson, Allison N Phayre, and Antonio A Garcia. Flow-based microimmunoassay. *Analytical chemistry*, 73(24):5896–5902, 2001.

[158] Jin-Woo Choi, Kwang W Oh, Jennifer H Thomas, William R Heineman, H Brian Halsall, Joseph H Nevin, Arthur J Helmicki, H Thurman Henderson, and Chong H Ahn. An integrated microfluidic biochemical detection system for protein analysis with magnetic bead-based sampling capabilities. *Lab on a Chip*, 2(1):27–30, 2002.

[159] Guifeng Jiang and D Jed Harrison. mrna isolation in a microfluidic device for eventual integration of cdna library construction. *Analyst*, 125(12):2176–2179, 2000.

[160] Yan-Jun Liu, Shi-Shang Guo, Zhi-Ling Zhang, Wei-Hua Huang, Damien Baigl, Min Xie, Yong Chen, and Dai-Wen Pang. A micropillar-integrated smart microfluidic device for specific capture and sorting of cells. *Electrophoresis*, 28(24):4713–4722, 2007.

[161] Sunitha Nagrath, Lecia V Sequist, Shyamala Maheswaran, Daphne W Bell, Daniel Irimia, Lindsey Ulkus, Matthew R Smith, Eunice L Kwak, Subba Digumarthy, Alona Muzikansky, et al. Isolation of rare circulating tumour cells in cancer patients by microchip technology. *Nature*, 450(7173):1235, 2007.

[162] Eric Stern, Aleksandar Vacic, Nitin K Rajan, Jason M Criscione, Jason Park, Bojan R Ilic, David J Mooney, Mark A Reed, and Tarek M Fahmy. Label-free biomarker detection from whole blood. *Nature nanotechnology*, 5(2):138, 2010.

[163] Matthew Moran, Danielle Wesolek, Bruk Berhane, and Keith Rebello. Microsystem cooler development. In *2nd International Energy Conversion Engineering Conference*, page 5611, 2004.

[164] Dongzhi Guo, Alan JH McGaughey, Jinsheng Gao, Gary K Fedder, Minyoung Lee, and Shi-Chune Yao. Multiphysics modeling of a micro-scale stirling refrigeration system. *International Journal of Thermal Sciences*, 74:44–52, 2013.

[165] Gregory D Bixler and Bharat Bhushan. Bioinspired rice leaf and butterfly wing surface structures combining shark skin and lotus effects. *Soft matter*, 8(44):11271–11284, 2012.

[166] Gregory D Bixler and Bharat Bhushan. Fluid drag reduction and efficient self-cleaning with rice leaf and butterfly wing bioinspired surfaces. *Nanoscale*, 5(17):7685–7710, 2013.

[167] Humberto Bocanegra Evans, Serdar Gorumlu, Burak Aksak, Luciano Castillo, and Jian Sheng. Holographic microscopy and microfluidics platform for measuring wall stress and 3d flow over surfaces textured by micro-pillars. *Scientific reports*, 6:28753, 2016.

[168] Humberto Bocanegra Evans, Ali M Hamed, Serdar Gorumlu, Ali Doosttalab, Burak Aksak, Leonardo P Chamorro, and Luciano Castillo. Engineered bio-inspired coating for passive flow control. *Proceedings of the National Academy of Sciences*, 115(6):1210–1214, 2018.

[169] PG Coelho, JM Guedes, and HC Rodrigues. Multiscale topology optimization of bi-material laminated composite structures. *Composite Structures*, 132:495–505, 2015.

[170] Liang Xia and Piotr Breitkopf. A reduced multiscale model for nonlinear structural topology optimization. *Computer Methods in Applied Mechanics and Engineering*, 280:117–134, 2014.

[171] Junuthula Narasimha Reddy and David K Gartling. *The finite element method in heat transfer and fluid dynamics*. CRC press, 2010.

[172] Khaled S Al-Athel, Shahzada P Aly, Abul Fazal M Arif, and Javad Mostaghimi. 3d modeling and analysis of the thermo-mechanical behavior of metal foam heat sinks. *International Journal of Thermal Sciences*, 116:199–213, 2017.

[173] M Paknezhad, AM Rashidi, T Yousefi, and Z Saghir. Effect of aluminum-foam heat sink on inclined hot surface temperature in the case of free convection heat transfer. *Case studies in thermal engineering*, 10:199–206, 2017.

[174] Lawrence E Murr, Sara M Gaytan, Diana A Ramirez, Edwin Martinez, Jennifer Hernandez, Krista N Amato, Patrick W Shindo, Francisco R Medina, and Ryan B Wicker. Metal fabrication by additive manufacturing using laser and electron beam melting technologies. *Journal of Materials Science & Technology*, 28(1):1–14, 2012.

[175] Christiane Beyer and Dustin Figueroa. Design and analysis of lattice structures for additive manufacturing. *Journal of Manufacturing Science and Engineering*, 138(12):121014, 2016.

[176] Ronald S Bunker. Latticework (vortex) cooling effectiveness: Part 1—stationary channel experiments. In *ASME Turbo Expo 2004: Power for Land, Sea, and Air*, pages 909–918. American Society of Mechanical Engineers, 2004.

[177] Sumanta Acharya, Fuguo Zhou, Jonathan Lagrone, Gazi Mahmood, and Ronald S Bunker. Latticework (vortex) cooling effectiveness: Rotating channel experiments. *Journal of turbomachinery*, 127(3):471–478, 2005.

[178] Yu Rao and Shusheng Zang. Flow and heat transfer characteristics in lattice-work cooling channels with dimple vortex generators. *Journal of Turbomachinery*, 136(2):021017, 2014.

[179] KM Au and KM Yu. A scaffolding architecture for conformal cooling design in rapid plastic injection moulding. *The International Journal of Advanced Manufacturing Technology*, 34(5-6):496–515, 2007.

[180] KM Au and KM Yu. Modeling of multi-connected porous passageway for mould cooling. *Computer-Aided Design*, 43(8):989–1000, 2011.

[181] Hadley Brooks and Kevin Brigden. Design of conformal cooling layers with self-supporting lattices for additively manufactured tooling. *Additive Manufacturing*, 11:16 – 22, 2016.

[182] Ole Sigmund. Design of multiphysics actuators using topology optimization–part i: One-material structures. *Computer methods in applied mechanics and engineering*, 190(49):6577–6604, 2001.

[183] Ole Sigmund. Design of multiphysics actuators using topology optimization–part ii: Two-material structures. *Computer methods in applied mechanics and engineering*, 190(49-50):6605–6627, 2001.

[184] J-H Choi, S-H Choi, D Park, C-H Park, B-O Rhee, and D-H Choi. Design optimization of an injection mold for minimizing temperature deviation. *International Journal of Automotive Technology*, 13(2):273–277, 2012.

[185] Tong Wu, Suchana A Jahan, Yi Zhang, Jing Zhang, Hazim Elmounayri, and Andres Tovar. Design optimization of plastic injection tooling for additive manufacturing. *Procedia Manufacturing*, 10:923–934, 2017.

[186] JC Lin. Optimum cooling system design of a free-form injection mold using an abductive network. *Journal of Materials Processing Technology*, 120(1-3):226–236, 2002.

[187] Alban Agazzi, Vincent Sobotka, Ronan LeGoff, and Yvon Jarny. Optimal cooling design in injection moulding process–a new approach based on morphological surfaces. *Applied Thermal Engineering*, 52(1):170–178, 2013.

[188] Yu Wang, Kai-Min Yu, Charlie CL Wang, and Yunbo Zhang. Automatic design of conformal cooling circuits for rapid tooling. *Computer-Aided Design*, 43(8):1001–1010, 2011.

VITA

EDUCATION

Ph.D., Mechanical Engineering

Purdue University, Indiana, USA May 2019

Master of Science, Infrastructure and Environmental Engineering

Chalmers University of Technology, Sweden July 2019

Bachelor of Science, Hydraulic and Hydroelectric Engineering

Tianjin University, China July 2007

Bachelor of Engineering, International Project Management

Tianjin University, China July 2009

PROFESSIONAL EXPERIENCE

IUPUI August 2013 – May 2019

Dept. of Mechanical and Energy, Indianapolis, IN

- Develop CAD and CAE software for the research group
- Writing high-quality research articles such as journal and conference paper and technical report, and present research findings in academic conferences.
- Co-instructor of course Topology optimization, Design of Complex and Origami Structures, Optimal Design of Complex Mechanical Systems and Additive Manufacturing.

Tianjin Innovative Financial Investment Co. Ltd, Tianjin, China

Dept. of Urban planning and Construction June 2012 – June 2013

- Policy and urban planning strategy research and promotion of sustainable city development.
- Organize and draft APEC proposal APEC Low carbon model town capability building development,

COWI Engineering Consultant June 2012 – June 2013

Dept. of energy, Beijing, China

- Provide optimal solution for district energy network system.
- Report and present solutions and cooperate with clients optimal solution for district energy network system.

Tianjin Innovative Construction Material Research Institute June 2007 – June 2008

Tianjin, China

- Structural design of concrete-steel structure.

PUBLICATIONS

- **Wu, T.**, & Tovar, A. (2018) Multiscale, thermomechanical topology optimization of self-supporting cellular structures for porous injection molds , Rapid Prototyping Journal, https://doi.org/10.1108/RPJ-09-2017-0190.
- Liu, K., **W, T.**, Detwiler, D., Panchal J., and Tovar, A. (2018) Design of categorical multimaterial structures using meta-model-based optimization with mixed design variables. Journal of Mechanical Design (accepted)
- **Wu, T.**, & Tovar, A. Design of conformal cooling channels using a versatile thermal-fluid topology optimization and application in Injection molds. (submitted to Journal of Mechanical Design).
- **Wu, T.**, & Tovar, A. Design of conformal cooling channels using a versatile thermal-fluid topology optimization and application in Injection molds. (submitted to Journal of Mechanical Design).

- **Wu, T.**, Liu, K., & Tovar, A. (2017). Multiphase topology optimization of lattice injection molds. Computers & Structures, 192, 71-82.
- **Wu, T.**, Jahan, S. A., Zhang, Y., Zhang, J., Elmounayri, H., & Tovar, A. (2017). Design optimization of plastic injection tooling for additive manufacturing. Procedia Manufacturing, 10, 923-934.
- Jahan, S. A., **Wu, T.**, Zhang, Y., Zhang, J., Tovar, A., & Elmounayri, H. (2017). Thermo-mechanical design optimization of conformal cooling channels using design of experiments approach. Procedia Manufacturing, 10, 898-911.
- **Wu, T.**, Jahan, S. A., Kumaar, P., Tovar, A., El-Mounayri, H., Zhang, Y., ... & Nalim, R. (2015). A framework for optimizing the design of injection molds with conformal cooling for additive manufacturing. Procedia Manufacturing, 1, 404-415.
- Jahan, S. A., **Wu, T.**, Zhang, Y., El-Mounayri, H., Tovar, A., Zhang, J., ... & Lee, W. H. (2016). Implementation of conformal cooling & topology optimization in 3D printed stainless steel porous structure injection molds. Procedia Manufacturing, 5, 901-915.
- **Wu, T.**, Joel N, Acheson D, Tovar A. (2019) Thermomechanical Topology Optimization of Lattice Heat Transfer Structure Including Nature Convection and Design-dependent Heat Source. ASME. International Design Engineering Technical Conferences and Computers and Information in Engineering Conference (accepted)
- **Wu, T.**, & Tovar, A. (2018) Design for Additive Manufacturing of Conformal Cooling Channels Using Thermal-Fluid Topology Optimization and Application in Injection Molds. ASME. International Design Engineering Technical Conferences and Computers and Information in Engineering Conference, Volume 2B: 44th Design Automation Conference (): V02BT03A007. doi:10.1115/DETC2018-85511.
- **Wu, T.**, Upadhyaya N, Acheson D, Tovar A. (2017) Structural Optimization of Injection Molds With Lattice Cooling. ASME. International Design Engineering Technical Conferences and Computers and Information in Engineering Conference, Volume 2B: 43rd Design Automation Conference (): V02BT03A008. doi:10.1115/DETC2017-67975.

- **Wu, T.**, Brand, K., Hewitt, D., & Tovar, A. (2017, June). Multiscale, Thermomechanical Topology Optimization of Cellular Structures for Porous Injection Molds. In World Congress of Structural and Multidisciplinary Optimisation. Springer, Cham.
- **Wu, T.**, Liu, K., & Tovar, A. Multiscale thermomechanical topology optimization and additive manufacturing of lattice injection mold with conformal cooling. 5th International Conference on Engineering Optimization, Iguassu Falls, Brazil, 19-23 Jun 2016.
- **Wu, T.**, Liu K, Tovar A. (2016) Multiphase Thermomechanical Topology Optimization of Functionally Graded Lattice Injection Molds. ASME. International Design Engineering Technical Conferences and Computers and Information in Engineering Conference, Volume 2A: 42nd Design Automation Conference (): V02AT03A036. doi:10.1115/DETC2016-60538.

PUBLICATIONS

- IURTC Project 2016-104: Porous 3D Topology Optimization Design Algorithm: A. Tovar, K. Liu, and **T. Wu**, 2016.
- IURTC Project 2015-080: Computational Design Algorithm: Thermo-Mechanical Topology Optimization: A. Tovar, K. Liu, and **T. Wu**, 2015.
- IURTC Project 2015-178: Algorithm for Modeling Solids as Porous Materials in CAD: A. Tovar, K. Liu, and **T. Wu**, 2015.